FLUID-FLUID, FLUID-MINERAL INTERACTIONS AND REACTIVE TRANSPORT IN POROUS MEDIA

A DISSERTATION
SUBMITTED TO THE DEPARTMENT OF ENERGY RESOURCES ENGINEERING
AND THE COMMITTEE ON GRADUATE STUDIES
OF STANFORD UNIVERSITY
IN PARTIAL FULFILLMENT OF THE REQUIREMENTS
FOR THE DEGREE OF
DOCTOR OF PHILOSOPHY

Wen Song

November 2018

I certify that I have read this dissertation and that, in my opinion, it is fully adequate in scope and quality as a dissertation for the degree of Doctor of Philosophy.

Anthony Kovscek, Primary Adviser

I certify that I have read this dissertation and that, in my opinion, it is fully adequate in scope and quality as a dissertation for the degree of Doctor of Philosophy.

Sally Benson

I certify that I have read this dissertation and that, in my opinion, it is fully adequate in scope and quality as a dissertation for the degree of Doctor of Philosophy.

Hamdi Tchelepi

Approved for the Stanford University Committee on Graduate Studies.

Patricia J. Gumport, Vice Provost for Graduate Education

This signature page was generated electronically upon submission of this dissertation in electronic format. An original signed hard copy of the signature page is on file in University Archives.

Abstract

Subsurface flow of multiphase, multicomponent fluids is complex and not well understood. Pore-scale phenomena dictate the overall behavior of the reservoir. The root of multiphase, multicomponent pore-scale dynamics lies in fluid-fluid and fluid-mineral interactions at the microscopic scale. Fundamental understanding of the pore-scale interactions between the various phases and components in subsurface formations is essential to optimize the design of subsurface energy and environmental resources. Management methods of subsurface resources, for example improved oil recovery and CO_2 storage security, are assessed in terms of recovery effectiveness, economic benefit, and cost. These factors are all strewn with open questions in complex fluid transport through porous rock materials.

To address questions of fluid-fluid and fluid-mineral interactions at the fundamental pore-level, microfluidics, or the study of fluids at the sub-millimeter scale, is well positioned to contribute improved understanding. Specifically, microfluidics lends a direct eye into the microscale world of porous materials. In this work, microfluidics with representative geometry, length scales, and, importantly, surface mineralogy, are developed and used to delineate the fundamental mechanisms dictating the pore scale fluid behavior of multiphase, reactive fluid transport through porous materials. Fundamental mechanisms dictating (i) low salinity waterflooding, a method to improve oil recovery with low economic and environmental costs; (ii) reactive transport, important to the assessment and design of geological CO_2 storage security; and (iii)

miscible fluid interactions, of industrial interest to heavy oil recovery are delineated in this work. The following describes each contribution briefly.

First, low salinity waterflooding is a promising technique to increase oil recovery in an economic manner. The fundamental mechanisms that dictate this process, however, are poorly understood due to conflicting core flooding and field evidence. It has been suggested that the presence of clay significantly impacts pore wettability and low salinity oil recovery from sandstones. Direct visualization of the pore-scale dynamics during low salinity waterflooding is required to provide a mechanistic understanding of the low salinity effect. In this work, two-dimensional silicon microfluidic networks with representative pore geometry (*i.e.*, micromodels) are modified to achieve the surface characteristics required for representative crude oil, brine, and rock interactions. Specifically, clay particles are deposited into the micromodel pore space to enable direct pore-scale, real-time visualization of fluid-solid interactions with representative pore-geometry and realistic surface interactions between the reservoir fluids and the formation rock. The surface functionalized micromodels are then used to determine the conditions at which stably adhered clay particles detach and to study the pore-level interactions between the crude oil, brine, and solid surfaces during aging and during low salinity brine injection. The experimental results provide a basis for improving the basic understanding of the mechanisms at play. Pore-scale flow simulation is used to corroborate experimental observations of the dominant mechanism(s) at play during low salinity waterflooding in sandstones. Mechanistic understanding of pore-level behavior sets the basis for upscaling and informing the design of optimal injection fluids at the field scale.

Second, formation damage is observed during field-scale low salinity waterflooding due to fine clay particles mobilization. The overall effect on the pore-scale, and its impact on oil recovery, is not well understood. Using the clay-functionalized micromodel developed in this work, the mobilization of clay particles, its impact on flow paths,

and its effect on oil recovery is investigated. Pressure measurements showed 6-fold reductions in permeability as a result of kaolinite migration and flow path blockage under low salinity conditions. Swelling of montmorillonite clay particles were observed at low salinities. Significantly, pores most susceptible to particle mobilization and flow path blockage are correlated inversely with improved oil recovery. Flow diversion due to preferential flow path blockage is proposed as a mechanism dictating improved oil recovery at low salinities.

Third, evolution of pore-surface wettability, or, aging, and the interplay between clay minerals and the crude oil and brine remain an open question in creating initial subsurface reservoir conditions in the laboratory and in understanding the underlying mechanisms of the low salinity effect. The ability to recreate wetting and fluid-mineral conditions similar to realistic subsurface systems is central to the design of improved oil recovery methods. In this work, we provide direct observation of water-wet surfaces shift towards mixed-wettability due to attraction between charged clay particles and crude oil. Low salinity waterflooding of this aged system reveals a new Pickering emulsification mechanism by which preferential flow paths are obstructed, leading to flow diversion through oil-filled pores to improve overall oil recovery.

Fourth, transport through carbonates is complicated by the reactive nature of the rock. Carbonates are reactive and highly susceptible to dissolution. Formation stimulation (*i.e.*, acidizing) and CO_2 storage involve the flow of acidic fluids through the carbonate pore space. Importantly, reactive flow alters both the surface properties of the pore space and the pore geometry. Dissolution and flow behavior at the pore scale must be understood to engineer effective formation stimulation and safe CO_2 storage projects. In this work, calcite-functionalized microfluidic systems are developed and used to delineate the interplay between dissolution, flow, and surface wettability. Specifically, two-dimensional calcite-functionalized micromodels with representative

pore geometry and surface properties are developed in this work to study the dissolution of carbonates under acidic flows. Significantly, a new mechanism is discovered whereby the reaction product, CO_2, is wetted on the reactive grain surface and protects the grain from further dissolution. Experiments show similar effects at a range of temperatures, pressures, and acidities corresponding to surface and subsurface conditions. To further delineate the conditions required for the grain-engulfment effect to dominate, a polymer-based non-reactive microchannel containing an embedded reactive calcite post is developed. Flow regimes corresponding to the observed grain-engulfment mechanism in porous media were delineated using the one-dimensional reactive transport devices and provide a first order understanding for large-scale CO_2 storage security assessments.

Fifth, miscible fluid interactions underlie many physical processes in natural and engineered systems. Injection of solvents that are miscible with crude oil, or solvent-enhanced oil recovery, aims to improve heavy-oil recovery that tends to be highly viscous and immobile. This work investigates the interactions between the fluids under microconstrained geometries similar to geological porous media. Importantly, spontaneous fingering between the crude oil with complex composition and the solvent is observed. That is, fractal-like fingers are generated in the absence of an applied external pressure gradient, i.e., zero imposed Peclet number. The surprising dynamics observed are a result of the complex composition of the crude oil; light crude-oil components are mobile and are exchanged with the solvent phase while heavy crude-oil components are less so and remain. Recursive diffusion-driven mass exchange leads to local instabilities at the interface that result in differences in dynamic interfacial tension along the interface and leads to fractal-like fingering. The resulting Marangoni flow enhances the mass exchange until components in the crude oil phase reach local equilibrium with those in the solvent phase.

The surface-functionalized devices developed in this work enables a wide range of

investigations to the fundamental mechanisms dictating transport through subsurface systems. Importantly, the new fundamental mechanisms delineated in this work are of fundamental importance to the understanding and design subsurface energy and environmental resources management and to the broader field of engineering science.

Acknowledgments

First and foremost, I thank my advisor, Professor Anthony R. Kovscek for his guidance and support throughout my academic and professional pursuits. Tony, thank you for educating me as an academic, a teacher, and on the meaning of being a scholar. Importantly, thank you for showing me the power of honesty, truth, and fairness. You are a true mentor and role model, and I hope to represent you well as your student and as an educator in my own career.

I am blessed to be championed by many mentors and teachers across the Department of Energy Resources Engineering, the Schools of Earth, Energy, and Environmental Sciences and Engineering, and through my service with the Stanford Energy Club. In particular, I thank the members of my committee, Professors Hamdi Tchelepi, Sally M. Benson, John O. Dabiri, and Arun Majumdar, for their guidance throughout my education and for their comments on this work. I am grateful to Professor John O. Dabiri for being my advisor in my pursuit of the Ph.D. minor in Mechanical Engineering. I thank Professors Roland Horne, Lou Durlofsky, Lynn Orr, Adam Brandt, Robert Lindblom, and the faculty members in general of the department of Energy Resources Engineering for their dedication to excellence in teaching and their continued support of me throughout my Ph.D. and my future career. I thank Professor Martin Ferno for hosting my research visit to Norway. Further, I am fortunate to have interacted with many outstanding faculty, staff, and student

leaders during my involvement with the Stanford Energy Club, including Leigh Johnson, Jimmy Chen, Cindy Williams, and Dian Grueneich, and I am grateful for the opportunities and friendships that I have been blessed with from that community. I thank the ERE staff and the lab members of the SUPRI-A research group for their support in my research and academic endeavors.

I am grateful to the Hormoz and Fariba Ameri Graduate Education Fellowship in Earth Sciences and the Gerald J. Lieberman Fellowship for supporting my graduate studies financially. Support from the Stanford University Petroleum Research Institute (SUPRI-A) Industrial Affiliates is also acknowledged.

I thank my friends and colleagues who helped me and supported me through the community that we built and for educating me outside of academics. In particular, I wish to acknowledge Thomas C. Underwood, Halldora Gudmundsdottir, Olga Fuks, Negar Nazari, Matthias Cremon, Mustafa Al Ibrahim, Ahinoam Pollack, Amir Delgoshaie, Kelly Guan, Larry Jin, Holger Teichgraeber, Forest Rui Jiang, Chuan Tian, Raja Ramesh, Robert Kasse, Rahul Kini, Austin Sendek, Arnav Mariwala, Paricha Duangtaweesub, Donghee Song, Rachel Orsini, Sindhu Sreedhara, Jacques de Chalendar, Malcolm Bean, Alexander Piggott, Jingfan Wang, Beibei Wang, Marguerite Graveleau, Lewis Li, Tim Anderson, Jack Norbeck, Phil Brodrick, Jacob Englander, Bryce Anzelmo, Chris Zahasky, Charles Kang, Laura Froute, and Anshuman Pradhan for making my graduate education an unforgettable experience. Last, and importantly, I am forever grateful to my family who taught me right from wrong, and who gave me the love and courage to pursue my dreams.

Contents

List of Tables

List of Figures

Chapter 1

Introduction

1.1 Global Energy and Environmental Challenges

Energy, and access to reliable energy in particular, underlies global societal challenges in health, the environment, and poverty. The grand challenge of supplying reliable energy to meet rising societal demands while minimizing deleterious environmental impacts, therefore, is one of the most pressing global challenges that society faces in the 21st century.

Current energy infrastructure relies heavily on fossil fuels [1]. Specifically, transportation, aviation, manufacturing, and plastics are reliant upon petroleum liquids such as crude oil, extra-heavy oil, and bitumen. Associated with industrial productivity are CO_2 emissions to the atmosphere that contribute to climate change. Integration of renewable resources into the current energy infrastructure and storage of industrially produced CO_2 in the subsurface present opportunities to curb the associated environmental impacts.

Despite global efforts to advance renewable technology, global petroleum liquids consumption continues to increase, growing from 87 million barrels per day (b/d) in 2010 to 100 million b/d in 2018 [2]. The estimate of the petroleum liquids consumption

is projected to reach 115 million b/d by 2040 [2, 1]. With growing demands, methods of petroleum resources recovery must be developed that have lesser environmental impacts. It is important to recognize that the combined oil recovery from primary pressure-driven and secondary brine injection processes, the methods most used in the industry, are limited to 15 to 40 % of the original oil in place (OOIP) [3]. That is, the majority (60 to 85 %) of the available oil is not extracted.

Improved oil recovery methods aim to recover the remaining resource. Effective oil recovery and CO_2 storage, however, are challenged by the complexity of geological systems. First, the behavior of fluids in subsurface systems are described at multiple scales (i.e., multi-scale physics). Specifically, petroleum and CO_2 storage reservoirs are porous rock material that span several kilometers in the subsurface. The pore spaces of the geological reservoir material, however, are on the sub-millimeter length-scale. Fundamental understanding of the dynamics of subsurface reservoir engineering processes such as oil recovery and CO_2 storage therefore relies on delineation of the underlying pore-scale dynamics.

Second, heterogeneities in the geological reservoir material complicate fluid transport. Structural and compositional complexities such as grain- and pore-size distribution, pore surface morphology, and grain mineralogy are inherent in subsurface reservoir materials as a result of the natural geological deposition process. Specifically, mineralogically complex materials such as charged clay micro- and nano-particles, reactive carbonate minerals, and low permeability shale complicate the dynamics of fluid transport through fines migration, pore-plugging and formation damage, reactive transport, and complex fluid behavior in nanoscale pores. Thorough understanding of fluid-mineral interactions are therefore of fundamental interest to assess and design subsurface reservoir engineering processes.

Third, subsurface fluids are complex. In enhanced oil recovery, oil-containing pores are generally co-occupied by formation brine, crude oil, and an injection fluid.

That is, fluids of multiple phases are present in the porous medium. Moreover, reservoir fluids tend to be complex in composition. Thermodynamic and transport behavior of multi-component fluids, for example reservoir-scale flow patterns due to immiscible and miscible displacements and brine-acidification in the case of CO_2 storage, are complicated to predict and thus require studies to provide fundamental understanding.

Pore-level dynamics at the sub-millimeter length-scale dictate the fundamental transport and behavior of subsurface systems. To improve oil recovery from the earth, it is therefore of critical importance to first delineate the fundamental fluid-fluid and fluid-mineral interactions in subsurface systems. Fluid-fluid and fluid-mineral interactions assessed in this dissertation are (i) the interactions between crude oil, brine, and clay in the interest of identifying the underlying mechanisms dictating the low salinity effect in clay-rich sandstone, (ii) the reactive transport of acidified brine through carbonate porous materials in the interest of assessing CO_2 storage security, and (iii) the interfacial dynamics between two miscible fluids in the interest of understanding solvent-enhanced oil recovery. The following subsections provide context towards each theme.

1.2 Low Salinity Waterflooding

Low salinity waterflooding is a promising technique for increasing oil recovery from sandstone reservoirs, especially in an economic manner. Tang and Morrow [4] first suggested the use of smart water injection, i.e., injection of brine that is compositionally dissimilar from that of the formation brine, either with different ions or reduced concentration of ions, to increase oil recovery in sandstone cores. Since then, many experiments have been performed at the core and reservoir levels with mixed results. Specifically, core flooding experiments suggest that low salinity waterflooding may

lead to additional recovery of 5-20% of the original oil in place (OOIP) [5], while other experiments have shown little to no production response to low salinity brine injection.

Several mechanisms have been proposed to delineate the increase in oil production as a result of low salinity water injection (i.e., the low salinity effect), however significant disagreement exists among the literature. The current lack of understanding in the mechanisms dictating the low salinity effect is hindering our ability to (i) predict which reservoirs will respond to low salinity brine injection, and (ii) predict the recovery response of the reservoir. The remainder of this section presents a review of the necessary conditions for the low salinity effect as well as experiments and theories from the literature that aim to explain this phenomenon.

1.2.1 Necessary Conditions for the Low Salinity Effect

Crude oil/ brine/ rock (COBR) interactions are critical to the response of the reservoir to low salinity waterflooding [4, 6, 7, 8, 9]. Previous studies in the literature show that the necessary conditions for increased oil production with decreased injection brine salinity are: (i) crude oils with charged polar components, (ii) the presence of potentially mobile clay particles, and (iii) the establishment of initial reservoir condition [4, 9, 10]. Specifically, experiments performed (i) with mineral oils lacking charged components, (ii) in the absence of clay particles, and (iii) without sufficient aging (i.e., equilibration between the various components in the crude oil, brine, and rock) showed negligible increases in oil recovery with low salinity brine injection. It is therefore important to understand the interactions between the crude oil, brine, and rock surface that govern wettability and ultimately oil recovery during low salinity brine injection. This review proceeds with an overview of the required components for the low salinity effect to take place.

Components in Crude Oil

Crude oils are complex mixtures of organic molecules that range in size (from one carbon atom to hundreds of carbon atoms), composition (simple hydrocarbons to asphaltenes rich in oxygen, nitrogen, and sulfur), structure (straight chain hydrocarbons to aromatic rings), and polarity (nonpolar saturates to polar resins and asphaltenes). Physical and chemical properties are used to characterize crude oil based on its saturates, aromatics, resins, and asphaltenes (SARA) composition. Specifically, asphaltenes are the heaviest, most polar components of crude oil. The components of crude oil, by order of decreasing polarity, are asphaltenes, resins, aromatics, and saturates.

The presence of polar components in crude oil strongly affect the wettability of the reservoir rock and is a key component in the efficacy of low salinity waterflooding processes. In particular, adhesion of crude oil onto mineral surfaces can alter an initially water-wet system towards mixed- or oil-wet conditions. Experimental evidence shows that crude oil adhesion on solid surfaces, and hence wettability properties of the pore space, is a strong function of the pH, temperature, and salinity of the system [11]. Specifically, the strong dependence upon pH suggests that the polar acid/base components play a significant role in determining the wettability of the porous medium. Benner and Bartell [12] first suggested that surface active polar components in crude oil affected rock wettability by chemisorption of (i) basic polar compounds onto acidic silica surfaces or (ii) acidic polar compounds onto basic limestone surfaces.

Furthermore, Tang and Morrow [4] showed that low salinity waterfloods increased oil production in sandstone cores with crude oil but showed negligible effects for the cores with mineral oils. Oil composed of only saturates and aromatics (nonpolar components) is expected to be non-wetting on most mineral surfaces, whereas crude oils with a continuum of high molecular weight asphaltenes and resins (polar acid/base components) lead to oil-wet conditions, especially in the presence of charged clay

particles.

Clay in Sandstone

Naturally occurring sandstones that encompass petroleum reservoirs often contain significant amounts of clay that are natively adhered to the surface of sand grains. In this work, clay is defined by its mineral composition and crystalline structure. Specifically, clay are hydrous aluminium phyllosilicates ($(Al,Si)_3O_4$) organized in two-dimensional sheet-like structures. Clay constituents can drastically change the overall wettability and petrophysical properties of the rock due to its physiochemical attributes [13]. Specifically, physiochemical properties such as shape, size, surface charge, surface charge distribution, capacity to shrink/swell, and cation exchange capacity of clay minerals within the pore space dictate the interaction of fluids with the porous medium and the associated transport dynamics [14].

Physiochemical properties group clay minerals into four main categories: kaolinite, montmorillonite/smectite, illite, and chlorite [15, 16]. Kaolinite ($Al_2Si_2O_5(OH)_4$) is the predominant clay mineral found in sandstones. Figure 1.1 shows kaolinite as pseudohexagonal plates that are stacked in loose booklets.

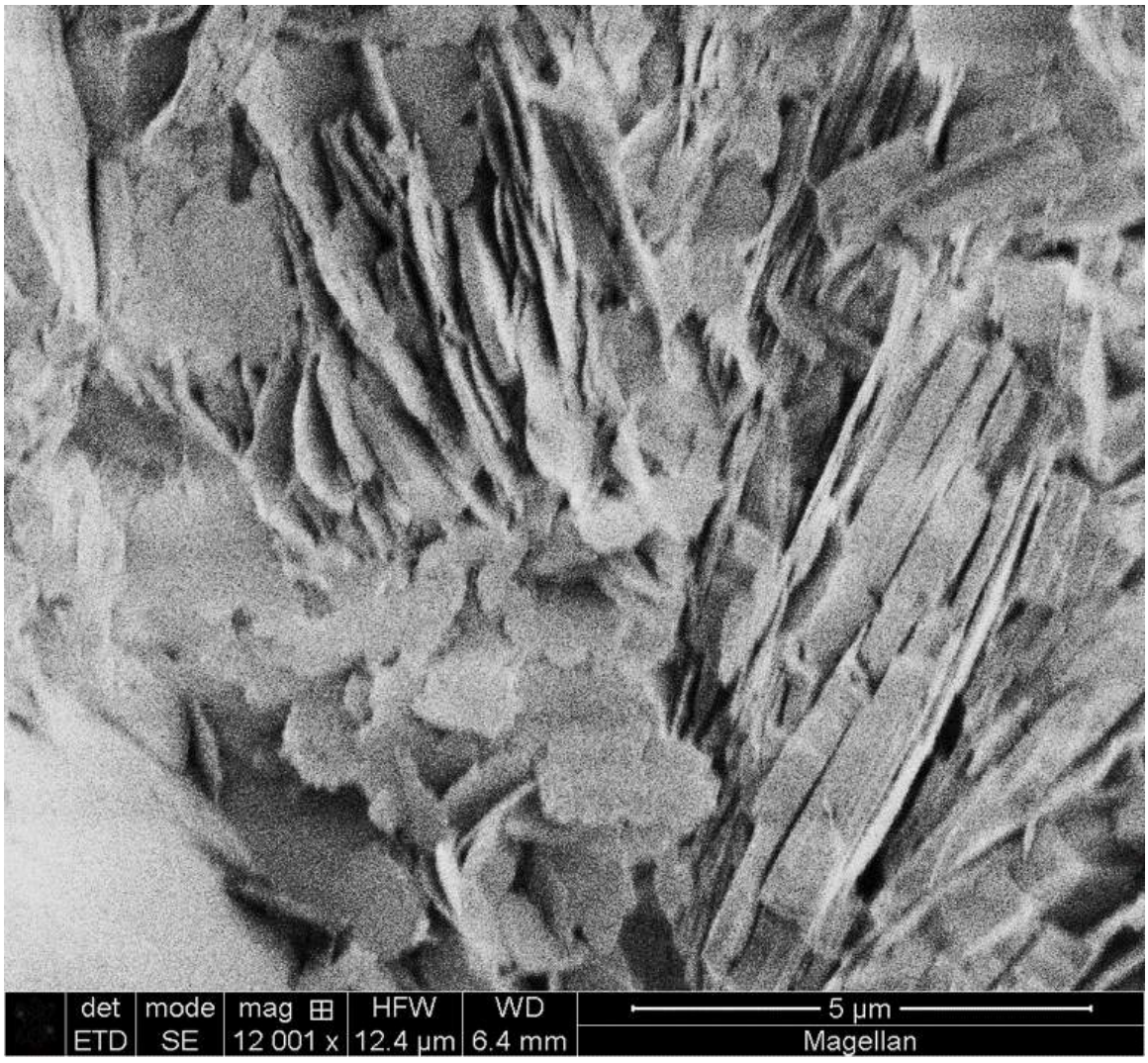

Figure 1.1: Kaolinite as booklets of stacked pseudohexagonal plates in natural sandstone. Image courtesy of C.M. Ross [17].

The surface charge of kaolinite is heterogeneous [18]. Specifically, the basal surface of kaolinite carries a small negative charge that is independent of pH due to the isomorphous substitution of Si^{4+} by Al^{3+} [18, 19]. Hydrogen bonding between the hydroxyl groups on the aluminum sheet and the oxygen molecules of the silica sheets on the basal surfaces give rise to the booklet structure of kaolinite. The edges of kaolinite, however, consist of aluminum atoms terminated by hydroxyl groups (OH^-).

Charges of clay edges are thus dependent upon pH due to the protonation/deprotonation of the surface hydroxyl groups [14, 18]. The reactivity of clay particles is therefore heavily dependent upon the composition of the fluids that surround it.

The cation exchange capacity (CEC) is a measure of the ability of a material to exchange cations with a solution. The CEC of kaolinite is due mostly to the edge charges. Kaolinite has a low CEC (3-15 meq/100g) and is non-swelling in nature. Montmorillonite ($(Na,Ca)_{0.33}(Al,Mg)_2(Si_4O_{10})\ (OH)_2 \cdot nH_2O$), in contrast, is a swelling clay with high CEC (60-100 meq/100g) [15, 20].

Surface properties impact the interactions between the clay particles, formation brine, and specific components in the hydrocarbon significantly and can drastically change the transport of fluids in the subsurface [21, 22, 23]. The impact of clay on microscale transport in porous materials is therefore of fundamental importance to our ability to manage our subsurface resources.

Crude Oil/ Brine/ Rock (COBR) Interactions

The complexity of charged crude oil components and of clay particles underlies the interactions between crude oil, brine, and rock in porous systems. In effort to explain the low salinity phenomenon, four main COBR interactions have been proposed (Fig. 1.2). First, polar interactions between the crude oil and the solid surface in the absence of a water film can lead to direct adsorption of asphaltenes onto mineral surfaces that alter the local wettablity (Fig. 1.2a). Specific factors that dictate oil-mineral adsorption include the type of clay present, cation exchange capacity of the clay, nitrogen content of the crude oil, and polar components in the crude oil [24, 25, 26]. Second, precipitation of asphaltenes onto the rock surface can arise from poor solubility of asphaltenes in the crude oil (Fig. 1.2b). Contact angle, imbibition rate, and adsorption measurements indicate that surface adsorption increases for oils with poor asphaltene solubilities, leading to increased oil-wetness of the pore space.

Third, acid/base interactions between the crude oil, brine, and solid surfaces control surface charges at the fluid/fluid and fluid/solid interfaces, leading to alterations in rock wettability (Fig. 1.2c). Specifically, oil and solid surfaces become charged in the presence of water by (i) depotonation of polar functional groups to become negatively charged acids, or (ii) protonation of polar functional groups to become positively charged bases [27]. Fourth, ion binding between charged sites and greater valency ions can dictate the extent of wettability alteration (Fig. 1.2d). Ion binding between crude oil, Ca^{2+}, and solid surfaces, for example, drastically promotes wettability alteration [11].

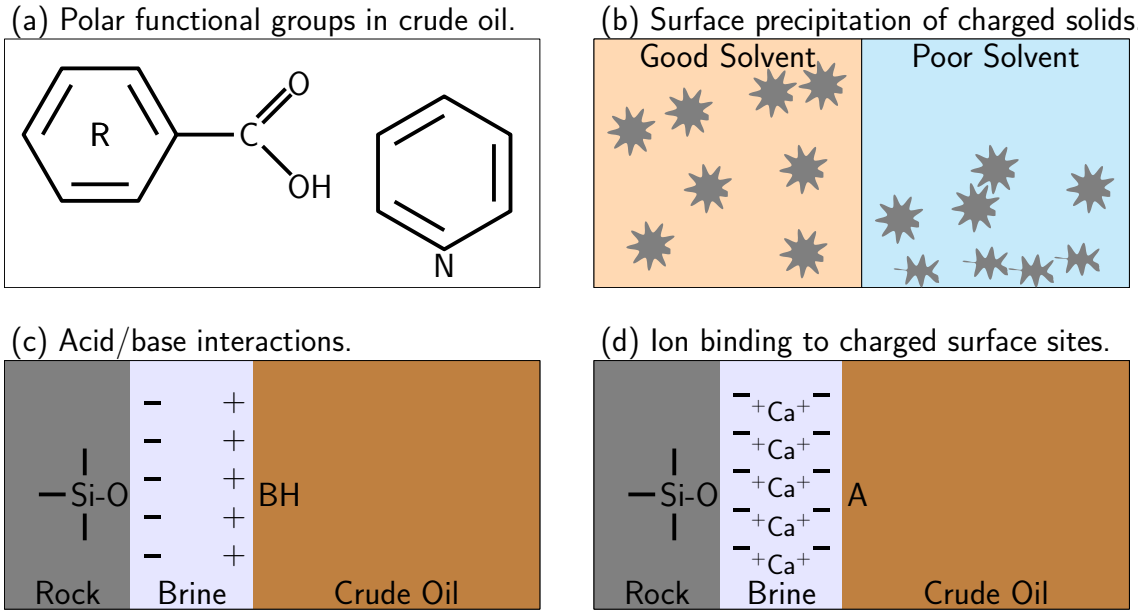

Figure 1.2: Interactions between crude oil, brine, and rock (COBR) that dictate pore-level wettability, modified from Buckley et al 1997 [28]. (a) Polar interactions between oil and rock in the absence of a water film increase oil-wettability. (b) Precipitation of heavy polar asphaltenes onto rock surfaces due to poor solubility of asphaltenes in the crude oil increases oil-wettability. (c) Protonation and deprotonation of oil and solid polar functional groups lead to water-film instability and increase in oil-wettability. (d) Ion binding between charged sites and salt ions in the brine promote oil-wettability of the rock.

Wettability of Porous Media

Rock wettability is a key determining factor in the recoverability of oil from the subsurface. Clean, unaltered sand is strongly water wet [11]. Clay, on the other hand, is oil wet [22, 29]. The presence of clay particles in the pore space drastically alter the overall wettability of the porous medium from water-wet to mixed- or oil-wet conditions. Laboratory experiments show that reservoir cores can imbibe both water and oil due to heterogeneous surface wetting properties [11].

Systems with increasing oil-wettability generally result in lower recovery factors as compared to those in mixed-wet or water-wet systems for economic amounts of water injection. It is therefore of practical interest to drive the wettability of the porous medium towards more water wetting conditions. In order to alter the wettability of the pore space towards increasing water-wettability, it is important first to understand the conditions that brought about the mixed-wet condition in initial reservoir rock. Mixed-wet pore surfaces are attributed to (i) Dalmatian or fractional wetting due to the heterogeneous distribution of pore lining minerals (clay particles) within the pore space [30], and (ii) initial fluid distribution due to initial water-wet conditions and subsequent COBR interactions within the porous medium [31].

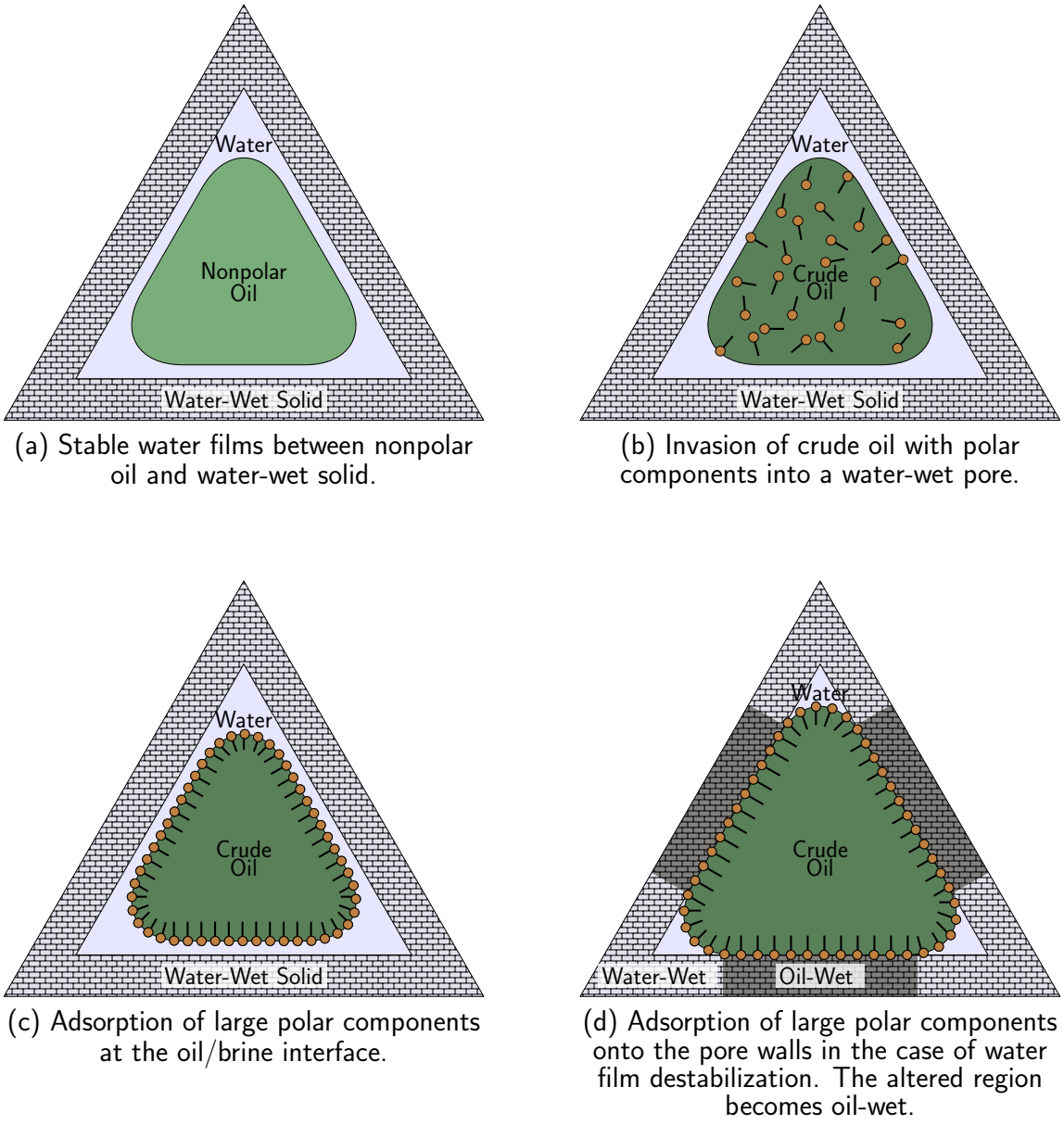

(a) Stable water films between nonpolar oil and water-wet solid.

(b) Invasion of crude oil with polar components into a water-wet pore.

(c) Adsorption of large polar components at the oil/brine interface.

(d) Adsorption of large polar components onto the pore walls in the case of water film destabilization. The altered region becomes oil-wet.

Figure 1.3: Wettability alteration of an initially water-wet pore due to COBR interactions. Modified from Kovscek et al., 1993 [11].

Figure 1.3 shows a possible mechanism for describing pore-space wettability alteration from water-wet to mixed-wet conditions due to COBR interactions [11]. A

triangular capillary is initially saturated with brine, followed by drainage due to invasion of (a) nonpolar oil (i.e., saturates and aromatics), and (b) crude oil (hydrocarbon mixture including polar resins and asphaltenes). The invasion of nonpolar oils (e.g., mineral oils) results in the formation of a stable water film between the solid surface and the oleic phase (1.3a) and the rock surface remains water-wet. The invasion of polar oils (e.g., crude oils), however, lead to interactions between the crude oil, brine, and rock that disrupt the initially stable water film and ultimately alter the pore surface towards increasing oil-wettability. Figure 1.3b shows the initial fluid distribution following crude oil invasion into a brine-filled water-wet pore. Interactions between the crude oil and the brine can lead to adsorption of polar components at the oil/brine interface (Fig. 1.3c). Further COBR interactions or disruptions to the system (e.g., change in pH, salinity, temperature) can destabilize the water film and lead to direct adhesion of polar oil components onto the pore surface, leading to local oil-wettability (Fig. 1.3d).

1.2.2 Proposed Mechanisms Driving the Low Salinity Effect

Five main mechanisms have been proposed to explain the increase in oil recovery associated with low salinity brine injection: (i) fines migration, (ii) multi-component ion exchange (MIE), (iii) pH variation, (iv) formation of micro-emulsions, and (v) salting in. This section provides a basic understanding of each of the proposed mechanisms.

Fines Migration

Tang and Morrow reported increased oil recovery as a result of low salinity brine injection into Berea sandstones with high clay content [4]. Importantly, significant production of kaolinite particles was observed in the effluent during low salinity brine injection. It was thus proposed that the presence of clay and the mobilization of clay

under low salinity conditions was critical to the increased oil recovery associated with low salinity brine injections.

Mobilized fine clay particles, however, can impact rock wettability and ultimately oil recovery by two antithetical mechanisms: (i) the detachment of oil-wet pore-lining clays from the pore surface exposes the underlying water-wet sand and shifts the system towards a more water-wet condition and hence increased oil production [4], and (ii) the flocculation and agglomeration of the mobilized fines obstructs pore throats and leads to formation damage [32, 33, 34]. Lager et al. reported increased oil production with low salinity waterfloods in clay-rich sandstones without apparent fines migration and permeability reduction [10]. Furthermore, core- and field-scale experiments in clay-rich sandstones have shown mixed responses to reduced salinity brine injection [35, 36, 37, 38]. These results suggest the possibility of other mechanisms at play, and that the impact of the presence of clay particles in the pore space must be thoroughly investigated.

The literature presents several studies to delineate the fundamental mechanisms that cause clay particles to detach from the pore surface [23, 32, 39, 40]. Specifically, the DLVO (Derjaguin, Landau, Verwey, and Overbeek) theory has been applied to describe the interplay of attractive van der Waals forces and repulsive double layer forces between the clay particles and sand grains; these interactions define the conditions at which clay particles are released. Effects such as the impact of cation species on clay detachment, however, are not well accounted for by the DLVO theory without other considerations (e.g., electroselectivity) [41]. A mechanistic understanding of pore-level clay mobilization under different reservoir conditions is required.

Multi-Component Ion Exchange (MIE)

Multi-component ion exchange involves the competitive exchange of injection brine ions for polar organic compounds at the exchange sites on the pore surface [42].

Specifically, cation type and concentration of the injection brine play a key role in determining the release of oil from the pore space. At high salinity, crude oil can be adsorbed onto reservoir rock by (i) multivalent cations at a clay surface bonding with polar components of the crude oil, and (ii) displacing the most mobile cations on the clay surface for direct adsorption of the polar oil components onto the pore surface [42]. Injection of low salinity brines, however, replaces the polar organic compounds with multivalent cations and leads to release of polar oil components from the pore surface.

The DLVO theory suggests that oil adsorbs onto clay surfaces via eight mechanisms: cation exchange, protonation, anion exchange, water bridging, cation bridging, ligand bridging, hydrogen bonding, and van der Waals interaction. Specifically, the four mechanisms that are strongly affected by low salinity brine injection are cation exchange, cation bridging, ligand bridging, and water bridging [10, 42]. First, cation exchange refers to the replacement of metal cations that were initially bound to the clay surface by molecules that contain quaternized nitrogen or a heterocyclic ring [10]. Second, cation bridging is a weak adsorption mechanism between polar functional groups and exchangeable cations on the clay surface. Third, ligand bridging involves direct bonding between multivalent cations (M^+) and carboxylate groups ($RCOO^-$); this leads to the detachment of organometallic complexes ($RCOO^-M$) from the mineral surface. Fourth, water bridging is similar to cation bridging and occurs in the presence of exchange cations that are strongly solvated (e.g., Mg^{2+}). Specifically, water bridging refers to the complexation between polar functional groups of the organic molecule and the water molecule that solvated the exchangeable cation.

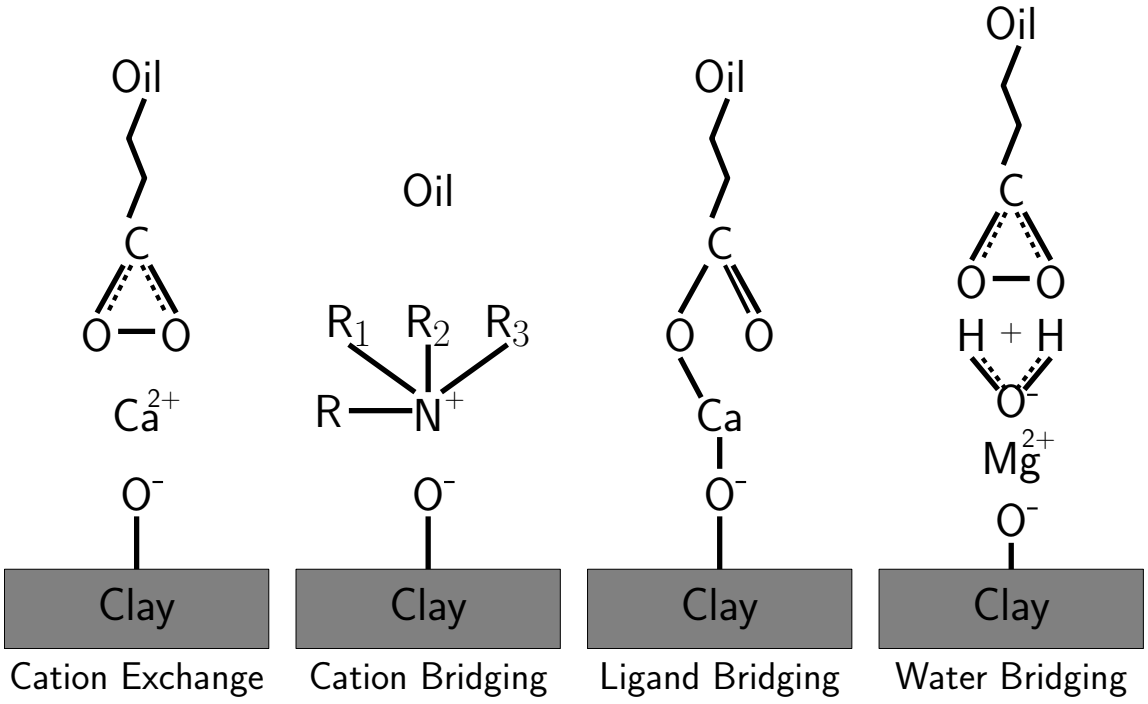

Figure 1.4: Four mechanisms of crude oil adsorption onto clay surfaces that are strongly influenced by brine salinity. Modified from Lager et al., 2008 [42].

pH Variation

Tang and Morrow [4] showed increased effluent pH due to low salinity brine injections that resulted in increased oil recovery similar to alkaline flooding. Two mechanisms have been proposed to explain the increase in alkalinity: (i) dissolution of carbonate material in the rock, and (ii) cation exchange on clay mineral surfaces [10]. The dissolution reaction of carbonate material results in an excess of OH^-, thereby raising the pH of the reservoir fluids. Carbonate dissolution is a slow process described by the following two simultaneous reactions:

$$CaCO_3 \rightleftharpoons Ca^{2+} + CO_3^{2-} \tag{1.1}$$

$$CO_3^{2-} + H_2O \rightleftharpoons HCO_3^- + OH^- \tag{1.2}$$

Cation exchange, in comparison, is a faster process. Specifically, cation exchange describes the process where previously adsorbed cations are replaced by H^+ in the injection brine. The adsorption of H^+ onto the solid surface results in a reduction of its concentration in the aqueous phase, thereby raising the pH of the reservoir fluids.

At the displacement front, the alkaline brine increases oil recovery effectiveness by reducing the oil/brine interfacial tension, altering the wettability of the pore surface, formation of oil droplets inside the crude oil, and emulsification of the oil and brine [43]. Conflicting experimental evidence, however, suggest that proton buffering (i.e., desorption of H^+ from oxides and organic matter as well as desorption of complexes) will prevent the pH of the system from reaching high degrees of alkalinity [44]. Other mechanisms must therefore be explored to explain the increase in oil recovery with the injection of low salinity brines.

Micro-Emulsions

The formation of water-in-oil emulsions have been observed during low salinity flooding in micromodels [45]. It has been proposed that the spontaneous generation of the micro-emulsions is due to the release of surface-active components from the oil-water interface. Specifically, the generation of micro-emulsions increased oil recovery by two mechanisms: (i) alteration of oil-wet pores towards increasing water-wettability, and (ii) swelling of high salinity connate water to remobilize trapped oil. First, the release of surface-active agents from the oil/water interface disrupts the surface charges at the oil/water interface (e.g., more negatively charged interface following from release of positively charged basic surfactants) and leads to expansion of the electrical double layer. This results in a more water-wet condition. Second, the formation of water-in-oil emulsions at the low salinity injection brine/oil interface and the coalescence of the emulsions at the high salinity formation brine/oil interface can induce connate water swelling and trapped oil remobilization.

Salting-In and Salting-Out

Surface wetting conditions can be altered by salting-in and salting-out organic matter. Salting-in refers to the increase of organic material solubility in brine with reduced ionic strength, and salting-out refers to the decrease of organic material solubility in brine with increased ionic strength [46]. Specifically, at low salinities the hydrophobic portion of organic materials form hydrogen bonds with water structures that allow for water solubility. Inorganic ions such as Ca^{2+}, Na^{+}, and Mg^{2+}, however, break up the water structures and reduce the solubility of the organic material in water. The salting-in effect predicts that low salinity brine injection will increase the water-wettability of the rock and lead to release of immobilized oil droplets previously adhered to the pore surface.

The literature agrees that the five mechanisms presented above play a role in the low salinity effect, however there is little agreement as to the extent of the roles that each of the proposed mechanisms play in increasing oil recovery. Furthermore, there is little consensus in core- and field-scale experimental results on the effectiveness of low salinity brine injection in general. The design of the injection brine composition for enhanced oil recovery requires a thorough understanding of the mechanisms that are dictating the low salinity effect. Pore-level visualization of the dynamics during low salinity brine injection must be achieved to understand the fundamental mechanisms related to the low salinity effect.

1.3 Reactive Transport and CO_2 Storage in Carbonate Formations

Carbonate formations encompass both significant hydrocarbon deposits as well as deep saline aquifers suitable for carbon dioxide (CO_2) storage [47, 48, 49, 50]. Carbonate reservoirs, namely limestones and dolostones, account for more than 60% of global oil reserves and more than 40% of global natural gas reserves [48]. Combined CO_2-enhanced oil recovery (CO_2-EOR) and long-term CO_2 storage post-production in the carbonate layers of the Weyburn-Midale field currently comprise the largest CO_2 storage project worldwide. It is therefore of great economic and public safety interest to understand the behavior of fluids in carbonate rock. The following sections provide an overview of carbonates and their surface properties, mechanisms associated with the dissolution of carbonates, and the low salinity effect in carbonates.

1.3.1 Carbonate Rock

Carbonate rock are classified as either limestone (i.e., calcite-dominant rock, $CaCO_3$) or dolostone (i.e., dolomite-dominant rock, $CaMg(CO_3)_2$). Fluid transport through carbonates drastically differ from that of sandstone formations due to its complex pore geometry and surface characteristics. Six highly complex pore types can be found in carbonate rock: interparticle, intraparticle, intercrystaline, moldic, fracture, and vuggy pore structures [51]. Commonly, carbonates are described by a bimodal pore size distribution consisting of macro- and micro-pores that lead to the generation of mixed-wet reservoir conditions [11]. Furthermore, poor pore connectivity, complex surface charges, and highly reactive pore surfaces further complicate fluid transport through carbonates.

1.3.2 Reactive Flow in Porous Media

Reservoir engineering involves the flow of complex fluids through subsurface formations. Carbonate reservoir rock are highly reactive, and the flow of acidic fluids drastically alter the pore structure and permeability of the formation. The dissolution of calcite plays a significant role in numerous reservoir-engineering applications. For example, deep carbonate reservoirs amenable to CO_2 storage are subject to pore-scale dissolution due to the CO_2-acidification of the reservoir brine. Furthermore, injection of hydrochloric acid (HCl) is a common reservoir stimulation technique aimed at carbonates with poor connectivity to enhance reservoir permeability and hence overall hydrocarbon recovery.

The chemical reactions involved with (i) acidizing poorly connected hydrocarbon containing carbonate reservoirs and (ii) CO_2–acidified brine migration through storage reservoirs are as follows:

$$CaCO_{3(s)} + 2HCl_{(aq)} \rightarrow CaCl_{2(aq)} + CO_{2(g)} + H_2O_{(l)} \tag{1.3}$$

$$CaCO_{3(s)} + CO_{2(aq)} + H_2O_{(aq)} \rightarrow Ca(HCO_3)_{2(aq)} \tag{1.4}$$

Despite the differences in the overall reactions for the two engineering applications, mineral dissolution at the calcite crystal surface is governed by the same set of simultaneous reactions given below:

$$CaCO_3 + H^+ \rightleftharpoons Ca^{2+} + HCO_3^- \tag{1.5}$$

$$CaCO_3 + H_2CO_3 \rightleftharpoons Ca^{2+} + 2HCO_3^- \tag{1.6}$$

$$CaCO_3 + H_2O \rightleftharpoons Ca^{2+} + HCO_3^- + OH^- \tag{1.7}$$

Calcite Dissolution

Calcite dissolution in acids is a rapid heterogeneous reaction. The dissolution rate of calcite in acids is influenced by (i) the reaction kinetics at the solid-liquid interface, and (ii) the mass transfer of the reactants to and of the products away from the fluid boundary layer. The pH of the injection fluid determines the rate-limiting mechanism of the dissolution process. Specifically, for low pH fluids (i.e., pH < 4 at ambient conditions), calcite is readily dissolved and thus the rate of dissolution is limited only by the mass-transfer of reactants to the solid-liquid interface and the reaction rate. For pH greater than 3.7, the reactants and products form a buffer system in the boundary layer and thus calcite dissolution is limited by the rate of surface reaction kinetics [52]. At low pressures (~ 1 atm) the reaction releases CO_2 in its gaseous phase at the solid-liquid interface; this introduces a second, compressible phase to the fluid flow problem that further complicates the pore scale hydrodynamics and the rate of dissolution [53]. Currently, the strong pressure dependence of calcite dissolution in acids is not well understood and must be studied for reservoir engineering applications such as CO_2 storage and formation stimulation.

Acidizing

Acidizing involves the injection of hydrochloric acid (HCl) into low permeability carbonates to dissolve pore-plugging minerals and enhance reservoir permeability. Typically brines with 1-15% HCl is injected due to its rapid reaction with the carbonate matrix. Under these conditions, the dissolution of calcite is rapid, irreversible, and mass transport limited. The literature presents numerous experimental studies on acidizing carbonate reservoirs at the field and core scales, with the goal of finding the optimal conditions to generate low resistance flow conduits to enhance reservoir

permeability and thus overall oil recovery. Two conflicting recommendations with respect to the optimal injection rates have been made: (i) the acids should be injected at the highest rate possible without initiating fractures [54, 55]; and (ii) the acids should be injected at low flow rates to result in optimal reservoir stimulation for a given acid volume [56].

The evolution of rapid matrix-dissolution and the generation of heterogeneous flow profiles due to HCl injection over time leads to the formation of highly conductive flow channels (i.e., wormholes) [52]. Initial preferential flow paths due to pore-level heterogeneities are enlarged due to dissolution of the rock matrix, and lead to further preferential flow through that region. The magnification of the preferential paths creates a low resistance channel for fluids to flow through. Wormholing increases the permeability of the porous carbonate system and allows for petroleum to be extracted more readily. Similarly, matrix dissolution as a result of reaction with CO_2-acidized brine can influence the storage capacity and effectiveness of the reservoir for CO_2-sequestration. Previous studies have attempted to model the dissolution of the carbonate rock matrix as a function of dimensionless parameters such as the Peclet number (ratio of convective transport to diffusive transport) and the Damkohler number (rate of dissolution to rate of convective transport). The Damkohler number was found to provide a suitable description of the various wormholing phenomena observed [52]. Specifically, for mass-transfer limited dissolution, the Damkohler number is given by $Da_{mt} = aD_e^{2/3}l/Q$, Where D_e is the effective diffusion coefficient, Q is the flow rate, l is the pore length, and a is a core-specific constant. Core-scale experiments, however, cannot sufficiently capture the pore-scale dynamics that are required to understand the reactive transport of fluids in carbonate rock. Pore-scale dynamics dictate the overall flow behavior of fluids in porous media. Therefore pore-level fluid-solid interactions, changes in pore structure, connectivity, and surface properties must be studied to provide a fundamental understanding of reactive transport

through porous media.

1.4 Miscible Fluid Interactions

Immiscible fluid injection corresponding to high mobility ratios $M = M_{disp}/M_{inj}$ results in multiphase instabilities that diminish the volumetric sweep, or overall recovery, of the crude-oil resource. Generally, the mobility M_i of each phase is defined as $M_i = kk_{ri}/\mu_i$, where k is the permeability of the porous material, k_{ri} is the relative permeability of the porous material to fluid phase i, and μ_i is the viscosity of the fluid phase i. In the case of oil recovery where the reservoir is initially saturated with crude oil, the injection fluid may be brine and the displaced fluid the crude oil. Brine is used widely due to its low economic requirements. Viscosity ratios between crude oil and brine generally range from $\mu_{oil}/\mu_{brine} \sim 10^0$ to 10^5 [57, 58]. Relative permeability is a dimensionless term from 0 to 1 one and is hence of low significance in comparison. The high mobility ratio and the interfacial tension effects of multiphase tranpsort lead to interfacial instabilities of the Saffman-Taylor type [59] that destabilize the injection front and thus create preferential flow paths, or fingers, that drastically reduce the overall oil recovery efficacy from petroleum systems (Fig. 1.5a).

Injection of solvents that are miscible with crude oil, on the other hand, presents an opportunity to circumvent the instabilities related to high mobility ratios and multiphase transport (Fig. 1.5b). Of particular interest is the recovery of viscous oils. Specifically, viscous oil such as heavy oil, extra heavy oil, and bitumen consist of approximately 70 % of global oil resources [60]. Extraction of viscous oils, as discussed above, is limited due its significant viscosity and susceptibility to fingering instabilities. Fingering in petroleum reservoirs leads to early breakthrough where the injection fluid following the path of least resistance flows through a single path from the injector well to the producer well and hence bypasses the remainder of the reservoir. Solvent injection aims to stabilize the injection front by eliminating the interface between crude oil and the injection fluid, hence reducing the effect of

fingering instabilities.

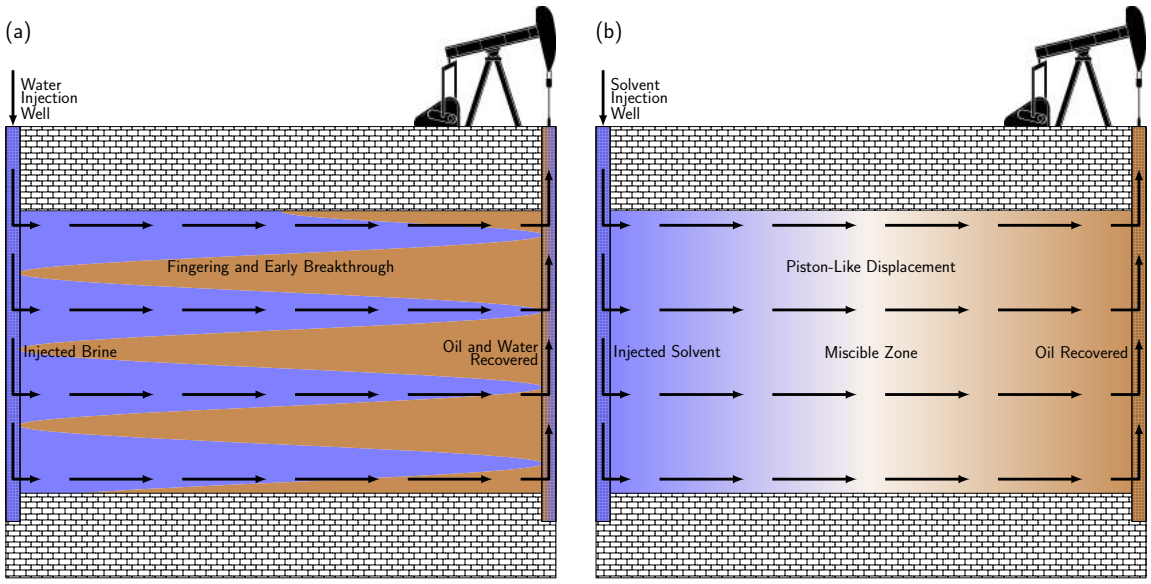

Figure 1.5: Illustration of oil recovery methods at the reservoir-scale. (a) Injection of low-cost brine introduces multiphase, interfacial instabilities as a result of immiscible fluid transport. Resulting fingering and early breakthrough of the injected brine reduces the overall recovery of the crude oil resource. (b) Injection of miscible solvents potentially circumvents the instability issues that plague water-based injections. A piston-like displacement is expected due to the lack of interfacial tension at the miscible zone.

Complex crude oil composition, however, introduces significant uncertainty in the macroscopic behavior of solvent- enhanced oil recovery processes. Specifically, mixing efficacy of solvent into the crude oil, swelling of crude oil due to solvent dissolution [61], and potential formation damage due to solvent particle (e.g., asphaltene) precipitation [62] must be resolved. Importantly, these are all dynamics at the fundamental microscopic pore- and interface-scales.

Fluid-pair interactions under imposed flow have been studied extensively [59, 63, 64, 65, 66]. Specifically, Hele-Shaw cells, where the fluids are confined between two parallel plates, are used to replicate the effect of porous reservoir rock. Typical Hele-Shaw configurations (Fig. 1.6) involve a viscous fluid, for example oil, that

saturates the gap spacing between the two parallel plates, with a less viscous fluid, for example brine, that is injected into the gap spacing to displace the original fluid phase. Advantageously, by manipulating the optical properties of the parallel plate material, direct visual observation of the fluid fingering process is achieved [65].

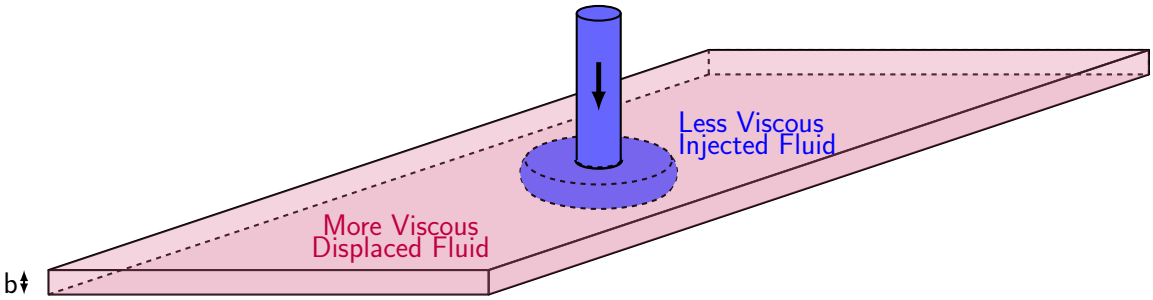

Figure 1.6: Hele-Shaw type experimental setup. Fluid of low viscosity is injected into the gap spacing between two parallel plates that is initially saturated with a high viscosity fluid.

Direct observation of flow instabilities under the Hele-Shaw configuration, in combination with its simple geometric constraints, allowed the development of analytical delineations such as the Saffman-Taylor solution [59] for interfacial instabilities as a smaller viscosity fluid displaces one of larger viscosity [59, 67, 68, 69]. The developed models have enabled improved understanding of oil recovery processes such as the injection of immiscible brine as a method to displace crude oil. Recent emphasis on enhanced oil recovery and subsurface CO_2 storage have given rise to studies on partially miscible fluid-pairs. In particular, the low interfacial tension fluid-pair water and glycerol is used extensively as a proxy to miscible subsurface fluids [70, 71]. Low interfacial tension experiments using the single-component water-glycerol pair show surprising interactions, namely regular interfacial instabilities and ramified fingers, during the injection of one fluid phase into the other.

Subsurface systems are characterized by slow or no flow (velocity $\sim$ 1 m/day) conditions and complex fluid compositions (e.g., crude oil). Studies of such low Peclet

number (Pe = advection rate/ diffusion rate) systems, especially those in microconfined geometries, have been sparse. To understand and design solvent- enhanced oil recovery, much progress is required in the study of complex fluids, for example crude oils, and their interaction with fluids that are miscible completely (i.e., not partially or slowly miscible) at the microconfined scale.

1.5 Geological Complexity and the Need to go Small

Geological systems containing energy and environmental resources such as petroleum and water reservoirs are large and complicated by an abundance of geometric, mineralogical, and compositional heterogeneity (Fig. 1.7). Hydrocarbon recovery and CO_2 storage, for example, are reservoir engineering processes that span the field- ($\sim 10^3$ m), reservoir- ($\sim 10^0$ to 10^2 m), and ultimately microscopic pore-scales ($\sim 10^{-9}$ to 10^{-4} m) [72]. Due to the porous character of geological systems, pore-scale dynamics ultimately dictate the overall outcome of reservoir engineering processes. Small length scales and large surface area to volume ratios mandate that the interactions between fluids and solid surfaces, i.e., the rock matrix, underlie all transport dynamics in geological systems. It is therefore important to recognize the complexities present in geological systems.

Two main geological complexities impede current understanding of subsurface transport: (i) geological fluids, and (ii) geological materials. Geological fluids such as crude oil and brine are multicomponent, multiphase systems with complex phase and interfacial behavior that fundamentally dictate the dynamics of pore-scale transport through the subsurface. Geological materials (Fig. 1.7), commonly sandstones, carbonates, and shale, are geometrically and mineralogically complex porous media

where reactive transport and surface interactions are important. Large-scale geological systems, particularly those encompassing hydrocarbon and environmental resources, are exceptionally complex and fundamental, small-scale understanding is required to resolve these complexities.

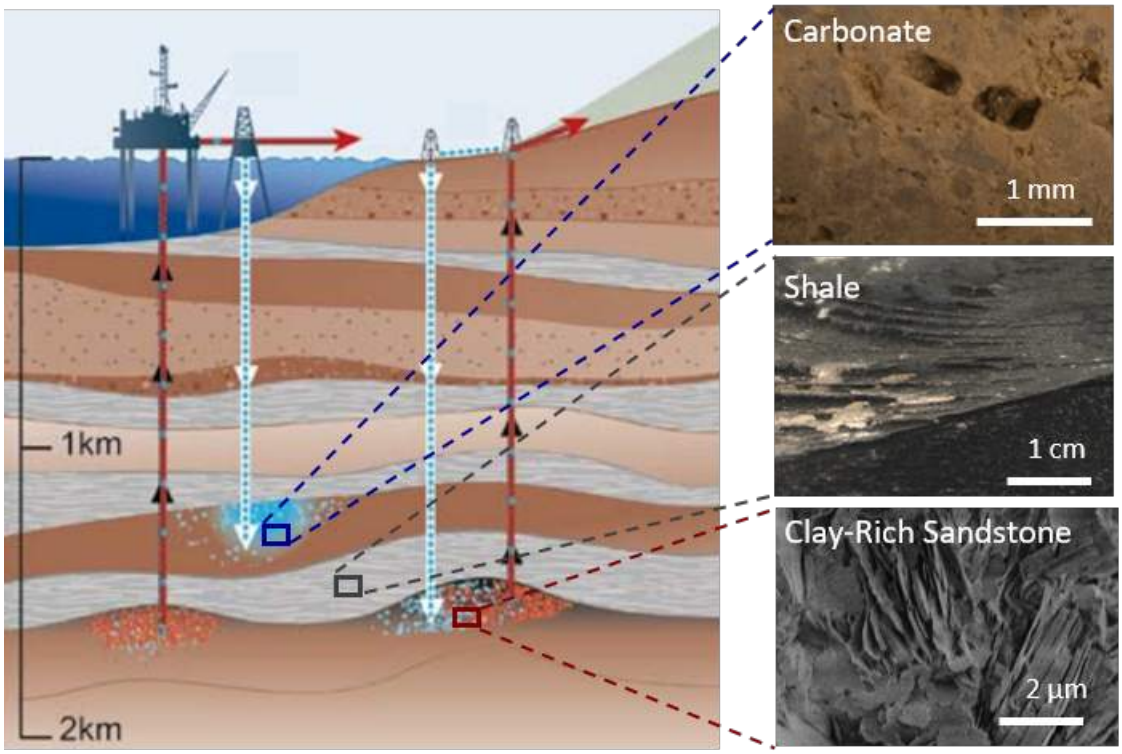

Figure 1.7: Geological systems at industrially relevant reservoir-scale ($\sim 10^0$ to 10^2 m), ultimately dictated by fluid-rock interactions at the fundamental pore-scale ($\sim 10^{-9}$ to 10^{-4} m). Complexity arises due to the complex interactions between geological fluids (e.g., multicomponent crude oil, brine, CO_2) and geological materials (e.g., reactive carbonate, nanoscale shale, and charged clay-rich sandstone pore surfaces), therefore necessitating visualization. (Reservoir-scale schematic adapted from IPCC Special Report on Carbon Capture and Storage [73], and clay-rich sandstone SEM courtesy of C.M. Ross [17].)

1.6 Recent Advances in Microscale Visualization enabled by Microfluidic Technology

Complexity necessitates visualization. Microfluidics, the study of fluid behavior at the sub-millimeter-scale, lend well to direct visualization of pore scale fluid dynamics that dictate engineering of geological systems [74]. Microfluidic devices are widely deployed in biological and medical studies and are emerging as a powerful method of visualizing the fundamental pore-scale dynamics that dictate the subsurface (Fig. 1.8). This section reviews the current state-of-the-art in microfluidics in the context of geological systems, and highlights some recent advancements in capturing the full complexities, and hence, the full physics, of transport in geological materials through real-rock microfluidics.

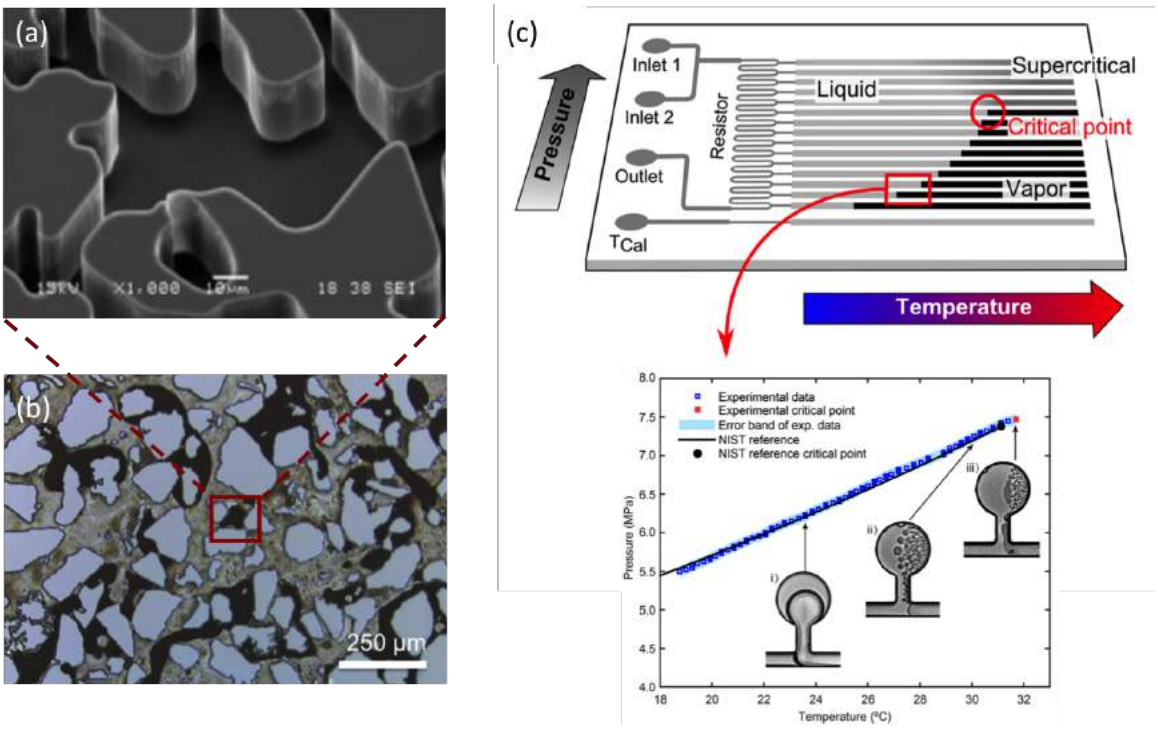

Figure 1.8: Microfluidic devices and applications towards subsurface engineering. (a) Current state-of-the-art high temperature, high pressure, solvent-compatible microfluidic visualization platforms with representative pore geometry, i.e., micromodels, are etched in silicon [75]. Corners and crevices important to transport through porous media are replicated due to crystallographic etching in silicon. [Reprinted (adapted) with permission from [75].] (b) Crude oil and brine transport dynamics is visualized in a clay-functionalized sandstone micromodel (real-rock micromodel) to develop fundamental pore-scale understanding towards improved oil recovery [76]. (c) Direct visual mapping of fluid phase diagram using a pressure-temperature microfluidic device [77]. [Reprinted (adapted) with permission from [77]. Copyright 2016 American Chemical Society.]

1.6.1 Current State-of-the-Art Microfluidic Porous Media

Some of the earliest microfluidics date back to the 1950's where glass-bead visualization cells were developed to understand transport through porous media [78]. Advances in micro/nano-characterization and fabrication and microscopy have since

given rise to a new generation of silicon-based microfluidic platforms that enable direct visualization of fluid transport through porous media with realistic pore geometry [75, 79, 76, 80, 81] at high temperature, high pressure [82, 83, 84, 85, 86, 87, 88, 89, 90, 91], and solvent resistivity [92, 93] conditions experienced in real subsurface systems. Nanofabrication techniques such as photolithography, plasma etching, and anodic bonding enable precise control and a high degree of reproducibility in etched pore geometry to give realistic geological pore geometries [75]. Microfluidic devices with realistic pore geometries are called micromodels. Current state-of-the-art micromodels etched into silicon and bonded to transparent glass that enable direct visualization of transport at the sub-millimeter scale [75]. Importantly, pore geometries etched in silicon reproduce the geometric corners and crevices that are important to flow in real geological materials (Fig. 1.8a). Surface chemistry and mineralogy, however, are not captured with silicon and glass alone [80, 94, 95, 96].

1.6.2 Capturing Mineralogical Complexity with Real-Rock Microfluidics

Practical approaches in designing CO_2 storage, hydrocarbon recovery, and contaminant remediation depend on the type of geologic material, i.e., rock, in the reservoir. Recent novel advances incorporate representative mineralogy to converge micromodels towards capturing real-reservoir behavior. Uniquely, mineralogically-functionalized micromodels and pore geometry etched into real-rock materials, i.e., real-rock microfluidics (Fig. 1.8b), enables direct visual observation into pore-scale transport dynamics between complex reservoir fluids with the rock mineral [94, 96, 97]. Real-rock microfluidics are especially useful for studies of fluid behavior in non-siliciclastic material, for example in carbonates and shale. The first implementation of real-rock microfluidics leveraged calcite, a crystalline carbonate material, to capture microscale

reactive transport dynamics in real-time [94]. Variations of the concept has similarly been demonstrated in carbonate [98], shale [96] and coal [97] to investigate fluid-mineral interactions at the fundamental microscale. In keeping with the advantages of high pressure, high temperature, solvent compatibility, repeatability, and ease of direct visualization, surface modifications to silicon- and glass-based microfluidics, i.e., surface-functionalized micromodels, have been developed to capture the real-rock behavior of fluid interactions with fine mineral particles [80, 76, 99, 100, 101] and wettability due to mineralogical heterogeneities [80, 102, 103, 104]. Polymer and glass-based microfluidics have also been developed to seed carbonate material into microfluidic devices to capture surface properties of carbonates such as wetting behavior and two-phase transport [105, 106, 104].

1.7 Microfluidics in Application towards Energy and the Environment

1.7.1 Reservoir Fluid Characterization

The small-scale nature of microfluidic platforms enables rapid and economic testing with minimal fluid sample consumption. The result is a powerful technique for rapid chemicals screening and fluid property characterization [107]. Specifically, rapid and economic measurements of fluid properties such as phase behavior [77, 108, 84, 109, 110] (Fig. 1.8c), rheology [111, 112, 113, 114, 115, 116], diffusivity and solubility [92, 117, 118, 119, 120], thermal properties [121], and interfacial interactions [122, 123, 124, 125, 126] have been demonstrated using microfluidic platforms. Suitability of microfluidics towards enhanced oil recovery chemicals design and screening, e.g., surfactant and nanoparticle foam stability, have also been fruitful [127, 128, 129]. Solids precipitation due to solvent-crude oil interactions and phase change have also

been characterized through microfluidic approaches [130, 131]. While the advantages and versatility of microfluidics in fluid property and fluid interactions characterization is clear, what is perhaps more powerful is the lens that microfluidics, and, real-rock microfluidics, lends to direct visualization of pore-scale fluid-mineral interactions that dictate fundamentally the transport of fluids such as crude oil or CO_2 through porous geological media.

1.7.2 Transport through Porous Media

The behavior of fluids through geological systems is complex due to the heterogeneity in geometry and in surface properties. Challenges in visualization stem from the opacity of rock materials. The ability that real-rock microfluidics and micromodels offer to visualize fluid-mineral interactions directly at the pore-scale in real-time provides an unprecedented opportunity to advance current gaps in fundamental understanding. Importantly, key areas in energy and the environment have benefitted. Microfluidic advancement of fundamental understanding in wettability and multiphase transport reveal basic transport mechanisms that help bridge previous gaps in knowledge [132, 133]. Direct visualization of pore-scale hydrate phase behavior provide knowledge of reservoir-scale transport parameters, e.g., effective porosity and permeability, that dictate the recovery of methane resources from such formations [88, 89]. Clay-functionalized microfluidics (Fig. 1.8b) enable direct studies of particle stability, migration, and influence on permeability during reservoir engineering processes that underlie oil recovery [80, 76, 100]. Microfluidic visualization of low salinity waterflooding, for example, have delineated the impact of wettability alteration, fines migration, and osmosis on increasing oil recovery [80, 76, 100, 91]. Geological CO_2 storage assessments using microfluidics provide direct insight on CO_2 migration and storage stability due to CO_2 trapping and due to reactive transport through carbonate materials [75, 94, 131]. Micromodels with porous geometries have similarly

been applied in fields pertaining to the study of reactive transport in groundwater remediation as well as fuel cell applications [134, 135]. Hydrodynamics, reactions, and fluid-solid interactions dictate multiphase, multicomponent transport through complex porous systems. Direct visualization of fundamental pore-scale dynamics enabled by microfluidics, and, specifically, real-rock microfluidics, presents a wealth of opportunities to impact practical engineering applications.

1.8 Outline of Dissertation

This dissertation elucidates the fluid-fluid and fluid-mineral interactions that dictate subsurface systems and engineering at the fundamental level. The contents of this dissertation are organized into five main sections.

First, a clay-rich sandstone microvisualization system is developed to investigate the interactions between crude oil, brine, and the solid rock matrix. This chapter is motivated by a need to understand the sandstone formations that are ubiquitous to both aquifers and petroleum reservoirs, and of which clay is a major constituent. The release of clay particles from pore surfaces as a result of reduced injection fluid salinity can greatly modify the recovery of hydrocarbons from subsurface formations by shifting the wettability properties of the rock. A microfluidic approach whereby kaolinite is deposited into a two-dimensional microfluidic network (micromodel) to enable direct pore-scale, real-time visualization of fluid-solid interactions with representative pore geometry and realistic surface interactions between the reservoir fluids and the formation rock is demonstrated. Structural characterization of deposited kaolinite particles agrees well with natural modes of occurrence in Berea sandstone; hence, the clay deposition method developed in this work is validated. Specifically, more than 90% of the deposited clay particles formed pore-lining structures and the remainder

formed pore bridging structures. Further, regions of highly concentrated clay deposition likely to lead to so-called Dalmatian wetting properties were found throughout the micromodel. Two post-deposition treatments are described whereby clay is adhered to the silicon surface reversibly and irreversibly resulting in microfluidic systems that are amenable to studies on (i) the fundamental mechanisms governing the increased oil recovery during low salinity waterfloods, and (ii) the effect of a mixed-wet surface on oil recovery, respectively. The reversibly functionalized platform is used to determine the conditions at which stably adhered clay particles detach. Specifically, injection brine salinity below 6000 ppm NaCl induced kaolinite particles to release from the silicon surface. Furthermore, when applied to an aged system with crude oil, the low salinity waterflood recovered an additional 14% of the original oil in place compared to waterflooding with the formation brine.

Second, an investigation into formation damage due to fines migration at low salinities is presented. Fines migration results, potentially, in significant decreases in reservoir permeability and, hence, the recoverability of crude oil from reservoirs. On the other hand, low salinity brine injection is a promising technique for increasing oil recovery from clay-rich sandstones in an economic manner. Clay detachment at low salinity conditions, however, drastically alters fluid flow. This chapter uses clay-functionalized micromodels to visualize directly the mobilization of clay at low salinity conditions in (i) the absence of oil, and (ii) the presence of oil. Study results include clay mobilization and pore plugging in the absence and presence of oil visualized by saturating the clay-functionalized micromodel with high salinity brine followed by injections of reduced salinity brines. Clay detachment and migration was observed in oil-free systems for 4000 ppm NaCl low salinity injection brine. The extent of fines detachment was quantified to determine the types of clay structures affected. Furthermore, fines migration, flocculation, and re-deposition were visualized directly. The types of structures formed (*i.e.*, pore-plugging, pore-lining, *etc.*) by the re-deposited

clay particles are characterized to determine their impact on formation damage. Clay detachment in the presence of oil was also visualized. Initial conditions analogous to clastic reservoirs were established by allowing the crude oil, brine, and solids to interact (*i.e.*, age). Clay detachment occurred during 4000 ppm NaCl low salinity oil recovery. Real-time, pore-level visualization revealed significant mechanisms during oil recovery processes and their influence on multiphase flow. Specifically, pore plugging particles in water-filled pores obstructed preferential flow paths and diverted injection fluid to unswept regions thereby increasing oil production.

Third, fundamental mechanisms dictating low salinity waterflooding are investigated. Low salinity waterflooding presents a low-energy, low-environmental impact method to improve oil recovery from clay-rich sandstone formations. Fundamental mechanisms dictating improved oil recovery at low salinity conditions are not well-understood currently. This chapter investigates low salinity waterflooding at the pore-level to delineate fundamental mechanisms underlying oil recovery. Clay-functionalized two-dimensional micromodels are used to provide direct visual observations of crude oil, brine, and clay particle interactions within the pore-space. Using this microvisual approach, establishment of initial reservoir conditions show wettability evolution of the initially water-wet system towards a mixed-wet condition due to clay-particle interactions with the reservoir fluids, i.e., crude oil and brine. Pore-scale behavior during low salinity waterflooding shows spontaneous emulsification of the crude oil and brine. Specifically, the emulsions generated are Pickering type stabilized by the clay particles that were mobilized at salinities below the critical salt concentration (CSC). Spontaneous generation of the stable Pickering emulsions reduces mobility through preferential flow paths, thereby resulting in flow diversion of subsequent injection fluids to mobilize oil-filled pores. Leveraging the stability of the Pickering emulsions, a sequential salinity cycling method is developed to improve overall oil recovery by an additional 8 % of the original oil in place. Flow diversion

due to spontaneous Pickering emulsification in preferential flow paths observed here provides fundamental insight to the design and application of low energy-input, low environmental-impacts techniques in the field.

Fourth, fluid-carbonate interactions are investigated under acidic conditions. As a means to mitigate anthropogenic CO_2 emissions, deep carbonate reservoirs hold significant potential for long-term geological CO_2 storage. Reactivity of carbonate reservoirs, however, negatively impact storage formation integrity and hence jeopardize sequestered CO_2 storage security. Motivated by a lack of mechanistic understanding of multiphase reactive transport through carbonate porous media, we develop a biogenically calcite-functionalized microvisualization device and find a new micro-scale phenomenon that dictates porous carbonate rock dissolution. Specifically, we observe the rock dissolution product, CO_2, forming a separate phase that engulfs carbonate grains and prevents further local reaction. Our findings demonstrate the importance of multiphase micro-scale effects in reactive transport processes that were previously not known. Overall, our results provide new fundamental understanding of the fluid-rock dynamics that dictate CO_2 storage security in carbonate reservoirs and an opportunity to develop predictive pore-scale reactive transport models. The new mechanism discovered here underlies many reactive transport processes in porous media and is of fundamental importance to advanced understanding and design of such systems.

Fifth, interactions between crude oil and solvents are investigated in the context of solvent-enhanced oil recovery. Specifically, diffusion-driven interfacial dynamics between the two miscible fluids are investigated. Heptane is diffused into viscous crude oil in a microscale Hele-Shaw cell. No external pressure gradients are applied; hence, the Peclet number is zero. The diffusive/dispersive process is dictated by a two-stage dispersive mechanism owing to the multicomponent character of the crude oil. Stage I is distinguished by the spontaneous fractal-like fingering of heptane into

the crude oil phase due to light components extraction from the crude oil. Stage II is characterized by diffusive interactions between the heptane and the heavy components in the crude oil. Extraction of light components exceeds the diffusion between heptane and heavy components in stage I, thereby allowing a distinct interface to form between heptane and the crude oil. Compositional gradients induce dynamic interfacial tension gradients that lead to Marangoni-effect-driven convection. Marangoni convection cells at the finger tips dictate local mass exchange and drive the self-similar fractal-like finger splitting. Fractal analysis of the fingering process shows increasing fractal dimensionality during the early diffusively-dominant fingering regime approaching that of diffusion-limited aggregation ($D_f \sim 1.67$), and a drastic decrease in fractal dimensionality thereafter due to Marangoni-effect-driven convection ($D_f \sim 1.55$). We characterize the fractal finger growth and mass exchange, and calculate the local dynamic interfacial tension. We find that spontaneous fingering, i.e., the presence of stage I, requires small gap spacing and the presence of light extractable components in the crude oil.

Lastly, this dissertation is rounded out with a review of the engineering science contributions developed in this work and some suggestions for future opportunities enabled by this work.

Chapter 2

Microfabrication and Microvisualization

Fundamental understanding of subsurface systems requires the direct observation of micro/nanoscale fluid-fluid and fluid-rock dynamics that ultimately underlie reservoir engineering processes. The work presented henceforth is in an effort to delineate the most fundamental micro/nanoscale dynamics that dictate the management of geological energy and environmental resources. Specifically, microscale investigations into the interactions between fluids and porous rock material were enabled by current state-of-the-art microfluidic systems. Silicon-based microfluidic devices, in particular, enable direct visual observation into the pore-space to delineate microscale dynamics in a geometrically-representative platform and is the grounds upon which contributions from this body of work are based. This chapter describes the method of silicon-based microfluidic device fabrication and the general framework of the experimental apparatus used.

2.1 Fabrication of Etched-Silicon Microfluidic Device

Microfludic devices with representative pore geometry, hereafter called micromodels, were fabricated in silicon to enable direct observation of the pore-scale dynamics. Silicon was chosen as the substrate material due to its resistance to extreme temperatures, pressures, and chemistry and its amenity to high precision etching. An added benefit to using silicon substrates is the associated anisotropic etching. That is, etched spaces in silicon preserve corners and crevices that are fundamental to flow through geological porous materials.

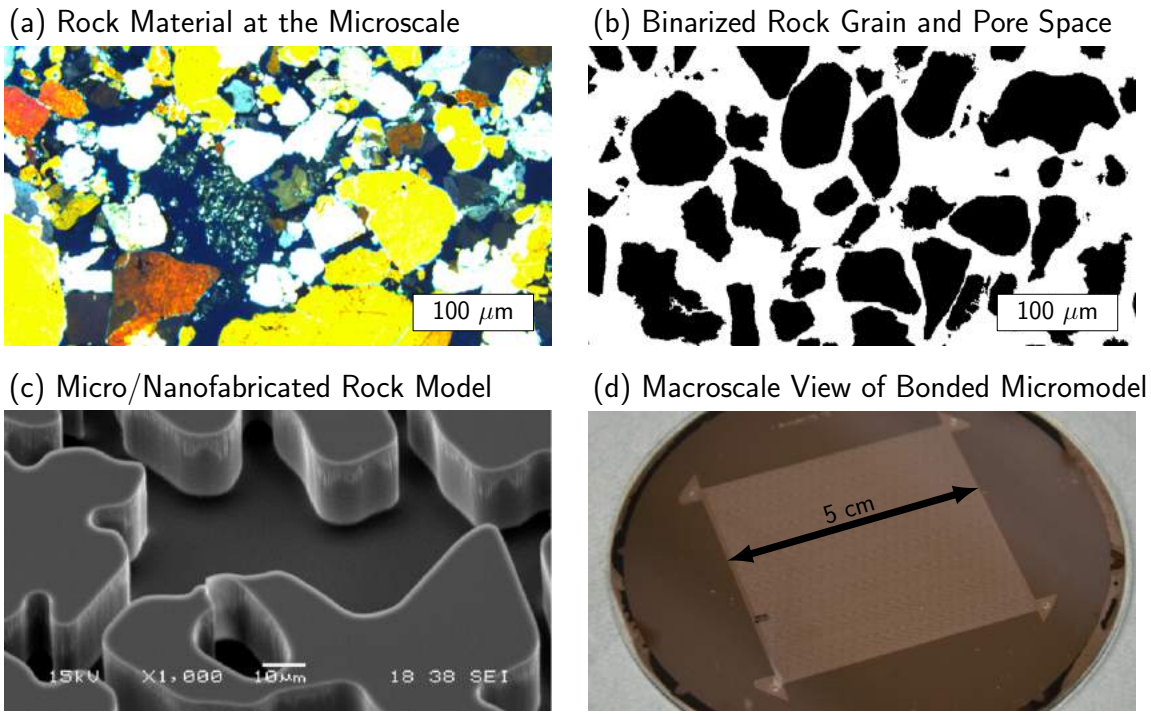

Figure 2.1: Overview of the etched-silicon microfluidic device (micromodel) fabrication process. (a) Representative pore geometry is delineated from a thin-section of real rock material. (b) Binarized photomask with representative opaque grains (black) and transparent pores (white) obtained through image processing of the thin-section image. (c) Etched pore-geometry in a silicon substrate using photolithography and plasma etching. [Reprinted (adapted) with permission from [75].] (d) A macroscopic view of the micromodel device. The etched silicon device is bonded with glass to enable direct visual observation of micro-confined flow in porous materials.

Techniques of etching into the silicon wafer are borrowed from existing methods in silicon-based semiconductor manufacturing. Specifically, the method of etched-silicon micromodel fabrication entails four main processes: (i) the recreation of representative pore geometry from real rock materials (Fig. 2.1a); (ii) the photolithographic transfer of the recreated pore geometry onto the silicon etching substrate (Fig. 2.1b); (iii) the permanent etching of the pore geometry into the silicon substrate (Fig. 2.1c); and (iv) the bonding of an optically transparent medium to enable flow and direct microvisual observation into the pore space (Fig. 2.1d). The following describes in detail each of

the four main processes used in this work.

2.1.1 Representative Pore Geometry

Porous rock material are complex in geometry, size, and chemistry. Specifically, size and morphology of the pore spaces are of fundamental importance to fluid transport due to the dominance of capillarity. Central to the pursuit of creating a model platform that provides fundamental insight to the pore-scale dynamics of subsurface systems is the achievement of geometric representation. The pore patterns used in this dissertation are derived from images of thin-sections taken from real rock samples such as the one shown in Fig. 2.1a. For example, in the thin-section shown in Fig. 2.1a, the polarized light micrograph shows grains in yellow, white, and orange, and pore spaces in blue. Colors of the grains indicate differences in the intrinsic refractive indices of the material, and, hence, the mineralogy.

For the purposes of achieving geometric representation of real rock, only the grains and pore spaces are delineated. Image segmentation is used to delineate between the solid grains and the pore spaces that fluids flow through. To transfer the pore geometry onto the silicon etching substrate, the segmented image is binarized such that the areas corresponding to the solid grains are opaque to light (black in Fig. 2.1b) and the areas corresponding to the empty pore spaces are transparent to light (white in Fig. 2.1b). The binarized image is used to create a photomask to enable transfer of the pore geometry pattern onto the silicon wafer through means of photolithography.

The segmented image is stitched into a repeated pattern in order to construct a porous matrix that is 5 cm $\times$ 5 cm. Inlet and outlet fractures are added to allow for even pressure fields at the injection and production ports. The porous matrix hence constructed has an average coordination number of 4; that is, each pore is connected to 4 other pores on average. These dimensions, given the pore sizes of $\sim$ 50 μm, give $\sim$ 300 $\times$ 300 pores, which far exceed the minimum number of pores required for

representative elementary volume scaling in two dimensions [136, 137].

Photomasks used are generally of the printed transparency type or the etched chrome mask type. In both cases, the areas corresponding to the grains, i.e., areas that we want to preserve, are opaque to light, and the areas corresponding to the pore spaces, i.e., areas that we want to etch, are transparent to light. Printed transparencies are limited by the precision of the printer and scattering, and thus features of the order of ~ 20 μm or less are difficult to realize [138]. Etched chrome masks, on the other hand, enable the precise transfer of geometries that are much smaller.

To create the chrome mask, a glass substrate coated with a thin layer of chrome ($\sim \mu$m) is covered with UV-sensitive photoresist. The segmented thin-section image is then printed onto the UV-sensitive photoresist and the exposed chrome is etched away. The resulting chrome photomask is such that the regions where the chrome remains are opaque to light, and thus correspond to the solid grains, and the regions where the chrome is removed are transparent to light, and thus correspond to the pore spaces to be etched away. The binarized chrome photomask is used to transfer the pore geometry onto the silicon wafer through photolithography.

2.1.2 Photolithography

Real rock pore geometry is transferred onto the silicon substrate through means of photolithography (Fig. 2.2a,b,c). Photoresist material is used to act as the transfer agent between the chrome mask and the silicon wafer. Photoresist, however, is organic, while silicon wafers are inorganic. As a result, adhesion of photoresist to the silicon surface directly is difficult to achieve. Central to the transfer of the chrome-mask pattern onto the silicon wafer is the adhesion of a uniform photoresist layer on the wafer.

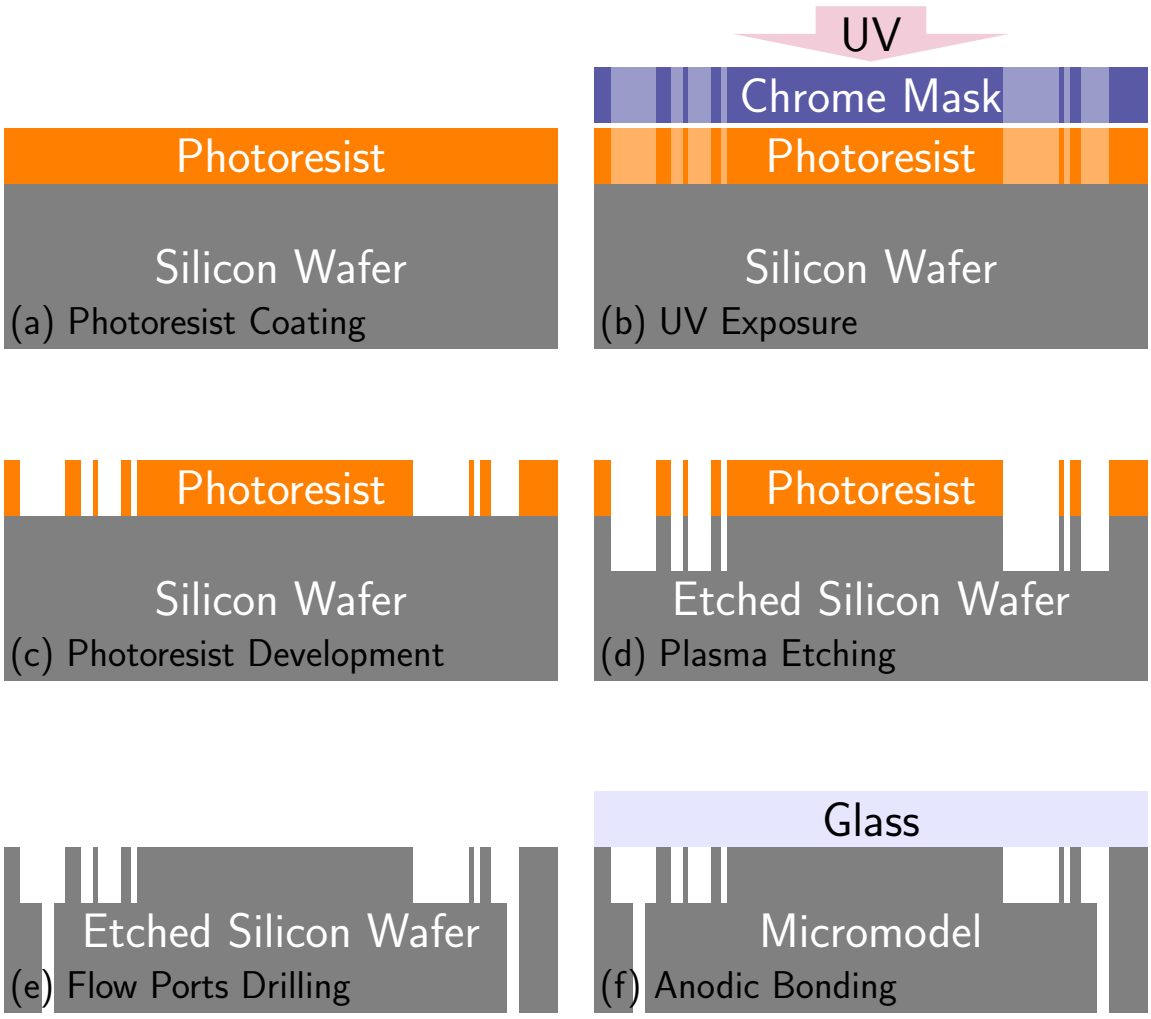

Figure 2.2: Nanofabrication methods used in transferring the rock pore geometry into the silicon substrate. (a) A thin layer of photoresis is spin-coated evenly onto the silicon wafer. (b) Ultraviolet (UV) light is shone through the chrome photomask onto the photoresist. Positive-tone photoresist is used in this work so that the regions of photoresist exposed to UV light, i.e., the transparent pore space, are removed and the regions of photoresist that is not exposed to UV, i.e., the opaque grains, are retained in compliance with the photomask. (c) Photoresist exposed to UV is degraded and becomes easily solublized in photoresist developer. (d) Removal of UV-exposed photoresist leaves regions of silicon wafer unprotected and susceptible to plasma etching. (e) Inlet and outlet flow ports are drilled to enable fluid delivery into the etched microfluidic device. (f) Optically transparent glass is bonded anodically to seal the device and to allow for direct visual observation of the microscale pore-level dynamics.

To enhance the transfer of pore geometry onto the silicon wafers (K prime, 100 mm diameter, orientation $< 1-0-0 >$, thickness 500 μm, front side polished, back side etched, WRS Materials), clean wafers are first dehydrated at 150 °C and primed with a coating of HMDS (Hexamethyldisilazane, HMDS Prime Oven, Yield Engineering Systems, Inc.). The priming treatment allows for improved coverage and adhesion between the inorganic silicon oxide surface on the wafer and the organic photoresist. Specifically, HMDS is a silane that bonds with both the inorganic wafer surface and the organic photoresist. Preheating the wafer removes all water, both surface and bound molecules, from the wafer to enable improved HMDS adhesion.

Upon priming, 1.6 μm of positive-tone photoresist (Shipley 3612) is spin-coated (Silicon Valley Group) onto the silicon wafer (Fig. 2.2a). The coating thickness is related to the etching time, and hence, etching depth. For an etch depth of 25 μm into the silicon wafer, a photoresist coating of 1.6 μm is sufficient. The photoresist-coated wafer is baked to aid in the stability of the photoresist material and to minimize the dark erosion of photoresist material during development.

To transfer the pore geometry onto the photoresist, the chrome mask is placed on top of the photoresist-coated wafer and is exposed to ultraviolet (UV) light (Karl Suss MA-6 Contact Aligner). Specifically, to treat the 1.6 μm photoresist coating, an exposure time of 1.6 s at a UV lamp intensity of 15 mW/cm^2 is sufficient. Care must be taken to ensure that the chrome-side of the photomask is in contact with the photoresist to minimize the effect of scattering. Positive photoresist is degraded upon exposure to UV light. In other words, the opaque grains that are protected are unaffected and the transparent pore spaces that are exposed are degraded (Fig. 2.2b).

Following UV exposure, the photoresist-coated wafer is immersed into a bath of photoresist developer to remove the destabilized photoresist that was exposed to UV light (Fig. 2.2c). That is, we remove the pore-space regions of the photoresist material

and expose the silicon surface to later etching. Photoresist in the unexposed grain regions, on the other hand, are left intact and protected from later etching. To solidify the remaining photoresist onto the surface of the silicon wafer to protect the grains from being etched, the wafer is hard-baked for 120 s.

2.1.3 Plasma Etching

The hard-baked wafers are dry-etched (Fig. 2.2d) using inductively-charged plasma deep reactive ion etching (Surface Technology Systems). The etching procedure is based on the Bosch Process that alternates between a passivating plasma (C_4F_4) and a silicon etching plasma (SF_6). The etching rate for silicon is $\sim$ 2-3 μm per minute. Generally, etch depths for the micromodels used in this work were $\sim$ 35 μm, or about 15 min of etch time. Importantly, due to the anisotropic etching associated with the K-prime silicon wafer, vertical walls with sharp corners are achieved. This is significant to studies on transport through porous media due to the importance of capillarity in corners and crevices.

2.1.4 Flow Enabling

To enable the ingress and egress of fluids into the etched microfluidic channels, entry ports were drilled into the etched silicon wafer (Fig. 2.2e). Specifically, a diamond drill bit (1 mm diameter, DRILAX) was used to drill through the wafer. Upon drilling, the etched wafer was cleaned atomically to remove all impurities, including photoresist, dust, and silicon particles from the drilling process. Atomically clean silicon and glass (Schott Borofloat 33 glass, S.I. Howard Glass, Worcester, MA) surfaces are required for proper bonding between the two. The etched wafer was cleaned using sulfuric acid/ hydrogen peroxide piranha (9:1 H_2SO_4:H_2O_2) at 120 °C for 20 mins to remove all organics followed by a deionized water rinse to remove all other particulates. The

clean silicon and glass substrates are then dried using nitrogen gas and subsequently bonded to enable microconfinement and direct optical visualization (Fig. 2.2f).

Anodic bonding techniques were used to seal the glass to the silicon surface. Specifically, the wafer is first heated for one hour at 500 °C to create an oxide layer. The oxide layer serves two purposes: (i) to encourage bonding with glass; and (ii) to functionalize the silicon surface closer to that of sandstone. Following the oxidation, the glass plate is placed on top of the etched silicon surface and a voltage of 1000 V DC is applied for one hour across top and bottom surfaces of the glass-silicon system to bond the glass to the silicon.

The method of device fabrication described here is general and can be applied to any type of desired geometry. The utility of silicon-based devices lies in their ability to withstand elevated temperature, pressure, and reactivity conditions, and in their ability to replicate a desired geometry. Importantly, silicon-glass microfluidics lends a direct view into the pore-scale fluid-fluid and fluid-mineral interactions that ultimately underlie the understanding and design of subsurface resources management. As such, silicon-based microfluidics are used throughout this work. A list of the equipment used in the fabrication process is listed in Table 2.1.

Table 2.1: Equipment used to fabricate etched-silicon microfluidic devices.

Equipment Name	Maker	Purpose
K-Prime silicon wafer	WRS Materials	Etching substrate
Borosilicate glass wafer	SI Howard Glass Co.	Bonding substrate
HDMS Prime Oven	Yield Engineering Systems	HDMS coating
Spincoater	Silicon Valley Group, Inc.	Photoresist processing
MA-6 Contact Aligner	Suss MicroTec	UV exposure
ICP Deep Reactive Ion Etcher	Surface Technology Systems	Plasma etching
1 mm diamond drillbit	DRILAX	Create ports for flow
Type 1900 Hot Plate	Thermo Scientific	Anodic Bonding
6215A Power Supply	Hewlett Packard	Anodic Bonding
Squaroid Vacuum Oven	Lab-Line	PDMS curing

2.2 Fluid-Fluid and Fluid-Solid Microvisualization Apparatus

Apparatus for direct optical microvisual observation of fluid-fluid and fluid-mineral interactions were comprised generally of the silicon-based micromodel, a microscope and camera for visualization, and a pump for fluid delivery (Fig. 2.3). Specifically, fluids were delivered to the micromodel using a syringe pump (Harvard Apparatus, Holliston, MA) at low pressures and a QUIZ-X pump (Quizix QX Pump) at high pressures. The micromodel was interfaced using a custom micromodel holder, with inlet and outlet ports to connect to tubing and the pump(s). Fluid-fluid and fluid-mineral interactions and dynamics were visualized using reflected light microscopes and images were captured using a mounted camera. The specific list of equipment used is listed in Table 2.2.

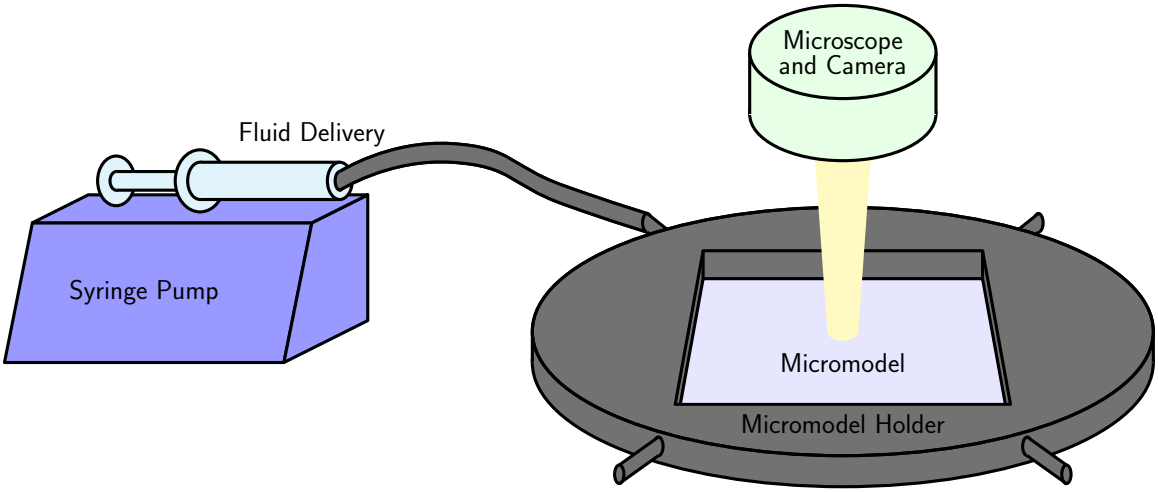

Figure 2.3: Experimental apparatus for direct optical microvisual observation of pore-scale fluid-fluid and fluid-mineral dynamics. Fluid delivery to and visualization of pore-scale dynamics in the micromodel was achieved generally using pumps and microscope-camera systems. used in experiments.

Table 2.2: Equipment used to observe microscale fluid-fluid, fluid-mineral dynamics directly.

Equipment Name	Maker	Purpose
LEICA Z16 APO Macroscope	Leica	Large field of view
Nikon SMZ 1500 Microscope	Nikon	Reflected light microscope
Sensofar Sneox 3D optical profiler	Sensofar	Confocal microscopy
Syringe Pump	Harvard Apparatus	Fluid delivery, low pressure
QX-1500 PUMP	QUIZIX	Fluid delivery, high pressure
Digital Plus NESLAB RTE17	Thermo Scientific	Water bath

Chapter 3

Clay-Functionalization of Microfluidics

Sandstone formations are ubiquitous to both aquifers and petroleum reservoirs, of which clay is a major constituent. The release of clay particles from pore surfaces as a result of reduced injection fluid salinity can greatly modify the recovery of hydrocarbons from subsurface formations by shifting the wettability properties of the rock. This chapter demonstrates a microfluidic approach whereby kaolinite is deposited into a two-dimensional microfluidic network (micromodel) to enable direct pore-scale, real-time visualization of fluid-solid interactions with representative pore geometry and realistic surface interactions between the reservoir fluids and the formation rock. Structural characterization of deposited kaolinite particles agrees well with natural modes of occurrence in Berea sandstone; hence, the clay deposition method developed in this work is validated. Specifically, more than 90% of the deposited clay particles formed pore-lining structures and the remainder formed pore bridging structures. Further, regions of highly concentrated clay deposition likely to lead to so-called Dalmatian wetting properties were found throughout the micromodel. Two

post-deposition treatments are described whereby clay is adhered to the silicon surface reversibly and irreversibly resulting in microfluidic systems that are amenable to studies on (i) the fundamental mechanisms governing the increased oil recovery during low salinity waterfloods, and (ii) the effect of a mixed-wet surface on oil recovery, respectively. The reversibly functionalized platform is used to determine the conditions at which stably adhered clay particles detach. Specifically, injection brine salinity below 6000 ppm NaCl induced kaolinite particles to release from the silicon surface. Furthermore, when applied to an aged system with crude oil, the low salinity waterflood recovered an additional 14% of the original oil in place compared to waterflooding with the formation brine.

3.1 Introduction

Rock wettability is a key determining factor in the recoverability of oil from the subsurface. Clean, unaltered sandstone is strongly water wet [11]. Clay, however, is oil wet [29, 22]. Naturally occurring sandstones that encompass petroleum reservoirs contain significant amounts of clay that are natively adhered to the surface of sand grains. Interaction between the clay particles, connate water, and specific components in the hydrocarbon drastically change the transport of fluids in the subsurface [22, 21, 23]. Oil-wet systems generally result in lower recovery factors as compared to those in mixed-wet or water-wet systems for economic amounts of water injection.

Waterflooding is a recovery technique that is widely practiced to increase the recovery of hydrocarbons from the subsurface. Specifically, brines with various components (*e.g.*, salts, acids, etc.) are commonly injected into hydrocarbon-containing formations to drive out the remaining oil. With the introduction of other fluids during secondary and tertiary recovery, primarily with the injection of brine that is compositionally dissimilar to the connate water, clay particles have been found to detach

from the pore space and subsequently plug the available pore throats during their migration. In particular, the salinity and pH of the injected brine along with the temperature of the system have been found to play a significant role in the release of the fine clay particles from sand grains [23, 32, 4].

The literature presents several studies to delineate the fundamental mechanisms that cause clay particles to detach from the pore surface [23, 32, 39, 40, 139]. Specifically, the DLVO (Derjaguin, Landau, Verwey, and Overbeek) theory has been applied to describe the interplay of attractive van der Waals forces and repulsive double layer forces between the clay particles and sand grains; these interactions define the conditions at which clay particles are released. Effects such as the impact of cation species on clay detachment, however, are not well accounted for by the DLVO theory without other considerations (*e.g.*, electroselectivity) [41]. A mechanistic understanding of pore-level clay mobilization under different reservoir conditions is required.

Mobilized clay particles affect the reservoir, and ultimately the recovery of hydrocarbons, in a number of ways. Two important mechanisms by which detached clay significantly impacts subsurface flow are as follows. First, the flocculation of detached clay particles in the presence of low salinity brine results in larger particles that easily plug pore throats. Blocked pore throats drastically decrease the paths available for flow, and thus reduce the permeability of the formation and ultimately its recovery. This is known as formation damage [7]. Second, the release of oil-wetting clay particles from the water-wetting sand surface shifts the wettability of the system to one that is increasingly water-wet, and hence increases the ability to recover hydrocarbons from the subsurface [45]. Therefore, it is crucial to understand (i) the mechanisms that cause clay particles to detach from the pore space, and (ii) the consequences resulting from its release and migration.

Understanding of pore-scale behavior is critical to the design and execution of effective oil-recovery schemes. Core-scale experiments have previously been conducted

to study fluid-fines interactions and the effects of various parameters (*e.g.*, temperature, pH, and salinity of injection fluid) on clay detachment [29, 22, 32, 40, 41, 33, 140]. Through these experiments, indirect measures of changes in the porous medium (*e.g.*, formation damage, wettability alteration) are deduced. Core experiments, however, are unable to capture the pore-scale events that dictate the low salinity effect. Advanced visualization techniques such as X-ray computed tomography (X-ray CT) [141] and micro X-ray computed tomography (micro X-ray CT) [142] are able to obtain pore-scale visualization in core flood experiments; however, individual scans can take upwards of 40 minutes, rendering them opaque to the dynamics of microscale clay detachment studies in the time frame that is required. Real time pore-scale visualization of the interactions between the fluids, grains, and clay particles is required to develop a fundamental understanding of the mechanisms that dictate recovery efficiency of hydrocarbons from the subsurface.

Microfluidics is an emerging technology that enables the direct visualization of pore-scale phenomena in real time [107]. Recently, glass and silicon microfluidic devices with representative pore-scale geometries have enabled the study of fluid behavior in petroleum related applications [75, 79, 108, 94, 131, 143, 144, 145, 146]. Specifically, microfluidic techniques have been applied to reservoir fluid property measurements such as asphaltene content and solvent diffusion in crude oil [145, 130, 117, 119]. In particular, Buchgraber et al. 2012 [79] describe the creation of two-dimensional microfluidic devices (micromodels) with pore-scale geometry that is identical to real rocks using thin section images obtained with a scanning electron microscope (SEM). These micromodels allow for the direct visualization of flow behavior through a two-dimensional porous medium that is geometrically representative. This approach however is limited by the lack of representative surface heterogeneity that dictates pore-scale flow dynamics. Silicon and glass substrates, like the quartz grains that comprise the majority of sandstones, are strongly water wet. The presence of clays and their

associated properties, however, are not represented in this micromodel. That is, previous micromodels could not replicate the presence of clays within the pore space and their influence on hydrocarbon recovery processes through phenomena such as (i) detachment in the absence of salt ions, (ii) fines migration, and (iii) its role in increasing recovery during low salinity water flooding and in formation damage.

In this chapter, a process is developed to functionalize a silicon micromodel by adding clay to pore surfaces. The resulting micromodel allows us to better understand the mechanisms dominating particle release and subsequent formation damage. In the following, a method for coating the micromodel with kaolinite - a non-swelling, dispersive clay typically present in sandstones - is described. Specifically, methods for depositing the clay both reversibly (*i.e.*, adhered to the silicon surface at high salinities but its attachment is sensitive to reductions in injection fluid salinity) and irreversibly (*i.e.*, attached to the pore surface and is insensitive to changes in the injection fluid salinity) are described. To validate the approach, the modes by which kaolinite particles were attached to the silicon surface were characterized and compared to their mode of occurrence in sandstones as indicated in the literature. Visualization experiments using the reversibly clay-coated micromodel show evidence of clay migration and of permeability reduction as a result of low salinity water flooding. Furthermore, experiments involving crude-oil displacement resulted in wettability alteration of the system, emulsion generation, and increased oil recovery after low salinity waterflooding.

3.2 Experimental Methods

Pore-scale visualization of the impact of salinity and temperature on clay mobility in sandstone was achieved using a two-dimensional microfluidic device with pore structures representative of those found in reservoir rock. Specifically, the microfluidic

device (micromodel) used in this work follows the description in Chapter 2. Silicon and glass substrates were chosen in this work due to their inherent water-wettability and compositional similarity to sandstone. The following section describes the novel method by which the surface of the pore space within the micromodel was functionalized using clay to obtain a system that is well representative of a real reservoir and the subsequent treatments resulting in mobile and immobile clay particles.

3.2.1 Clay solution preparation and deposition into the micromodel

Deionized (DI) water was used to create a 15000 ppm NaCl (Sodium Chloride, S271-3, Fisher Scientific) solution typical of formation brine. A 1 wt% clay suspension was prepared by adding kaolinite powder (Kaolin, K2-500, Fisher Scientific) to the vigorously stirred saline solution at atmospheric pressure. Kaolinite clay was chosen to replicate the initial conditions within the reservoir due to its prevalence in Berea sandstone and hydrocarbon reservoirs [32]. Moreover, kaolinite is non-swelling in nature. That is, changes in the porous medium permeability are expected to be solely due to clay detachment from the silica surface, its migration, and its blockage of pores/pore throats.

The kaolinite powder was mixed into to the high salinity reservoir brine in order to (i) deliver the kaolinite particles evenly into the microfluidic system without severe plugging (and consequently permeability reduction) and (ii) allow for sufficient clay adsorption on the silica surface because the presence of cations is critical to clay attachment, as explained by the DLVO theory [40]. Specifically, it has been shown previously that the introduction of low salinity brine to a system initially in contact with high salinity brines can (i) increase oil recovery, and (ii) stimulate fines migration [29, 41, 33, 140]. Furthermore, clay particles require the presence of specific cations

in the aqueous phase in order to attach to the silica surface; the absence of the required ions lead to clay particle release, increased flocculation, and ultimately pore plugging (*i.e.*, formation damage) [7]. The kaolinite mixture was stirred vigorously for 15 minutes until a homogeneous solution was obtained. The suspension was then sonicated (Bransonic 220) for one hour to disperse the kaolinite particles throughout the mixture and to prevent flocculation from occurring. A well-dispersed kaolinite solution delays premature particle settling in the fluid delivery tubing and enables injection into the micromodel without significant plugging at the inlet fracture.

The experimental setup is shown in Chapter 2, Fig. 2.3. Deionized water was injected into the micromodel using a 12 mL syringe (Monoject) and a syringe pump (Harvard Apparatus, Holliston, MA) to displace the initial gas phase at a superficial velocity of 30 m/day. The syringe pump was nominally pulseless and a stainless steel syringe was used to inject the saline fluids (no stick-slip) to minimize pressure pulses during experiments. Fluids were delivered at a constant flow rate, with the outlets open to the atmosphere. All experiments were conducted at room temperature. The fluid behavior within the microfluidic system was visualized under brightfield imaging using a reflected light metallurgical microscope (S/N: MT1000T2006120001) and images were captured using a mounted camcorder (Canon VIXIA HF S200 HD Camcorder). The microfluidic system was continuously flushed with deionized water until all trapped gas bubbles were displaced by or dissolved into the aqueous phase. After the micromodel was fully saturated with water (no more gas phase present), several pore volumes of deionized water were flowed through to ensure that the system contained no other ions.

Once the micromodel was fully saturated with DI water as shown in Fig. 3.1(a), several pore volumes of the reservoir brine were injected using the syringe pump. The motivation for this is two fold: (i) to replicate the connate water in the reservoir, and (ii) to avoid clay flocculation during deposition as a result of low salinity shock. The

well-dispersed kaolinite suspension was then injected using the syringe pump at a rate of 20 m/day for several pore volumes to deposit a sufficient coating of kaolinite in the system. The optimal injection rate was found to be 20 m/day to minimize pressure buildup and maximize homogeneous clay deposition. To prevent plugging at the inlet fracture, the kaolinite suspension may be introduced while sonicating the micromodel. Sonicating the system during injection also aids in creating an evenly distributed clay coating within the micromodel; however, sonication for extended periods (*e.g.*, continuous sonication during kaolinite deposition) inhibits the clay from attaching to the surface of the micromodel.

Once the micromodel was sufficiently coated with clay, as shown in Fig. 3.1(b), the system was injected with air to remove plugged particles at the pore throats. The strong interfacial tension between the air and the brine was able to dislodge throat plugging clays as well as kaolinite particles that were not firmly attached to the silica surface. Fig. 3.1(c) shows the clay-coated micromodel that is well representative of reservoir rock, in which the pores are evenly coated with a significant amount of clay and with very few plugged pore throats.

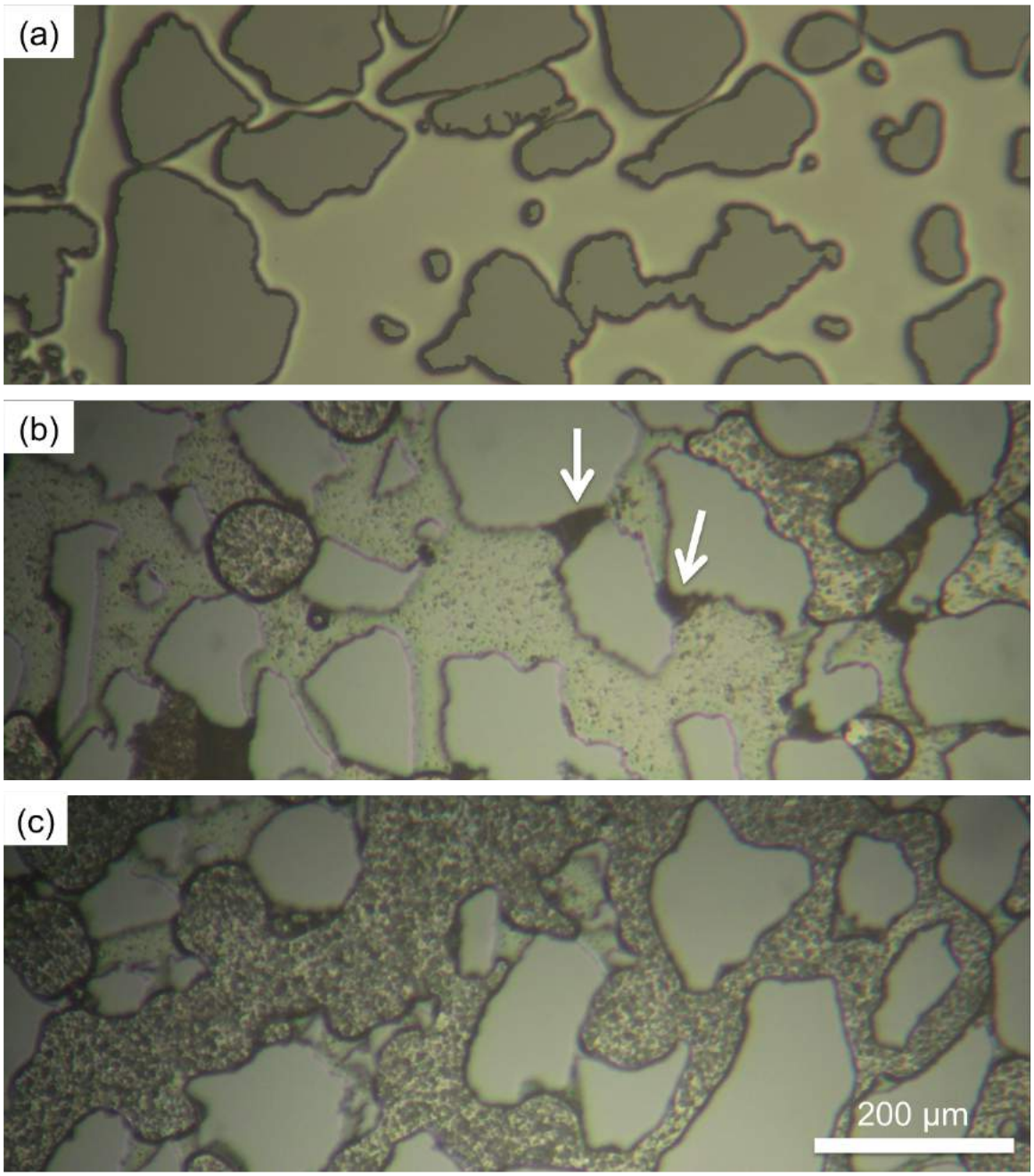

Figure 3.1: Kaolinite deposition into micromodel pore space. (a) Water-saturated micromodel prior to clay introduction. (b) Some plugging is seen in pore throats after clay addition, which does not well replicate initial conditions in reservoir rock (refer to white arrows). (c) The throat-plugging clay particles are removed by the strong interfacial tension between the brine and the air, providing a clay coated silica surface that is well representative of reservoir rock.

3.2.2 Micromodel treatment determining clay mobility

After the dislodgement of throat-plugging kaolinite, the micromodel was treated in one of two manners to create a system in which (i) the clay may be mobilized in response to decreases in brine salinity, or (ii) the clay is immobile in the system for all salinities. First, for the detachment studies conducted here, a reversible (mobile clay) system was desired. In this case, the microfluidic system was re-saturated and flushed with the initial reservoir brine at 20 m/day in order to eliminate any particles that were not adhered to the grain surface. Brine flooding was conducted for several pore volumes and images were taken at a fixed location until no more changes in the deposited clay could be observed.

Second, for wettability alteration studies requiring the presence of immobilized clay in the pore space, an irreversible system was desired. Consequently, the silicon surface was functionalized through heating the vacuum-dried micromodel. The clay-coated micromodel was placed on a hot plate that was initially at room temperature, and heated gradually to 120 °C for 25 minutes. This treatment ensured the clay particles were firmly attached to the micromodel surface, while the temperature does not induce chemical degradation of the clay [147]. It was critical for the micromodel to be drained of water (saturated with air) in order to avoid breaking the micromodel due to the rapid volume expansion and subsequent pressure buildup from boiling during heating. The heated micromodel was then allowed to cool and was ready for visualization experiments to demonstrate the irreversibility of this process (*i.e.*, its lack of clay particle detachment in response to low salinity water).

3.2.3 Sensitivity experiments of salinity on clay detachment

Deionized water was used to create NaCl solutions at concentrations spanning the range of salinities typically used during secondary and tertiary recovery processes.

Specifically, for each low salinity sensitivity experiment, the micromodel was flooded with the initial reservoir brine (15000 ppm NaCl) followed by the reduced salinity brine. Salt concentrations in the reduced salinity brines ranged from 8000 ppm to 0 ppm NaCl (fresh water) in decrements of 2000 ppm. The low salinity solutions were injected into the micromodel to study the sensitivity of clay detachment from the pore surface in response to reduction in NaCl concentration. The solutions were delivered at constant flow rates corresponding to a superficial velocity of 30 m/day. Each saline solution was injected for 1 hour to allow for sufficient interaction between the solids and the fluid. For each waterflood that did not result in clay detachment, high salinity (15000 ppm NaCl) brine was injected to generate the initial condition for the next experiment. In each experiment, the sensitivity of clay detachment to brine salinity was determined by visualizing the clay particles through the microscope in real time. Images were taken at the same location (for both high and low salinity brines) to isolate changes in the attached clay. The microfluidic system was maintained at atmospheric pressure downstream.

For reuse purposes, the micromodel was most effectively cleaned by alternating 1M nitric acid (CAS: 7697-37-2, Sigma-Aldrich) injection with air injection for multiple pore volumes such that the strong interfacial tension between the gas and liquid phases could sweep away the particles loosened by acid. Sonication of the micromodel during acid injection aided the cleaning process by preventing the mobilized clay particles from flocculating or reattaching to the pore spaces downstream.

3.2.4 Water flooding experiments on Low Salinity Effect

For studies on the effect of injection fluid salinity on oil recovery, formation brine and crude oil were introduced to the reversibly kaolinite-coated micromodel to replicate initial reservoir conditions. Table 3.1 lists the composition of the brine chosen.

Table 3.1: Composition of brine used to simulate initial reservoir conditions.

Reagent	Concentration (g/L)
$CaCl_2 \cdot 2H_2O$ (Calcium chloride dihydrate)	0.183
$MgCl_2 \cdot 6H_2O$ (Magnesium chloride hexahydrate)	0.585
NaCl (Sodium chloride)	20.461
KCl (Potassium chloride)	0.611
Na_2SO_4 (Sodium sulfate)	0.109

The vacuum dried micromodel (*i.e.*, micromodel that was reversibly coated with clay) was continuously flushed with several pore volumes of the brine using the syringe pump to create a fully water saturated system. The motivation for saturating the micromodel with brine typical of a reservoir was two fold: (i) to replicate the connate water in the reservoir, and (ii) to avoid clay detachment as a result of low salinity shock.

Once the microfluidic system was fully saturated with the initial reservoir brine, crude oil was injected into the micromodel at 30 m/day and images were taken to observe the drainage process. The properties of the crude oil are as listed in Table 3.2. The interactions between kaolinite and the acid/base groups and asphaltenes in the crude oil are critical to the wettability alteration of the system, and thus crude oil was chosen in this dissertation as opposed to mineral oils. Crude oil was injected for several pore volumes and water saturation was monitored over time until such a point at which the residual water saturation remained constant. The microfluidic system was then set aside and allowed to age for two weeks at ambient conditions to allow for sufficient interaction between the crude oil and the kaolinite particles to alter the silicon surface towards oil-wettability. The resulting system was deemed the initial reservoir condition.

Table 3.2: Crude oil characterization [148].

Crude oil properties	Value
Acid number (mg/g)	2.36
Base number (mg/g)	6.02
Asphaltene content (wt%)	2.69
Density (°API)	21
Viscosity at 22.8°C (cP)	105.7

After the microfluidic system was aged, a high salinity waterflood was performed followed by a freshwater waterflood to study the low salinity effect. The high salinity waterflood consisted of injecting the synthetic reservoir brine (as listed in Table 3.1) at a rate that corresponds to a superficial velocity of 30 m/day. The water and oil saturations were continuously monitored using the microscope setup. The high salinity waterflood was continued until the water saturation plateaued (*i.e.*, no incremental increases in water saturation was observed). The plateau corresponded to the residual oil saturation as a result of the high salinity waterflood. Subsequently, the micromodel was injected with fresh water at the same conditions as the high salinity waterflood and images were taken at fixed locations before and after the freshwater flood to visually determine any additional oil recovery from the system.

3.3 Results and Discussion

Micromodels coated with kaolinite reversibly (mobile clay particles for detachment sensitivity studies) and irreversibly (heat-facilitated immobilization of clay particles for wettability alteration studies) were created. Specifically, clay mobilization was (i) observed for brines with salinities between 6000 and 4000 ppm NaCl in the reversibly coated system, in agreement with core-flooding experiments for Berea sandstone; and

(ii) not observed for any salinities for the irreversibly coated micromodel. Further, the presence of clay was found to change drastically the pore-space wettability properties from strongly water-wet to mixed-wet, and resulted in increased oil recovery after low salinity waterflooding.

With respect to the locations that fines were deposited, clay accumulation patterns were well-correlated to the in-situ flow conditions. In general, very little clay deposition occurred in high velocity flow paths. Minimal deposition in the high velocity regions occurred as pore-bridging structures as a result of mechanical pore blockage under high flow velocities. Interestingly, Fig. 3.2(b) shows that large, plate-like kaolinite crystals overlapped one another to form bridge structures across narrow pore throats (high velocity paths). The high degree of connectivity between the pores (coordination number ~ 4) and large number of pores in the system gives rise to flow in both series and in parallel. Pore-scale flow simulation of this system, however, shows that the predominant direction of transport is in series, in accordance with the imposed pressure drop across the micromodel. Furthermore, the flow here is single phase and can be approximated as incompressible and at steady state. As such, fluid velocity is significantly higher through narrow pore throats, as required to carry the large particles before mechanical immobilization. Pore-bridging clay structures were not found across wide pore throats (low velocity regions). Significant clay deposition was found in enclosed low velocity regions immediately adjacent to high velocity paths where the clay particles are being carried into the pore space by the high-energy fluid and is then propelled into and retained in the enclosed stagnant regions due to the lack of flow. Minimal clay deposition, however, was observed in open stagnant regions due to the absence of a trapping mechanism to retain the free particles. Similar deposition patterns were observed for different positions with the same grain structure, further suggesting the dependence of clay deposition on carrier fluid velocity.

Sediment transport is commonly characterized by the Rouse number, $P = w_s/\kappa u^*$,

where w_s is the particle fall velocity, $\kappa = 0.41$ is the von Karman constant, and u^* is the shear velocity of the flow. Specifically, the Rouse number is a dimensionless number that compares the rate at which particles fall versus the shear velocity of the flow that is keeping the particles in suspension. The experimental conditions during kaolinite deposition correspond to a Rouse number of ~ 0.2, where particles are expected to be transported as a wash load under which the flow velocity far exceeds the maximum velocity required for particles to settle. The significant deposition of pore-lining clays in the experiments, however, suggests that the ionic strength of the solution is the key driving force for particle attachment, as opposed to flow shear rates.

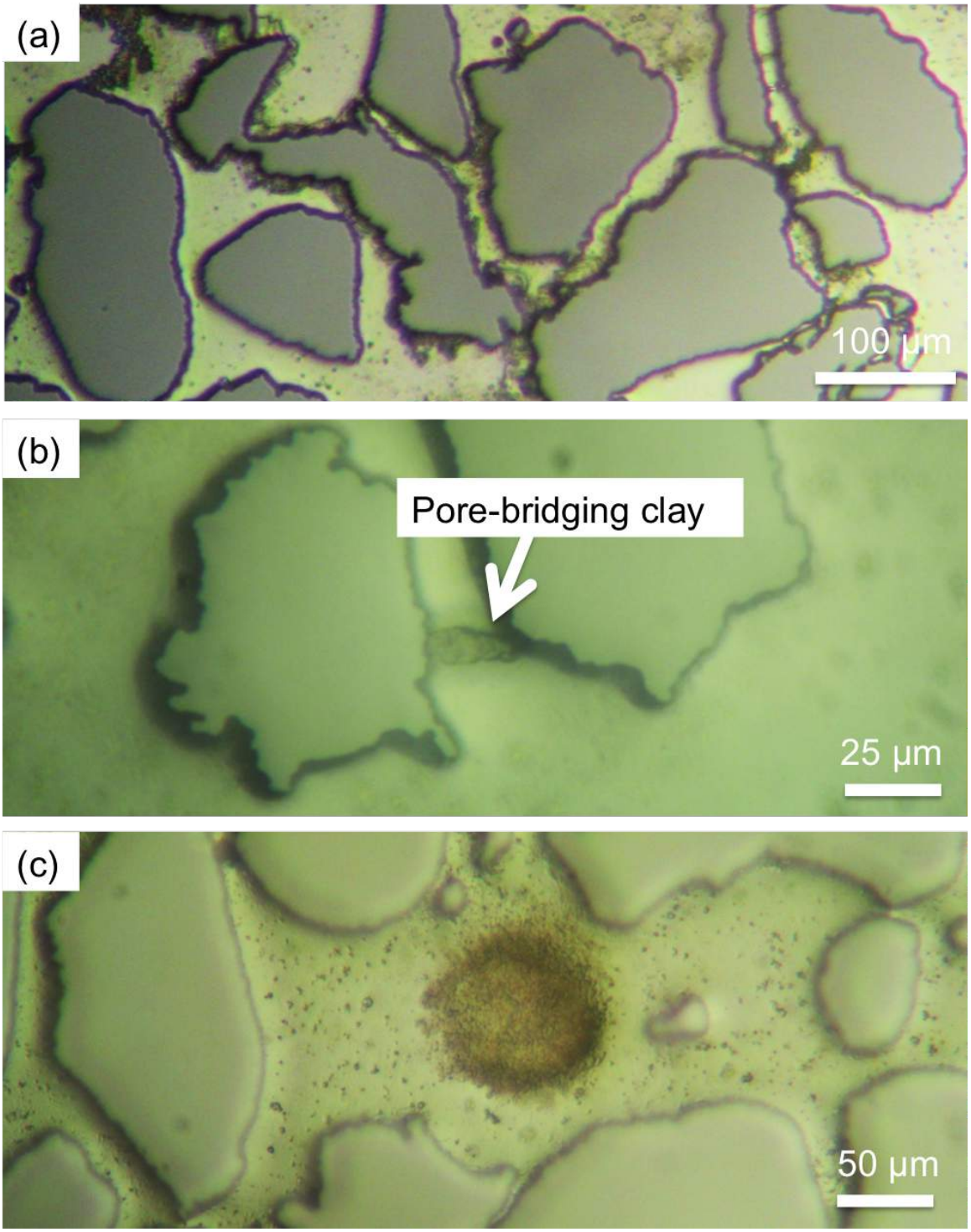
(a)
100 µm
(b)
Pore-bridging clay
25 µm
(c)
50 µm

Figure 3.2 *(previous page)*: Clay deposition structures and their incidence as a percent of total clay in the micromodel. Kaolinite was most commonly deposited ($> 90\%$) as discrete particles and in pore lining structures (a), while the remainder formed pore-bridging structures (b) as well as heterogeneous structures (c).

Clay structures were characterized and compared to those in naturally occurring sandstones to validate the deposition method developed. Specifically, discrete particles/pore-lining structures and pore-bridging clay structures were observed, as shown in Fig. 3.2(a) and Fig. 3.2(b), respectively. Furthermore, anomalous deposits of kaolinite were also observed in which clay was concentrated within specific regions, as shown in Fig. 3.2(c). These patches of discontinuous mineralogy may lead to the formation of Dalmatian wetting patterns, cf., Cueic et al 1991 [27]. It was found that discrete particles and pore lining structures (Fig. 3.2(a)) were the most prevalent modes for attachment to the silica surface, accounting for $\sim 90\%$ of the total kaolinite particles deposited into the micromodel, while pore bridging structures rounded out the remainder of the deposited clay. These results are consistent with kaolinite occurrence in sandstone cores as reported in the literature [149], and demonstrate that the deposition method described here resulted in a pore space that was structurally representative of a clay-rich sandstone.

To validate the wettability characteristics of the clay-coated micromodel, 15000 ppm NaCl brine was introduced to the initially dry micromodel under spontaneous imbibition conditions. Specifically, the spontaneous imbibition experiments showed that while the brine was able to penetrate the vast majority of the pore space, the anomalous clay clusters were extremely non-wetting to brine (in the presence of air) upon re-introduction. Fig. 3.3(a) shows a vacuum-dried micromodel with anomalous clay clusters, and Fig. 3.3(b) shows the same location after 2 minutes of spontaneous imbibition with 15000 ppm NaCl brine. It is evident that the brine did not easily penetrate the pores where the highly concentrated clay clusters were located. In fact,

after some time of spontaneous imbibition, the water-air interface closely followed the outline of the clay clusters, clearly demonstrating that the system has shifted from being homogeneously water-wet to heterogeneously mixed-wet.

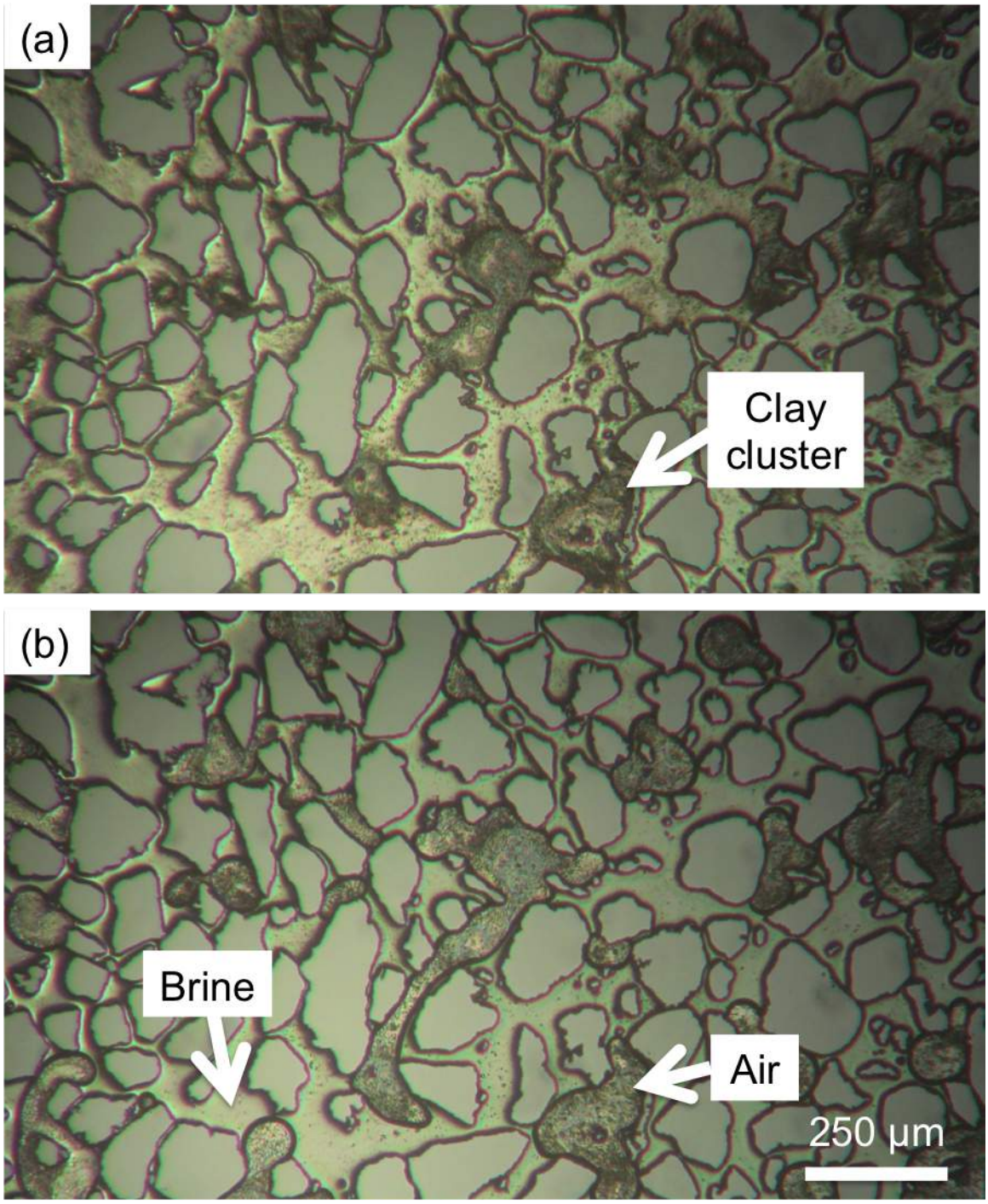
(a)
Clay cluster
(b)
Brine
Air
250 µm

Figure 3.3 *(previous page)*: Dry anomalously concentrated regions of kaolinite (a) is spontaneously imbibed with 15000 ppm NaCl brine (b). The initial phase is air, shown in (a), with significant deposits of kaolinite clusters. Upon spontaneous imbibition of brine, shown in (b), the kaolinite clusters are extremely non-wetting to water in the presence of air. Note the water-air interface in (b) that contours the kaolinite clusters. The water does not generally cross the circular outline of the kaolinite cluster during spontaneous imbibition.

3.3.1 Sensitivity of reversibly deposited clay to salinity

Initiation of significant fines release from the pore surface was visualized for injection brine salinities between 6000 and 4000 ppm NaCl, in alignment with core experiments in Berea sandstone where the critical salt concentration for kaolinite release was found to be around 4000 ppm NaCl [39, 41]. The effect of injection fluid salinity on kaolinite detachment from the silicon surface was quantified by injecting brine through the micromodel at a constant flow rate corresponding to a near-well superficial velocity of 30 m/day. The micromodel was imaged at fixed locations to visualize any changes in clay deposits. Low salinity brines with NaCl concentrations of 8000 ppm, 6000 ppm, 4000 ppm, 2000 ppm, and 0 ppm were injected into the clay-coated micromodel, in that order. The sensitivity of the attached kaolinite to salt ion concentration in the system was directly visualized using the microscope to identify the critical salt concentration at which kaolinite detaches from the silicon surface.

Images were taken at 25 fixed locations evenly distributed throughout the micromodel at initial reservoir conditions (15000 ppm NaCl) and during reduced salinity brine injection to identify the salinity at which clay particles are released. Quantitative analysis of the collective set of images is shown in Fig. 3.4(a) using image analysis. Effluent analysis was difficult to perform due to the microscale of the system. The strength of this method, however, is in enabling the direct visualization of clay

detachment; this is not possible with conventional core flooding experiments that require effluent analysis. Figure 3.4(a) shows the fraction of the pore space whereby clay particles were mobilized due to changes in NaCl concentration for various locations throughout the visualization platform. No clay mobilization was observed for injection brine concentrations above 6000 ppm NaCl. At 6000 ppm NaCl, however, minor clay particle detachment and migration was observed after the low salinity brine was injected. Specifically, the observed clay mobilization was confined to within ~ 15 pore spaces of the inlet. Figure 3.4(a) shows a sharp rise in the fraction of mobilized clay particles after flooding with 4000 ppm NaCl brine, corresponding to significant clay detachment observed. These observations are consistent with those of core flooding in Berea sandstone and hence validate the method developed here [4, 41]. Pore-scale heterogeneities invariably introduce discrepancies from one pore to another; the collective analysis obtained using images at the 25 fixed locations throughout the micromodel, however, provides a good generalization for the system observed. Error associated with image analysis was small; the largest uncertainty associated with the data is as displayed by the error bar corresponding to 0.9 ± 0.05 at 4000 ppm NaCl. That is, all other error bars were less than this. Figure 3.4(b) and (c) show the micromodel before and after 1 hour of 4000 ppm NaCl brine injection. Specifically, Fig. 3.4(c) shows that (i) clay particles were stripped from large channels and (ii) were re-deposited in regions with large pore body to pore throat ratios. These patterns resemble those of sedimentation in macro-systems such as riverbeds. Moreover, a significant increase in the number of large pore-bridging structures (spanning one to 3 pores) were found after the system was in contact with 4000 ppm NaCl brine, as highlighted in Fig. 3.4(c,iii). These large bridge configurations were the most predominant structures after the pore space was in contact with brine below 4000 ppm NaCl. The formation of the large bridging structures correspond well to a decrease in

injectivity of brine into the micromodel, suggesting a negative impact on the transport of fluids with decreased salinity brine injections. Drastic clay mobilization was observed throughout the entirety of the micromodel after both 2000 ppm NaCl brine and freshwater (0 ppm NaCl) flooding.

Figure 3.4(a) shows that while the release of kaolinite from the silicon pore surface was induced after flooding with 4000 ppm NaCl brine throughout the direct visualization platform, the fraction of the affected pore space were varied. The reverse lower axis serves to demonstrate that clay mobilization occurs only when a critical salt concentration has been reached. That is, the reverse lower axis shows the progression of waterflooding that goes from high salinity to low salinity. Specifically, high fractions of mobilized clay were found in regions corresponding to preferential flow paths, as determined through single-phase pore-scale flow simulations, where the low salinity brine was delivered effectively through advection, whereas low clay mobilization was found in regions corresponding to stagnant flow conditions where salt dilution was mostly driven by diffusion. Pore-level permeability reductions due to the formation of bridging structures across preferential flow paths resulted in drastic increases in clay mobilization at lower salt concentrations, as shown by the cases denoted by the dashed lines in Fig. 3.4(a). These results confirm that the release of kaolinite particles from silicon is indeed sensitive to both the salt ion concentration in the system as well as the interstitial flow velocity. This, however, is in contrast to experiments conducted by Khilar and Fogler, where the detachment of clay particles from a Berea sandstone core was found to occur around 4000 ppm NaCl but was insensitive to flow rate for velocities between 4 m/day to 720 m/day.

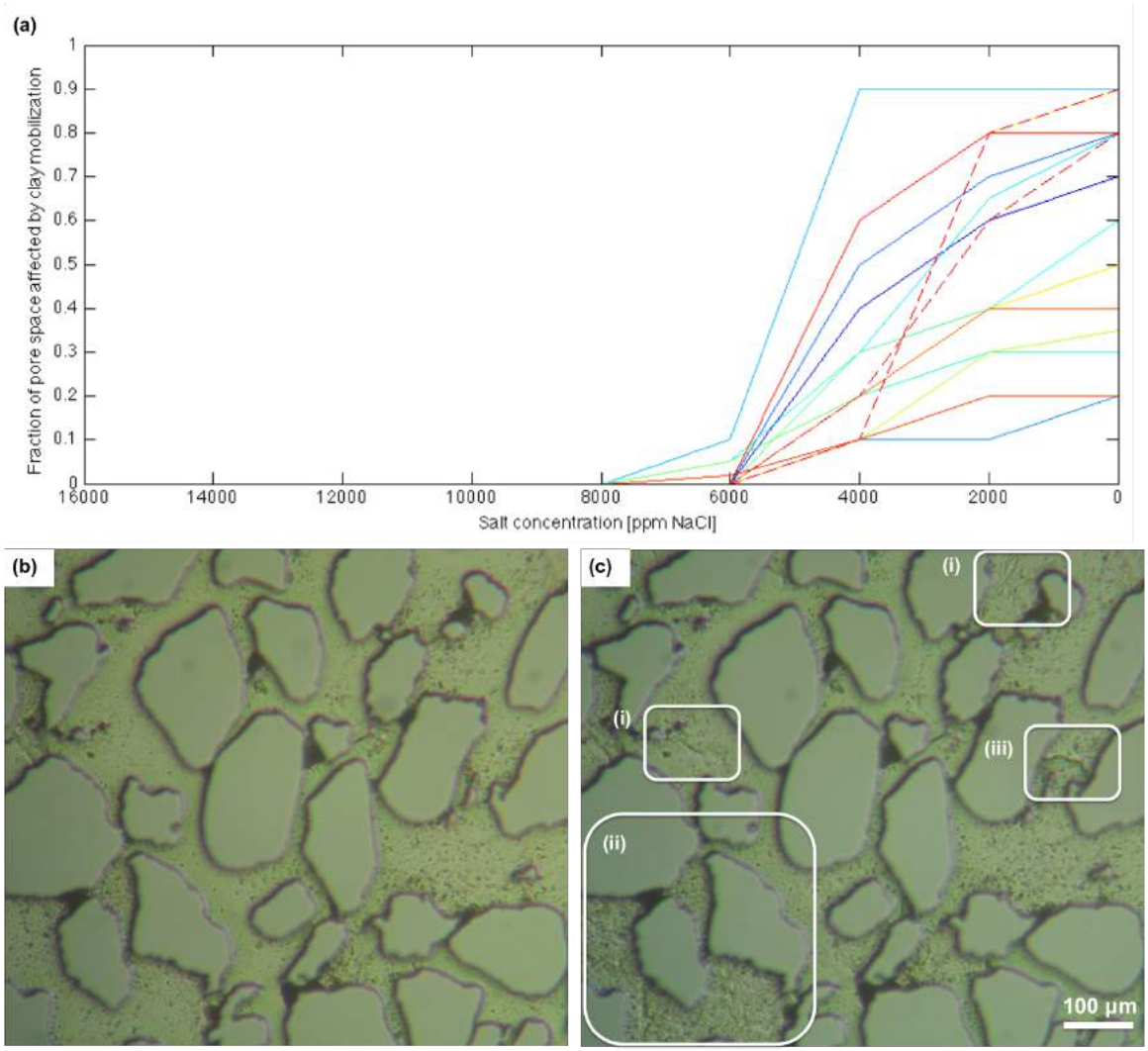
(a)
Fraction of pore space affected by clay mobilization
Salt concentration [ppm NaCl]
16000
14000
12000
10000
8000
6000
4000
2000
0
(b)
(c)
(i)
(i)
(iii)
(ii)
100 µm

Figure 3.4 *(previous page)*: Clay detachment from the silicon pore surface in response to changes in salt concentration. (a) shows the fraction of mobilized clay particles within the pore space at the different salt concentrations for various locations throughout the micromodel determined through image analysis. The reverse lower axis shows the progression of low salinity waterflooding (high to low salinity). The largest error associated with the data is as displayed by the error bar corresponding to 0.9±0.05 at 4000 ppm NaCl. Mobilization of clay particles was observed for salinities below 6000 ppm NaCl. High fractions of mobilized clay were found in regions corresponding to preferential flow paths where the low salinity brine was delivered effectively through advection, whereas low clay mobilization was found in regions corresponding to stagnant flow conditions where salt dilution was mostly driven by diffusion. Mobilization of clay particles is determined by direct visualization of the pore space (b) before and (c) after a low salinity waterflood with 4000 ppm NaCl. Significant kaolinite particle migration was observed. Pore-lining particles were drastically reduced in large channels (i), while deposition in regions with high pore body to pore throat size ratios were observed (ii). Furthermore, large numbers of pore-bridging particles were found after the low salinity waterflood (iii).

3.3.2 Irreversibly deposited clay

The heat-treated microfluidic system was saturated with 15000 ppm NaCl brine to replicate initial reservoir conditions. The system, especially the clay particles, was found to be water-wetting. Specifically, cornering/crevice flow was observed during spontaneous imbibition where thin water films wet the clay patches before the bulk pore body was filled with water. This is in stark contrast with the unheated system, where the clay patches were extremely non-wetting to water (water could not infiltrate clay-dense pore bodies). Following brine saturation, fresh water (0 ppm NaCl) was injected into the irreversibly coated micromodel. Images were recorded at fixed locations throughout the micromodel before and after the freshwater flood. Clay mobilization was not observed after the freshwater flood; this demonstrates the permanent attachment of the clay particles to the silicon surface with respect to salt concentration after the heat treatment and validates the irreversible clay deposition method developed.

3.3.3 Injection fluid salinity and crude-oil recovery

The reversibly clay-coated micromodel was fully saturated with formation brine and injected with crude oil to replicate the initial reservoir conditions, shown in Fig. 3.5. Image analysis shows that the connate water saturation was $\sim 5\%$. The system was aged for two weeks to allow for sufficient interaction between the clay and oil components. Immediately upon introducing the crude oil to the micromodel, shown in Fig. 3.5(a), the oil-water interface was smooth and the system appeared to be strongly water-wet. After aging, however, "kinks" were observed in the water-oil interface where clay particles were located and localized oil-wet regions were observed, shown in Fig. 3.5(b). This change is indicative of the altered wettability properties of the porous medium due to the affinity of kaolinite towards oil.

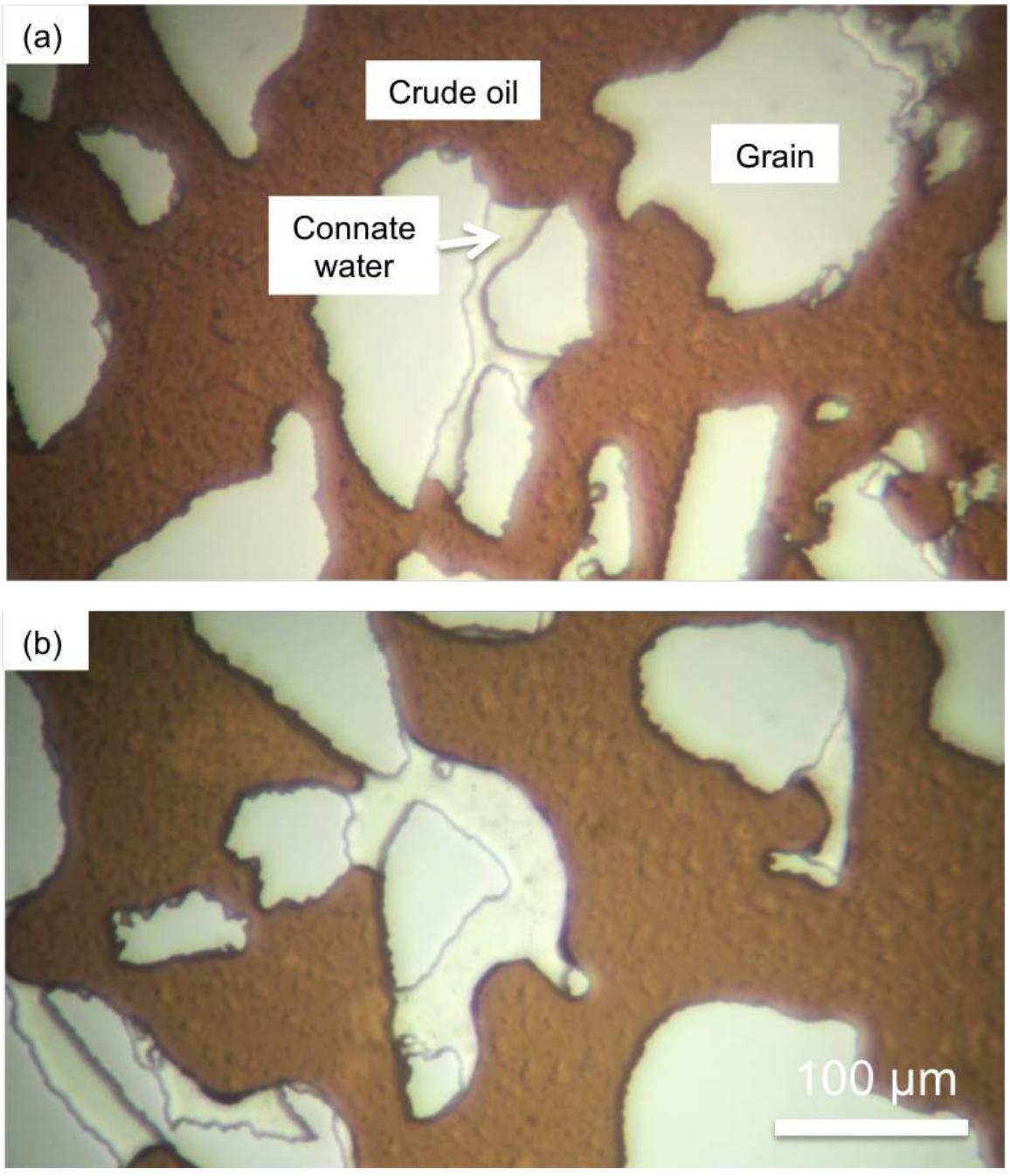
(a)
Crude oil
Grain
Connate water
(b)
100 µm

Figure 3.5 *(previous page)*: Reversibly clay-coated micromodel representing initial reservoir conditions (a) immediately upon injection of oil and (b) after aging for two weeks. The system was filled with initial reservoir brine, followed by injection of crude oil. Crude oil was injected for several pore volumes and the water saturation of the system was monitored until such a point at which further injection of oil could not displace the residual water. The connate water saturation was $\sim 5\%$. The water-oil interfaces are smooth curves pre-aging and are deformed by kinks about clay particles after aging, indicating a shift in the wettability properties of the system.

To study the effect of injection fluid salt concentration on oil recovery, high salinity (*i.e.*, the initial formation brine) and low salinity (deionized water) fluids were injected sequentially into the aged micromodel at a flow rate of 20 m/day until no further reductions in the oil saturation were observed. That is, the imaged oil phase remained immobile in the pore space with brine injection. The resulting systems were imaged at several locations to obtain representative residual oil saturation, as shown in Fig. 3.6(a) and Fig. 3.6(b). The segmented images shown in Fig. 3.6(c) and Fig. 3.6(d) were created using ImageJ to differentiate between the oil, aqueous, and solid phases. Specifically, thresholds were applied to each image and the interfaces between the oil, water, and solid phases were identified using the "find edges" function. The images were then binarized and analyzed to find the oil/water saturations. Non-uniform lighting and the presence of clay particles makes the process difficult to automate and thus individual treatment was applied. This approach was applied to quantify the oil and water saturations (volume fraction of oil or water in the pore space, $S_{oil} = A_{oil}/(A_{total} - A_{grains})$ and $S_{brine} = A_{brine}/(A_{total} - A_{grains})$ where the saturations sum to unity, $S_{oil} + S_{brine} = 1$). Residual oil saturations in the system as a result of the high and low salinity waterfloods were quantified in this manner. The residual oil saturations after the high salinity brine flood and the low salinity freshwater flood were $S_{or} = 36\%$ and 22%, respectively. This recovery increase of 14% of the original oil in place provides direct evidence of improved oil recovery using

fresh water flooding.

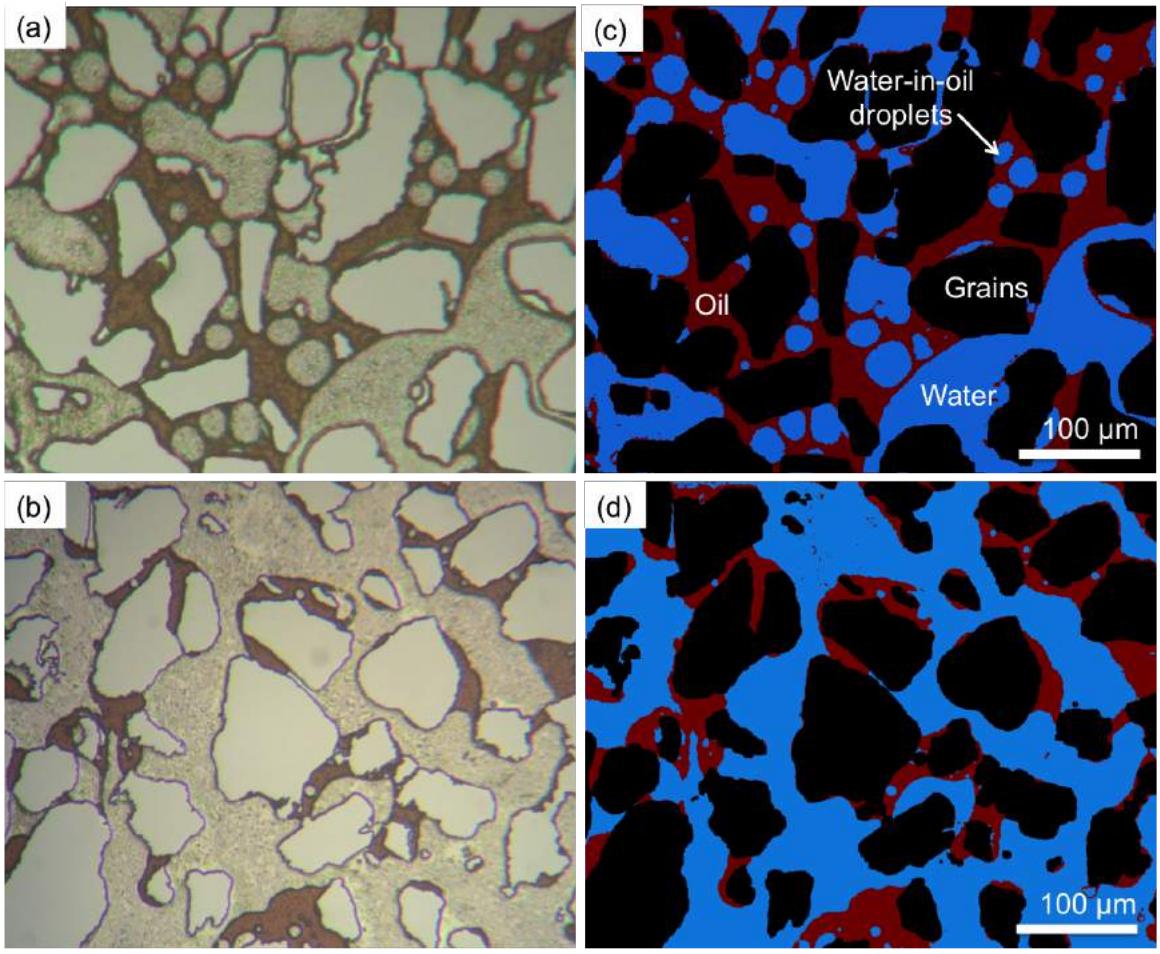

Figure 3.6: Clay-coated micromodel after (a) high salinity (synthetic formation brine) flood and (b) low salinity (deionized water) flood. The water (blue), oil (red), and grains (black) are differentiated using image processing techniques in (c) and (d). The residual oil saturations following the high salinity and low salinity waterfloods were $S_{or} = 36\%$ and 22%, respectively, indicating a 14% increase in oil recovery using deionized water.

To understand the underlying mechanisms driving the increase in oil recovery, images were taken prior to (Fig. 3.7(a)) and during (Fig. 3.7(b)) the low salinity waterflood at fixed locations. It was found that the low salinity shock resulted in the rapid remobilization of adhered clay particles in the pore space that led to a

subsequent increase in the water-wettability of the porous medium. Figure 3.8 shows images obtained using a confocal microscope (Sensofar Sneox 3D optical profiler) that illustrate the four phenomena that contributed to the improved oil recovery of oil using low salinity flooding from the reversibly clay-coated micromodel. First, significant clay stripping at the pore-scale after the fresh water flood, as indicated by the regions that are cleansed of clay in Fig. 3.8(a). This is consistent with low salinity flooding of sandstone cores [4, 41]. Second, the irregularly shaped oil-water interfaces in Fig. 3.8(b) demonstrate the wettability alteration of the micromodel to one that is mixed-wet. The altered wettability of the system is due to the introduction of the oil-wet clay particles in the pore space and the adherence of crude-oil components to that clay as well as adherence to other pore surfaces. Third, a large number of water-in-oil emulsions were found throughout the micromodel after the freshwater flood, shown in Fig. 3.8(c). Although there is disagreement within the literature on emulsion generation during low salinity flooding [45], the results here suggest that emulsions may be generated spontaneously during low salinity waterflooding. Fourth, immobile clays exhibited some oil retention, as observed in Fig. 3.8(d) by the brown discoloration of the clay particles in the water phase. This, again, is due to the affinity of clay towards oil as opposed to water [10]. Overall, the four microscopic pore-scale observations described here appear to fit the inferences from macroscopic core-scale studies in sandstones.

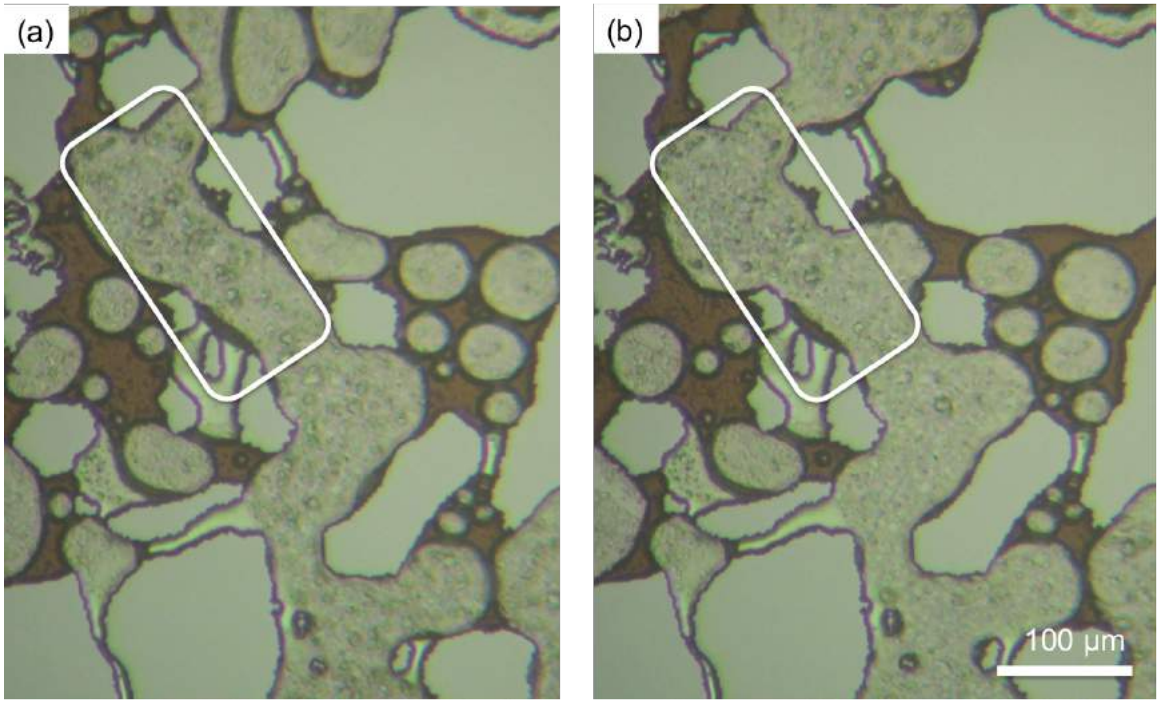

Figure 3.7: Clay-coated micromodel before (a) and 5 minutes after (b) the low salinity waterflood. Clay particles appear to have relocated in the latter case, compared to the initial system.

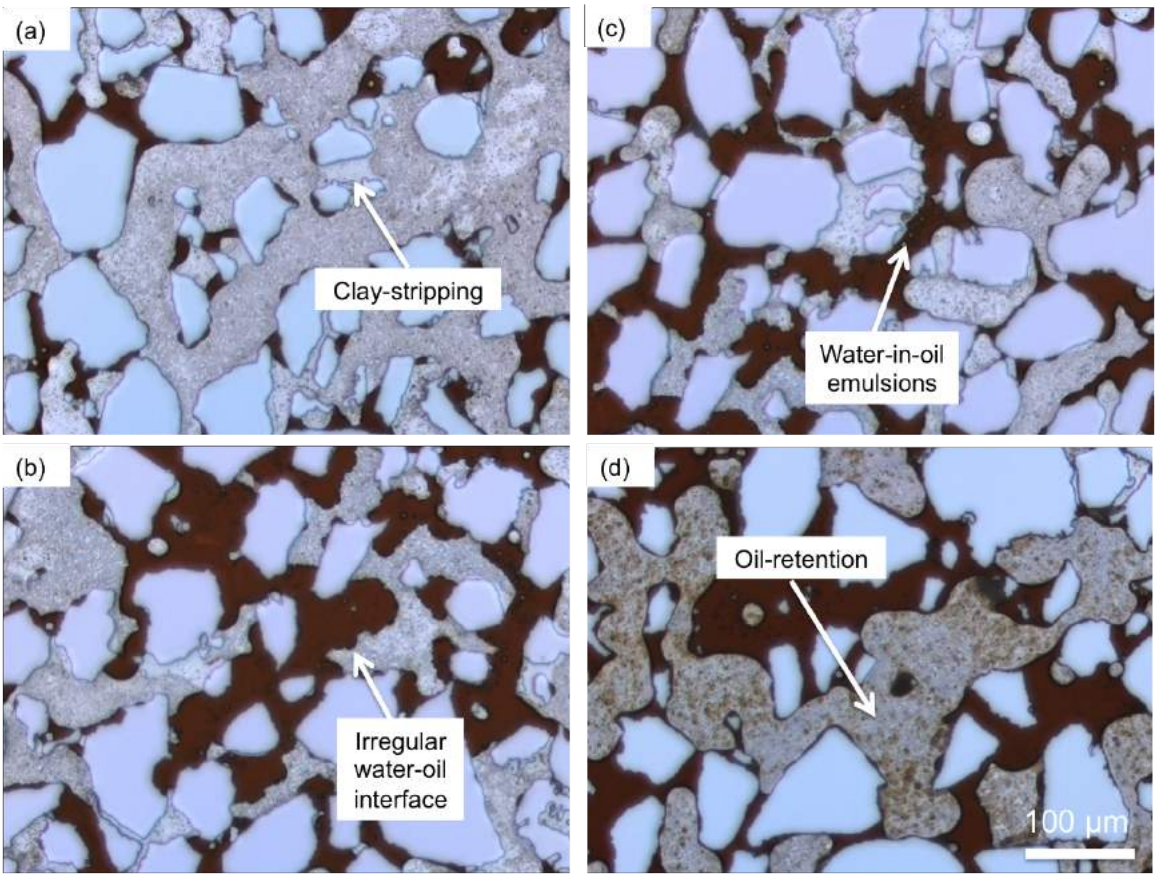

Figure 3.8: Clay-coated micromodel following the low salinity waterflood imaged using a confocal microscope. Water-in-oil emulsions are found throughout the micromodel as shown in (a) and fit macroscopic descriptions by Emadi et al 2013 [45]. The oil-water interface in (b) is deformed due to the oil-wettability of the kaolinite particles. Regions of clay stripping are observed in (c), similar to core-flooding experiments reported in the literature [4]. Oil retention on clay particles is observed in (d) and fit macroscopic inferences [10].

Surface functionalized microfluidics enables direct visualization of the impact of fluid composition on the stability of kaolinite that is attached to sandstone surfaces. In particular, micromodels provide a direct means of visualizing the behavior of clay under a range of saline conditions. Specifically, pore-lining clay was found to have been removed from the surface of the grain, whereby exposing the water-wet surface and potentially aiding the recovery of hydrocarbons from such a system. Pore-bridging

clay, however, was found to have been dislodged from the grain surface and had subsequently plugged pore throats downstream. Furthermore, mobile clay particles were found to have accumulated in small pore throats, especially those with pore-bridging clay structures impeding flow.

The work presented here provides the necessary groundwork for further studies in understanding the real-time fluid flow and fluid-solid interaction at the pore scale in real rocks. Specifically, this work is particularly amenable to the study of increased oil recovery as a result of the low salinity effect. Several directions are outlined for future work as follows.

First, it is desirable to map the mobilization characteristics of the clay functionalized silicon micromodel. Specifically, brine composition and fluid velocity sensitivity experiments should be conducted to determine the mobility of attached clay particles. Furthermore, three dimensional characterization of clay structures in the pore space using confocal microscopy can lead to better understanding of the role that the various clay structures (pore lining, pore bridging, anomalous structures) have on oil recovery. Specifically, the impact of clay mobilization during low salinity flooding is proposed to depend on the type of clay structure that is released. For example, the role that detached pore lining clays have on wettability change and consequently oil recovery is expected to differ from the role that pore bridging clays have during the low salinity flood. In the former, stripping the oil-wet clays from pore surface enhances the water-wettability of the matrix and hence contributes to increased oil recovery, whereas in the latter, large pore bridging structures may flocculate to congest the available flow paths and hence resulting in formation damage. Furthermore, the formation of oil-water emulsions during low salinity flooding and its subsequent effects on the overall recovery mechanism is of interest. In terms of oil recovery, changes in the micromodel wettability behavior due to clay can be studied by investigating the interactions between the oil, water, and clay particles during spontaneous

and forced imbibition. Specifically, the salinity of the injection brine can be decreased to determine the effect of salinity on the imbibition process. Moreover, this study focused on the role that kaolinite – a predominant clay mineral present in sandstones that is non-swelling – has in fluid interactions in the pore space. Another important process, however, is the swelling and shrinking of clay particles. The work presented here provides the basis for future studies on the swelling and/or shrinking of clays, for example smectite and montmorillonite, under low salinity conditions.

3.4 Conclusion

In this chapter, we presented a method to deposit clay particles into micromodels as a means of creating a visualization platform with more representative surface interactions between the reservoir fluids and the formation rock. Specifically, the silicon micromodel was coated with kaolinite in two manners, reversibly and irreversibly, to enable the study of (i) the fundamental mechanisms governing the increased oil recovery during low salinity waterflooding, and (ii) the effect of a mixed-wet surface on oil recovery, respectively. We demonstrated the successful deposition of kaolinite particles in the sandstone pore space, where the majority of clay deposited was pore lining ($\sim$ 90%) with the remainder forming pore-bridging structures across narrow pore throats. Furthermore, anomalous regions of highly concentrated clay deposits in the pore space were also observed, and were found to be extremely non-wetting to water in the presence of air. High and low salinity brine injection in the micromodel identified the dependence of clay attachment and release on salt concentration. Formation brine and crude oil were introduced to the clay-coated micromodel and aged for two weeks to create initial reservoir conditions and resulted in a mixed-wet pore space. High and low salinity brine floods were performed sequentially and image

processing was applied to quantify the impact of injection fluid salinity on oil recovery. Specifically, the low salinity (deionized water) flood yielded a 14% increase in oil recovery after the high salinity flood.

Chapter 4

Formation Damage in Clay-Rich Sandstone

Formation damage due to fines migration results, potentially, in significant decreases in reservoir permeability and, hence, the recoverability of crude oil from reservoirs. On the other hand, low salinity brine injection is a promising technique for increasing oil recovery from clay-rich sandstones in an economic manner. Clay detachment at low salinity conditions, however, drastically alters fluid flow. In this work, clay-functionalized micromodels are used to visualize directly the mobilization of clay at low salinity conditions in (i) the absence of oil, and (ii) the presence of oil. Results include clay mobilization and pore plugging in the absence and presence of oil visualized by saturating the clay-functionalized micromodel with high salinity brine followed by injections of reduced salinity brines. Clay detachment and migration was observed in oil-free systems for 4000 ppm NaCl low salinity injection brine. The extent of fines detachment was quantified to determine the types of clay structures affected. Furthermore, fines migration, flocculation, and re-deposition were visualized directly. The types of structures formed (*i.e.*, pore-plugging, pore-lining, *etc.*) by the re-deposited clay particles are characterized to determine their impact on formation damage. Clay

detachment in the presence of oil was also visualized. Initial conditions analogous to clastic reservoirs were established by allowing the crude oil, brine, and solids to interact (*i.e.*, age). Clay detachment occurred during 4000 ppm NaCl low salinity oil recovery. Real-time, pore-level visualization revealed significant mechanisms during oil recovery processes and their influence on multiphase flow. Specifically, pore plugging particles in water-filled pores obstructed preferential flow paths and diverted injection fluid to unswept regions thereby increasing oil production.

4.1 Introduction

Petroleum reservoirs often contain large quantities of both swelling and nonswelling clay [41, 150, 151]. Surface interactions between clay and its surroundings, *i.e.*, brine, crude oil, and the bulk matrix significantly influence the petrophysical properties of the reservoir and the transport of fluids through the reservoir. Specifically, clays such as kaolinite and montmorillonite are prone to migration and swelling, respectively, as a result of contact with injection brines of altered compositions [4, 33, 32, 10, 34]. In reservoir engineering, formation damage, *i.e.*, permeability reduction in the reservoir, is a key problem that arises during low salinity waterflooding (*i.e.*, injection of brines with reduced salinity compared to the connate water or initial injection brine) in clay-rich sandstones [41, 151, 152, 153, 154].

Three main mechanisms have been proposed to explain reservoir formation damage under low salinity conditions: fines migration, particle swelling, and swelling-induced migration [151]. First, fines detachment and mobilization within the pore space may result in pore plugging phenomena that reduce the availability of flow paths. Specifically, the detachment and subsequent transport, flocculation, and redeposition of the free clay particles leads to significant pore-plugging, and ultimately formation damage. Kaolinite is particularly susceptible to this type of behavior under

low salinity conditions. Second, clay swelling in the absence of stabilizing salt ions reduces the amount of pore space available to flow, and in severe cases of formation damage, blocks the smaller pore throats and hence destroys the permeability of the reservoir. Montmorillonite is a smectite clay prone to swelling under low salinity conditions. Third, the swelling of pore-lining clays that subsequently break off fines during flow may lead to pore blockage and formation damage.

Low salinity brine injection, on the other hand, is a promising technique to increase oil recovery in clay-rich reservoirs. Specifically, Tang and Morrow 1999 [4] first reported increases in oil recovery of an additional 5-20% of the original oil in place. Several mechanisms have been proposed to delineate the increase in oil recovery due to low salinity waterflooding, including fines migration, cation exchange, and emulsion formation. The effects of fines migration and possible formation damage on oil recovery, however, are not well understood. Disagreement in the literature and field-scale experiments suggests that fundamental understanding of the mechanisms dictating the low salinity effect is required [35, 36, 37, 38].

Pore-scale understanding of crude oil-brine-rock (COBR) behavior is critical to the optimal design of oil-recovery techniques with respect to formation damage. Coreflooding experiments have been conducted to study the fluid-fines interactions on clay detachment. Specifically, Khilar and Fogler 1984 [41] studied the effect of injection brine salinity on overall fines migration and identified a critical salt concentration (CSC) that was required to mobilize kaolinite particles in Berea sandstone based on indirect pressure and effluent analysis. More recently, Hussain et al 2014 [154] performed both single- and two-phase low salinity waterflooding experiments in Berea sandstone cores to study the effect of fines migration on oil recovery. Specifically, significant permeability loss and slight increase in oil recovery were found. Core-scale experiments, however, are unable to resolve the fundamental formation damage mechanisms at the pore-scale. Current imaging technologies such as x-ray computed

tomography cannot reach the spatial and temporal resolution that is required to visualize directly the *insitu*, real-time pore-scale phenomena related to the behavior of the clay particles.

Microfluidics is an emerging technology that enables the direct visualization of pore-scale phenomena in real time [75, 107, 79]. Recently, glass and silicon microfluidic devices with representative pore-scale geometries have enabled the study of petroleum fluid behavior in the subsurface [79, 75, 80, 108, 94]. Specifically, Buchgraber et al 2012 [79] described the creation of two-dimensional microfluidic platforms with etched geometries identical to those of real rock pores. These micromodels are unique microfluidic devices with the pore networks of real sandstones or carbonates etched into silicon and enable real-time, direct visualization of pore-scale phenomena that could not otherwise be observed in a core. Recently, Song and Kovscek 2015 [80] incorporated clay particles within the micromodel to enable a visualization platform with both representative pore geometries and surface properties of real sandstone. These surface-functionalized micromodels incorporate the pore-scale surface heterogeneities that are associated with the presence of clays and enable the direct visualization of pore-level clay behavior such as clay sensitivity to injection brine composition, particle mobilization and swelling, and formation damage.

In this work, clay-functionalized micromodels were used to visualize directly the response of clay to low salinity brine injection. Montmorillonite and kaolinite clays were deposited onto the pore-wall surfaces of micromodels to enable the study of swelling and dispersive clays under low salinity conditions, respectively. Similarly, kaolinite was deposited into the pore space to enable pore-scale study of crude oil / brine / rock interactions in a microfluidic platform with both realistic pore geometry and surface properties. Specifically, the effect of low salinity injection in rock rich in swelling clays (*e.g.*, montmorillonite) and non-swelling clays (*e.g.*, kaolinite) was

studied through single-phase brine injection experiments, and the effect of fines migration and formation damage during low salinity oil recovery was studied through waterflooding experiments (i) the absence of oil, and (ii) the presence of oil. The extent of fines detachment was quantified to determine the types of clay structures affected. Structures formed (*i.e.*, pore-plugging, pore-lining, *etc.*) by the re-deposited clay particles were characterized to determine their impact on formation damage. Clay detachment in the presence of oil was also visualized. Initial conditions analogous to clastic reservoirs were established by allowing the crude oil, brine, and solids to interact (*i.e.*, age). Clay detachment occurred at roughly similar salinity. Real-time, pore-level visualization revealed significant mechanisms during oil recovery processes and their influence on multiphase flow. Specifically, pore plugging particles in water-filled pores obstructed preferential flow paths and diverted injection fluid to unswept regions thereby increasing oil production.

4.2 Experimental Methods

Pore-scale visualization of formation damage in clay-rich sandstones due to low salinity waterflooding was achieved using surface-functionalized micromodels. The surface-functionalized micromodels are two-dimensional microfluidic visualization platforms with pore geometries and surface properties representative of those found in real reservoir rock. The design and fabrication of the etched-silicon micromodels used here follow methods described in Chapter 2. To functionalize the surface of the micromodel to replicate representative surface wettability and structural properties of clay-rich sandstone, clay particles were deposited onto the pore walls. Kaolinite and montmorillonite were chosen to study the effect of low salinity injection on formation damage due to fines migration and swelling, respectively. The clay-functionalization of the micromodel pore surfaces in this work are similar to the methodology described in

Chapter 3 [80]. Specifically, a 1 wt.% kaolinite solution was prepared by adding kaolinite powder (Kaolin, K2-500, Fisher Scientific) to 15000 ppm NaCl (sodium chloride, S271-3, Fisher Scientific) solution and vigorously stirred at atmospheric conditions. The solution was sonicated (Bransonic 220) for 1 hour before injection into the micromodel to prevent particle flocculation and pore plugging. The solution was then injected into the brine-saturated micromodel at 20 m/day to maintain particle dispersion and to minimize pressure buildup [80]. Montmorillonite was deposited into the micromodel in a similar fashion by injecting a solution with 1 wt.% montmorillonite (Montmorillonite K 10, powder, CAS: 1318-93-0, Sigma-Aldrich) in 15000 ppm NaCl into the brine-saturated micromodel to prevent swelling. Alternating air/brine injections were conducted to remove mobile clay particles; this ensured that the remaining clay particles were firmly adhered to the silicon surface. The clay-coated micromodel was continuously flushed with several pore volumes of the high salinity brine using the syringe pump to create a fully brine saturated system. The motivation of saturating the micromodel with brine typical of a reservoir was two-fold: (1) to replicate the initial conditions in the reservoir, and (ii) to avoid clay detachment as a result of low salinity shock. All experiments were performed with constant injection rates and the micromodel outlets were maintained at atmospheric pressure.

4.2.1 Single phase montmorillonite experiments

Once sufficient montmorillonite was deposited onto the pore space, the surface-functionalized microfluidic network was flooded with 15000 ppm NaCl solution to determine the initial single-phase permeability of the system. Specifically, the high salinity brine was injected at constant flow rate corresponding to a superficial velocity of 30 m/day using a 60 mL syringe (BD 60 mL syringe, 309653) and a syringe pump (Harvard Apparatus, Holliston, MA) setup, as shown in Chapter 2, Fig. 2.3. The superficial velocity was determined using the injection flow rate, Q, and the cross sectional

area, A, of the micromodel, *i.e.*, $v = Q/A$. The system outlets were maintained at atmospheric pressure. Permeability was determined by measuring the pressure drop across the micromodel at constant injection rate. The micromodel was then imaged using a confocal microscope (Sensofar Sneox 3D optical profiler) at 100 fixed locations across the micromodel to visualize the clay particle structure and distribution at initial conditions.

Formation damage due to clay swelling during low salinity brine injection was studied by flooding the system with deionized (DI) water to create a salinity shock. Pressure drop was measured across the micromodel to determine the impact of low salinity waterflooding on formation damage in the presence of swelling clays. The micromodel was imaged at the same locations to visualize any changes in the structure and distribution of the clay particles following the freshwater flood.

4.2.2 Single phase kaolinite experiments

Formation damage due to clay mobilization during low salinity brine injection was studied by flooding the kaolinite-functionalized micromodel with high and low salinity brines. Specifically, the micromodel was first saturated with high salinity brine (15000 ppm NaCl) and imaged at 25 fixed locations across the micromodel to determine the initial clay distribution throughout the system. The basis for choosing the 25 locations was to create an evenly distributed grid of sampling locations throughout the micromodel. Specifically, the imaging grid formed 5 rows and 5 columns, each separated by 1 cm. We chose the origin to be at the bottom left corner of the 5 cm $\times$ 5 cm micromodel and coordinates of the first imaging location was (x = 0.5 cm, y = 0.5 cm). The 25 fixed pore locations were spaced evenly across the micromodel (*i.e.*, a grid of 5 $\times$ 5 locations across the micromodel) to minimize the impact of pore-level heterogeneities. The selection process of the imaging locations was unbiased and thus allows for a more representative understanding of the pore-level behavior such as fluid

saturations. Low salinity brine with 4000 ppm NaCl was injected into the micromodel to study the behavior of kaolinite under low salinity conditions. This salinity is below the critical salt concentration required to mobilize kaolinite in sandstone cores [41] and was thus chosen here. Images were taken at the same 25 fixed locations across the micromodel to determine the effect of low salinity brine injection on formation damage in the presence of dispersive clays.

4.2.3 Two phase kaolinite experiments

Kaolinite was chosen to study oil recovery mechanisms in the presence of clay due to its prevalence in sandstone and the abundance of edge charges on the particle surface. The kaolinite-functionalized micromodel provided a two-dimensional visualization platform that was well representative of a real reservoir rock. Initial conditions representative of real reservoirs were required to conduct meaningful low salinity waterflooding experiments. In order to establish the initial conditions that were representative of clastic reservoir systems, the kaolinite-functionalized micromodel was saturated with formation brine and crude oil as follows. Table 4.1 lists the composition of the formation brine used. This is the formation brine composition that corresponds to the crude oil we chose to test with.

Table 4.1: Composition of brine used to simulate initial conditions analogous to clastic reservoirs

Reagent	Concentration (g/L)
$CaCl_2 \cdot 2H_2O$ (Calcium chloride dihydrate)	0.183
$MgCl_2 \cdot 6H_2O$ (Magnesium chloride hexahydrate)	0.585
NaCl (Sodium chloride)	20.461
KCl (Potassium chloride)	0.611
Na_2SO_4 (Sodium sulfate)	0.109

The brine-saturated system was then imaged using confocal microscopy at 25 locations distributed evenly across the micromodel to determine the initial pore-scale clay distribution. The micromodel was then flooded with crude oil by injecting the crude oil at 30 m/day until residual water saturation was reached. The system was imaged during this process to observe the drainage process. The crude oil properties are described in Table 4.2. This particular crude oil/ brine system is of industrial relevance and was chosen here.

Table 4.2: Crude oil characterization [148].

Crude oil properties	Value
Acid number (mg/g)	2.36
Base number (mg/g)	6.02
Asphaltene content (wt%)	2.69
Density (°API)	21
Viscosity at 22.8°C (cP)	105.7

Low salinity experiments were conducted using crude oil due to the importance of surface interactions between kaolinite and the acid/base groups and asphaltenes in the crude oil. The micromodel was imaged immediately following the drainage process at the same 25 fixed locations to provide a basis for studying the effect of aging. The micromodel was aged for two weeks to allow for sufficient surface interactions between the various components in the crude oil, brine, clay, and silicon. Specifically, the system was submerged in a closed container of crude oil to avoid air from invading the pore space. The same 25 pore spaces were re-imaged after the aging process (i) to determine the effect that the interactions between the various phases had on the fluid distribution and wettability of the system and (ii) to obtain a pore-scale visualization of the initial condition.

After establishing the initial conditions that are representative of clastic reservoirs, the micromodel was subjected to a conventional high salinity waterflood. The high salinity waterflood was performed to serve as a benchmark against conventional oil recovery for subsequent flow experiments. Specifically, a 10000 ppm brine was injected at a superficial velocity of 30 m/day for many pore volumes to benchmark the experiments against conventional waterflooding techniques. Pore-level saturations were directly visualized at the same 25 locations using confocal microscopy. To assess the effect of low salinity brine injection on the clay-functionalized micromodel system, a 4000 ppm low salinity brine was then injected. All experiments were conducted at ambient conditions with the outlets of the micromodels open to atmosphere.

4.2.4 Image processing

Images were processed to provide both quantitative and qualitative insight into the experimental results. Imaging at fixed locations across the micromodel allowed for visualization of fluid distribution evolution due to altered injection conditions. Specifically, images of fixed pore spaces were aligned to enable comparison of pore-level fluids/solids distributions between each stage of the flow experiments. Furthermore, images from two-phase experiments (*i.e.*, waterflooding oil reservoirs) were binarized to distinguish between the various phases, *i.e.*, crude oil, brine, and pore matrix. These image sequences provided (i) quantitative data on the saturations of the phases, and hence, oil recoveries after each injection process, and (ii) qualitative data on the pore-scale oil/brine distribution and preferential regions for clay and oil mobilization. All image processing was performed using Matlab and ImageJ.

4.3 Results and Discussion

Kaolinite and montmorillonite particles were deposited into the microfluidic network to study directly the effect of low salinity brine injection on formation damage in clay-rich rock and its impact on oil recovery. The deposition techniques described by Song and Kovscek 2015 [80] successfully achieved the representative fines structures, wettability properties, and salinity response of real sandstone. Specifically, montmorillonite particles were deposited as pore-lining particles and kaolinite particles exhibited both pore-lining and pore-plugging behavior. These deposition patterns correspond to the clay structures found in real sandstones. Second, wettability alteration of the micromodel due to the presence of clay was observed. Specifically, clay-dense pore-spaces were found to be non-wetting to the water phase in the presence of air. Third, a critical salt concentration (CSC between 4000 ppm NaCl and 6000 ppm NaCl) for kaolinite mobilization from the pore surface was identified and corresponds well to the literature for Berea sandstones. The clay deposition process was thus deemed valid to replicate real rock properties within a micromodel and flow experiments were henceforth carried through to visualize directly the effect of low salinity fluids on the system.

4.3.1 Montmorillonite response to low salinity shock

Montmorillonite-functionalized micromodels were first saturated with a 15000 ppm high salinity brine and subsequently flooded with a 4000 ppm low salinity brine. Pressure drop measurements across the clay-functionalized micromodel indicated significant formation damage due to the low salinity shock. Specifically, a 6-fold decrease in system permeability was measured from $\sim$ 800 mD to $\sim$ 130 mD. Alignment of the images at fixed locations before and after the low salinity waterflood allowed for direct monitoring of the effect of low salinity brine injection at the pore scale. Clay particle

swelling was not visualized in this system, however significant fines migration was observed. Specifically, detachment of montmorillonite particles was highly sensitive to the injection brine salinity, as shown in Fig. 4.1 where the stably attached montmorillonite particles at high salinity (Fig. 4.1(a)) were released with the introduction of the low salinity brine (Fig. 4.1(b)). The visualization results here suggest that the dominant formation damage mechanism in the montmorillonite-rich micromodel was caused by swelling-induced fines migration, where clay swelling causes the detachment of other particles within the pore structure. Interestingly, low salinity core flooding experiments performed by Mohan et al 1993 [151] concluded that swelling-induced fines migration contributed significantly to formation damage in montmorillonite-rich sandstones.

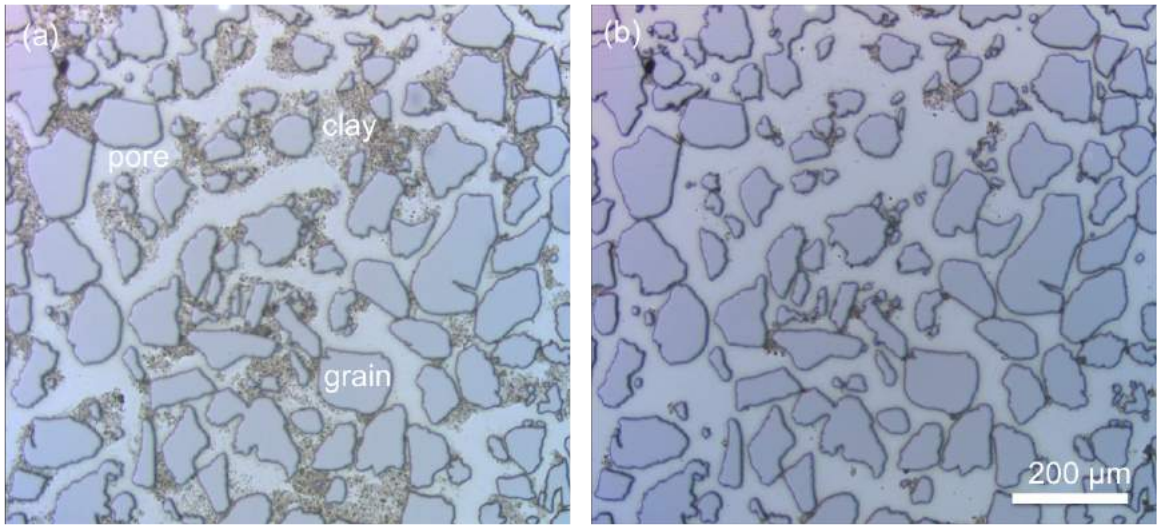

Figure 4.1: Fines release and mobilization due to low salinity brine injection in a montmorillonite-rich sample. Initial clay particle distribution at 15000 ppm high salinity conditions (a) and mobilized montmorillonite distributions after the 4000 ppm low salinity waterflood (b) at the same pore location show significant fines release due to the low salinity shock.

4.3.2 Kaolinite response to low salinity shock

Kaolinite-functionalized micromodels were initially saturated with a 15000 ppm NaCl high salinity brine and subsequently subject to reduced salinity brine injections by order of decreasing salinity. Specifically, the single-phase brine injection experiments showed significant kaolinite mobilization at 4000 ppm NaCl. Fine clay particles were stably attached on the pore surface for injection brines from 15000 ppm NaCl to 8000 ppm NaCl. Initial clay detachment was observed after 6000 ppm NaCl injection, and significant kaolinite mobilization was found for brine salinities at and below 4000 ppm NaCl. These results correspond well to experimental core data and theoretical particle stability calculations in the existing literature on the sensitivity of kaolinite mobilization to salinity [32, 41, 151].

Pore-level clay mobilization was quantified through image analysis of fixed pore spaces after each flow experiment. Regions affected by clay mobilization (*e.g.*, detachment and redeposition) were recorded for each fixed pore location. Pore-scale images were obtained at each of the 25 fixed locations after high salinity (15000 ppm NaCl) brine injection and low salinity (4000 ppm NaCl) brine injections were compared. Formation of pore-lining deposits and pore-bridging structures were observed. The regions affected by clay mobilization were aligned to the base image of the micromodel pore network. Summation of the images enabled characterization of the regions that were particularly susceptible to formation damage due to clay particle redeposition during low salinity waterflooding. Comparison between the formation damage map and single-phase flow simulation through the porous medium is shown in Fig. 4.2. Initial clay particle distributions within the pore space are shown in Fig. 4.2(a), while the effect of low salinity waterflooding is shown for the same pore space in Fig. 4.2(b). Figure 4.2(c) shows the single-phase velocity map of the pore space obtained by solving the full Navier-Stokes equations for the micromodel pore geometry under the corresponding experimental conditions. All velocities shown in

Fig. 4.2(c) are normalized against the maximum velocity of the simulation and thus vary from 0 (blue) to 1 (red). Furthermore, all velocities shown are consistent with the scale bar.

Formation damage due to clay mobilization was observed following the low salinity waterflood. Specifically, formation damage due to clay particle redeposition was most prevalently found in large pores that were experiencing flow of intermediate velocity (*e.g.*, Fig. 4.2(i) and (ii)). Figure 4.2(iii) and (iv) show that formation damage due to pore-bridging structures, however, were found to span small pores with high fluid velocity. While pore-bridging structures were not found at every pore with high fluid velocity, there was a higher probability of clay particles to form pore-bridging structures in those regions (*i.e.*, the constrictions). These observations are consistent with current theories on pore-plugging mechanisms due to fines migration for non-swelling clays such as kaolinite [151].

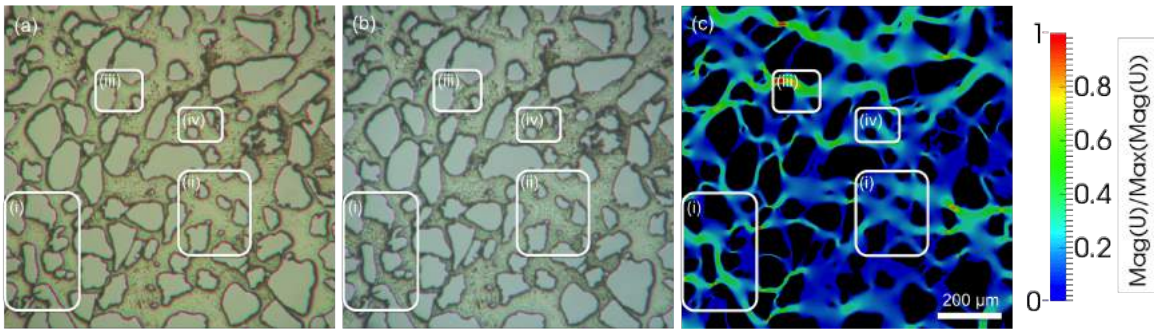

Figure 4.2: Formation damage due to kaolinite mobilization during low salinity waterflooding. Initial clay particle distribution at 15000 ppm high salinity conditions (a) and mobilized kaolinite particles after 4000 ppm low salinity waterflooding (b) at the same pore location are compared with the single-phase velocity map from pore-scale simulation. Regions (i) and (ii) show the re-deposition of mobilized particles as pore-lining clays in the pores that were experiencing intermediate/slow velocities, while regions (iii) and (iv) show the formation of pore-bridging structures across high velocity flow paths. All simulated velocities shown in (c) are normalized against the maximum velocity of the porous system. Pore-scale simulations provided by Soulaine 2016 (Personal communication) [155].

4.3.3 Oil recovery from kaolinite- and montmorillonite rich systems in response to low salinity shock

Two-phase experiments were conducted with kaolinite- and montmorillonite-functionalized micromodels, respectively. The system was saturated with the formation brine and subsequently injected with the corresponding crude oil. The system was aged at ambient conditions for two weeks to establish initial conditions representative of clastic reservoirs. Two weeks of aging allowed for sufficient interactions between the various components in the crude oil, brine, and solids and to reach thermodynamic equilibrium. No significant changes in the pore-level fluid behavior were observed for longer interaction time. Images were obtained at the 25 fixed locations across the micromodel after the aging process to establish the pore-level initial conditions.

Figure 4.3 shows the direct visualization of the fluid distributions at a particular pore location near the center of the micromodel. Specifically, Fig. 4.3(a) shows the kaolinite-functionalized micromodel saturated with formation brine and Fig. 4.3(b) shows the initial condition at the same pore location. To understand the impact of low salinity waterflooding experiments and formation damage on the system, an initial 10000 ppm high salinity waterflood was performed to provide a basis for comparison with conventional waterflooding results. The result of the high salinity brine injection is shown in Fig. 4.3(c). Next, a 4000 ppm low salinity brine was injected to investigate the effect of low salinity waterflooding on the system. The result of the low salinity brine injection is shown in Fig. 4.3(d). Oil was collected at the outlets of the microfluidic system, corresponding to a decrease in oil saturation throughout the micromodel and thus an increase in oil recovery.

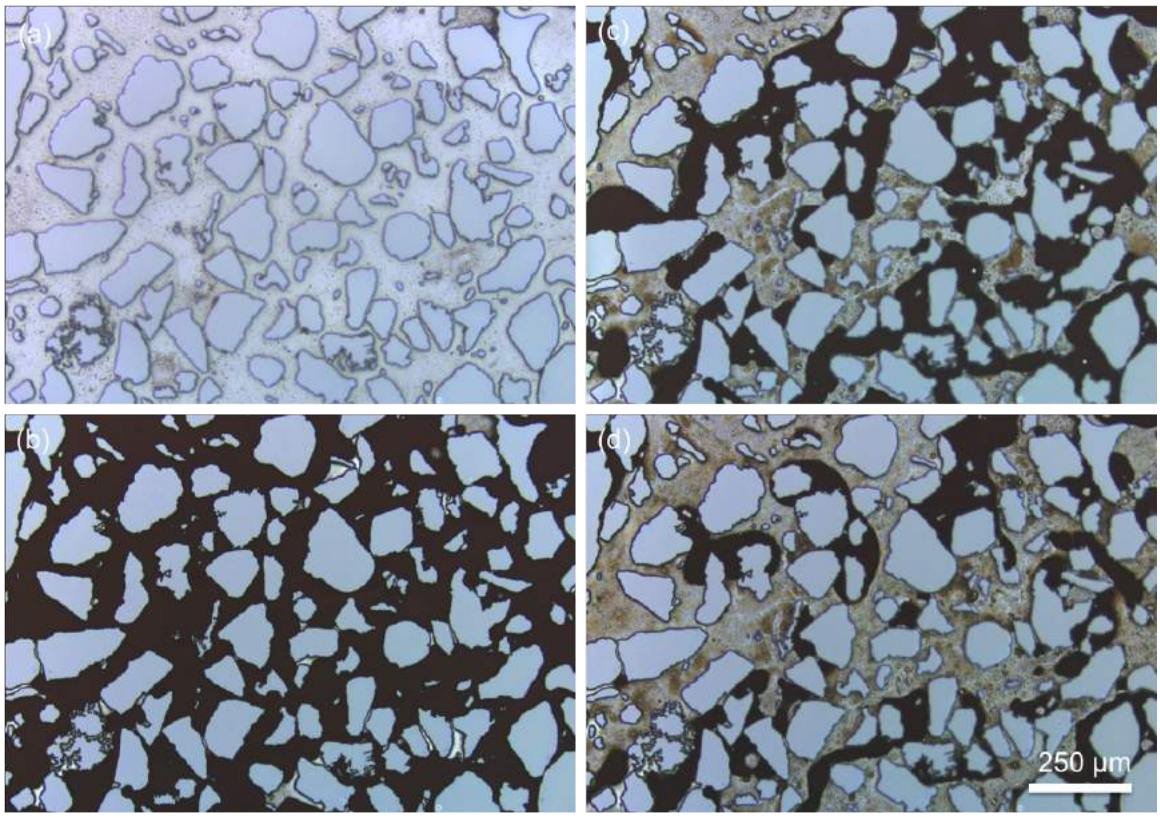

Figure 4.3: Direct visualization of pore-level water-oil-clay-silicon phenomena at a fixed pore location near the center of the micromodel. The clay-functionalized pore space that is fully saturated with formation brine (a) is injected with crude oil until residual water saturation is reached and aged to create initial conditions analogous to clastic reservoirs (b). High salinity (10000 ppm brine) waterflooding of the system is performed to standardize the experimental results (c). Low salinity (4000 ppm) brine injection shows decreased pore-level oil saturation, *i.e.*, increased oil recovery.

Overall clay mobilization in the oil-brine system was difficult to quantify due to the relative opacity of the crude oil combined with the visual artifacts associated with the adhesion of oil on the pore surface. Mobilization of kaolinite particles in regions with high clay density, however, was observed following the low salinity brine injection, as shown in Fig. 4.4. Specifically, Fig. 4.4(a) shows the initial clay particle distribution in formation brine. No clay particle mobilization was observed after the high salinity brine injection, as shown in Fig. 4.4(b). Clay particle distributions after

the low salinity brine injection, however, show that fines mobilization occurred in this case. Comparison between the boxed regions in Fig. 4.4(b) and Fig. 4.4(c) shows a deficit of clay particles after the low salinity flood. This correlates well with the mobilization of particles at low salt concentrations in the single-phase experiments.

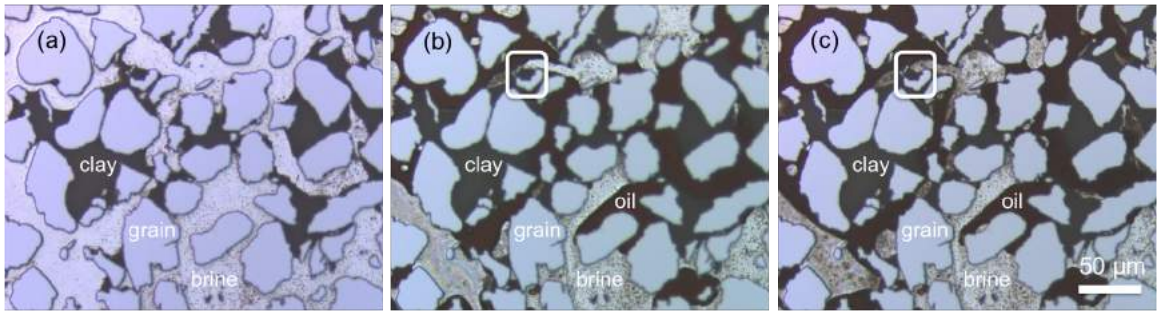

Figure 4.4: Mobilization of pore-plugging kaolinite particles as a result of low salinity waterflooding. The initial clay particle distribution is shown for the pore-space saturated in formation brine (a). The deficit of clay particles in the white box after the 4000 ppm low salinity flood (c) in comparison to the clay particles after the 10000 ppm high salinity flood (b) show that similar to the single-phase experiments, clay particles in the two-phase experiments were also sensitive to the salinity of the injection brine.

The minimal local oil mobilization associated with the detachment of clay particles, however, does not correlate well with the significant increase in oil production observed. Because the micromodel was constructed by repeating a single unit of pore geometries across the micromodel, comparison of fluid behavior in repeated pore structures across the micromodel allows for the identification of specific pore geometries that were most sensitive to the experimental conditions. In other words, if a pore geometry was consistently affected by clay mobilization across the micromodel then it was identified as a problematic pore, and similarly, if a pore was consistently affected by oil mobilization across the micromodel then it was deemed an oil mobilization pore. A comparison map identifying the locations of pore-level formation damage was generated at each of the 25 fixed locations across the micromodel by comparing

the experimental images before and after the low salinity waterflood. The pores were then matched to the pore geometry map of a single base unit to identify the pores that were most commonly affected by formation damage due to single-phase low salinity waterflooding. A similar treatment of the oil mobilization pores was performed to identify the pores that were most susceptible to increased oil recovery due to low salinity waterflooding. These results are shown in Fig. 4.5. Specifically, the pores that were consistently affected by formation damage are highlighted in red, while the pores where the brine consistently displaced the oil phase during low salinity waterfloods are highlighted in blue. This analysis was performed for both kaolinite- and montmorillonite-functionalized systems, as shown in Fig. 4.5(a) and Fig. 4.5(b), respectively.

Importantly, for the kaolinite-functionalized micromodels, the pores most affected by pore-level formation damage showed minimal increases in oil recovery, and vice versa. Low salinity brine injection most commonly mobilized oil in the smaller pores, *i.e.*, pore radius between roughly 30 to 80 μm, whereas formation damage most commonly occurred in the larger pores, *i.e.*, pore radius between $\sim$ 50 μm to 150 μm. These results suggest that the significant redeposition of the mobilized clay particles as pore-plugging structures resulted in drastic blockage of preferential flow paths within the micromodel. As a result, injected brine was diverted to previously unfavorable paths (i.e., pores that were filled with oil) and therefore contribute to the increase in oil recovery observed at concentrations below the critical salt concentration.

Similarly, low salinity waterflooding in montmorillonite-functionalized micromodels showed an 8.5% increase in oil recovery. The pores most affected by clay detachment also showed minimal increases in oil recovery, and vice versa. In this case, however, oil was mobilized in larger pores as a result of low salinity waterflooding, *i.e.*, pore radius between $\sim$ 80 μm to 130 μm, whereas formation damage most commonly occurred in the smaller pores, *i.e.*, pore radius between $\sim$ 20 μm to 80 μm.

Pore-lining montmorillonite was most commonly found in smaller, low velocity pores at initial conditions and was less prevalent in larger, high velocity flow paths. The mobilization of swollen montmorillonite did not appear to result directly in improved recovery under the conditions studied.

The contrast of results obtained using kaolinite and montmorillonite illustrates, potential, important effects of the clay type on low salinity waterflooding. Such differences may be related to the nature of non-swelling versus swelling clays and/or the microstructure of clay deposition on pore walls.

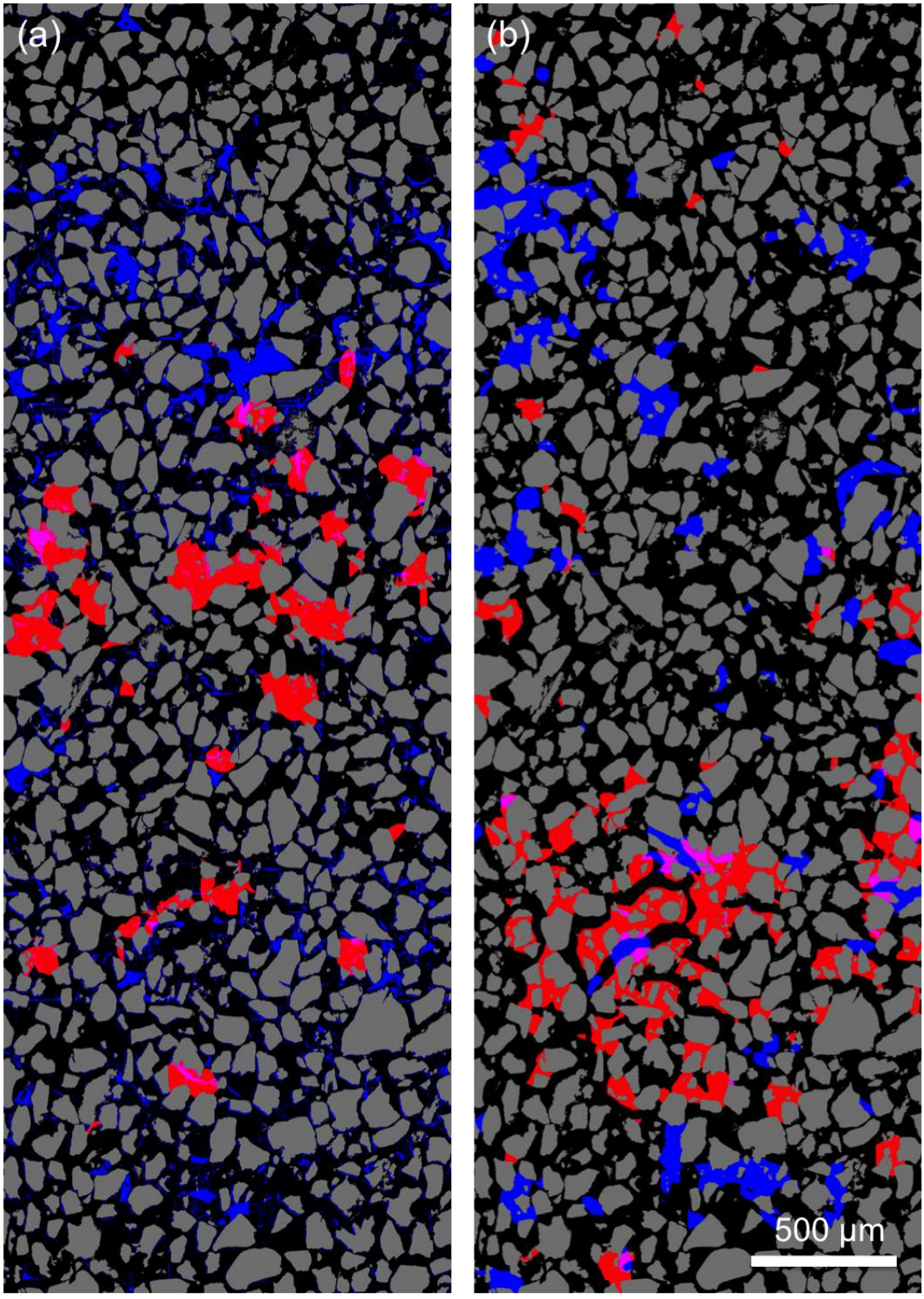
(a)
(b)
500 µm

Figure 4.5 *(previous page)*: Comparison of regions affected by clay mobilization (red) and regions of increased oil recovery (blue) compiled on a single base image unit for a kaolinite-functionalized micromodel (a) and a montmorillonite-functionalized micromodel (b). Macroscopic comparisons between the regions that were most susceptible to formation damage with the regions that were most susceptible to oil mobilization of the kaolinite-functionalized system suggest that flow diversion due to formation damage plays a dominant role in low salinity increased oil recovery.

4.4 Conclusion

In this work, pore-level clay particle behavior was visualized directly to delineate the mechanisms contributing to formation damage under low salinity conditions. In contrast to many prior studies, two-phase flow conditions were employed. Montmorillonite- and kaolinite-functionalized pore spaces were subject to low salinity waterfloods. Pressure measurements showed 6-fold reductions in permeability, *i.e.*, significant formation damage in the system accompanying fines mobilization. Drastic swelling-induced fines migration was observed in the montmorillonite-rich system and fines migration was observed in the kaolinite-rich system as brine salinity was reduced below the critical salt concentration. These direct visualization results correspond well to those obtained from previous core-flooding experiments in the literature. Kaolinite detachment and flocculation resulted in (i) the formation of pore-bridging structures across small pores that experienced high velocities and (ii) the redeposition of pore-lining structures on larger pores that experienced intermediate velocities. Two-phase experiments showed increased oil recovery in kaolinite- and montmorillonite-rich rock during low salinity waterflooding where fines mobilization occurred. Mechanisms dictating the increased oil recovery due to low salinity waterflooding were explored by characterizing the pores that were most susceptible to oil mobilization and comparing those to the pores that were most susceptible to formation damage in the kaolinite- and montmorillonite-rich micromodels. Flow diversion from blocked preferential flow

paths due to formation damage to smaller pores was a major mechanism for increased oil recovery during low salinity waterflooding in kaolinite-rich systems, whereas mobilization of pore-lining swollen montmorillonite did not appear to result directly in improved recovery under the conditions studied.

Chapter 5

Spontaneous Clay Pickering Emulsification

Clay-rich sandstone formations contain vast deposits of petroleum resources. Low salinity waterflooding presents a low-energy, low-environmental impact method to improve oil recovery from these systems. Fundamental mechanisms dictating improved oil recovery at low salinity conditions are not well-understood currently. This chapter investigates low salinity waterflooding at the pore-level to delineate fundamental mechanisms underlying oil recovery. Clay-functionalized two-dimensional micromodels are used to provide direct visual observations of crude oil, brine, and clay particle interactions within the pore-space. Using this microvisual approach, establishment of initial reservoir conditions show wettability evolution of the initially water-wet system towards a mixed-wet condition due to clay-particle interactions with the reservoir fluids, i.e., crude oil and brine. Pore-scale behavior during low salinity waterflooding shows spontaneous emulsification of the crude oil and brine. Specifically, the emulsions generated are Pickering type stabilized by the clay particles that were mobilized at salinities below the critical salt concentration (CSC). Spontaneous generation of the stable Pickering emulsions reduces mobility through preferential flow

paths, thereby resulting in flow diversion of subsequent injection fluids to mobilize oil-filled pores. Leveraging the stability of the Pickering emulsions, a sequential salinity cycling method is developed to improve overall oil recovery by an additional 8 % of the original oil in place. Flow diversion due to spontaneous Pickering emulsification in preferential flow paths observed here provides fundamental insight to the design and application of low energy-input, low environmental-impacts techniques in the field.

5.1 Introduction

Clay-rich sandstones contain vast deposits of global petroleum resources. Recovery of oil from these systems, however, is often limited [156]. Low salinity waterflooding, the injection of brine that is reduced in salinity compared to the original reservoir formation brine, presents an opportunity to improve overall oil recovery significantly [4, 156, 101, 100, 36, 29, 91, 5]. Specifically, low salinity brine injection is of industrial interest due to its low economic requirements as well as its ability to recover oil without significant energy or environmental impacts. Results from laboratory- and field-scale experiments, however, lack agreement.

Fundamental understanding of the underlying mechanics that dictate the improvements in oil recovery with low salinity brine injection, i.e., the low salinity effect, must be understood for large-scale field-level implementation. Several mechanisms have thus far been suggested in an attempt to explain the low salinity effect. Specifically, three of the proposed mechanisms include (i) fines migration, whereby clay particles are mobilized in the pore-space and alter the overall wettability of the rock [4]; (ii) multicomponent ion exchange (MIE), in which the adsorbed charged components of the crude oil are replaced by an aqueous-phase ion such that the adsorbed oil molecules are released into the free-flowing phase [42]; and (iii) saponification, or, the generation of emulsions, due to the release of naturally present surface-active agents

(surfactants) from the crude oil at the oil-brine interface [45]. Lack of agreement in the literature on the role of each proposed mechanism in inducing the low salinity effect necessitates mechanistic studies at the fundamental scale.

Fundamental behavior of petroleum reservoirs is dictated by pore-scale dynamics due to their porous nature [107]. Direct pore-level understanding of fluid transport through petroleum reservoirs has been limited due to the opacity and heterogeneity of rock. Advances to in-situ visualization techniques such as X-ray computed tomography (CT) has enabled observations of fluid distributions in real rock samples [141, 142, 157, 158]. Spatiotemporal resolution of such techniques, however, is poor in comparison to those required to delineate the fundamental pore-scale dynamics.

Microfluidic systems are emerging as a useful tool for the direct visual study of petroleum systems behavior at the fundamental pore-scale. Specifically, micromodels, microfluidic platforms that have representative pore geometry of real rock, lend direct insight into the pore space by allowing real-time, micro-scale visualization [79, 107]. Current state-of-the-art techniques for micromodel fabrication imprints rock pore geometry into silicon wafers through plasma etching, and the etched silicon wafer is subsequently bonded anodically with glass to enable flow and direct visualization [79]. Most recently, real-rock microfluidics [94] was developed to replicate the rock material more closely. Specifically, pore geometries have been etched into real-rock substrates such as calcite [94], shale [96], and coal [97]. Further, glass- and silicon-based microfluidics have been surface-functionalized with minerals such as clay [80, 76] and calcite [106] (see Chapter 6) to enable direct visual observation of fluid transport through and interactions with real rock material.

In this work, clay-functionalized micromodels are used to investigate the interactions between crude oil, brine, and clay particles that underlie the low salinity effect in clay-rich sandstones. The clay-functionalized micromodel is initialized to reservoir conditions by formation brine and crude oil injection, respectively, and by

aging to allow for sufficient equilibration. The crude oil used in this chapter is of industrial interest. Wettability changes to the pore space as a result of the clay particles are monitored. Pore-scale dynamics due to the injection of brines at high and low salinities were visualized directly through a microscope. Surprisingly, spontaneous generation of large-diameter emulsions were observed at very low salinity (i.e., freshwater) conditions throughout the preferential flow paths. We determine stable emulsions to be a result of the mobilized clay particles that stabilize the water-oil interface, thereby forming stable Pickering emulsions. Presence of the stable emulsions is leveraged to design a salinity cycling scheme that further improves overall oil recovery by an additional 8.5 % original oil in place (OOIP).

5.2 Experimental Methods

Experimental investigation of crude oil, brine, and clay interactions were conducted at the microscopic pore-scale and at the bulk scale. The following sections describe the pore- and bulk-scale methods taken, respectively.

5.2.1 Direct Visualization of Pore-Scale Dynamics

Direct, real-time visualization of pore-scale dynamics was enabled by a geochemically-representative micromodel, fluid delivery system, and a microscope and camera (Chapter 2, Fig. 2.3). Clay-functionalized micromodels with representative pore geometry and surface properties of real reservoir rock were used to visualize pore-scale oil recovery dynamics in clay-rich sandstones. The etched-silicon micromodel fabrication and clay-functionalization methods follow the processes described in Chapters 2, 3, and 4 [80, 76]. Kaolinite clay (Kaolin, K2-500, Fisher Scientific) was used in this work due to its mobility with decreasing salinity and to mimic the target reservoir properties. The micromodels used in this work follow a sandstone grain pattern obtained from

binarized thin-section images of real sandstone.

Fluids correspond to a specific clay-rich reservoir of industrial relevance. The composition of the formation brine is listed in Table 5.1. Properties of the crude oil are shown in Table 5.2.

Table 5.1: Composition of brine used to simulate initial reservoir conditions.

Analytical Grade Reagents	Concentration (g/L)
$CaCl_2 \cdot 2H_2O$ (Calcium chloride dihydrate)	0.183
$MgCl_2 \cdot 6H_2O$ (Magnesium chloride hexahydrate)	0.585
NaCl (Sodium chloride)	20.461
KCl (Potassium chloride)	0.611
Na_2SO_4 (Sodium sulfate)	0.109

Table 5.2: Crude oil characterization [148].

Crude oil properties	Value
Acid number (mg/g)	2.36
Base number (mg/g)	6.02
Asphaltene content (wt%)	2.69
Density (°API)	21
Viscosity at 22.8°C (cP)	105.7

To replicate natural geological deposition, the clay-functionalized micromodel was first saturated with the formation brine (Fig. 5.1a). Crude oil was injected at $\sim$ 1 m/day until residual water saturation was reached to mimic the process of oil migration into the reservoir (Fig. 5.1b).

The oil- and brine-filled micromodel was then submerged under crude oil at ambient conditions for two weeks to allow for sufficient interactions and equilibration

between the phases (Fig. 5.1c). This is referred to as aging. The aged micromodel is taken as the initial reservoir condition, analogous to the industrial oil reservoir that this study is modeled around.

In keeping with industrial practices, several pore-volumes of high salinity brine (10 000 ppm NaCl) were injected into the aged micromodel to standardize the model system with primary and secondary recovery processes commonly practiced in the industry (Fig. 5.1d). Low salinity brine (4000 ppm NaCl) was injected to study the dynamics of the clay-rich sandstone system during low salinity waterflooding (Fig. 5.1e). Brine with 4000 ppm NaCl was chosen here in accordance with the critical salt concentration for kaolinite mobilization found in Chapter 3 [80] to investigate the importance of clay during low salinity waterflooding.

Freshwater (i.e., deionized water) was injected to investigate the effect of reduced salinity on overall oil recovery from the clay-rich sandstone model rock (Fig. 5.1f). All fluids were injected into the micromodel at a nominal velocity of 1 m/day to represent realistic subsurface flow conditions. Fluids were delivered using a syringe (BD 60 mL syringe, 309653) and syringe pump (Harvard Apparatus, Holliston, MA) at ambient conditions. Microvisual imaging was achieved immediately following each injection process using a confocal microscope (Sensofar Sneox 3D optical profiler). Images were captured at 25 fixed locations across the micromodel to minimize pore-scale variations. Fluid phases from the captured pore-scale images were segmented to quantify the fluid saturations and oil recoveries from the clay-rich sandstone model system.

5.2.2 Bulk-Scale Measurements

Interactions between crude oil, brine, and clay were characterized at the bulk scale. Specifically, emulsification with and without clay was tested using the crude oil (Table 5.1), the formation brine (Table 5.2), and deionized (DI) water through a simple

shake-test in glass scintillation vials (20 mL Borosilicate Scintillation Vials, DWK Life Sciences Wheaton). Clay contents were varied for fixed water-oil ratios to investigate the minimum clay presence required to generate stable emulsions. Specifically, clay contents were varied from zero to 4.78 wt% in DI water with crude oil mixtures, and zero to 4.68 wt% in reservoir brine with crude oil mixtures. The vials of brine/DI water, crude oil, and/or clay were shaken vigorously for 1 minute and allowed to equilibrate. The emulsification process, or lackthereof, was monitored over time and emulsions sizes, if available, were characterized.

5.3 Results and Discussion

5.3.1 Aging

Clay-functionalized micromodels with representative geometric and surface characteristics of real clay-rich sandstone (see Chapters 2 and 3 [80] for validation study) were used to study crude-oil, brine, and rock interactions. Specifically, functionalized micromodels were saturated with reservoir formation brine to recreate initial geological deposition processes (Fig. 5.1a). Crude oil migration into the reservoir rock was replicated by crude-oil injection into the micromodel until residual water saturation was reached, i.e., no more water could be removed (Fig. 5.1b). Immediately following crude-oil migration, the clay-functionalized micromodel was strongly water-wet, as in silicon-based systems. Recall that petroleum fluids migrate to, accumulate, and reside in subsurface reservoirs over geological time (i.e., on the order of $\sim$ 10's to 100's of million years). To achieve more realistic initial reservoir conditions, the model system was aged for two weeks to replicate the equilibration process underground to achieve representative initial reservoir conditions. Two weeks were deemed sufficient through monitoring of fluid distribution over time, in agreement with established practice

[6, 159].

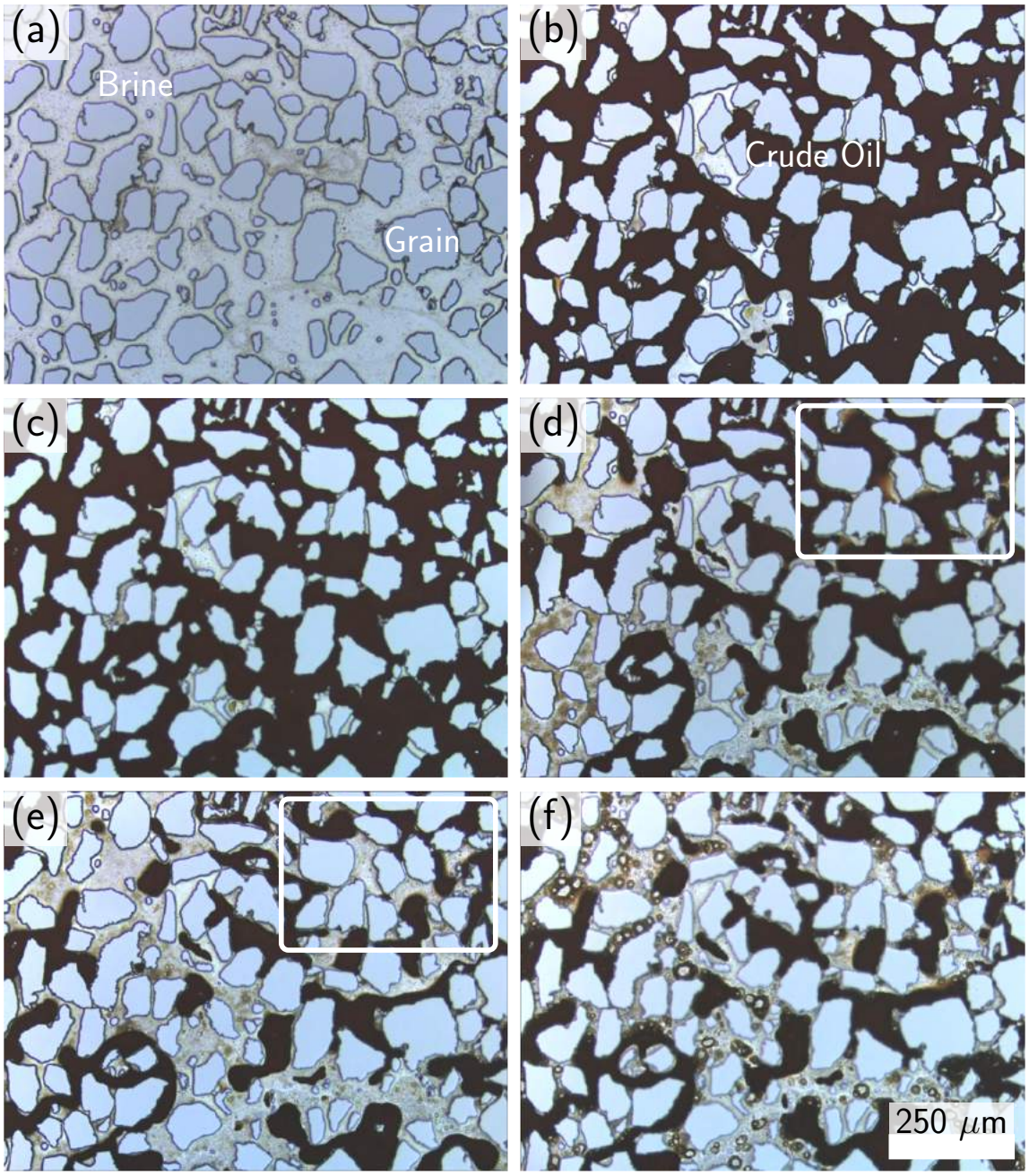
(a)
Brine
Grain
(b)
Crude Oil
(c)
(d)
(e)
(f)
250 μm

Figure 5.1 *(previous page)*: Pore-level dynamics of the micromodel. (a) Clay-functionalized micromodel is saturated with formation brine (see 5.1 for composition) to mimic in-situ conditions. (b) Crude oil (see 5.2 for properties) corresponding to the formation brine is injected until the residual water saturation is reached to mimic the process of petroleum migration into the reservoir. (c) The micromodel is aged for two weeks to allow for the crude oil, brine, and solids to interact and equilibrate. This is the initial reservoir condition. (d) Initial high salinity brine (10 000 ppm NaCl) is injected to benchmark the experiment with secondary recovery results. (e) Improved oil recovery ($\sim$ 6.5 % OOIP) is observed following low salinity brine (4000 ppm NaCl) injection. (f) Surprisingly, large (diameter $\sim$ 5 to 30 μm) emulsions form throughout the pore-space during injection of deionized (DI) water. Emulsions are formed spontaneously throughout the preferential flow paths along the water-oil interfaces.

Importantly, a mixed-wet condition is observed in the aged micromodel, away from the initial strongly water-wet condition. Equilibration between the fluid and solid constituents, i.e., aging, showed fluid redistribution from an initially water-wet condition (Fig. 5.2a) towards one that is more mixed-wet (Fig. 5.2b,c). Specifically, immediately following crude oil introduction to the system, water is found in the smallest pores and macroscopic water films line the grains (Fig. 5.2a). This is a classic example of the strongly water-wet condition. After aging, however, invasion of moderate-sized pores by crude oil (dashed box in Fig. 5.2a,b) and disappearance of the macroscopic water films are observed (Fig. 5.2b). The altered state at the end of aging is attributed to crude-oil, brine, and clay interactions. Specifically, charged edges of kaolinite clay particles attract charged components in the crude oil and hence alter the pore region towards oil-wetness. Mixed-wettability in the aged micromodel is further validated through observation of irregular water-oil interfaces due to pinning (Fig. 5.2c,i) and thin oil-films (Fig. 5.2c,ii). These results are consistent with the scenario for development of mixed-wettability [11] and are comparable to mixed-wettability of real clay-rich sandstone at initial reservoir conditions [156].

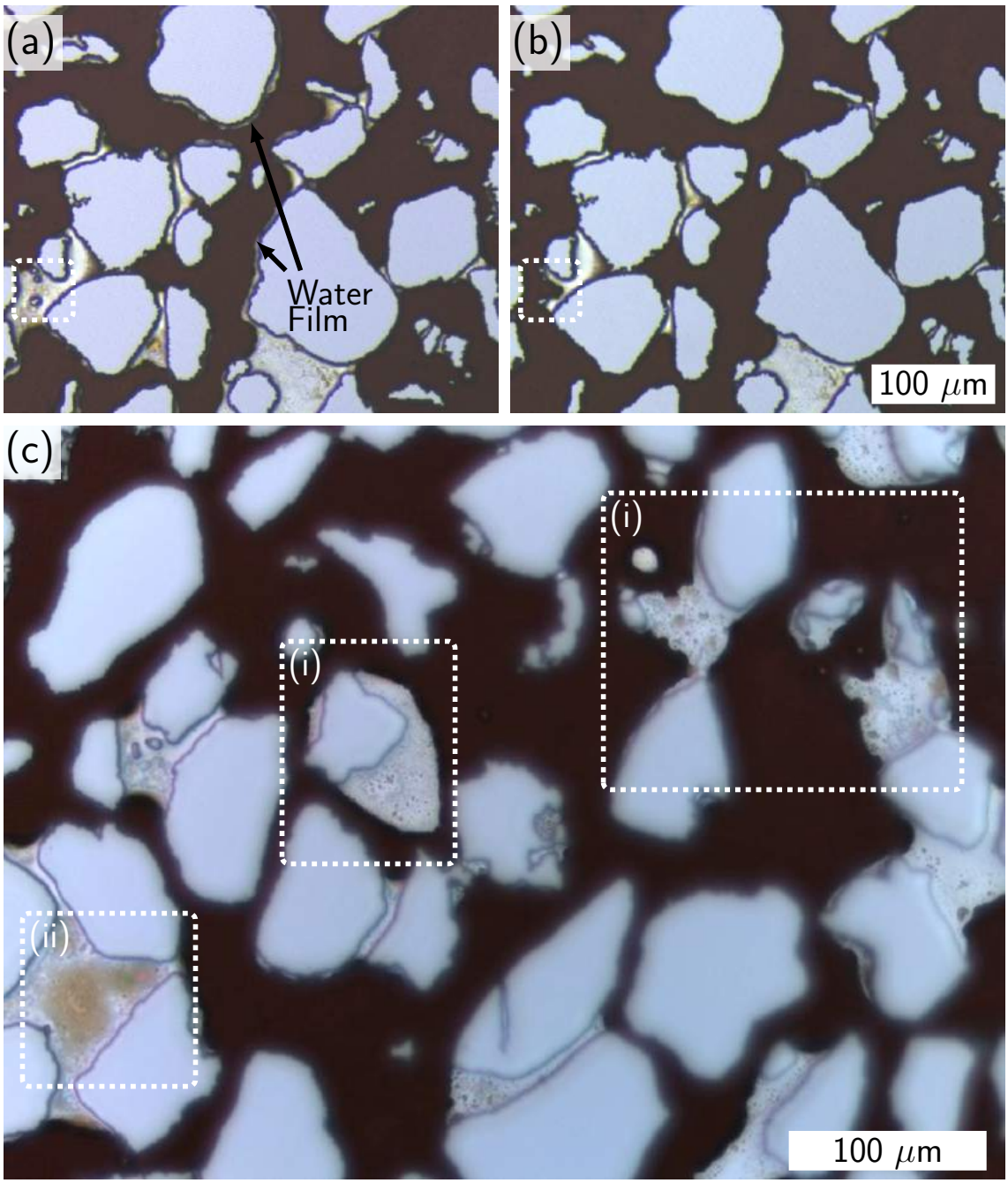
(a)
Water
Film
(b)
100 μm
(c)
(i)
(i)
(ii)
100 μm

Figure 5.2 *(previous page)*: Transition to mixed-wet behavior at the pore-scale due to aging. (a) Prior to aging, water resides in smallest pores and macroscopic water films surround silicon grains, consistent with water-wet systems. (b) Following aging, macroscopic water films are no longer visible due to crude-oil interactions with clay. Mixed-wet behavior is further exemplified by crude oil displacement of brine in smaller pore-spaces (dashed box areas in (a) and (b)). (c) Mixed-wettability at the pore-scale is evident through observation of irregularly-shaped water-oil interfaces due to interfacial pinning on the clay particles (c,i), presence of thin oil films on the pore surface (c,ii), and occupancy of oil in smaller pore spaces (a,b, dashed boxes).

5.3.2 Oil Recovery

Upon aging, the micromodel system is deemed representative of initial reservoir conditions. Injection of high salinity (10 000 ppm NaCl) brine displaced some of the crude oil and created preferential flow paths through the porous medium (Fig. 5.1d). Connected groups of water-saturated pores enables flow preference for the injection brine, and thus the bypass of oil-filled pores. Oil from the bypassed pores is not recovered. Notice, however, that not all oil-filled pores are bypassed pores, but instead are pores where the oil-wet pore-surfaces have retained the crude oil. This is especially apparent when comparing the boxed region in Fig. 5.1d after the high salinity waterflood to the corresponding region at initial reservoir conditions in Fig. 5.1c.

As a means to improve oil recovery from clay-rich sandstone reservoirs, low salinity waterflooding presents a method that minimizes the environmental and energetic impact associated with oil recovery. Of industrial interest, low salinity (4000 ppm NaCl) brine injection resulted in an increase in oil recovery, i.e., less oil saturation, from the micromodel system (Fig. 5.1e). With the low salinity brine, the wettability of the pore surfaces appear to shift from a mixed-wet condition to a water-wet condition. Specifically, development of macroscopic water films and removal of the thick residual oil films following low salinity brine injection (Fig. 5.1e, boxed region) serve as direct evidence. It is worth noting that the concentration of the low salinity brine

chosen here corresponds to the critical salt concentration (CSC) that was measured for kaolinite clay particle mobilization in this micromodel system (see Chapter 3 for details [80]) and that clay particles are mobilized in this system (see Chapter 4 for details [76]).

Sensitivity of oil recovery to injection brine salinity was delineated with a tertiary injection of freshwater (DI water, Fig. 5.1f). Surprisingly, water-in-oil emulsions formed spontaneously throughout the micromodel. The emulsions were large (diameter $\sim$ 5 to 30 μm) and populated the preferential flow paths forged during the high and initial low salinity brine injections. Unlike the small (diameter < 1 μm) emulsions due to the release of surface-active components at the oil-water interface (Fig. 5.4a) postulated previously [45], the emulsions generated in the present system are much larger in size.

Equilibration of the spontaneously generated emulsions shows that the emulsions are stable (Fig. 5.3). Emulsion surfaces appear rigid in structure, unlike surfactant-stabilized emulsions. Recall that the critical salt concentration (CSC) for kaolinite clay particle detachment and mobilization in this micromodel system is 4000 ppm NaCl. In other words, salinities below the CSC, as in the current system, results in an abundance of mobile detached clay particles.

The stability of the emulsions combined with its spontanous generation, its rigidity, and the availability of mobile clay particles in the low salinity pore space leads to the conclusion that the emulsions generated are of Pickering type (Fig. 5.4b). Pickering emulsions are those stabilized by the charged surfaces of particles at the fluid interface. In the present system, mobile kaolinite clay particles, on the order of μm, serve as the stabilizing agents. Recall that kaolinite clay particles have charged edges by nature.

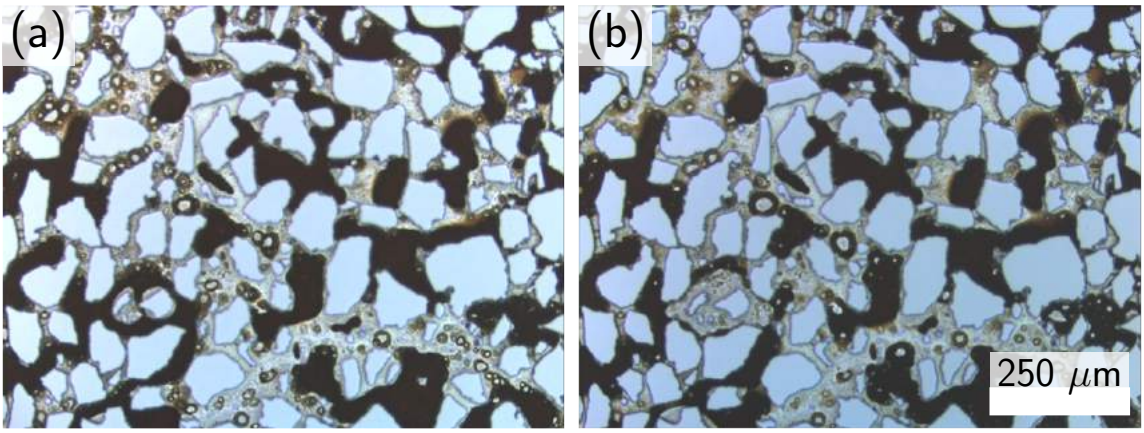

Figure 5.3: Stability of 5 to 30 μm diameter emulsions at the pore-scale. (a) Emulsions throughout the preferential flow paths after freshwater injection. (b) Emulsions are stable after one week of equilibration.

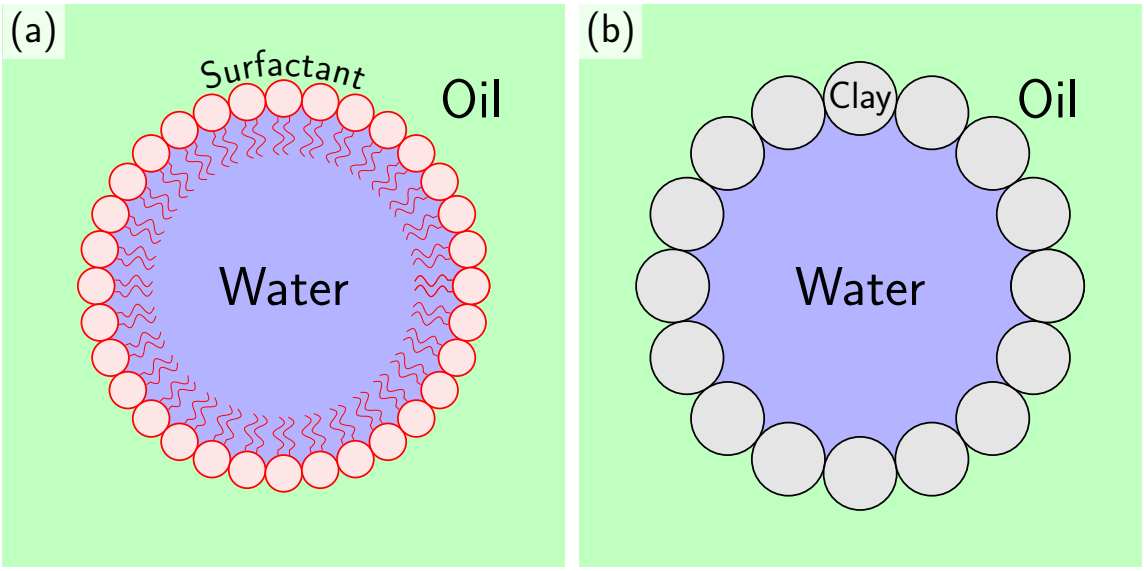

Figure 5.4: Cartoon illustrations of the emulsion stabilizing agents. (a) Surface-active components (surfactant) stabilized emulsions due to added crude oil and brine chemistry. This is the type that has been reported previously to aid in low salinity improved oil recovery [45]. (b) Pickering emulsions, as observed, are stabilized due to charged surfaces of the clay particles that have been mobilized at salinities below the CSC for clay particle detachment (i.e., at low salinities).

Comparison between clay-present and clay-absent systems at both the microscopic

pore-scale and at the bulk-scale confirm the spontaneous generation of Pickering emulsions (Fig. 5.5). Specifically, in the absence of clay, a clean, distinct interface between the crude oil phase and the aqueous phase is observed at both the pore-level (Fig. 5.5a) and at the bulk-level (Fig. 5.5c). No emulsions were generated without clay particles present, as expected for this surfactant-poor crude oil-brine system. In the presence of clay, however, Pickering emulsions were generated at both the pore-scale (Fig. 5.5b) and the bulk-scale (Fig. 5.5d). Bulk- and pore-scale Pickering emulsions, importantly, have been stable since January 2016.

Due to the requirement of clay-particle availability on the formation of Pickering emulsions, emulsification as a function of clay content was investigated in bulk (Fig. 5.6) as a proxy of the pore-scale dynamics. Specifically, fixed volumes of aqueous phase (reservoir brine or DI water) and crude oil were added to varying kaolinite clay masses to delineate the impact of clay content and salinity on Pickering emulsification. For both brine/crude-oil and freshwater/crude-oil systems, a minimum clay content was required to generate a stable emulsion. In the case of crude oil with DI water, the minimum clay content required for stable Pickering emulsification was 1.64 wt% kaolinite (Fig. 5.6a,c). Crude oil and reservoir brine systems, however, required less clay (0.81 wt% kaolinite) to generate stable Pickering emulsions (Fig. 5.6b,c). The reduced requirement on clay content may be explained by the increased ion availability due to the dissolved salts. Interestingly, the sizes of the Pickering emulsions generated in both brine/crude-oil and freshwater/crude-oil systems decrease with increasing clay availability (Fig. 5.6c).

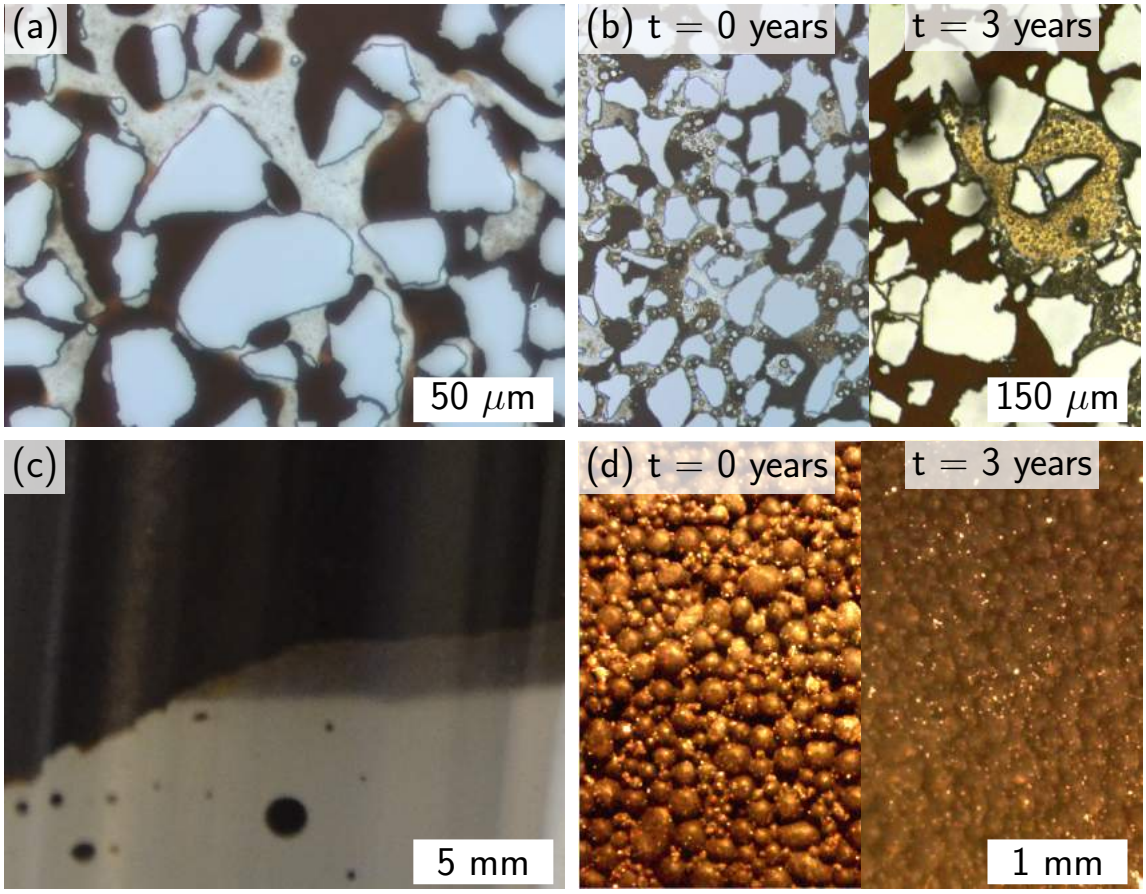

Figure 5.5: Comparison of crude oil - brine system in the absence and presence of clay. Pore-scale micromodel experiments show clean water-oil interfaces in the absence of clay (a) and stable emulsions in the presence of clay (b), respectively. Bulk experiments show that in the absence of clay (c), brine and the crude oil prefer to reside in their individual phases, i.e., no emulsions are formed. In the presence of clay (d), however, stable Pickering emulsions are formed. The Pickering emulsions are stable over three years (b,d). We do not add surfactant to the oil-water system, and thus no stable emulsions were formed in the absence of clay (a, c). Charged clay-particle surfaces act to stabilize the Pickering emulsions observed at both bulk- and pore-scales (b, d).

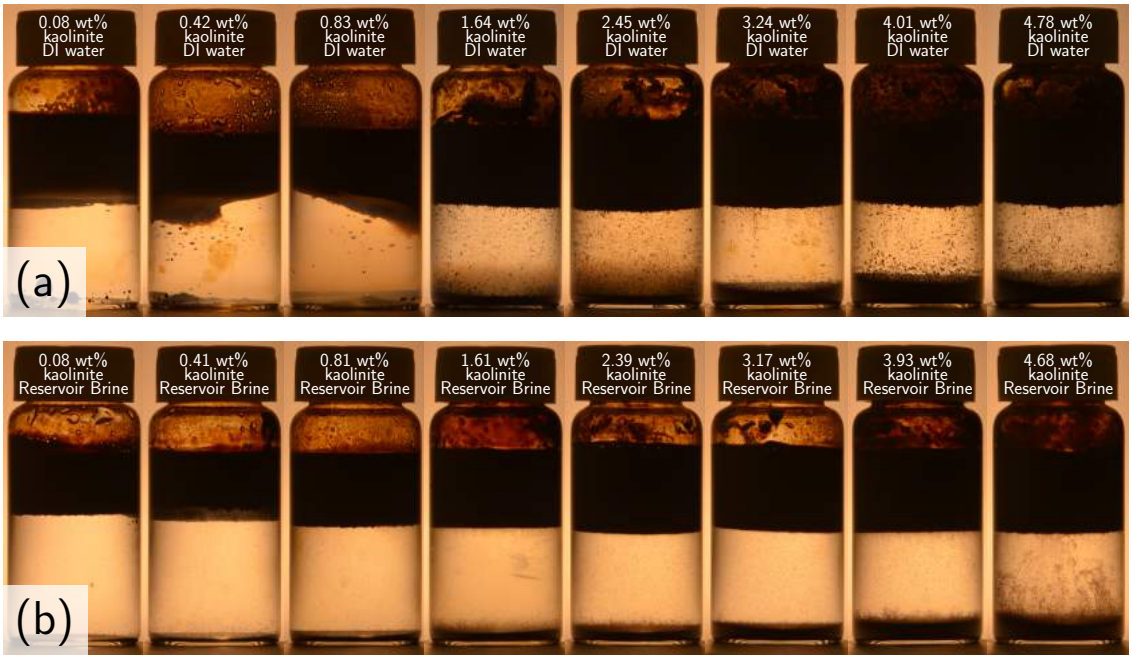
0.08 wt% kaolinite DI water
0.42 wt% kaolinite DI water
0.83 wt% kaolinite DI water
1.64 wt% kaolinite DI water
2.45 wt% kaolinite DI water
3.24 wt% kaolinite DI water
4.01 wt% kaolinite DI water
4.78 wt% kaolinite DI water
(a)
0.08 wt% kaolinite Reservoir Brine
0.41 wt% kaolinite Reservoir Brine
0.81 wt% kaolinite Reservoir Brine
1.61 wt% kaolinite Reservoir Brine
2.39 wt% kaolinite Reservoir Brine
3.17 wt% kaolinite Reservoir Brine
3.93 wt% kaolinite Reservoir Brine
4.68 wt% kaolinite Reservoir Brine
(b)
(c)
Pickering Emulsions
Reservoir Brine
Deionized Water
Oil-Water Interface (No Emulsions)
Emulsion Diameter (μm)
Kaolinite Content (wt%)
0
100
200
300
400
500
600
700
0
0.5
1
1.5
2
2.5
3
3.5
4
4.5
5

Figure 5.6 *(previous page)*: Pickering emulsification as a function of clay content in bulk-scale shake tests. (a) Emulsification between crude oil and freshwater. No emulsions were formed for clay contents below 1.64 wt%. (b) Emulsification between crude oil and the reservoir brine. No emulsions were formed for clay contents below 0.81 wt%. (c) Characterization of emulsions sizes as a function of kaolinite clay content shows a minimum clay content to form stable emulsions in the system, and that emulsions sizes decrease with increasing clay availability.

Decreased emulsion sizes with increasing clay availability may explain some core-scale observations of increased oil recovery with clay content from the literature. Specifically, generation and residence of emulsions in the preferential flow paths create pressure buildups across those paths as a result of the large number of interfaces, and thus, capillarity forces, needed to overcome for flow. Presence of high clay content in the reservoir enables the formation of Pickering emulsions of smaller diameters in the preferential flow paths. Dense populations of small emulsions in the preferential flow paths exacerbate the flow blockage through the water-saturated preferential flow paths by increasing the number of interfaces present.

The resulting resistance to pore-scale flow due to increased numbers of interfaces from small, dense emulsions thus reduces the local permeability of subsequent injection fluids. As a result, subsequent injection fluid, such as brine, is diverted to pockets of the continuous crude oil phase with few interfaces to overcome. The macroscopic pressure gradient is largely unchanged because of the flow diversion mechanism. That is, the emulsification of the previous preferential flow paths forces fluids to forge new paths through the oil-filled pores. The pressure required to overcome a single interface, in comparison to that required in the emulsion-filled pores, is akin to the macroscopic pressure gradient at initial high salinity conditions. This may explain some field observations that show the lack of clay production and pressure buildup with increased oil recovery under low salinity conditions [42, 10].

The combined spontaneous Pickering emulsification and flow diversion mechanisms here enable a tertiary increase in oil production from the system. Pore-scale micromodel experiments show that with subsequent injection of high salinity (20 000 ppm) brine, overall oil saturation in the system is reduced. In other words, overall oil recovery is increased.

Direct visual quantification of oil recovery from the clay-rich sandstone system is achieved through imaging and image processing. Representative averages were obtained by imaging at 25 fixed locations across the micromodel (Fig. 5.7a). Images were taken at each specified location following each injection process to track the evolution of the local fluid distribution at initial reservoir conditions (Fig. 5.7b,i), following the high salinity brine injection (Fig. 5.7b,ii), the low salinity 4000 ppm brine injection (Fig. 5.7b,iii), and the freshwater Pickering emulsification and subsequent high salinity brine injection (Fig. 5.7b,iv).

Image sets from each location were segmented (Fig. 5.7c) to delineate the oil (green), brine (blue), and solid (black) phases. The segmented images enable direct calculation of fluid phase saturations, i.e., oil recovery factors, of each location after each injection process. The two-dimensional nature of the micromodel enables quantification of volumetric saturations of crude oil, $S_o = V_o/V_{pore} = A_o/(A_o + A_w)$, and brine, $S_w = 1 - S_o$, directly from the images. Here, the volumes of oil, V_o, and pore space, $V_{pore} = V_o + V_w$, are determined from the areas that the brine and oil occupy. Oil recoveries following each injection process are averaged across the micromodel to determine the overall oil recovery (Fig. 5.7d). In this work, we find that the initial high salinity 10 000 ppm waterflood recovered $\sim 38\%$ of the original oil in place (OOIP), consistent with core- and field-scale studies [9]. Traditional low salinity 4000 ppm brine injection increased overall oil recovery by $\sim 6.5\%$ OOIP, again corroborated by core-flooding experiments [9]. The new salinity cycling method that we implement here, whereby freshwater is injected to mobilize clay particles and to

generate stable Pickering emulsions spontaneously that block preferential flow paths and divert flow towards oil-filled pores followed by an additional high salinity flood, increased the overall oil recovery by an additional $\sim$ 8% OOIP.

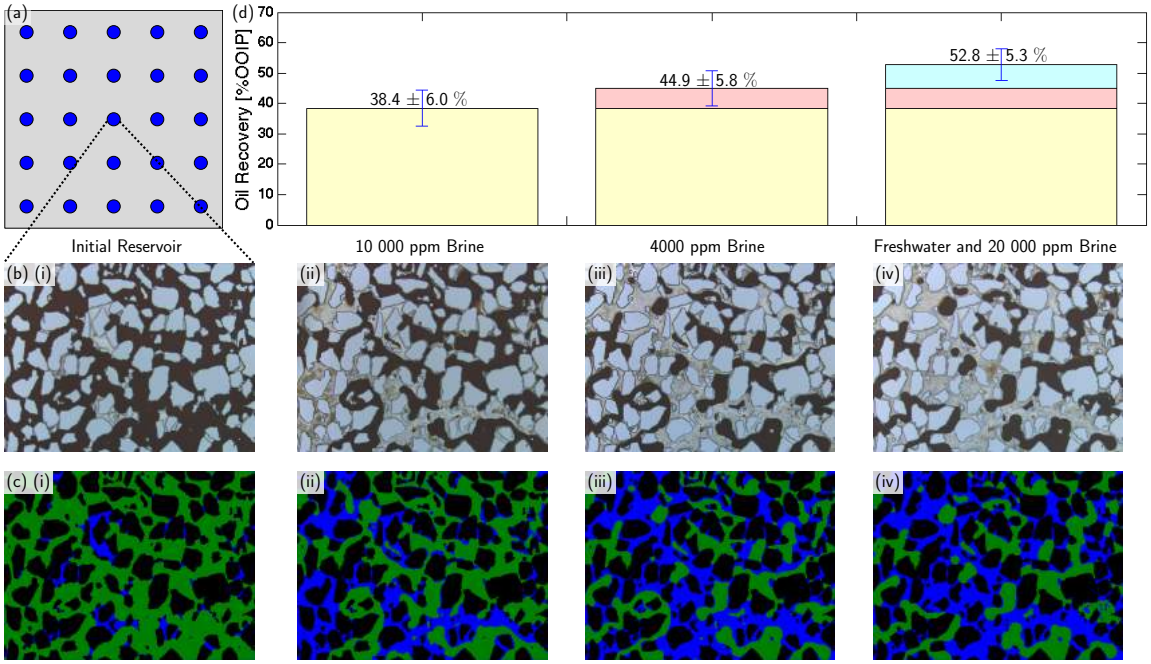

Figure 5.7: Quantification of oil recovery from the clay-rich sandstone model system. (a) Images are taken at 25 fixed locations across the micromodel after each injection process to obtain a pore-averaged oil recovery factor. (b) Pore-level images of crude oil and brine distribution in the micromodel at initial reservoir conditions (i), following the initial 10 000 ppm high salinity brine injection (ii), following the 4000 ppm low salinity brine injection (iii), and following the freshwater and subsequent high salinity brine injection (iv). (c) Segmented images delineating the oil (green), brine (blue), and grains (black) corresponding to each stage in (b) are obtained through image processing. Due to the two-dimensional nature of the micromodel platform, segmented images delineating the area of each phase enables quantification for volumetric saturations of the crude oil, S_o, and brine, S_w. (d) Oil recoveries calculated from the segmented images across the micromodel show an initial oil recovery of $\sim$ 38% OOIP, followed by an increase of $\sim$ 6.5 % OOIP after the low salinity waterflood, and an increase of $\sim$ 8 % OOIP after the freshwater injection due to flow diversion from the spontaneous Pickering emulsification of the crude oil.

5.4 Conclusion

In this chapter, we delineate pore-scale dynamics underlying the presence of clay in crude-oil and brine systems. Specifically, we observe directly the alteration of pore-surface wettability due to the presence of clay. We observe the evolution of mixed-wet surfaces where oil films exist and are retained, and the absence of macroscopic water films as in strongly water-wet systems. Fundamental mechanisms underlying the low salinity effect in clay-rich sandstone were investigated using the mixed-wet clay-functionalized micromodel. In particular, wettability appears to shift towards water-wetness under low salinity (4000 ppm) conditions, evidenced by the disappearance of thick oil films and the appearance of macroscopic water films. Of particular interest to the industry, we discover that the mobilized clay particles at low salinity (freshwater) conditions act to stabilize the oil-water interface and enable spontaneous generation of Pickering emulsions in the preferential flow paths. The Pickering emulsions are characterized and stable over long times. Spontaneous emulsification in preferential flow paths reduces the local apparent permeability and thus requires a large pressure differential for flow. As a result, flow is diverted to oil-filled pores that become amenable for flow at smaller pressure gradient. The overall effect of the spontaneous Pickering emulsification and flow diversion is quantified, showing an additional increase in oil recovery of $\sim 8\%$ OOIP.

Chapter 6

Grain-Engulfment during Reactive Transport

Dissolution of carbonate minerals in porous media is important to many instances of subsurface flow, including geological carbon dioxide (CO_2) sequestration, karst formation, and reservoir stimulation and acidizing. Of particular interest, geological CO_2 storage in deep carbonate reservoirs presents a significant long-term opportunity to mitigate atmospheric carbon emissions. Reactivity of carbonate reservoirs, however, may negatively impact storage formation integrity and hence jeopardize sequestered CO_2 storage security. In this work, we develop a novel biogenically calcite-functionalized microvisual device to study the fundamental pore-scale reactive transport dynamics in carbonate formations. Importantly, we discover a new microscale mechanism that dictates the overall behavior of the reactive transport phenomenon, where the reaction product, CO_2, due to carbonate rock dissolution forms a separate, protective phase that engulfs the carbonate rock grain and reduces further dissolution. The presence of the separate, protective CO_2 phase determines overall dissolution patterns in the storage reservoir, and leads to formation of preferential leakage paths. We scale these results using nondimensional numbers to demonstrate

their influence on industrial CO_2 storage security, safety, and capacity, and suggest optimal design of CO_2 injection techniques that ensure long-term secure storage.

6.1 Introduction

Energy demand and climate tensions present some of the most pressing challenges facing the 21st century [160, 161]. Global atmospheric CO_2 concentration increased from 270 ppm in 1750 [162] to 410 ppm in 2018 [163] due, in large part, to emissions from fossil fuel consumption [164, 165]. Reducing atmospheric CO_2 emissions from fossil fuel combustion and other industrial sources is a key component in transitioning towards a low-carbon future.

Geological CO_2 storage in subsurface reservoirs provides an immediate industrial solution to limit large-scale CO_2 emissions and to transition to a low-carbon future [166, 167, 168]. Geological formations suitable for long-term carbon storage include deep saline aquifers, depleted oil and gas reservoirs, and unmineable coal seams [50]. Deep saline aquifers within carbonate formations, i.e., limestones and dolostones, are ubiquitous and present the largest storage capacity worldwide [169, 170].

Carbonates, however, are extremely reactive and susceptible to dissolution in the presence of CO_2-acidified brines [94, 171]. Storage reservoir rock dissolution undermines subsurface CO_2 storage security; uncertainty in injected CO_2 storage security currently forestalls large-scale implementation of subsurface CO_2 storage [50, 172, 173]. Predictive models describing reactive transport in geochemically complex carbonate reservoirs are thus required to design CO_2 injection schemes that maximize both storage capacity and storage security.

Predictive models assessing long-term geologic CO_2 storage potential require fundamental understanding of reservoir integrity [174, 175] and CO_2 migration [176] based on fluid-rock interactions [177, 178]. Core-scale reactive transport experiments

provide pressure measurements, effluent analyses, and X-ray computed tomography that show significant reservoir rock dissolution due to CO_2-acidified brine [142, 52]. Empirical relations derived from core-scale experiments have been developed to map the influence of acidity and advection on acid-rock reaction rates and dissolution patterns. Fredd and Fogler 1998 [52] visualized uniform core-scale dissolution under high Damkohler number (Da) conditions and extended finger-like flow conduits under low Da conditions. The Damkohler number is defined as Da = reaction rate/ advection rate. The reactions are represented by $2H^{+}_{(aq)} + CaCO_{3(s)} \rightarrow CO_2 + H_2O_{(l)} + Ca^{2+}_{(aq)}$ [52, 179, 180, 53]. Importantly, current macroscopic core-scale literature do not assign a phase to the reaction product CO_2; all reaction products are assumed to be solubilized in the aqueous phase and reaction rates are assumed constant for prescribed acid fluxes [52, 179, 180, 53]. Reactive transport models based on these assumptions require sample-specific correction factors to match physical rock dissolution configurations [178, 179, 180]. New fundamental understanding of reactive transport mechanisms is therefore required to develop general predictive models for CO_2 storage [181]. More broadly, fundamental understanding of reactive transport in porous media applies to fields such as acidization of conventional petroleum reservoirs, acidization of shale reservoirs, geothermal reservoirs, food processing [182], and pharmaceutical manufacturing and uptake.

Pore-scale fluid-rock mechanisms ultimately dictate reactive transport in CO_2 storage reservoirs [183]. Specifically, pore-scale interfacial reaction dynamics determine macroscopic reaction rates and rock dissolution patterns [184, 185]. Microfluidics provides direct real-time, pore-scale visualization of fluid transport and fluid-solid interactions through porous media [94, 107, 75, 79, 186, 108, 80, 76, 143, 117, 131]. Glass- and silicon-based microfluidic platforms with realistic pore geometries (micromodels) have been developed to enable pore-scale investigations at high-temperature,

high-pressure geological conditions [79, 186, 108, 80, 76, 99, 143, 187, 88, 89]. Pore-scale transport and reaction dynamics depend on mineralogy and rock surface chemistry. Mineral-functionalized pore surfaces enable direct visualization of the fundamental fluid-mineral interactions in microfluidic devices [94, 80, 76, 96].

In this chapter, we capture the physics describing pore-level reactive transport within carbonates in order to advance understanding and design of secure geologic CO_2 storage. Novel carbonate-functionalized microfluidic devices are developed to study reactive transport at the interfacial-, pore-, and the pore-ensemble-scales using microfabrication and bacterial biogenesis. High-temperature, high-pressure, reactive transport experiments are scaled to replicate realistic CO_2 storage conditions. We find a new fundamental mechanism, grain-engulfment, that dictates reactive transport and CO_2 storage security in carbonates through direct pore-scale visualization. Mechanistic understanding of fundamental interfacial dynamics is extended to determine practical implications within storage reservoirs through dimensionless analysis. The new, fundamental grain-engulfment mechanism impacts CO_2 storage security significantly close to injection wells in carbonate storage reservoirs.

6.2 Materials and Methods

Pore-scale visualization of reactive transport through carbonates was achieved using calcite-functionalized microfluidics. Specifically, two types of calcite-functionalized flow devices were developed: (i) biogenically calcite-functionalized etched silicon micromodels that enable direct pore-scale visualization of reactive transport dynamics at elevated reservoir temperatures and pressures, and (ii) crystalline calcite embedded polymer microchannels that enable direct quantitative studies of reactive transport under simpler hydrodynamic conditions. We define mineral-functionalized microfluidics as those with the mineralogy, morphology, and surface properties representative

of the analogous real-rock system. That is, the calcite-functionalized micromodels developed here contain calcite grains in the pore space and are susceptible to reactive dissolution. The calcite functionalized etched silicon micromodel provides a direct approach to visualize reactive transport dynamics at elevated temperature and pressure conditions typical of subsurface systems that was previously not attainable, and the calcite-embedded microchannel supplements the study by providing insight to the fundamental dynamics dictating reactive transport.

6.2.1 Biogenic calcite-functionalization of 2D porous medium

Current state-of-the-art etched silicon micromodels capture two-dimensional pore geometry accurately [79, 76, 80] to enable direct pore-scale visualization of fluid dynamics at elevated reservoir temperatures and pressures in rigid, non-reactive geological systems. Surface chemistry and reactive alteration of the pore structure, however, are not replicated. These properties underlie transport through carbonate porous media. The micromodels used in this work replicate pore-geometries from thin-section images of real rock in order to capture realistic pore-geometry and pore-size distribution. Detailed design and fabrication methods are described in Buchgraber et al., 2012 [79, 75, 188] and are not the focus of this work. This section, instead, describes the novel method by which etched silicon micromodels are functionalized with calcite grains using bacteria.

Biogenic calcite-functionalization of the two-dimensional porous-media micromodels used the bacterium *Sporosarcina pasteurii* [189]. The bacterium *S. pasteurii* was chosen due to its well-documented ability to enable calcite precipitation and growth on solid surfaces [190, 189, 191, 192, 193]. That is, the calcite grains grown using this bacterial method are attached securely to the solid surfaces of the micromodel pore-space. The bacteria were cultivated in brain-heart infusion growth media prior

to delivery into the 2D silicon porous medium. The bacterial growth media was prepared by mixing 47 g of brain heart infusion into 900 mL of deionized (DI) water. The well-mixed solution was sterilized for 15 minutes at 121 °C in an autoclave. The sterilized solution was cooled to $\sim$ 30 °C and a concentrated urea solution was added to make a 2 wt% urea broth. The urea solution was prepared by mixing 20 g of urea into 100 mL of DI water and was added to the broth by injecting the solution through a 0.2 μm filter. The bacteria were added to the growth medium to incubate to create the bacteria-broth injection solution.

The 2D silicon porous medium (micromodel) was initially saturated with DI water at atmospheric conditions to ensure an even deposition of bacteria. Microbial deposition within the pore spaces of the micromodel was achieved by injecting the bacteria-broth solution into the system. The bacteria-permeated micromodel was submerged in bacteria-free growth media for 24 h to encourage in situ growth of the bacteria and to encourage adherence of the bacteria on the micromodel surface.

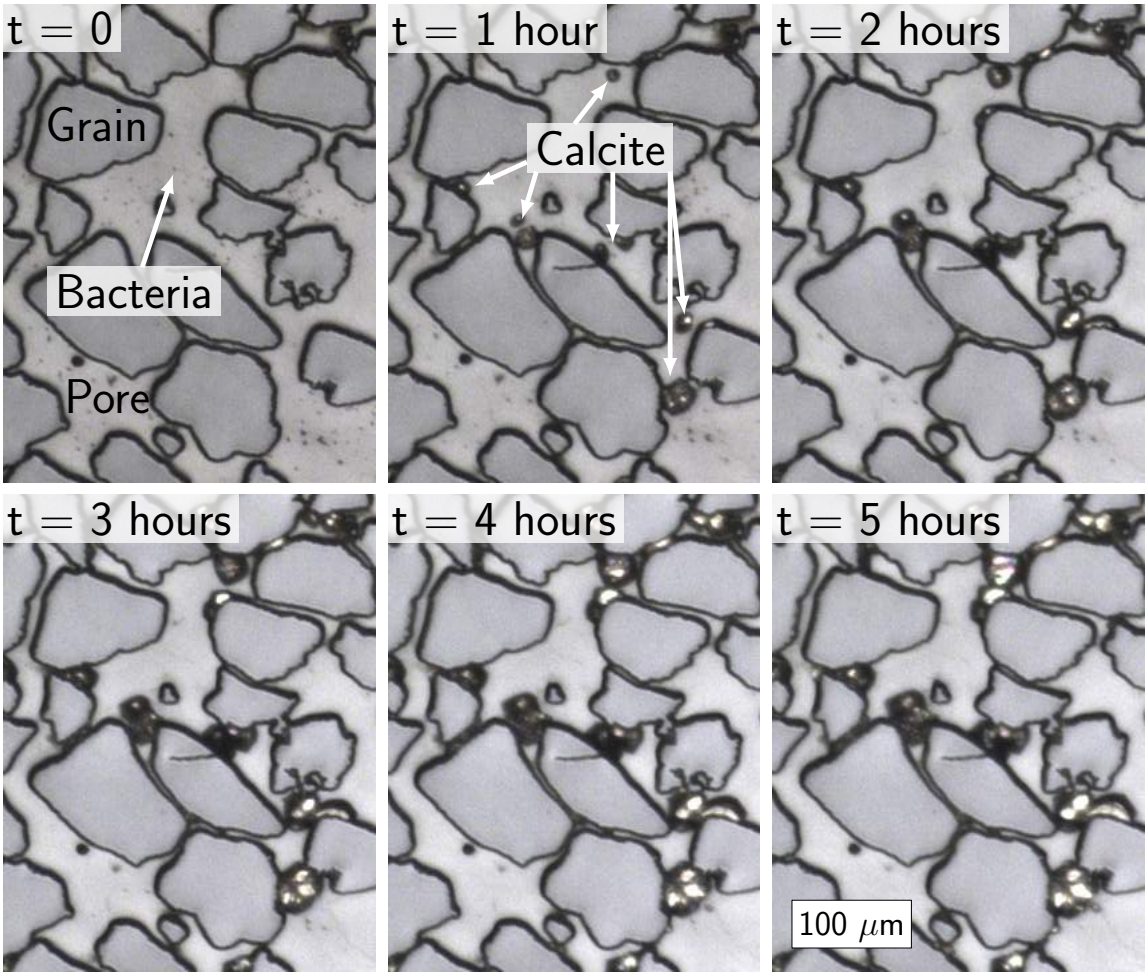

Figure 6.1: *In situ* growth of calcium carbonate (calcite) crystals within the micromodel pore space. *Sporosarcina pasteurii* bacteria were deposited into the micromodel and in situ microbial growth was encouraged by injection of the brain heart growth media (t = 0). Calcite precipitation was induced with the injection of the urea/$CaCl_2$ cementation solution (t $\geq$ 1 hour). Calcite grains were grown securely on the pore surfaces throughout the micromodel after $\sim$ 3 hours. Calcite grains appear white due to their natural refractive tendencies without digital image enhancement.

A cementation solution was injected into the bacteria-activated micromodel to induce calcite ($CaCO_{3(s)}$) precipitation. Specifically, the cementation solution was prepared by mixing 1 M urea (urea, U5378, Sigma) and 1 M calcium chloride (calcium chloride dehydrate, 31306, Sigma-Aldrich) in DI water. The cementation solution was

injected into the bacteria-activated micromodel at a constant injection velocity of 10 m/day for 20 hours (Quizix QX pump). Calcite crystal growth was monitored using a microscope (Nikon SMZ 1500) and DSLR camera (Nikon D7100). In situ growth of calcite crystals initiated after $\sim$ 3 hours of the cementation process (Fig. 6.1). All biogenic calcification was conducted at constant injection rate conditions and flow outlets were open to atmosphere.

6.2.2 Reactive transport in 2D porous media micromodel

Pore-scale reactive transport in carbonate media was visualized using the biogenically calcite-functionalized micromodels. High temperature, high-pressure experiments corresponding to subsurface conditions (i.e., supercritical CO_2 conditions) were conducted. High pressure fluid delivery to the micromodel was enabled using an aluminum manifold and nanoports (Upchurch/IDEX). Two high-pressure pumps (Quizix QX) supplied the pressurized acidic injectant fluids at a constant rate and maintained the outlet of the micromodel at a constant pressure (Fig. 6.2). Specifically, CO_2 was added to an accumulator (Swagelok 304L-HDF4-300) filled with 200 mL of acidic fluid (0.5, 1, and 2 wt% HCl) at 8.27 MPa to ensure that the injection acid was fully saturated with $CO_{2(aq)}$. The acid was equilibrated with pressurized CO_2 overnight to ensure CO_2 saturation in the aqueous phase. Backpressure was maintained at 8.27 MPa with DI water. The pressurized micromodel was submerged in a heated water bath maintained at 35 °C to ensure that the separate CO_2 phase was supercritical to model reservoir conditions. Hot water was circulated to the water bath using an external heated bath (Digital Plus Thermo Scientific NESLAB RTE17). Flow and dissolution dynamics were visualized using a microscope (Nikon SMZ 1500) and DSLR camera (Nikon D7100).

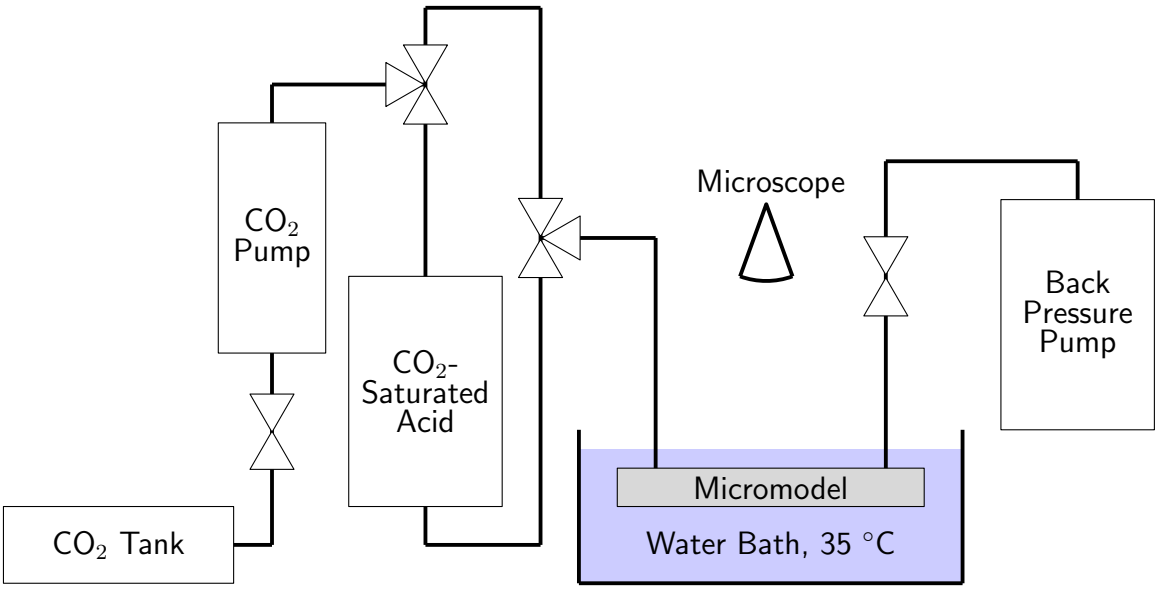

Figure 6.2: Experimental setup for high temperature, high-pressure microvisualization of reactive transport in 2D calcite micromodel. The micromodel is submerged in a heated water bath and two high pressure pumps are used to deliver injection fluids and maintain system pressure. The CO_2 pump was used to reach reservoir pressures and deliver the CO_2-saturated acid to the calcite micromodel. The backpressure (BP) pump was filled with DI water to maintain system pressure at 8.27 MPa.

6.2.3 Calcite-embedded polymer microchannel

Single-channel polymer microfluidics facilitated systematic investigation of the parametric influence of injection acid concentration, flow rate, and solubility on reactive transport in carbonate formations. A single octagonal calcite post embedded in a soft, nonreactive PDMS polymer channel enabled controlled experimental parameters, i.e., local advection and reaction rates (Fig. 6.3(b)). To fabricate the visualization platform, a silicon mold (rectangular ridge 37 mm in length, 1.5 mm in width, and 200 μm in depth) was first created using standard photolithography and deep reactive ion etching techniques, Fig. 6.3. Non-reactive polymer (10:1 PDMS, Silicone Elastomer, Sylgard) was mixed, degassed, and poured onto the silicon mold to cure and form the chemically inert microchannel. A slight modification of standard PDMS curing

procedures (70 minutes at 50 °C) was made such that the PDMS was under-cured to embed the calcite crystal securely. The under-cured PDMS channel was then peeled from the silicon mold and inlet and outlet ports were drilled to allow for flow. The PDMS was then cleaned with soap and DI water and placed on a clean glass plate. Trapped air bubbles between the PDMS and the glass plate lead to optical artefacts that impair visualization, and thus a good seal between the two materials is desired. A single octagonal calcite post (500 μm wide, 300 μm height) was then placed in the center of the channel. Note that the calcite post was taller than the channel walls to ensure (i) the calcite crystal was firmly embedded in the channel and (ii) the top and bottom surfaces of the octagonal calcite post were firmly sealed to the polymer to minimize any two-dimensional effects. Teflon tweezers were used to avoid damaging the crystal surface because scratches on the calcite surface create additional reaction sites and bubble nucleation sites that reduce the repeatability of the experiments. Lastly, a flat sheet of under-cured PDMS was placed on top of the calcite-embedded open channel and heated on a hot plate at 110 °C for 15 minutes to cure and bond completely.

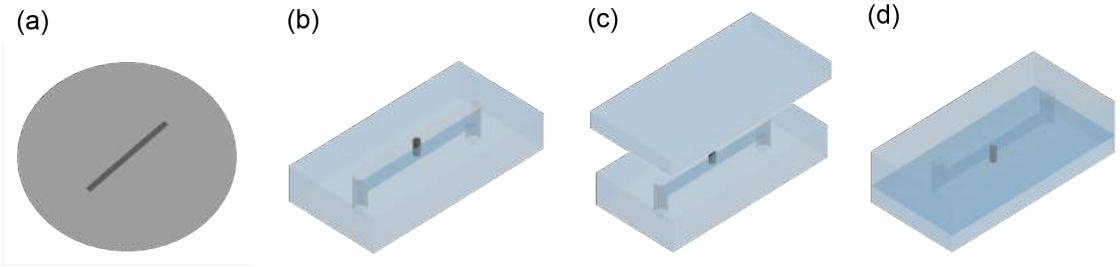

Figure 6.3: Fabrication technique for the single-crystal, single-channel polymer microfluidic platform. (a) A single rectangular ridge was molded onto a silicon wafer using standard photolithography and deep reactive ion etching techniques. (b) PDMS was poured onto the silicon mold and under-cured to ensure a secure seal between the embedded calcite crystal and the channel surface. (c) The calcite-embedded open channel was sealed with a second PDMS plate and heated until fully cured and bonded (d). The embedded calcite crystal was 500 μm wide and the channel was 1.5 mm x 200 μm in cross-section.

6.2.4 Reactive transport in 1D polymer micro-channel

Reactive transport parameters were studied systematically using the single-grain polymer-based microchannel platforms. Acid concentrations of 0.5, 1, and 2 wt% HCl injected at flow rates of 10, 50, and 100 m/day were tested. All experiments were conducted at ambient conditions and the outlet was open to atmosphere. The corresponding dimensionless quantities comparing rates of reaction, advection, and diffusion are listed in Table 6.1. The dimensional experimental parameters, while different from real geological systems, are nondimensionalized to correspond to realistic conditions regardless of scale. Specifically, the Peclet (Pe = advection/ diffusion), Damkohler (Da = reaction/ advection), and modified Stanton (St = solvation/ advection) numbers are extracted from the experiments (see detailed explanations in Results and Discussion). Acids were delivered using a syringe pump (Harvard Apparatus, Holliston, MA) and a 10 mL syringe (BD 10 mL syringe, 309604). Reactive transport dynamics were visualized using a microscope and camera setup (Leica Z16 APO).

Table 6.1: Dimensionless quantities corresponding to the experimental conditions used. The column labeled regime corresponds to the phase map in Fig. 6.9.

Pe	Da	St	PeDa	Regime
1.94	7.52	0.516	14.6	III
10.5	2.51	0.095	26.5	III
10.5	0.677	0.095	7.13	III
2.10	16.6	0.475	34.9	III
124.45	0.0750	2.50	9.33	I
12.45	0.0121	0.00478	0.150	II
62.23	0.0196	0.816	1.22	I
62.23	0.0310	1.08	1.93	I

6.3 Results and Discussion

New grain-engulfment mechanism during reactive transport

Dynamics at the reactive interface underlies reactive transport and CO_2 storage security fundamentally. Calcite-embedded microchannels were used to visualize directly the interface-scale transport dynamics. Importantly, direct interface-scale observations show a new fundamental mechanism, herein called the grain-engulfment mechanism, whereby the reaction product CO_2 forms a separate, protective phase around the calcite grain that prevents contact between the reactants (i.e., the acid and the dissolving carbonate grain, Fig. 6.4). Implications of the grain-engulfment effect extend past CO_2 storage and the subsurface; the protective effect is fundamental and of significance to reactive transport through porous media in general [182].

Recall that in this setup, a single reactive calcite grain is embedded within a non-reactive PDMS microchannel to control the reaction and advection rates delivered to the reaction interface (Fig. 6.4a). Dilute hydrochloric acid, a proxy to the CO_2-acidified brine that develops during CO_2 injection in underground aquifers, was injected into the microchannel to induce calcite dissolution. Downstream pressure was maintained at 1 atm. Whereas the pH of CO_2-acidified reservoir brine in geological storage systems is high (pH $\sim$ 3.4 - 4) [47], the low pH here (pH $\sim$ 0.26 - 0.86) provides a method to speed up dissolution kinetics in the laboratory. Despite the low pH and pressures here, we scale our experimental parameters such that they correspond to the dimensionless parameters that represent realistic geological CO_2 storage conditions. Importantly, considering the impurities such as Sulfur and Nitrogen oxides that are inevitably present in the injected CO_2 stream [108] due to economics, the pH of the reservoir is reduced to pH $\sim$ 1 [194, 195]. The experimental conditions that we impose are thus representative of industrial-scale geological CO_2 storage conditions.

The grain-engulfment mechanism that is observed here is of fundamental importance to the understanding and the prediction of reactive transport in the subsurface. The grain-engulfment mechanism is characterized by an initial constant rate of reaction (Fig. 6.4a, t = 0 to t = 393.08 s, Fig. 6.4b, steady dissolution) followed by a subsequent phase of zero grain dissolution (Fig. 6.4a, t = 393.40 s onwards, Fig. 6.4b, grain engulfment) due to the lack of a direct reaction interface (i.e., grain engulfment). Specifically, a separate CO_2 phase was generated and retained at the calcite grain surface (Fig. 6.4a). The retained separate CO_2 phase prevents reaction between the rock and the acid due to a lack of direct solid/ aqueous phase interface (Fig. 6.4a, t = 37.40 s to t = 695.00 s). The time resolution of the pore-level dynamics here is 0.04 s due high-resolution video recording capabilities at 25 frames per second.

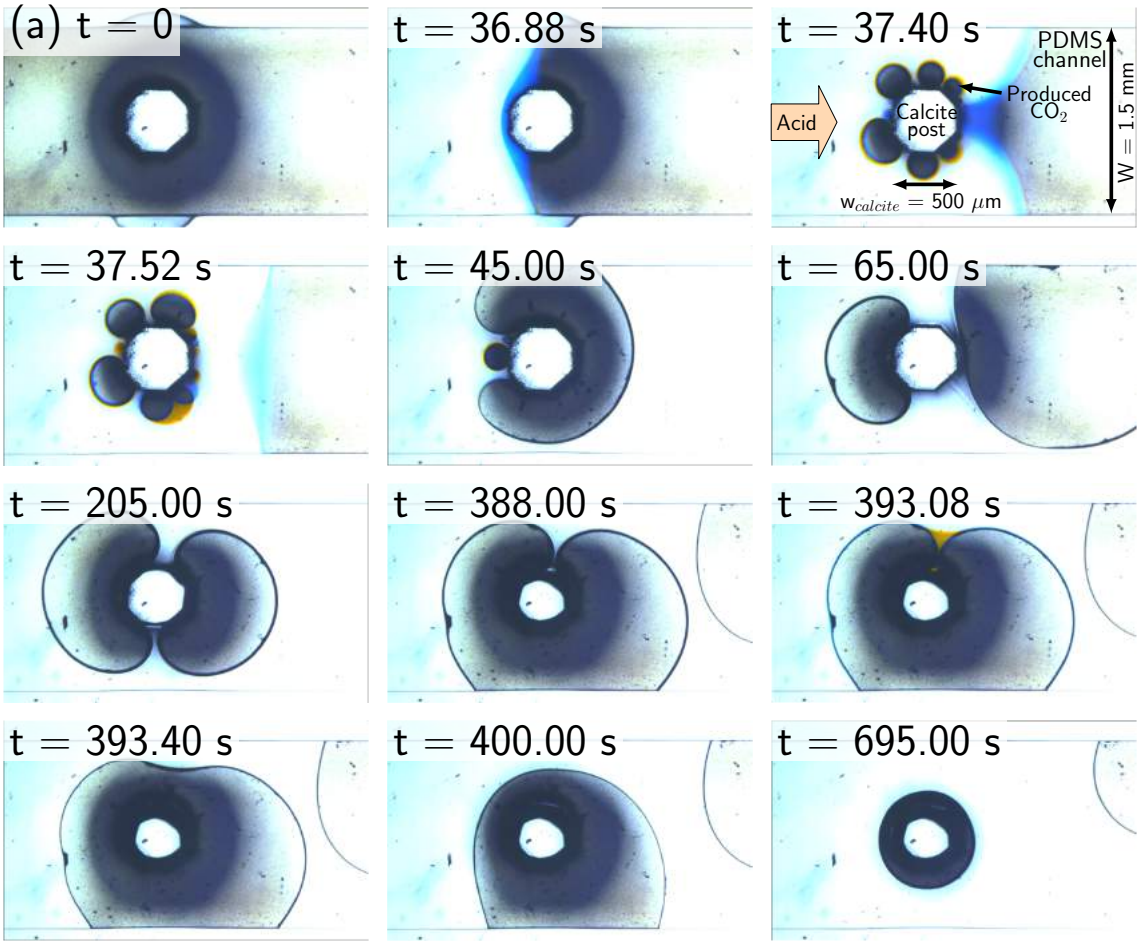
(a) t = 0
t = 36.88 s
t = 37.40 s
PDMS channel
Produced CO_2
Acid
Calcite post
$w_{calcite}$ = 500 μm
W = 1.5 mm
t = 37.52 s
t = 45.00 s
t = 65.00 s
t = 205.00 s
t = 388.00 s
t = 393.08 s
t = 393.40 s
t = 400.00 s
t = 695.00 s

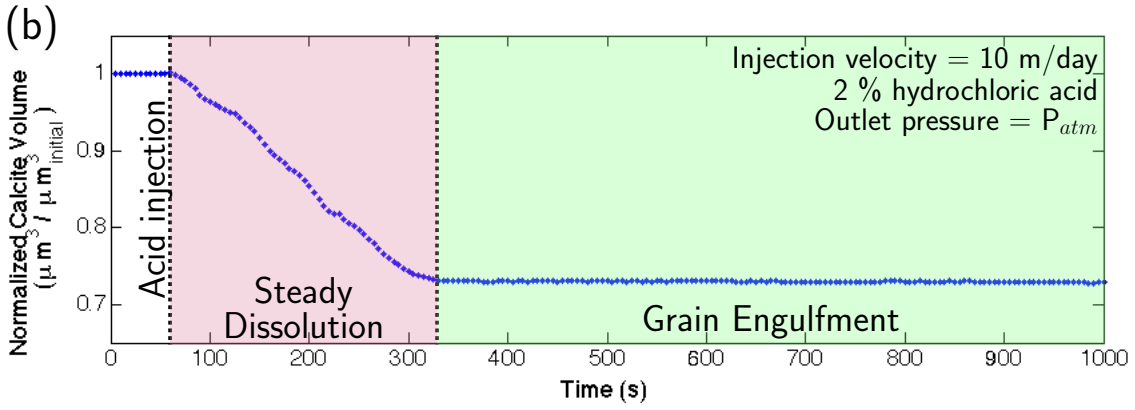
(b)
Injection velocity = 10 m/day
2 % hydrochloric acid
Outlet pressure = P_{atm}
Acid injection
Steady Dissolution
Grain Engulfment
Normalized Calcite Volume (μm^3 / $\mu m^3_{initial}$)
Time (s)
1
0.9
0.8
0.7
0
100
200
300
400
500
600
700
800
900
1000

Figure 6.4 *(previous page)*: Grain-engulfment phenomenon in single-grain polymer microchannels. (a) Time evolution of a single grain in an initially air-filled channel (t = 0). Acid is introduced (t = 36.88 s), and thereafter the reaction with the calcite grain is observed. Specifically, initial dissolution reaction (t = 37.40 s, 37.52 s) is rapid and produces small CO_2 bubbles due to exposed reaction sites introduced through the fabrication process. Expenditure of the active sites and coalescence of small bubbles result in large bubbles (t = 45.00 s). Large bubbles are advected downstream due to pressure buildup across its body (t = 65.00 s). Continued growth of the CO_2 bubbles around the calcite grain, however, is sustained (t = 205.00 s) and its coalescence leads to partial engulfment (t = 388.00 s, 393.08 s) that results in asymmetric grain dissolution. Occurrence of the grain-engulfment event (t = 393.40 s) due to bubble collapse around the calcite grain isolates the grain from further reaction, and subsequent dissolution is halted (t = 400.00 s, t = 695.00 s) until the separate CO_2 phase is diffused into the aqueous phase. (b) Calcite grain volume decreases linearly over time prior to complete grain-engulfment and remains constant thereafter until all of the engulfing CO_2 is solubilized into the aqueous phase (not shown).

Simple flow geometries sustain bubble retention and growth around the calcite grain and result in complete calcite grain-engulfment (Fig. 6.4a, t = 393.40 s). Quantitative analysis showed constant overall dissolution rates prior to complete engulfment and no dissolution afterwards (Fig. 6.4b). Calcite grain dissolution resumed once the engulfing separate CO_2 phase was completely solubilized into the aqueous phase and fresh reaction interfaces were exposed; the grain-engulfment/ CO_2-solvation cycle continued until all of the local calcite dissolved. This stepwise dissolution phenomenon due to separate CO_2 phase grain-engulfment delays local dissolution and preserves the acid for downstream reactions. Prior to full grain-engulfment, partial grain-envelopment did not drastically alter the rate of overall grain dissolution. Local dissolution, however, was halted in regions occupied by the CO_2-phase due to the lack of a direct reaction interface and was expedited in regions where grains were exposed to acidic solution. Reactive transport around semi-engulfed grains thereby resulted in asymmetric grain dissolution. We interpret this as characteristic of a

transport-limited process.

The importance of the separate CO_2 phase on reactive transport is explained by comparing dominant forces about evolved CO_2 bubbles. For typical subsurface flows, the retaining surface tension force, $F_{IFT} = \gamma 2\pi r \cos\theta \sim O(10^{-8}N)$, is approximately three orders of magnitude greater than the inertial viscous drag force, $F_d = 6\pi\mu Ru \sim O(10^{-11}N)$. We use values for interfacial tension $\gamma \sim 34$ mN/m, [196] bubble radius $r \sim 1$ μm, viscosity $\mu \sim 0.7$ mPa·s, and a pore velocity $u \sim 1$ to 50 m/day, typical of subsurface flows. Contact angle contributions ($\cos\theta$) to the retaining force are order one and therefore have little influence on the mobility of the CO_2 bubble away from the reaction interface. Dominance of surface tension, importantly, retains the separate CO_2 phase in the pore space and enables grain-engulfment.

6.3.1 Significance of separate CO_2 phase at pore- and ensemble-scales

The grain-engulfment effect holds in porous configurations regardless of pressure so long as a separate CO_2 phase is present. Grain-engulfment implications at pore- and pore-network-ensemble-scale on reactive transport through porous media were investigated using the chemically- and geometrically-representative biogenic calcite-functionalized micromodels developed in this work. SEM-Energy dispersive X-ray spectroscopy (EDS) and X-ray crystallography (XRD) characterization of the calcite grains resulting from biogenic functionalization show comparable composition and crystallography, respectively, to natural calcite crystals [192, 190, 193]. The ensemble-scale is defined here to be a set of pores on the order of the representative elementary volume of the porous medium. In the following, pressures and temperatures corresponding to gaseous and supercritical CO_2 were imposed to investigate grain-engulfment and separate CO_2 phase evolution at the pore- and ensemble-scales

under ambient (Fig. 6.5) and at reservoir conditions close to (Fig. 6.7) and far from (Fig. 6.6) the well.

We find that gas-phase CO_2 evolves rapidly at low-pressures (Fig. 6.5) and supercritical-phase CO_2 develops at later times at storage reservoir pressures (Fig. 6.7) due to increased CO_2 solubility in water. At reservoir conditions, ensemble-scale dissolution rates remain constant and pore-scale dissolution is dictated by grain-engulfment (Fig. 6.7), consistent with low-pressure observations. Specifically, exposed grains dissolve at a constant rate, whereas engulfed grains experience no dissolution (Fig. 6.7), hence, capillary trapping of the separate CO_2 phase determines the spatial allocation of grain dissolution in porous media. Pore-body grain dissolution dominates over pore-throat grain dissolution (Fig. 6.7) due to exposure to non-wetting acid phase in pore bodies and separate CO_2 phase residence in pore throats. Pore- and ensemble-scale grain-engulfment therefore dictates reactive transport through porous media at atmospheric and subsurface reservoir conditions due to separate CO_2 phase formation.

6.3.2 Pore-Scale Grain-Engulfment at Ambient Conditions

Similar to the single grain micro-channel study, micromodel experiments show that grain-engulfment dictates the structural deterioration of the calcite porous medium due to CO_2 phase-evolution. Separate CO_2 phase produced and retained on calcite surfaces (Fig. 6.5a,b) insulated calcite grains from acidic constituents and thereby inhibited local dissolution. Following separate CO_2 phase evolution in the pore space, grains exposed to acid continued to dissolve rapidly (Fig. 6.5, b, square-hatched region, and c) whereas grains bounded by CO_2-wetted surfaces did not dissolve at all (Fig. 6.5, b, diagonal-hatched region, and c).

Interestingly, an episodic CO_2 bubble-induced flow distortion mechanism was observed that dissolved CO_2-engulfed calcite grains adjacent to water-wet surfaces.

Specifically, continuous aqueous phase flow is initially distorted by reaction-induced CO_2 bubble formation. The nucleated bubble is initially immmobile because the differential pressure drop across its short length is insufficient to overcome capillary forces. Upon growth to its critical mobilization length, the bubble advects downstream and aqueous acid refills the pore space. Pore pressure-instabilities in the continuous acid phase disperse protective CO_2 bubbles away from water-wet silicon surfaces momentarily and introduce acid to the previously protected calcite surface. Protective CO_2 bubbles resume their original configuration following pore-pressure re-equilibration and thus create small acid pockets for reaction. Calcite grains adjacent to acid pockets dissolve locally until complete acid consumption. Our porous media experiments show that grain-engulfment reduces the local rate of calcite dissolution and prolongs the spatial distribution of acidic constituents through flow diversion.

6.3.3 Pore-Scale Grain-Engulfment at Reservoir Conditions

Subsurface systems are characterized by elevated temperatures and elevated pressures (e.g., P $\gtrsim$ 1000 psi). Two important fluid properties impact the significance of the grain-engulfment effect under extreme reservoir conditions. First, CO_2 enters its supercritical phase at high temperature and pressure conditions. Supercritical CO_2 density (567 kg/m^3 at 35 °C and 1200 psi) is much higher than gaseous CO_2 density at ambient conditions (1.8 kg/m^3 at 25 ° and 14.7 psi). Increased separate CO_2 phase density reduces the local CO_2 volume fraction, i.e., saturation, as CO_2 is produced due to calcite grain dissolution. Recall that the local saturation of the separate CO_2 phase determines the extent to which the grain surfaces are protected from the encroaching acidic brine.

Second, the solubility of CO_2 into the aqueous phase varies with pressure and temperature. Importantly, CO_2 solubility increases drastically with increasing pressure and decreases with temperature. Solubility of CO_2 into the aqueous phase determines

the formation of a separate CO_2 phase: increased separate CO_2 phase formation is due to decreased solubility, whereas increased solubility results in decreased formation of a separate, protective CO_2 phase. Here, we focus on elevated pressure systems due to its minimizing impact on the grain-engulfment effect in reservoirs.

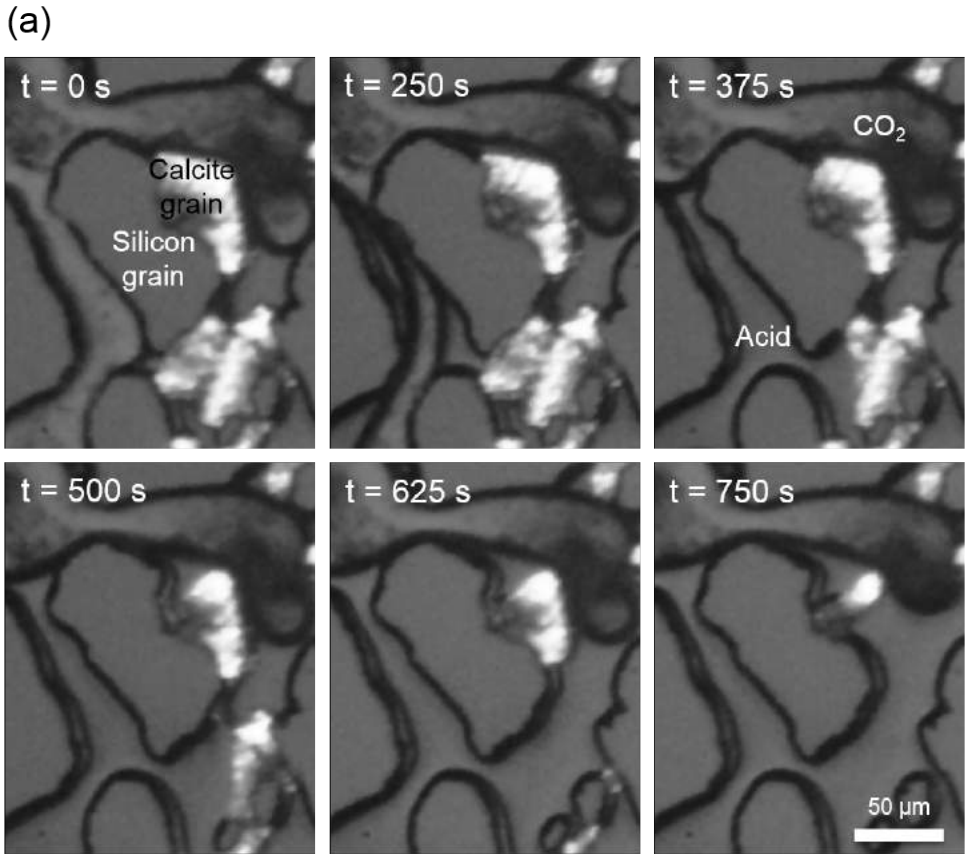
(a)
t = 0 s
Calcite grain
Silicon grain
t = 250 s
t = 375 s
CO_2
Acid
t = 500 s
t = 625 s
t = 750 s
50 µm

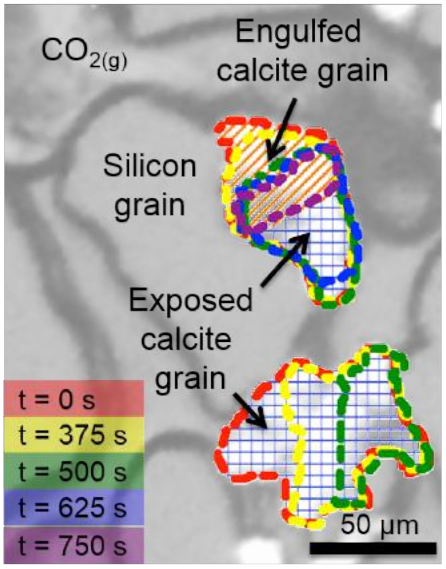
(b)
$CO_{2(g)}$
Engulfed calcite grain
Silicon grain
Exposed calcite grain
t = 0 s
t = 375 s
t = 500 s
t = 625 s
t = 750 s
50 µm

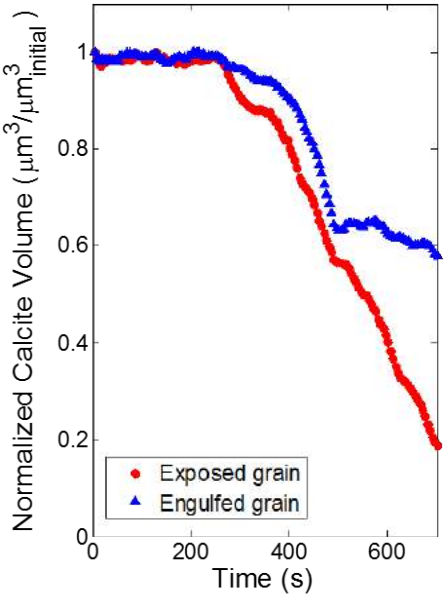
(c)
Normalized Calcite Volume ($\mu m^3/\mu m^3_{initial}$)
1
0.8
0.6
0.4
0.2
0
0
200
400
600
Time (s)
Exposed grain
Engulfed grain

Figure 6.5 *(previous page)*: Grain-engulfment due to separate CO_2-phase formation in a calcite-silicon micromodel. a, Grain-engulfment dominates the top calcite grain that is shielded by the separate CO_2 phase and rapid, dissolution rates dictate dissolution of the bottom acid-exposed calcite grain. b, Time-evolution of calcite grain boundaries. Regions protected by CO_2 (diagonally-hatched) experience little dissolution and regions exposed to acid (square-hatched) dissolve rapidly. c, Size of exposed (red) and engulfed (blue) calcite grains show rapid, constant rate of carbonate dissolution for single-phase regions and minimal dissolution for CO_2-wetted surfaces.

6.3.4 Pore-Scale Grain-Engulfment at Reservoir Conditions of Slow Reaction relative to CO_2 Solvation.

Far away from the well, reservoir fluids are unaltered and in their initial geological state (i.e., not perturbed and/or saturated with CO_2). The capacity for CO_2 solvation into the aqueous phase is, as a result, large. Injection of 2 wt% HCl that is not saturated with CO_2 into the pore space shows rapid dissolution of the carbonate matrix without production of a separate, protective CO_2 phase (Fig. 6.6).

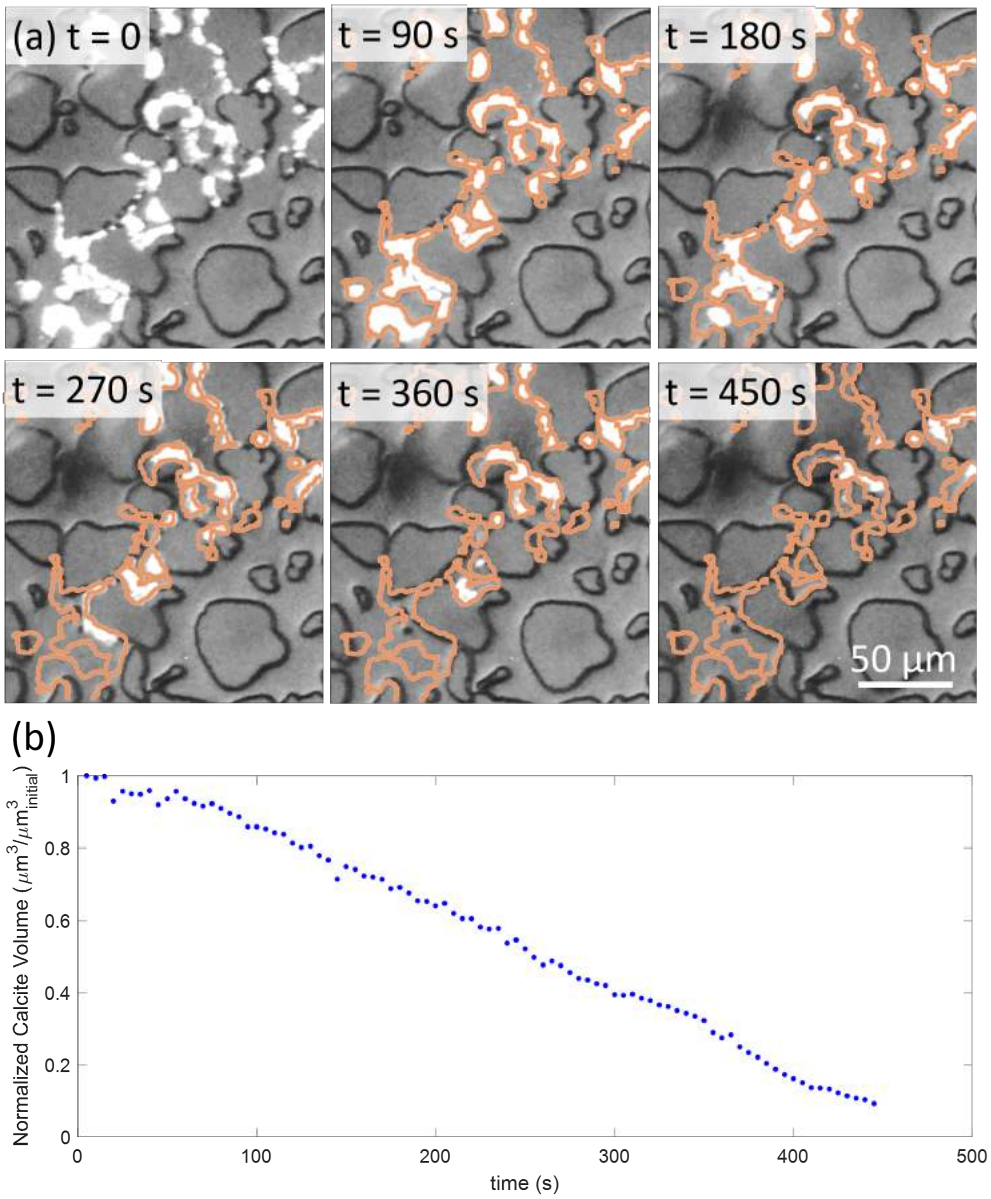

Figure 6.6: Extent of the grain-engulfment effect is minimized at conditions of slow reaction rate relative to solubilization of CO_2 in the aqueous phase. (a) A separate, protective CO_2 phase is not developed due to high solubility of CO_2 into the aqueous phase at elevated pressures. Calcite dissolution (original grain outlines are traced for comparison) is rapid. (b) Calcite was dissolved at a constant and rapid rate due to the lack of a separate, protective CO_2 phase.

6.3.5 Pore-Scale Grain-Engulfment at Reservoir Conditions of Fast Reaction relative to CO_2 Solvation

In the vicinity of the CO_2 front, reservoir brine is displaced by and in contact with the injected CO_2. Local exposure and mixing enables equilibration between CO_2 and the aqueous brine, and, as a result, for CO_2 to saturate the aqueous phase. Under pre-equilibrated situations where the aqueous phase is saturated with CO_2, additional CO_2 that is released due to the calcite dissolution reaction is forced to develop into a separate, protective phase, as was observed under ambient conditions. Specifically, we inject CO_2-saturated acid and impose pressures (1200 psi) and temperatures (35 °C) that correspond to supercritical CO_2 to investigate grain-engulfment and separate CO_2 phase evolution at reservoir locations close to the well. We find that a separate, protective supercritical CO_2 phase develops at storage reservoir pressures (Fig. 6.7), similar to the gas-phase CO_2 that evolved rapidly at low-pressures (Fig. 6.5).

At near-wellbore reservoir conditions, ensemble-scale dissolution rates remain constant and pore-scale dissolution is dictated by grain-engulfment (Fig. 6.7), consistent with low-pressure observations. Specifically, exposed grains dissolve at a constant rate, whereas engulfed grains experience no dissolution (Fig. 6.7), hence, capillary trapping of the separate CO_2 phase determines the spatial allocation of grain dissolution in porous media. Interestingly, pore-body grain dissolution dominates over pore-throat grain dissolution (Fig. 6.7) due to exposure to non-wetting acid phase in pore bodies and separate CO_2 phase residence in pore throats. An approximately constant rate of dissolution is observed at the Darcy-scale as a result of the combined effects in protected and exposed pores. The total rate, while constant ($\sim$ 5 % total dissolution over 1500 s at the Darcy scale in Fig. 6.7c, blue), is less than would be expected if the system had remained single phase ($\sim$ 95 % total dissolution over 450 s at the Darcy scale in Fig. 6.6). Pore-scale effects that determine dissolution

patterns, however, are masked. Pore- and ensemble-scale grain-engulfment therefore dictates reactive transport through porous media at atmospheric and subsurface reservoir conditions due to separate CO_2 phase formation.

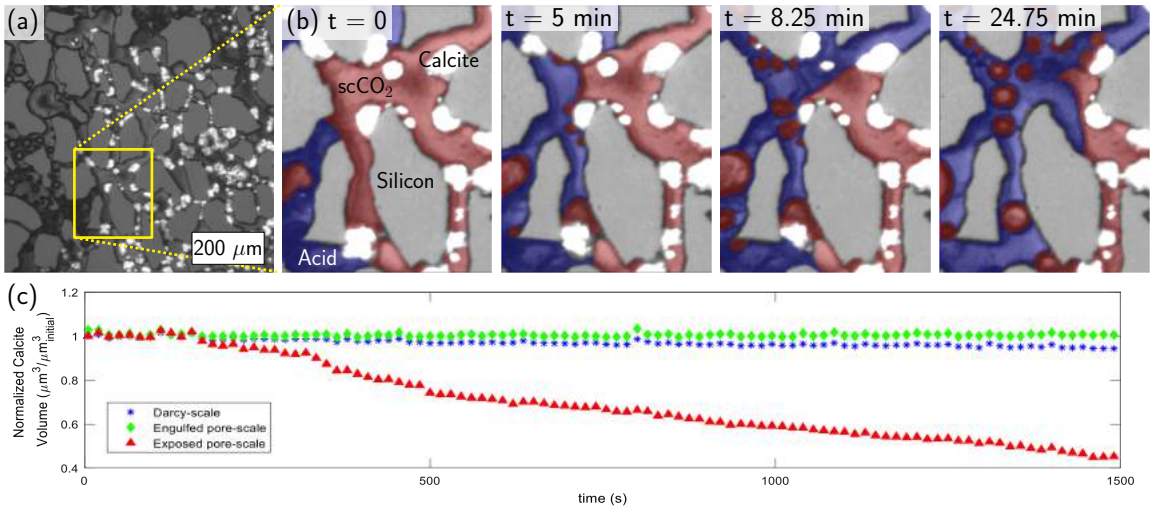

Figure 6.7: Grain-engulfment dictating calcite dissolution at pore- and pore-ensemble scales close to the well under geological conditions. (a) Ensemble-scale carbonate dissolution and separate supercritical CO_2 phase formation at storage reservoir conditions. CO_2-saturated 2 wt.% HCl acid is injected at 5 m/day, 8.27 MPa, and 35 °C and long dissolution paths (i.e., wormholes) are observed macroscopically. (b) Pore-level calcite grain-engulfment due to separate $scCO_2$ phase. Pore-throat grains engulfed by the separate CO_2 phase are isolated from acid and experience no dissolution whereas exposed pore-body grains dissolve rapidly. Initially at t = 0, the pore displayed is saturated with $scCO_2$ and CO_2-saturated acid is injected from left to right. Pressure fluctuations with flow induce CO_2-bubble snap-off in the small, water-wet pores and expose the calcite grain to acid (t = 5 min). $scCO_2$ bubbles are produced and wet the grain, leading to grain-engulfment (t = 5 min, t = 8.25 min). Local rates of dissolution are retarded due to calcite grain-engulfment by the $scCO_2$ (t = 24.75 min). (c) Comparison of ensemble- and pore-scale calcite dissolution. Ensemble-scale calcite dissolution occurs at a constant rate whereas pore-scale dissolution is dictated by local conditions (exposed vs engulfed).

6.3.6 The Grain-Engulfment Mechanism

Grain-engulfment underlies dissolution in pores and pore-ensembles (Fig. 6.8), much like in the hydrodynamically simple 1D geometry (Fig. 6.4). At the ensemble-scale, acidic fluid bypasses the CO_2-protected calcite grains and instead diverts to fresh, water-saturated calcite pores downstream that are susceptible to direct reaction (Fig. 6.8). Preferential flow paths were observed that span the entire micromodel. This is a macroscopic observation collected by imaging the whole micromodel (i.e., not pore-scale). Grain-engulfment restricts preferential flow path enlargement in the direction normal to flow and the resulting acid flow diversion promotes lengthwise preferential flow path extension. These model-scale observations are in consensus with core-scale experiments [197]. On the ensemble-scale, grain-engulfment protects initial conduits from further dissolution and leads to long and narrow preferential flow path development.

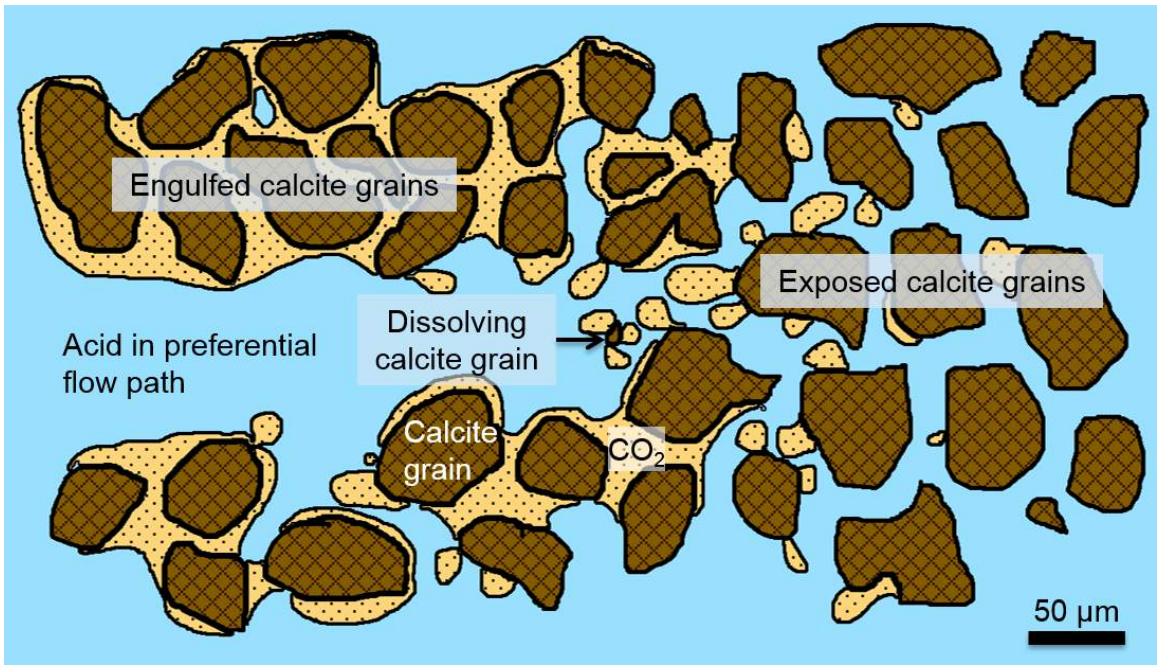

Figure 6.8: Ensemble-scale preferential flow path propagation due to separate CO_2 phase grain-engulfment and acid diversion.

6.3.7 Phase Map of Reactive Transport and of Grain Engulfment

The results of this chapter provide direct observations at the interface-, pore-, and pore-ensemble-scales to delineate the underlying grain-engulfment mechanism in reactive transport through carbonate systems. Importantly, we uncover the interplay between transport, reaction, and phase-evolution during the dissolution of a reactive porous matrix through experiments at conditions corresponding to ambient, near-well, and far-from-well locations. Geological CO_2 storage security implications due to the grain-engulfment mechanism requires up-scaled understanding of reactive transport in storage formations. Dimensionless quantities enable upscaling from the pore-scale, laboratory conditions to reservoir scales and conditions. Scaling parameters of transport, reaction, and CO_2 solvation into the aqueous phase were mapped systematically using the calcite-embedded polymer microchannel (see Table 6.1 for experimental conditions). The simple geometry here provides a means of systematic study while eliminating extraneous complexities associated with the hydrodynamics of porous media. Direct interface-scale observations show three distinct carbonate dissolution regimes (Fig. 6.9): constant slow dissolution with CO_2 dissolved in the aqueous phase at small acid fluxes (regime I), separate CO_2 phase generation at intermediate conditions (regime II), and stepwise, rapid dissolution with separate CO_2 phase grain-engulfment at large acid fluxes (regime III).

In regime I (see also Fig. 6.6), small acid flux to the reaction interface results in slow rock dissolution and hence slow CO_2 generation. CO_2 solubility at these conditions exceeds the rate of CO_2 generation and rate of CO_2 advection away from the interface, resulting in immediate CO_2 solvation into the aqueous phase. No separate CO_2 phase was observed as a result. Grain dissolution rates observed in regime I are

determined by acid flux to the reaction interface in agreement with single-phase reactive transport theory. This regime corresponds to the far-from-well reservoir condition study in the calcite-functionalized micromodel.

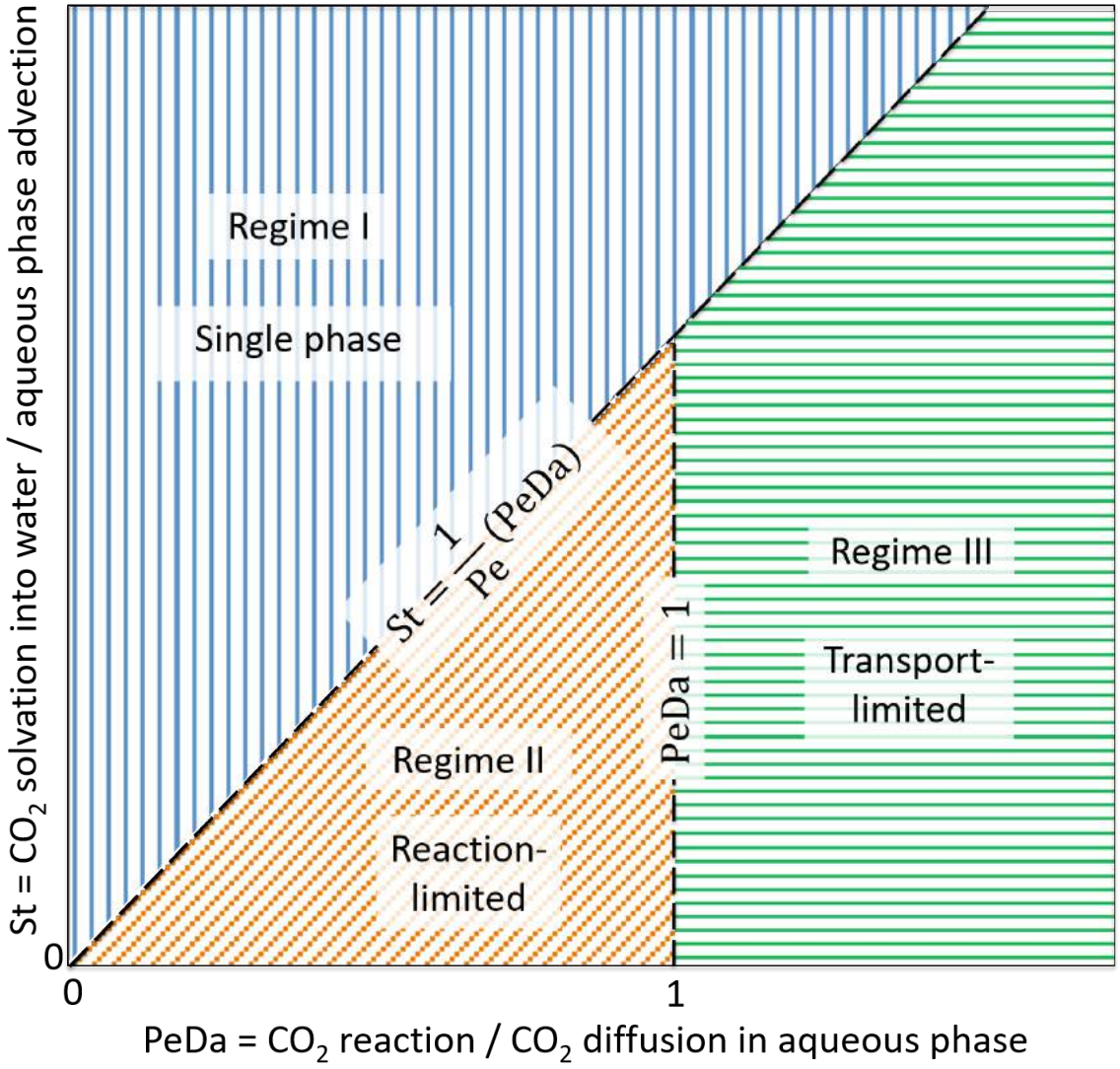

Figure 6.9: Phase map of grain-engulfment regimes. The grain-engulfment effect is significant in regime III (green horizontal hatching) where reactive CO_2 production rates exceed solvation rates of CO_2 into the aqueous phase (St $<$ Da) and where transport-limited conditions dominate (PeDa > 1). At the Darcy scale, wormholing occurs in regime III where the dissolution process is transport limited. Wormholing is a macroscopic observation. The reaction product CO_2 is diffused into the aqueous phase directly in regime I (blue vertical hatching). A separate CO_2 phase also forms in regime II (orange diagonal hatching). Reaction limited conditions encourage relatively uniform growth of the CO_2 phase.

Regimes II and III (see also Figs. 6.4, 6.5, and 6.7), by contrast, are characterized by rates of reactive CO_2 generation that far exceed the rate of CO_2 solvation into the aqueous phase and rate of CO_2 advection away from the reaction interface. Importantly, under these conditions, a separate CO_2 phase evolves. Regime II is distinguished by transport rates that exceed the rate at which CO_2 is produced from the reaction. This reaction-limited process generated separate CO_2 phase slowly. Constant calcite dissolution rates were observed in regime II, similar to regime I.

Regime III, however, is transport-limited and is governed by grain-engulfment. We describe the separate CO_2 phase evolution using (i) the Peclet-Damkohler number, PeDa, to compare the rate of CO_2 generation due to reaction with the rate of CO_2 diffusion in the aqueous phase, and (ii) the modified Stanton number, St, to compare the rate of CO_2 solvation into the aqueous phase to the rate of aqueous phase advection. We determine the necessary conditions for separate, protective CO_2 phase evolution as (i) St $<$ Da in order to achieve a separate CO_2 phase (i.e., rate of CO_2 solvation into the aqueous phase is less than the rate of CO_2 production due to reaction), and (ii) PeDa > 1 in order to achieve transport-limited conditions[178] to retain the separate CO_2 phase around the calcite grain (Fig. 5). The pore-scale studies at near-well reservoir conditions reside in regime III.

While it is true that full physics simulation of reactive transport is required to predict the security of a given geological CO_2 storage site, consideration of the local conditions delineated by the phase diagram (Fig. 6.9) provides a first-order understanding of the storage system. Here we demonstrate using direct, experimental observation and dimensionless scaling that the grain-engulfment effect is expected to extend into the reservoir. Specifically, the regimes delineated through experiments at the interface scale (Fig. 6.8) are applicable at reservoir conditions by mapping the dimensionless quantities Pe, Da, and St using pore-scale values of interstitial velocity, $V_{pore} = f(\phi, S)$, corrected for mutliphase flow from large-scale (i.e., Darcy-

and reservoir-scale) systems (e.g., porosity, ϕ, and saturation, S). Previous visualization in three dimensional core-samples provide more realistic geometric perspectives but is limited by spatiotemporal resolution. The question of additional geometric dimensions is addressed here through the upscaling from a 1D microchannel to a 2D porous network. Specifically, care was taken to increase the pore-connectivity of the 2D micromodel such that it is representative of a 3D core sample without forfeiting real-time pore-level visualization capability [80, 79].

6.3.8 Up-scaled separate CO_2 phase and reservoir implications

Implications of the protective separate CO_2 phase on subsurface storage security require up-scaled understanding of reactive transport in storage formations. We model the evolution of separate $scCO_2$ phase during reactive-advective transport of acids through a calcite storage reservoir with a simple reactive transport reservoir simulation. Specifically, coupled advection-diffusion-reaction equations were developed to delineate the impact of CO_2 phase-evolvement on reactive transport at the reservoir scale. For simplicity, steady state, single-phase mass conservation of water, $\nabla \cdot u = 0$, and the constitutive equation for velocity, $u = -(k/\mu)\nabla P$, were used to determine the pressure field, P:

$$\nabla \cdot (-\frac{k}{\mu}\nabla P) = 0 \tag{6.1}$$

The single-phase assumption is valid prior to separate phase CO_2 evolvement and is approximately valid following separate phase CO_2 evolvement, if it occurs, due to the immobility of the separate phase CO_2. Water viscosity is assumed constant across the reservoir and permeability, k, is determined using the Carman-Kozeny relation assuming spherical grains:

$$k = \frac{1}{72}\frac{\phi^3 D_p^2}{(1-\phi)^2} \tag{6.2}$$

An initial porosity field was generated for the reservoir with porosities randomly distributed between $0.1 < \phi < 0.3$. Tortuosity, τ, is generally between 2 to 5 for carbonate reservoirs and is chosen to be $\tau = 3$. Spherical grains with grain diameter, D_p, are assumed for simplicity. Mass fluxes were then calculated for each grid interface based on the pressure solution.

Mass balance for the acid proton H^+ was solved to determine reaction-induced porosity change over time. Transport limited reaction kinetics were assumed, consistent with hydrochloric acid dissolution of calcite. The mass balance for H^+ was written as:

$$\frac{\partial c_{H^+}}{\partial t} = -\nabla \cdot (u c_{H^+}) - \frac{\dot{Q}^{rxn}_{H^+}}{V_b} \tag{6.3}$$

where V_b is the bulk volume and the reaction rate $\dot{Q}^{rxn}_{H^+} = 2k_c c_{H^+} SA$ is in mole/s. The reaction rate constant is $k_c = 8.4 \times 10^{-5}$ m/s and the reaction surface area is $SA = V_{CaCO_3} a_v$. The shape factor, a_v, for spherical grains is $a_v = 6/D_p$ and the solid volume is $V_{CaCO_3} = (1-\phi)V_b$. For 2 wt% HCl, the concentration of the injection acid is $c_{H^+} = 550$ mol/m^3.

Dissolution was coupled with flow to find the time evolution of porosity. Specifically, the volume of calcite dissolved $V_{CaCO_3 dissolved} = 0.5\dot{Q}_{rxn,H^+} dt \frac{100.0869g}{mol} \frac{m^3}{2.71 \times 10^6 g}$ was used to update porosity after each time step:

$$\phi_{new} = \phi_{old} + \frac{V_{CaCO_3 dissolved}}{V_b} \tag{6.4}$$

The new grain diameter $D_{p,new}$ was determined using $\frac{4}{3}\pi \left(\frac{D_{p,new}}{2}\right)^3 N_{grains} = (1-\phi)V_b$, assuming uniform dissolution in a given grid block. The new grain size information was fed back into the Carman-Kozeny relation to find the corresponding permeability field to calculate the new flow and CO_2 concentration field.

The concentration of CO_2 in the reservoir was determined by the advection-reaction reaction:

$$\frac{\partial c_{CO_2}}{\partial t} = -\nabla \cdot (u c_{CO_2}) + \frac{\dot{Q}_{production,CO_2}}{V_b} \tag{6.5}$$

where the rate of CO_2 production $\dot{Q}_{production,CO_2}$ is half the rate of $\dot{Q}_{rxn,H^+}$ due to stoichiometry. The local CO_2 concentration is compared to the solubility of CO_2 in water at the local pressure condition, w_{CO_2}, and a separate CO_2 phase is deemed present if $c_{CO_2,new} > w_{CO_2}$.

Using this scheme, time evolution of the separate CO_2 phase evolution was simulated for a 100 m $\times$ 25 m reservoir according to aqueous phase advection, CO_2-water solubility, and acid-rock reaction rates typical of geological reservoirs (Fig. 6.10). Simulations for high (Fig. 6.10a) and low (Fig. 6.10b) geologic acidity conditions both show that the separate CO_2 phase evolves at very early injection time-scales. In these illustrative calculations we attempt to provide the groundwork in highlighting the significance of the separate CO_2 phase in reactive transport in carbonate reservoirs; reservoir structural changes due to the grain-engulfment shielding effects were not included. Diffusive effects were also neglected due to its small effect (order of 10^{-4}) in comparison with advective effects [117]. Accurate simulations of reactive transport requires consideration of the local conditions on the phase diagram (Fig. 6.9). The grain-engulfment shielding effects observed at interface-, pore-, and ensemble-scales, however, are expected to extend to the reservoir level to dictate reactive transport through carbonate reservoirs and to impact significantly the security of CO_2 storage formations.

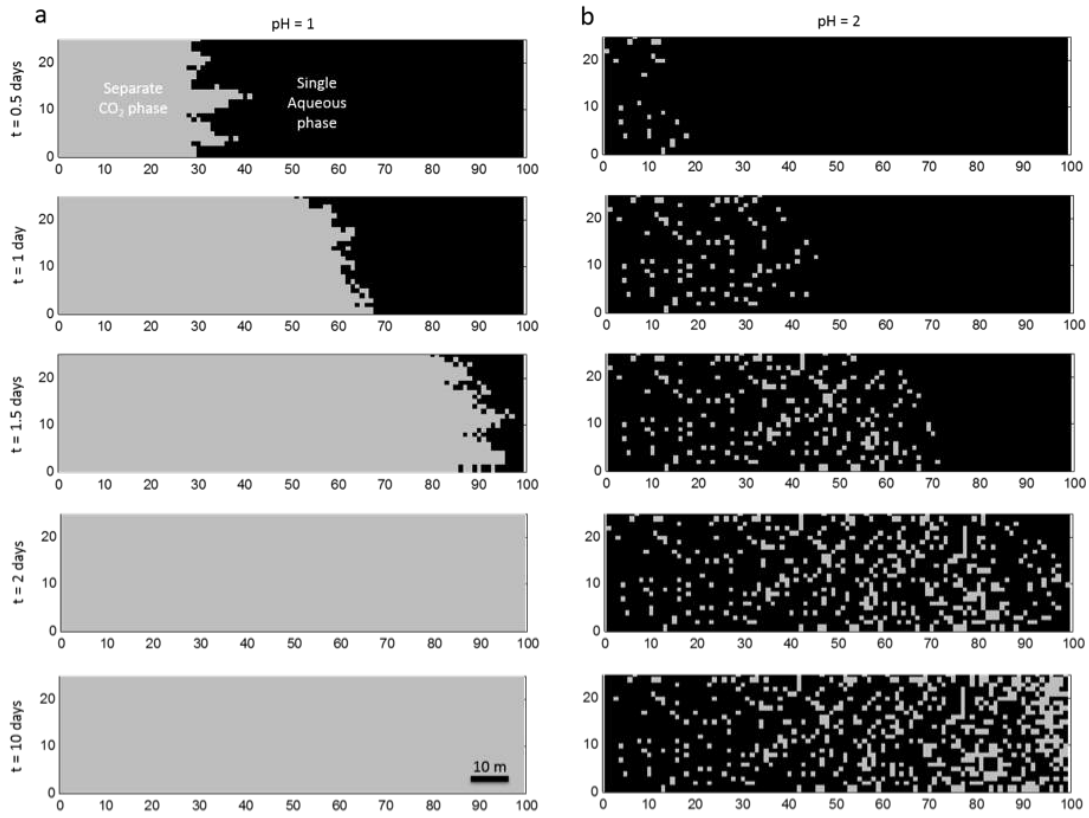

Figure 6.10: Grain-engulfment on the storage reservoir and sensitivity to acidity. An acidic aqueous phase is injected through the left boundary and pressure is maintained on the right boundary. No flow conditions are enforced on the top and bottom boundaries. Separate scCO$_2$ phase (gray) evolves quickly throughout the formation. (a) At high acidity conditions (pH = 1), separate CO$_2$ phase develops throughout the entire reservoir volume. (b) At low acidity conditions (pH = 2), separate CO$_2$ phase develops selectively in regions with local Da and St numbers that enable separate, retained phase development (regime III) dictated by reservoir heterogeneity.

The illustrative model developed enables investigation of the sensitivity of the grain-engulfment effect to acid concentration and advection rates within the reservoir. CO$_2$ solubility into the aqueous phase dictates that acid concentration increases with pressure, and therefore storage formation depth. We find that separate CO$_2$ phase evolution is strongly coupled to the acid concentration (Fig. 6.10a,b). Importantly, reservoir heterogeneity dictates separate CO$_2$ phase evolution at low acidities (Fig.

6.10b) due to variations in the local reactive transport. Local phase regimes within the reservoir are controlled by the resident PeDa and St (Fig. 6.9c) and separate CO_2 phase develops selectively in those regions that have the PeDa and St numbers corresponding to regime III.

The modeling findings on the importance of grain-enfulgment on overall reservoir behavior are corroborated by modifying a commercial simulation package (CMG GEM, Computer Modelling Group LTD Compositional and Unconventional Simulator). Specifically, CO_2 was injected into a representative carbonate storage reservoir to model the reactive transport and evolution of a separate CO_2 phase (Fig. 6.12). The time evolution of the separate CO_2 phase was simulated for a 90 m $\times$ 90 m areal two-dimensional section of a reservoir according to aqueous phase advection, CO_2-water solubility, and acid-rock reaction rates typical of geological reservoirs. The carbonate reservoir simulated here has a heterogeneous porosity, ranging from 0.1 % to 50 % and a mean of 35 %. The reservoir was treated as a single layer in depth (10 m) and was discretized into 1 m $\times$ 1 m cells in the areal plane. The reservoir was comprised of calcite, with heterogeneous porosity. The porosity of the region of interest is shown in Fig. 6.11. The dimensionless quantities corresponding to the simulated transport conditions are listed in Table 6.2.

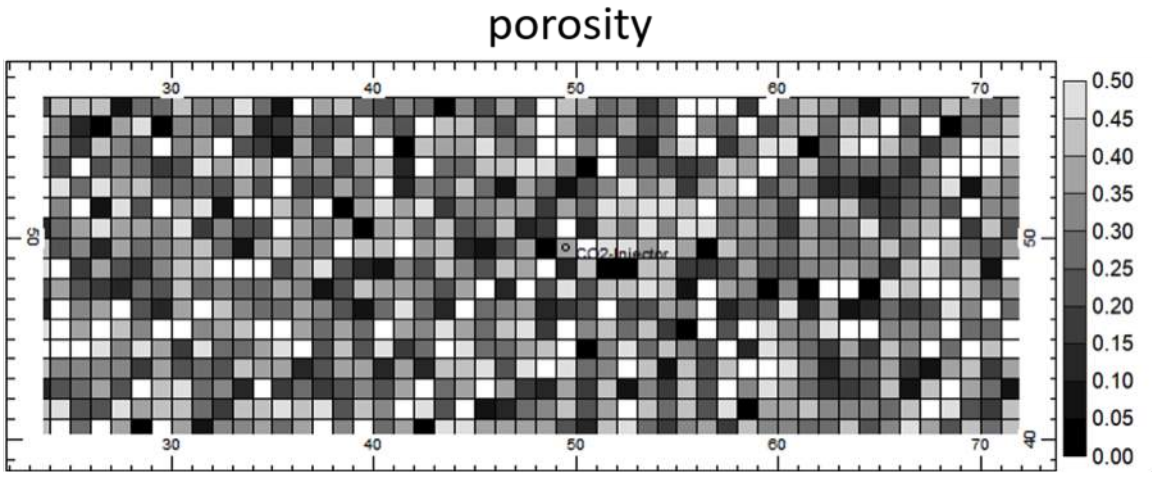

Figure 6.11: Porosity map of the simulated reservoir in the region of interest. The porosity ranges from 0.1 % to 50 %, with a mean of 35 %.

The permeability of the reservoir was set at 2000 mD. The reactions modeled are:

$$CO_2 + H_2O \rightarrow H^+ + HCO_3^- \tag{6.6}$$

$$CO_3^{2-} + H^+ \rightarrow HCO_3^- \tag{6.7}$$

$$OH^- + H^+ \rightarrow H_2O \tag{6.8}$$

$$CaCO_3 + H^+ \rightarrow Ca^{2+} + HCO_3^- \tag{6.9}$$

In these simulations, we highlight the significance of the separate CO_2 phase on reactive transport in carbonate reservoirs; reservoir structural changes due to the grain-engulfment shielding effects were not included. Diffusive effects were also neglected due to its small effect (order of 10^{-4}) in comparison to advective effects [117]. The reservoir temperature was maintained at 50 °C.

Table 6.2: Dimensionless quantities comparing rates of reaction, advection, and dissolution corresponding to simulation conditions.

Pe	Da	PeDa	St	Regime
72.3	0.0242	1.74	0.0138	III
145	0.0121	1.74	0.00691	III
723	0.00242	1.74	0.00138	III

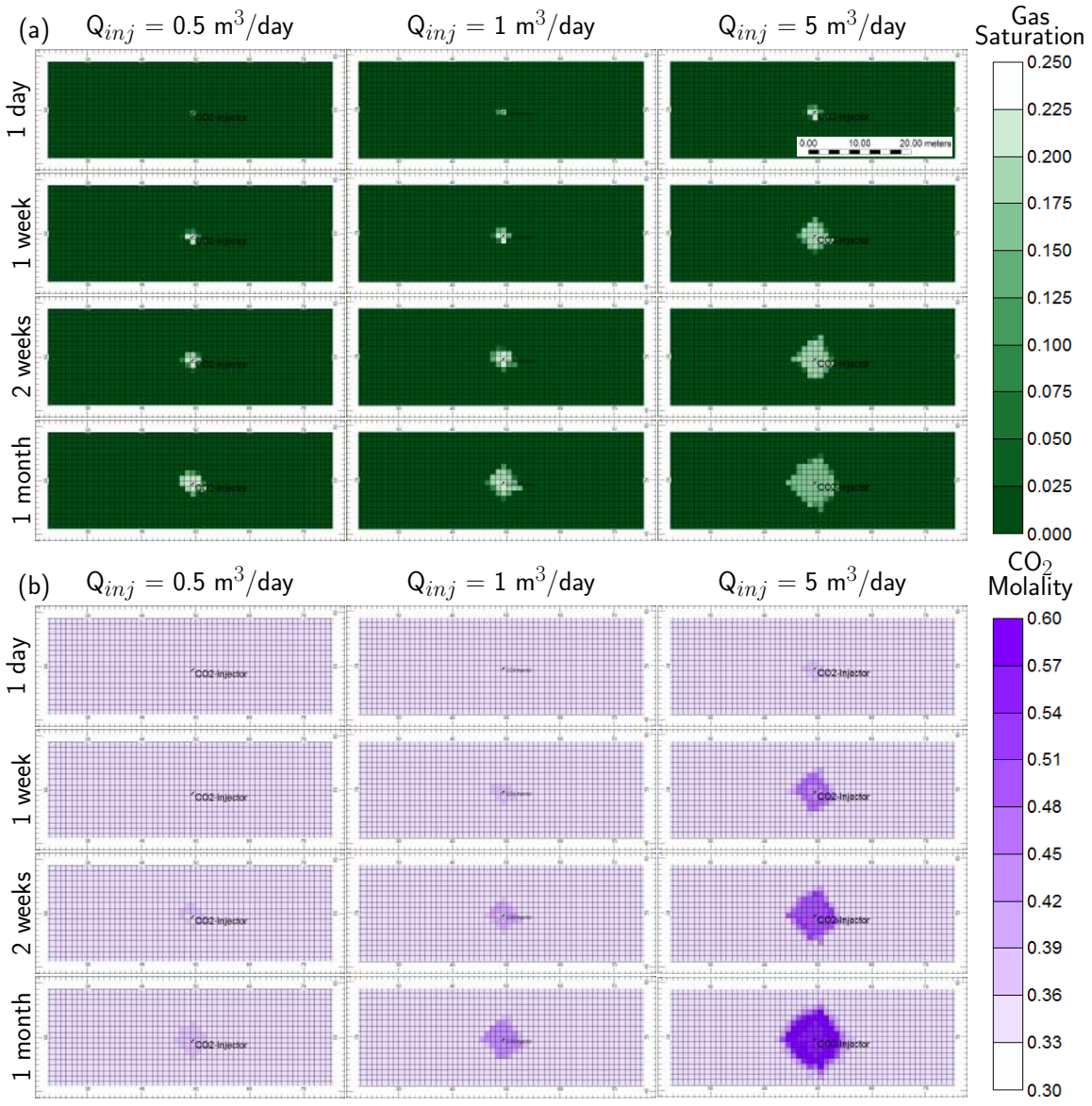

Figure 6.12: Early-time simulation of CO_2 injection into a heterogeneous carbonate reservoir to investigate grain-engulfment at the reservoir scale. Pure CO_2 is injected through the injection well and pressure build-up is prevented by withdrawing from the reservoir. The reservoir is maintained at 50 °C. No-flow conditions are enforced on the boundaries. Separate CO_2 phase evolves at early times close to the injection well (a), and acidified brine due to aqueous phase CO_2 (i.e., increased CO_2 molality) is identified ahead of the gas front (b). Sensitivity with respect to CO_2 injection rate shows that in comparison to low CO_2 injection rates (Q_{inj} = 0.5 m^3/day), the local separate CO_2 phase saturation at high CO2 injection rates (Q_{inj} = 5 m^3/day) is reduced but the local CO_2 molality is increased.

Reservoir-scale simulations for high and low CO_2 injection rates both show significant separate CO_2 phase development (Fig. 6.12a) at early injection time-scales and demonstrate the significance of grain-engulfment on reactive transport in practical CO_2 storage carbonate reservoirs. Specifically, separate CO_2 phase evolves close to the injection well (Fig. 6.12a) and acidified brine is generated (i.e., increased CO_2 molality) ahead of the gas front due to CO_2 solubility (Fig. 6.12b). Sensitivity with respect to CO_2 injection rate shows that near the injection wellbore, the local separate CO_2 phase saturation is largest for low CO_2 injection rates while increases in CO_2 molality is greatest for high CO_2 injection rates. Separate CO_2 phase saturation, i.e., the impact of grain-engulfment on reservoir rock dissolution, is dictated by local reservoir heterogeneities. As in the numerical model developed, local phase regimes within the reservoir are controlled by the resident PeDa and St numbers (Fig. 6.9) and separate CO_2 phase develops selectively in those regions that have the PeDa and St numbers corresponding to regime III. Full physics simulation of reactive transport requires consideration of the local conditions on the phase diagram (Fig. 6.9), still these scouting numerical efforts demonstrate that the grain-engulfment shielding effects observed at interface-, pore-, and ensemble-scales dictate reactive transport at the reservoir level and impact the security of CO_2 storage carbonate formations significantly.

6.4 Conclusions

We develop a novel biogenic calcite-functionalized mirovisualization device to delineate the fundamental dynamics dictating reactive flows through geologic carbonate formations. Using the novel device, we discover a new mechanism, grain-engulfment,

that underlies the complex rock dissolution dynamics in reactive carbonate formations and offers fundamental understanding to develop predictive models for subsurface CO_2 storage assessment. We find that carbonate dissolution at typical reservoir conditions results in a separate CO_2 phase that impedes local dissolution and promotes downstream reactions. Our experimental results and theoretical framework show that separate CO_2 phase induced grain-engulfment is an important mechanism in determining the overall storage and security of geologic storage reservoirs. When combined with advanced simulation and geological data, our results have the potential to provide an accurate predictive model to assess subsurface CO_2 storage security in carbonate formations.

Chapter 7

Spontaneous Fingering in Miscible Fluids

Diffusion-driven interfacial dynamics between two miscible fluids are investigated. Heptane is diffused into viscous crude oil in a microscale Hele-Shaw cell. No external pressure gradients are applied; hence, the imposed Peclet number is zero. The diffusive/dispersive process is dictated by a two-stage dispersive mechanism owing to the multicomponent character of the crude oil. Stage I is distinguished by the spontaneous fractal-like fingering of heptane into the crude oil phase due to light components extraction from the crude oil. Stage II is characterized by diffusive mixing between the heptane and the heavy components in the crude oil. Extraction of light components exceeds the diffusion between heptane and heavy components in stage I, thereby allowing a distinct interface to form between heptane and the crude oil. Compositional gradients induce dynamic interfacial tension gradients that lead to Marangoni-effect-driven convection. Marangoni convection cells at the finger tips dictate local mass exchange and drive the self-similar fractal-like finger splitting. Fractal analysis of the fingering process shows increasing fractal dimensionality during the early diffusively-dominant fingering regime approaching that of diffusion-limited

aggregation ($D_f \sim 1.67$), and a drastic decrease in fractal dimensionality thereafter due to Marangoni-effect-driven convection ($D_f \sim 1.55$). We characterize the fractal finger growth and mass exchange, and calculate the local dynamic interfacial tension. We find that spontaneous fingering, i.e., the presence of stage I, requires small gap spacing and the presence of light extractable components in the crude oil.

7.1 Introduction

Heavy oil, extra heavy oil, and bitumen consist of about 70 % of global oil resources [60]. Additionally, large deposits are stored in carbonate reservoirs [198]. Recovery of this resource, however, is impaired due to its large viscosity and low mobility [199] and the complexity of the oil-rock interactions [200]. Thermal methods have been applied successfully to reduce the crude oil viscosity in siliciclastic formations, including steam drive, cyclic steam stimulation (CSS) and steam assisted gravity drainage (SAGD) [201, 143]. Solvent-assisted extraction enhances oil recovery, reduces material and energy input, and limits environmental impacts associated with thermal recovery processes (c.f., Boone et al. 2012 [202]).

Light hydrocarbon solvents such as propane, butane, and pentane are able to diffuse into crude oils to reduce the oil viscosity [203]. Mobility increases at elevated temperatures due to thermal viscosity reduction and solvent-crude diffusivity provide a more economic and environmentally considerate path to increase heavy oil recovery [204, 205]. Complex crude-oil compositions and solvent-crude mixing lead to significant uncertainties in the macroscopic behavior of the recovery process. Specifically, solvation efficacy of solvent into the crude oil, swelling of crude oil due to solvent dissolution into the solvent [61], and potential formation damage due to solvent particle precipitation [62] must be resolved. These are all pore- and interface-level dynamics.

Overall efficacy of oil recovery is ultimately dictated by microscale behavior [75].

Microfluidics enable direct visualization of mixing and interfacial dynamics at the relevant length and time scales [93, 87]. Silicon-glass microfluidic platforms with representative pore geometries of real rock, i.e., micromodels [75, 79, 107, 80, 203], allow direct insight into the dispersive dynamics that dictate solvent-enhanced oil recovery in porous media. Recent advances in real-rock microfluidics have enabled visualization of fluids-solids interactions in carbonate [94, 106] and shale [96] substrates in addition to clay-functionalized silicon-based micromodels [80, 76]. Further, platforms with simple microchannel geometries enable fundamental studies of phase behavior, interfacial dynamics, and solvent-crude oil mixing [117, 108, 93, 87].

Immiscible fluid-pair dynamics under further simplified geometries (i.e., flow between two parallel plates in Hele-Shaw configurations) have been studied extensively [59, 63, 64, 65, 66]. Specifically, the literature shows experimental and theoretical developments wherein a low viscosity fluid is injected into the resident high viscosity fluid within the Hele-Shaw cell. The two parallel plates comprising the Hele-Shaw configuration are maintained at a fixed distance ($\sim$ mm - cm) so as to mimic the permeability of porous rock material. The Hele-Shaw configuration has formed the basis of analytical solutions to the interfacial instabilities observed when a low viscosity fluid (e.g., an injectant) displaces one with high viscosity (e.g., the crude oil) [59, 67, 68, 69].

More recently, studies on partially miscible fluid-pairs have been motivated by a number of practical applications, including CO_2 storage and enhanced oil recovery [206, 70, 207, 208, 204, 68, 203, 209, 69]. Notably, experiments conducted using fluid-pairs at the low interfacial tension condition, typically single-component fluids such as glycerol and water, show surprising dynamics between the initially distinct fluid phases, such as regularity in interfacial instabilities and the existence of ramified fingering [70, 208]. Such high capillary number (Ca = viscous forces/ surface

tension) and low Peclet number (Pe = imposed advection rate/ diffusion rate) systems show complex interfacial instabilities that arise due to competing driving forces. Furthermore, modeling of miscible fluid-pair mixing due to externally-driven flow- and buoyancy-forcing show complex fingering dynamics [210, 211], and use the idea of Korteweg stresses to describe the complex mixing behavior [212, 213, 214, 215]. Specifically, Korteweg stresses are introduced to account for diffusive mass exchange that is not present in classical immiscible fluid-pair descriptions of mass and momentum conservation. In keeping with conditions that represent subsurface processes such as oil recovery or carbon sequestration, further delineation of the dynamics at fully miscible, low flow, and complex fluid composition conditions are required.

Insofar as the literature has delineated the mechanisms underlying interfacial dynamics between simple miscible fluids, mixing between multicomponent, fully miscible fluids at the low flow, microconfined scale has scarcely been explored experimentally. In this work, we examine oil recovery mechanisms due to solvent-crude oil dispersion at microscopic length scales. Existing literature examines the interfacial dynamics between immiscible and miscible fluids due to injection of a low viscosity fluid into a high viscosity fluid. As an analog to far-from-well conditions and cyclic single-well processes, we probe the interfacial dynamics between miscible fluids in the absence of an external pressure gradient and an imposed flow.

7.2 Experimental Methods

Interface-level solvent-crude oil dynamics underlying solvent-enhanced oil recovery were visualized in a glass micro-Hele-Shaw cell. Heptane (Heptane, H350-4, Fisher-Scientific) was chosen as the solvent phase due to its miscibility with crude oils. Viscosity of heptane at the experimental conditions is 0.42 cP. The properties of the crude oil are listed in Table 7.1. Specifically, the crude oil chosen has a viscosity of

87.7 cP. The viscosity ratio of this fluid-pair is hence $\eta_{crudeoil}/\eta_{solvent} = 209$. Figure 7.1 shows the complex compositional character of the crude oil.

Table 7.1: Crude oil characterization [216].

Crude oil properties	Value
Acid number (mg g^{-1})	0.83
Base number (mg g^{-1})	2.87
Viscosity at 22 °C (cP)	87.7
Asphaltene content (wt %)	6.2
Specific gravity	0.918

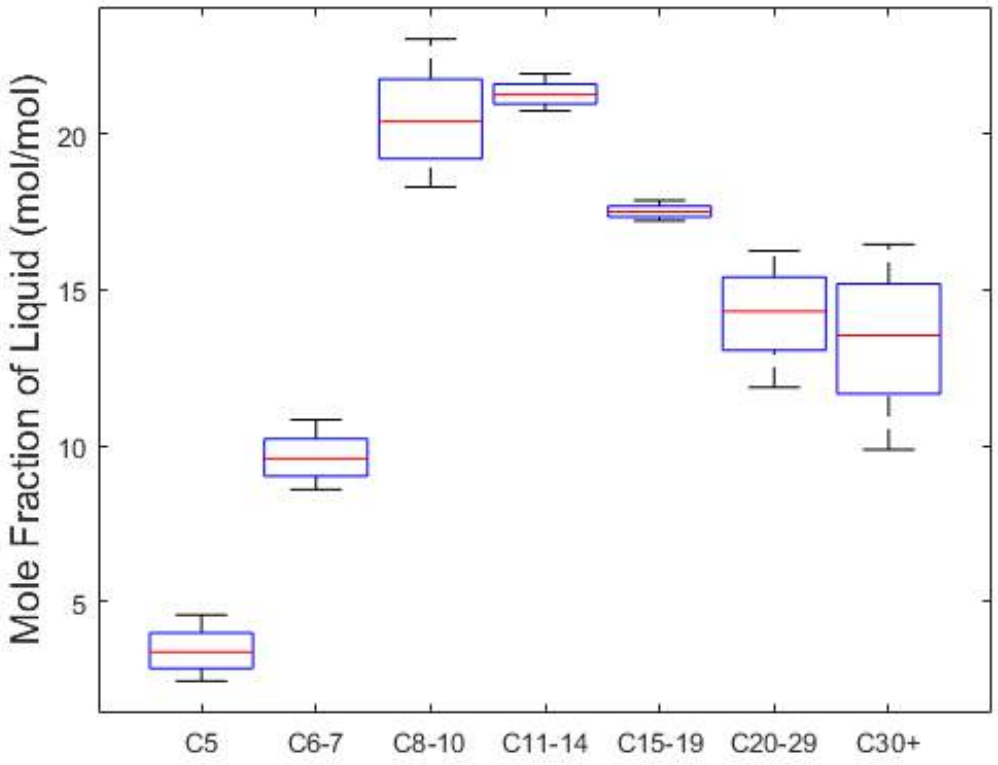

Figure 7.1: Composition of the crude oil by carbon number (C). This crude oil is comprised of both light (C5 –10) and heavy (C11+) components. Light components are mobile and capable of relatively rapid diffusion, whereas heavy components are less so.

Interfacial dynamics between the solvent and crude oil were examined in a microscale Hele-Shaw-type apparatus (Fig. 7.2). A single crude-oil droplet was sandwiched between two horizontal glass plates to minimize gravitational mixing. Gap spacing between the glass plates was set to 5, 15, and 30 μm to investigate the effect of scale. Stainless steel shim stock was used to maintain the gap spacing. Solvent droplets dispensed near the edges of the cover plate entered the flat cell via capillarity. No external pressure gradients or injections were applied to drive the flow. All experiments were conducted at ambient temperatures and pressures and the system boundary was held at constant pressure. Boundaries were also submerged in heptane. A microscope (Leica Z16 APO Macroscope) and camera (Leica DFC 450) were used to capture the dynamics directly. The dynamics were recorded at a frame rate of 25 frames per second.

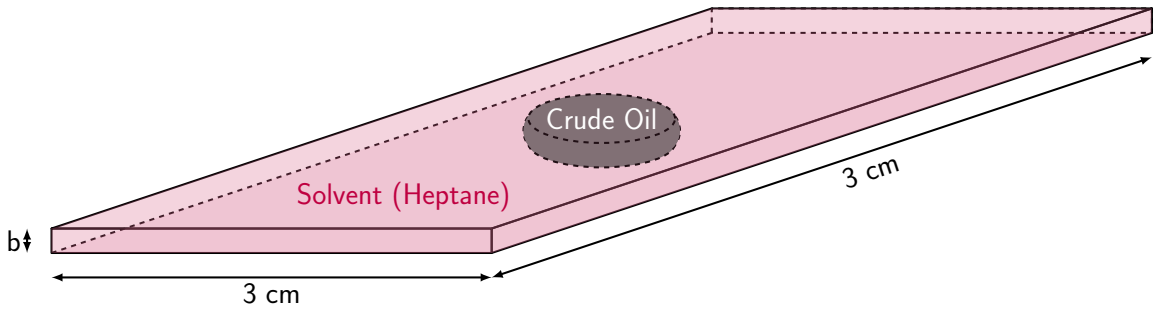

Figure 7.2: Microscale Hele-Shaw cell with gap spacing, b, of 5, 15, and 30 μm. A single crude oil droplet is encased between the top and bottom plates and heptane solvent is introduced. Heptane and crude oil are miscible and the system boundaries are held at constant pressure and immersed in heptane. No external pressure gradient or flow is imposed.

7.3 Results and Discussion

7.3.1 Two-stage mixing due to multicomponent character of crude oil

Figure 7.3 shows diffusion and mixing dynamics between the two miscible fluids in the absence of external pressure gradients or injections. The gap spacing, b, here is 5 μm. Surprisingly, heptane and crude oil mixed in two markedly distinct stages: spontaneous formation of fractal-like fingers at short times (Fig. 7.3, $t = 0$ s to $t = 24$ s) and slow diffusion similar to bulk mixing thereafter (Fig. 7.3, $t = 24$ s to $t = 91$ s).

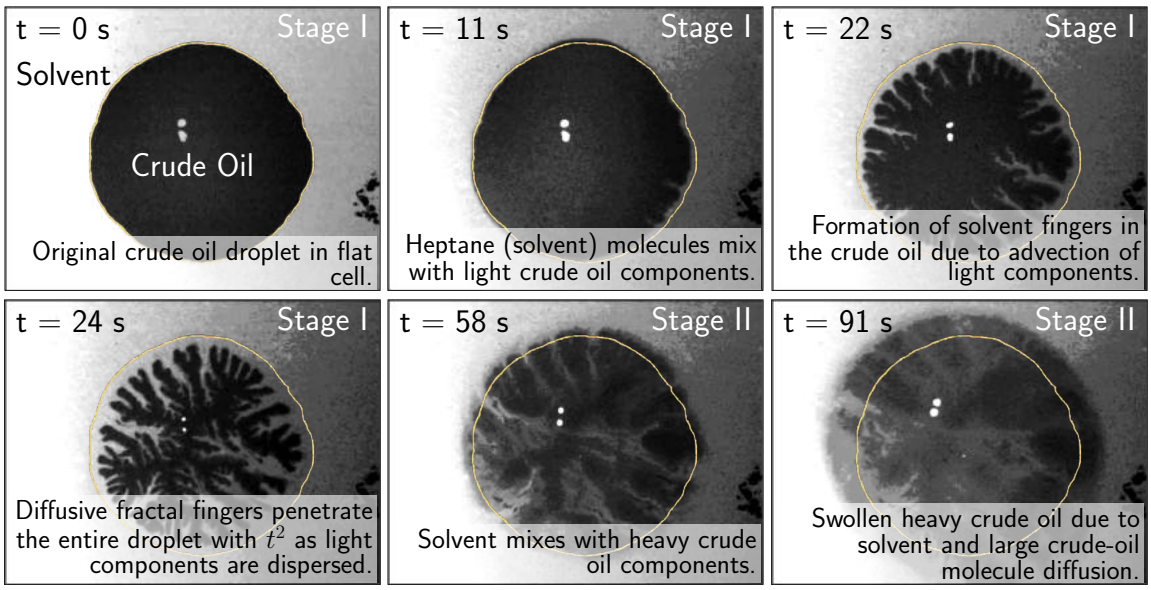

Figure 7.3: Hele-Shaw cell experiment of mixing dynamics between heptane and the crude oil. The orange circle denotes the original drop shape. Stage I (t = 0 s to t = 24 s) involves mutual diffusion of heptane into and light components out of the crude oil. Mixing and erosion of light crude oil components due to heptane diffusion forms heptane fingers into the crude-oil droplet. The fingers initiate and propagate in a fractal-like manner until light crude-oil components have been dispersed. This stage is fast and on the order of 30 seconds. Stage II (t > 24 s) involves the diffusion of heptane and heavy crude-oil components and is slower (on the order of minutes). Heptane diffusion into the heavy crude oil components causes crude oil swelling and blurs out the fractal-like fingers from the first light-component mixing stage.

The interaction timescale for crude-oil droplet radii of $\sim$ 2.5 mm was on the order of $\sim$ 1 minute. In contrast, purely diffusion driven interaction timescales are expected to be $\sim$ 1 hour for a typical crude oil-heptane diffusivity of D $\sim$ 1.5e-5 cm^2/s. The observed spontaneous fractal-like fingering was therefore not driven by diffusion alone (Fig. 7.4).

Robustness of this spontaneous fingering phenomenon is evidenced through two different oils, one that has both small, mobile molecules and large, immobile molecules that experiences the spontaneous fingering phenomenon (Fig. 7.3), and another that has only large, immobile molecules that does not exhibit the spontaneous fingering

phenomenon (Fig. 7.4). Similar spontaneous fingering is observed in experiments using other crude oils with both small and large molecules. Specifically, more viscous oils (i.e., crude oils with fewer small, mobile components) destabilize with shorter initial wavelengths in accordance to the Saffman-Taylor solution, however fewer stable fingers are generated. While it is difficult to ensure that these results will apply to all petroleum reservoirs owing to the heterogeneities in crude oil composition, the experimental results show that spontaneous fingering occurs for crude oils with both light and heavy components.

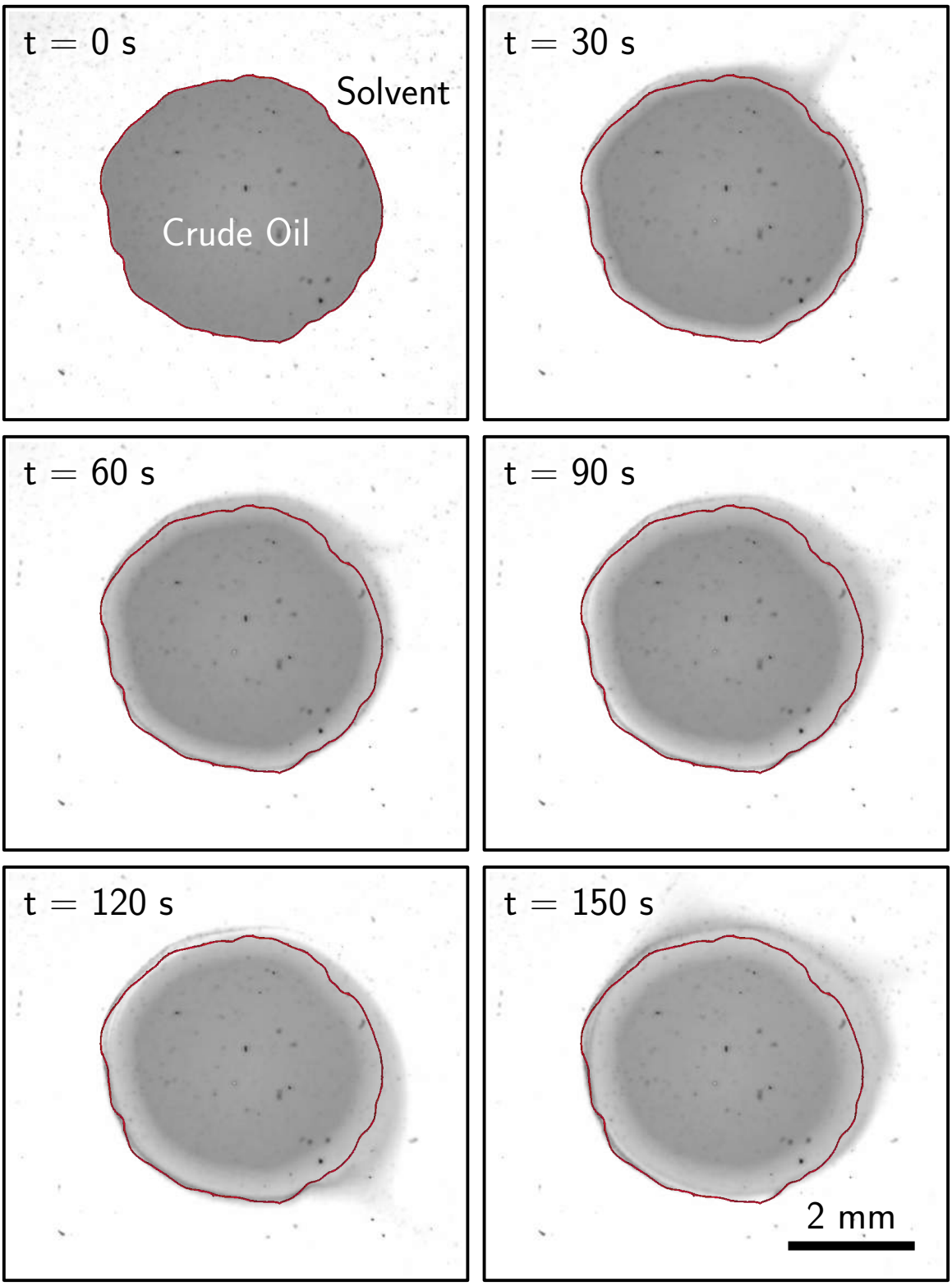
t = 0 s
Solvent
Crude Oil
t = 30 s
t = 60 s
t = 90 s
t = 120 s
t = 150 s
2 mm

Figure 7.4 *(previous page)*: Perturbations to the interface were not observed for non-volatile crude oil and solvent pairs where the light, volatile components in the crude oil were liberated in advance of the experiment.

The two-stage diffusion process is attributed to the multicomponent character of the crude oil. Importantly, spontaneous fingering was observed only for volatile crude-oil samples containing both heavy and light components. That is, in oil samples with only heavy components, fractal fingering was not observed spontaneously (Fig. 7.4). In volatile crude oil, small, lighter components are mobile (diffusivity $D \sim 1/d$, where d is the molecular diameter) and are susceptible to diffusion [217]. Heavy, branched components, on the other hand, are less mobile in comparison and remain in the original crude oil phase. During stage I, spontaneous fractal-like fingering is driven by mutual diffusion of light crude-oil components into the solvent phase and heptane molecules into the crude-oil phase. We observe extraction of light components out of and the diffusion of heptane into the crude-oil phase over time, as evidenced by reductions in droplet size compared to the initial conditions (Fig. 7.3, $t = 0$ s to $t = 24$ s). Sharp concentration gradients drive rapid migration of light component molecules out of the crude-oil phase and into the solvent phase and heptane molecules out of the solvent phase and into the crude-oil phase; immobile heavy components are left behind and concentrated in the crude-oil phase.

The self-similar fractal-like fingering process continues until light, mobile components are extracted. Full extraction of the light components marks the conclusion of spontaneous fingering in stage I and the onset of slow diffusion in stage II. Specifically, heavy crude-oil molecules diffuse into the solvent phase (Fig. 7.3, $t = 24$ to 91 s) and heptane molecules diffuse into the crude-oil phase, causing the crude oil phase to swell beyond its initial size (Fig. 7.3, $t = 58$ to 91 s). Swelling during stage II blurred out the fractal-like fingers formed during light-components extraction in stage I.

7.3.2 Interface characteristics: Self-similarity in finger splitting due to recursive diffusive-hydrodynamic perturbations

Existence of distinct finger interfaces suggest that the local advection rates induced by spontaneous fingering far exceed the local diffusive rates at the finger scale. [67, 68, 70]. In pressure-driven Saffman-Taylor fingering, instabilities are driven by the most unstable wavelength, λ_c, given by:

$$\lambda_c = \pi b \sqrt{\frac{\sigma}{\Delta\eta V}} \tag{7.1}$$

where b is the gap spacing between the glass plates, σ is the interfacial tension, $\Delta\eta$ is the difference in viscosity between the crude oil and solvent phases, and V is the interfacial velocity imposed by an external pressure gradient [59, 218, 70]. The present system, in contrast, is without an imposed velocity. The rate of interface retraction, *i.e.*, the induced velocity due to heptane and light components diffusion, can be viewed as an analog of the imposed interfacial velocity in the Saffman-Taylor instability. Characterization of the growth dynamics show that the unstable wavelength in the present system is $\lambda_c \sim 272\mu$m $\pm 69\mu$m for a gap spacing of 5 μm (Fig. 7.5). In this system, the viscosity difference is $\Delta\eta = \eta_{CrudeOil} - \eta_{Heptane} = 87.3$ cP. Maximum and minimum induced interfacial velocities are delineated by measuring the induced velocities at the finger tips and finger edges, respectively (Fig. 7.6a). Using the characteristic wavelength relation developed by Saffman and Taylor, the corresponding maximum and minimum dynamic interfacial tensions are calculated (Fig. 7.6a). Importantly, we calculate a finger-tip dynamic interfacial tension of $\sigma_{max} \sim 40$ mN/m and a finger edge dynamic interfacial tension of $\sigma_{min} \sim 8.4$ mN/m. Apparently, a spatial gradient in the dynamic interfacial tension is established across

the finger as a result of light components flux across the solvent-crude oil interface. In other words, rapid mass exchange of heptane and light components between the solvent and crude-oil phases create chemical potential gradients in the crude oil that lead to gradients in dynamic interfacial tension.

Due to the length-scale dependence of the importance of dynamic interfacial tension, it is plausible that there exists a cut-off length-scale, i.e., minimum pore-size, at which a specific miscible fluid-pair fingers spontaneously (Fig. 7.7). Specifically, the critical gap spacing was $b \sim 15$ μm for the crude oil and heptane pair used (Fig. 7.7, $b = 15$ μm). That is, fingering occurred spontaneously for gap spacings below the cut-off length scale, $b < 15$ μm (Fig. 7.7, $b = 5$ μm), and was absent for gap spacings above the cut-off length-scale, $b > 15$ μm (Fig. 7.7, $b = 30$ μm). Experiments with different crude oils show that the cut-off gap spacing is dependent upon the composition of the crude oil. In the subsurface, these results suggest that tighter formations, i.e., reservoirs with small pore-sizes, are most susceptible to the enhanced mixing due to spontaneous fingering.

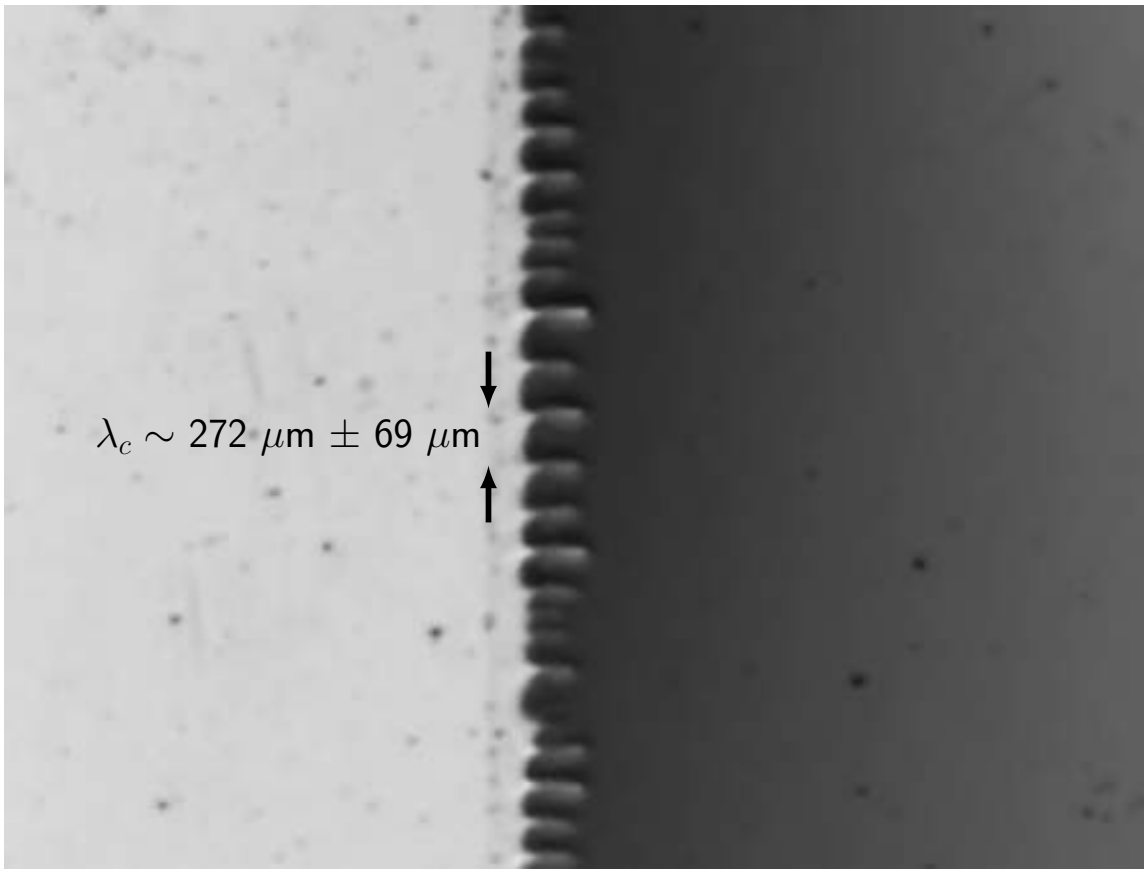

Figure 7.5: Most unstable wavelength. The system consistently exhibits fingering at the most unstable wavelength of $\lambda_c \sim 272\ \mu$m $\pm$ 69 μm for a gap spacing of 5 μm.

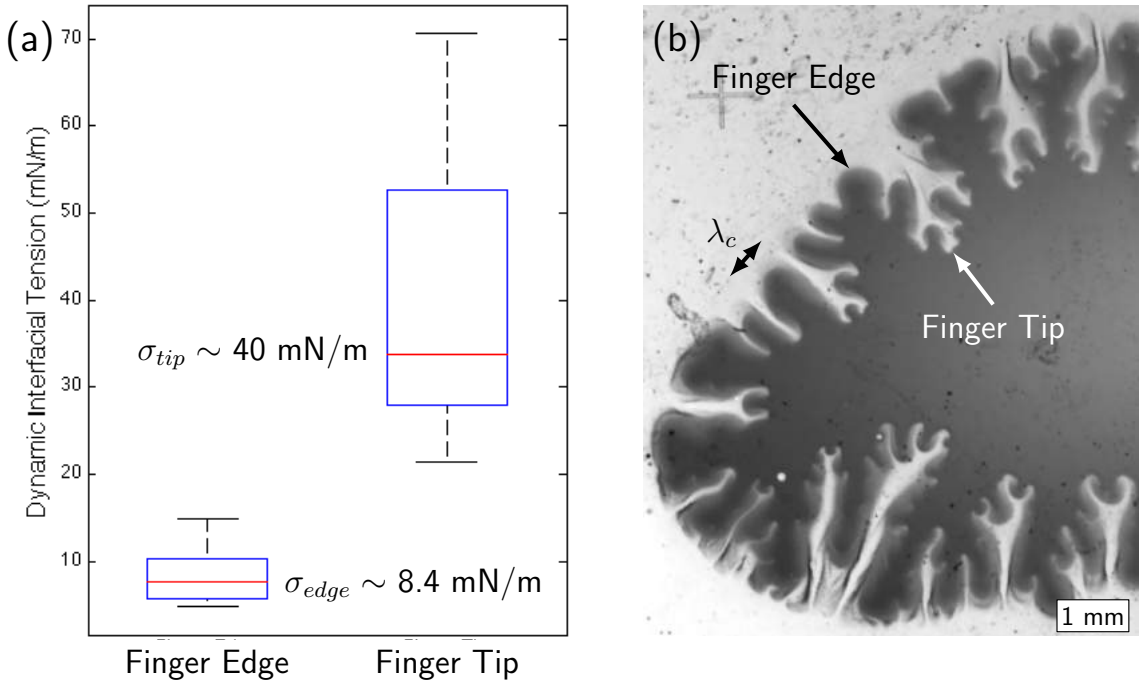

Figure 7.6: Dynamic interfacial tension between the crude oil and the heptane. Interfacial tension is estimated using experimental measurements of the characteristic wavelength, λ_c, the gap separation, $b = 5$ μm, and the interfacial velocity, V. The maximum and minimum induced interfacial velocities are measured at the finger tip and the finger edge, respectively, to calculate the maximum and minimum dynamic interfacial tension. The calculations show a clear gradient in the dynamic interfacial tension.

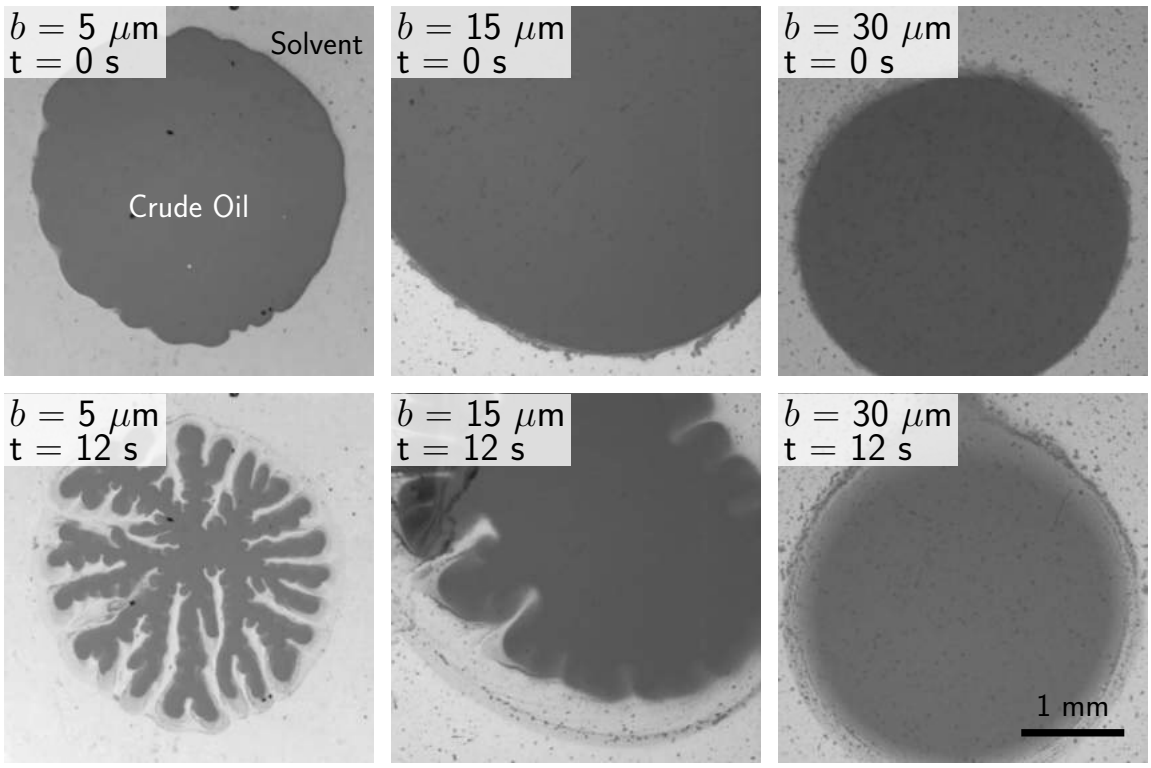

Figure 7.7: Occurrence of spontaneous fingering with gap spacing. The cut-off length-scale in the present crude oil - heptane system is a gap spacing of $b \sim 15$ μm. Larger gap spacings, i.e., larger pore spaces, do not benefit from the enhanced mixing of spontaneous fingering.

Gradients in interfacial tension result in a Marangoni instability that drives convection. In our system, light components extraction (*i.e.*, heavy components concentration) induce a gradient in dynamic interfacial tension that destabilizes the interface to drive the hydrodynamic fingering process. The fingers formed in this process are fractal-like in nature; characteristic fractal dimensions for a gap spacing of 5 μm are 1.55 to 1.67 (Fig. 7.8b). Fractal dimensions were obtained through characterization of the invading fingers using image processing. Specifically, the FracLac plugin from ImageJ was used to quantify the fractal dimensions. Spontaneous fingering decreased with increased gap spacing, and for large gap spacing, $b = 30\mu$m, minimal spontaneous fingering effects were observed. The spontaneous generation of fractal-like

fingers in stage I is therefore driven by gradients in dynamic interfacial tension. Importantly, the unstable wavelengths at the active tips of the fingers remain constant (Fig. 7.9a), however, these wavelengths are much shorter than those at the edge of the finger, where some fingers are inactive.

Two characteristics are suggested here: first, the diffusive finger splitting process is self-similar, and, second, the Marangoni convection cells generated by gradients in dynamic interfacial tension dictate propagation of the self-similar structures. Characterization of fingering fractal dimension and volumetric evolution (Fig. 7.8) show that the process is within the diffusion-limited aggregation regime [219]. Specifically, fingering characterization delineate three regimes: (i) a diffusively-dominant regime (Fig. 7.8b,c green) is characterized where fractal dimensionality increases and droplet size decreases linearly due to mutual mass exchange between the solvent and light components in the crude oil. Specifically, during the early diffusion-driven interfacial perturbation regime (Fig. 7.3, t = 0 to 1.84 s, green), fractal dimensionality increases from a flat interface towards $D_f = 1.67$ due to finger splitting, approaching diffusion-limited aggregation (DLA, $D_{f,DLA} = 1.68 \pm 0.04$) [220, 219]. Indeed, the pattern formed during the spontaneous fingering process is reminiscent of the DLA model of Witten and Sander [221, 222]. Specifically, the interfaces are destabilized in a recursive manner similar to the sticking of monomers to a cluster [223, 224, 220]. One can view the initial interfacial instabilities (Fig. 7.10b) as the "monomers", and its growth and recursive destabilization as the "sticking of additional monomers".

Interfacial destabilization due to diffusion-driven mass exchange is a fractal-like process in that each perturbed interface is perturbed recursively, resulting in an approximately linear growth in its fractal dimension. (ii) A hydrodynamically-dominant regime (Fig. 7.8, t = 7.84 to 12.08 s, b,c yellow) is characterized where both fractal dimensionality and droplet sizes decrease rapidly. Dominant Marangoni-driven

convection in place of diffusion-driven mixing results in enhanced mass exchange between the crude oil and solvent phases. Development of new interfacial perturbations, however, is hindered in this stage, resulting in more rectliniear, i.e., decreasing fractal dimensionality (D_f from 1.67 to 1.58), fingering. (iii) Return to a diffusively-dominant regime (Fig. 7.8b,c red) is characterized where fractal dimensions increase from D_f = 1.58 to 1.67 and droplet sizes decrease rapidly due to limited mass exchange in the presence of excess solvent and scarce availability of light components available for extraction from the crude oil.

Convective cells born of Marangoni stresses expedite mixing in the heptane phase; the result of this enables removal of the extracted light components from the interface and accelerates the rate at which light components are extracted subsequently. Characterization of the rate at which the light components are extracted (Fig. 7.9) shows that the volume of light components extracted from the crude oil scales initially with the 3/2 power of time (*i.e.*, Area$\sim t^{3/2}$ or Area$^{2/3} \sim$ t as in Fig. 7.9b), as with dispersive transport modes from t = 0 to 8 s (Fig. 7.9b), and transitions to a cubic scaling with time (*i.e.*, Area $\sim t^3$ or Area$^{1/3} \sim$ t as in Fig. 7.9c) with the onset of finger splitting at t = 8 s onwards (Fig. 7.9c). The cubic relation characterizes the domiance of the Marangoni-effect driven convection. The finger length (Fig. 7.9d) penetrates with the square of time (*i.e.*, Length $\sim t^2$ or Length$^{1/2} \sim$ t as in Fig. 7.9d).

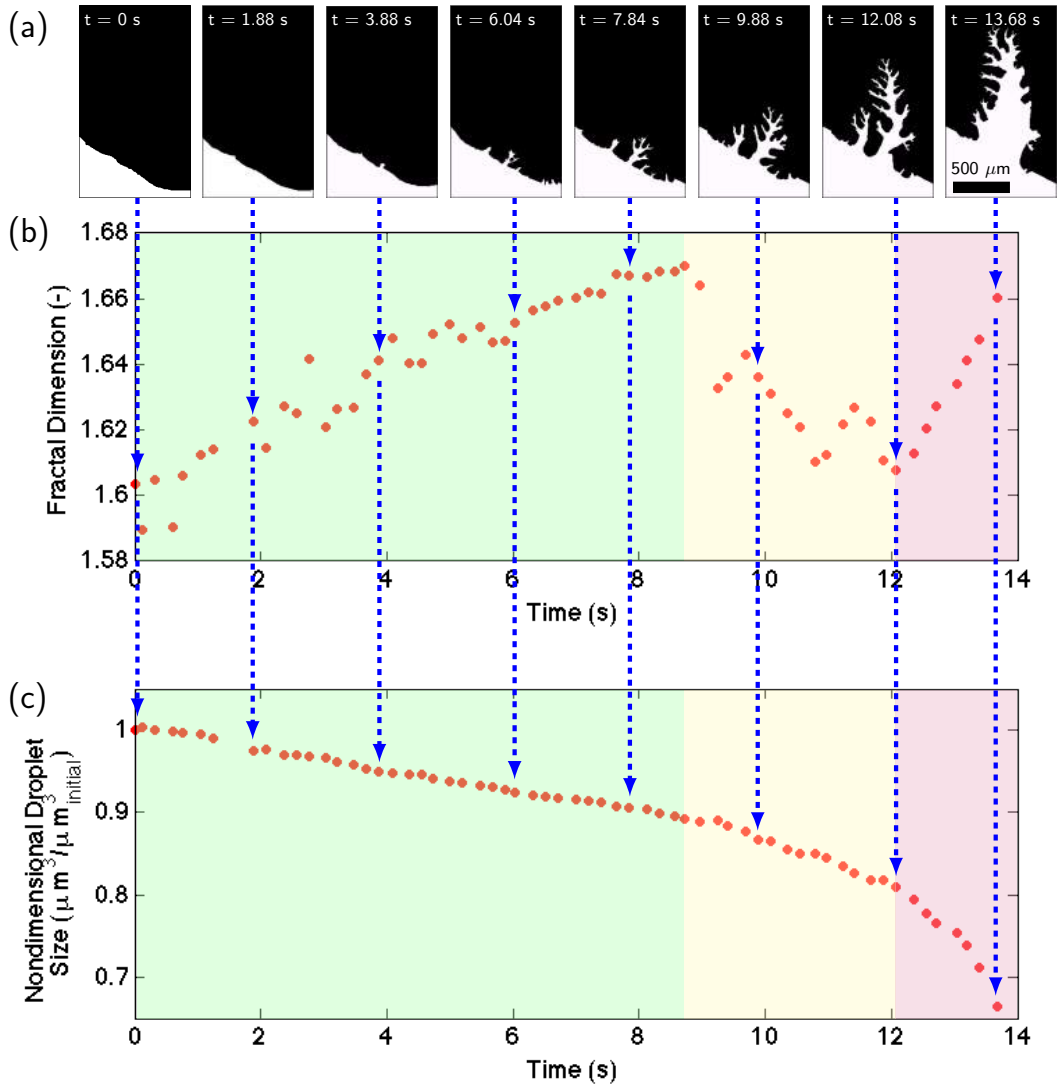
(a)
t = 0 s
t = 1.88 s
t = 3.88 s
t = 6.04 s
t = 7.84 s
t = 9.88 s
t = 12.08 s
t = 13.68 s
500 μm
(b)
Fractal Dimension (-)
1.68
1.66
1.64
1.62
1.6
1.58
0
2
4
6
8
10
12
14
Time (s)
(c)
Nondimensional Droplet Size ($\mu m^3/\mu m^3_{initial}$)
1
0.9
0.8
0.7
0
2
4
6
8
10
12
14
Time (s)

Figure 7.8 *(previous page)*: Time-evolution of interface fractal dimension showing the fingering process between one-dimensional advection and diffusion-limited aggregation [219]. Absence of an imposed flow on this system results in initial diffusively-dominant mass exchange between the solvent and light components in the crude oil (t = 0 s to t = 8.72 s). The resulting interfacial destabilization process is fractal-like in that each perturbed interface is perturbed recursively. Diffusively-driven interfacial perturbation from a flat interface ($D_{f,flat} = 1$) towards a diffusion-limited aggregation condition ($D_{f,DLA} = 1.68 \pm 0.04$) is characterized by a growth in fractal dimensionality from $D_f = 1.55$ to $D_f = 1.67$. Diffusion-driven growth is sustained until hydrodynamic forces, i.e., Marangoni forces dominate (t = 8.72 s to t = 10.96 s), resulting in enhanced mass exchange between the crude oil and the solvent. Reduced diffusive effects in relation to hydrodynamics hinder the interfacial instability, resulting in a more one-dimensional finger and the reduced fractal dimensions ($D_f = 1.67$ to 1.58) of the local interface. Mass exchange at late times (t > 10.96 s) is limited due to excess solvent and scarce light components available for extraction from the crude oil. This enables a return to the diffusively-dominant regime where interfacial instabilities develop and correspond to the increase in the local fractal dimension from $D_f = 1.58$ to 1.66.

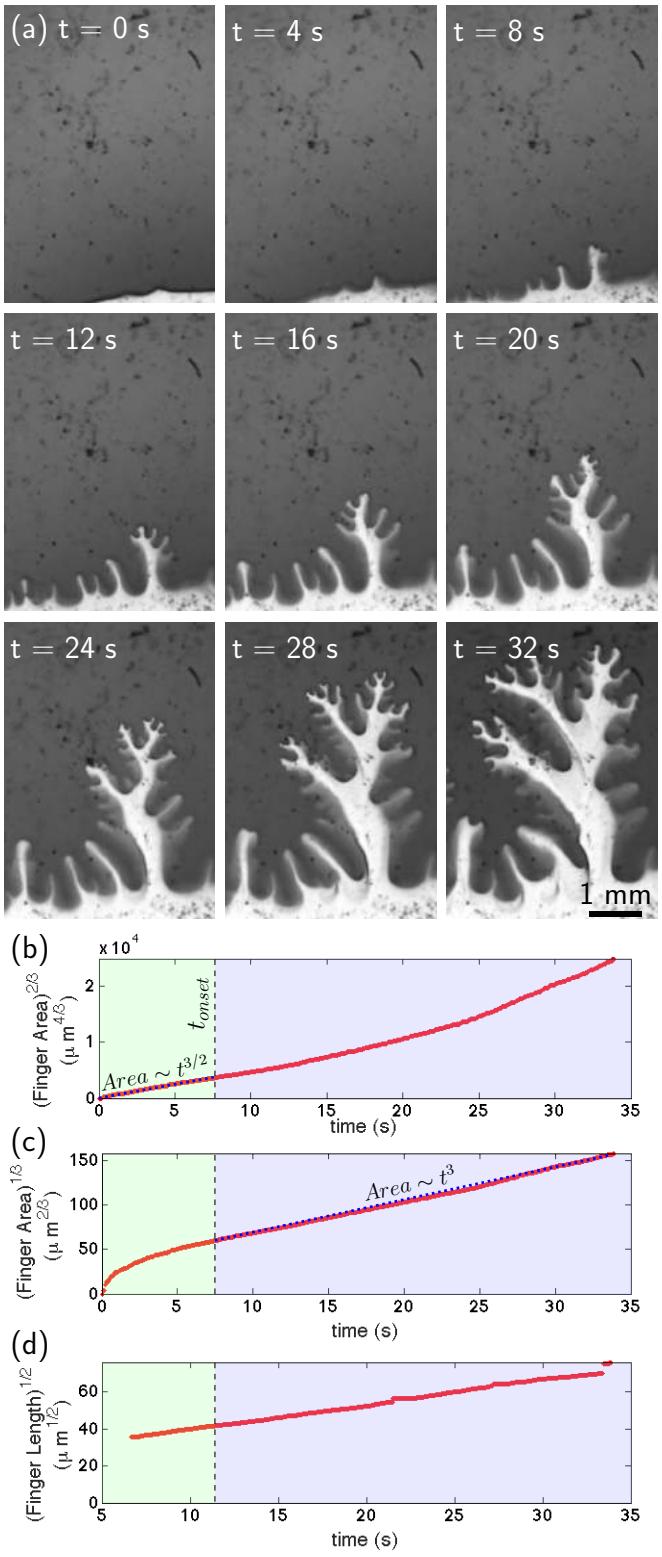
(a) t = 0 s
t = 4 s
t = 8 s
t = 12 s
t = 16 s
t = 20 s
t = 24 s
t = 28 s
t = 32 s
1 mm
(b)
x 10^4
(Finger Area)^2/3 (μ m^4/3)
t_onset
Area ~ t^3/2
time (s)
(c)
(Finger Area)^1/3 (μ m^2/3)
Area ~ t^3
time (s)
(d)
(Finger Length)^1/2 (μ m^1/2)
time (s)

Figure 7.9 *(previous page)*: Velocity of fractal-like finger propagation and light components extraction for a gap spacing of $b = 5$ μm. (a) Fingering evolution at different times. Self-similar fractal-like fingers propagate at a constant velocity into the crude-oil phase. Finger-splitting at the tip of the finger occurs at the same characteristic wavelengths (t = 8 to 32 s), demonstrating the self-similar nature of the fractal-like fingers. The finger tip wavelengths, however, are shorter than the finger edge wavelengths, suggesting that the Marangoni convection cells generated by gradients in dynamic interfacial tension dictate splitting of the self-similar structures. (b),(c) Finger area, a proxy for light components extraction from the crude-oil phase into the solvent phase, scaled to the 2/3 and 1/3 power with respect to time, respectively. (b) Finger area scales with the 3/2 power of time at early times (t = 0 to 8 s, green) scales in accordance with dispersion ($\text{Area}^{2/3} \sim$ t). (c) Onset of finger splitting at t = 8 s transitions finger area scaling to the cube of time ($\text{Area}^{1/3} \sim$ t) thereafter (blue). The cubic relation is accounted for based on the induced convection from the Marangoni effect. (d) Velocity of dominant finger propagation into the crude-oil phase scales with the square of time ($\text{Length}^{1/2} \sim$ t) as dictated by mixing in the Marangoni convection cells.

7.3.3 Spontaneous fingering: a mechanistic depiction

Mutual mass exchange between the miscible fluid pair (crude oil and solvent) underlies the spontaneous fingering observed at early times. In a simplified depiction of the fluid-pair system (Fig. 7.10), the solvent phase is initially composed of single component heptane molecules that are small and mobile (i.e., diffusive); the crude oil phase is comprised of small, light components that are mobile (i.e., diffusive) and large, heavy components that are relatively immobile (i.e., less diffusive).

Initial molecular configurations (t_0, Fig. 7.10a) are such that heptane molecules (small blue circles) are confined to the solvent phase (blue) and crude oil molecules (small yellow and large red circles) are confined to the crude oil phase (orange). The initial compositional distribution leads to sharp concentration gradients, and, thus, a large diffusive driving force that enables mixing in the absence of external driving forces.

Upon contact (t_{0^+}, Fig. 7.10b), miscibility between heptane and crude oil, in

combination with the steep concentration gradient across the interface, forces mutual diffusion of heptane molecules into the crude oil phase and smaller crude-oil molecules into the solvent phase. The diffusion-driven interfacial perturbations correspond to the early-time approach towards DLA (Fig. 7.8a, fractal dimension $D_f \rightarrow 1.67$, and Figs. 7.8b,c, shaded green).

The small gap-spacing requirement is explained here due to its effect on dynamic interfacial tension and capillarity that are length-scale dependent. Specifically, small length-scale scenarios enable large interfacial curvature, and thus, significant pressure differential across the dynamic interface. Recall that the initial rate of diffusion scales with the differential of chemical species partial pressure across the two fluid phases. At small gap spacings, diffusivity of small, mobile heptane and light crude-oil molecules enable rapid mass exchange between the two initial phases.

Large, viscous heavy crude-oil molecules, on the other hand, experience little mass diffusion within the solvent phase. Heavy components are viscous and so have lesser diffusivity, as diffusivity, D, correlates with viscosity, μ, as $D \sim \mu^{\epsilon}$, and the exponent ϵ is related to the molar volume, V, of the species as $\epsilon = 10.2/V - 0.791$ [225]. The intermolecular attraction between the large, immobile molecules retains the molecules in its original phase and thus the observed dark, crude oil phase. Different diffusion rates of the large and small crude-oil molecules result in differential local fluid compositions and thus gradients in local dynamic interfacial tension.

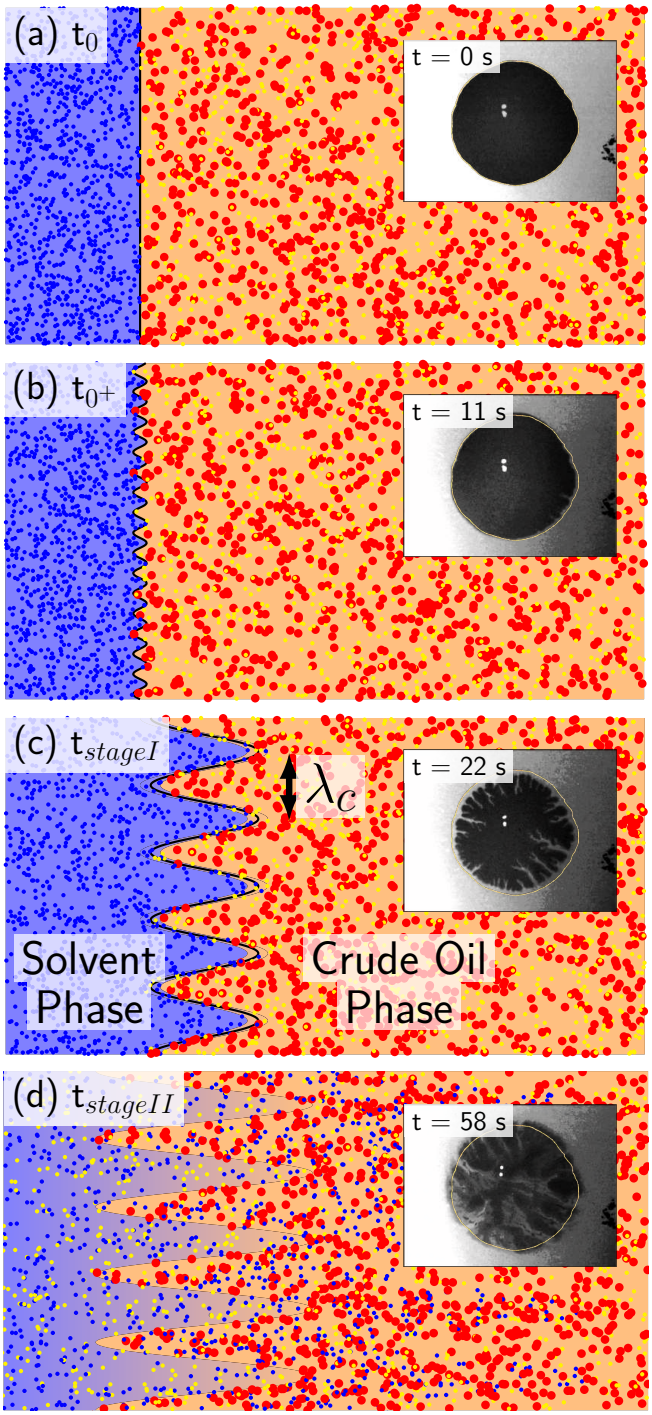
(a) t0
t = 0 s
(b) t0+
t = 11 s
(c) tstageI
λC
t = 22 s
Solvent Phase
Crude Oil Phase
(d) tstageII
t = 58 s
Small mobile heptane molecules
Light mobile crude oil molecules
Heavy immobile crude oil molecules

Figure 7.10 *(previous page)*: Mechanistic depiction of spontaneous fractal-like fingering between crude oil and heptane. (a) Initial fluid distributions ($t = 0$) with small mobile heptane molecules (blue) in the solvent phase (blue) and light, mobile (yellow) and heavy, relatively immobile (red) crude oil molecules in the crude oil phase (orange). (b) Mutual diffusion of heptane molecules and light, mobile crude oil molecules drive interfacial perturbations at very early times (t_{0^+}) that initiate interfacial stability. (c) Instabilities corresponding to the most unstable wavelength, λ_c, drive pressure and dynamic interfacial tension gradients during stage I (t_{stageI}). Local gradients in composition drive mass exchange across the interface and result in gradients in the local dynamic interfacial tension. The arising Marangoni stresses drive mass exchange hydrodynamically. Diffusive mass exchange across the new interface, i.e., finger, perturbs the local interface leading to ramified fingers. Fractal-like fingering due to recursive diffusive-hydrodynamic mass exchange is self-sustained until equilibrium is achieved between the solvent and the crude-oil phases. (d) Slow diffusion of heavy crude oil-components with the light solvent phase results in a diffusive mixing zone ($t_{stageII}$).

Gradients in interfacial tension, i.e., Marangoni stresses, resulting from variations in interfacial composition, lead to hydrodynamic perturbations to the flow (t_{stageI}, Fig. 7.10(c)) because interfacial fluid flows towards interface area with greater tension. With respect to fractal dimensionality, the convection dominance in this regime adds to the linearity of flow, resulting in a decreased fractal dimensionality towards one-dimensional advection and away from DLA (Fig. 7.8a, $D_f \rightarrow 1.55$, and Fig. 7.8b,c, shaded yellow). Marangoni convection enhances subsequent extension of the local diffusively-driven perturbations. Importantly, the composition-driven Marangoni hydrodynamics here enable finger propagation at wavelengths corresponding to the local critical wavelength, λ_c. Further diffusion normal to the newly generated finger interface perturb the local interface as in Fig. 7.10b. Ramified fingers at early times are attributed to the recursive perturbations to the growing local interface.

Recursive diffusive-hydrodynamic mass exchange is self-sustained prior to equilibrium between the solvent and crude-oil phases ($t_{stageII}$, Fig. 7.10(d)). Micro-confinement results in crude-oil droplets of finite volume, similar to crude-oil droplets

residing in petroleum reservoirs, and limits the fingering process to a finite lifetime. Specifically, as the heptane and light crude-oil molecules in the interface between the solvent and crude-oil phases approach equilibrium, the compositionally-driven diffusive-hydrodynamic transport underlying the fingering process is eliminated and stage II begins. Stage II is marked by the slow mixing of large, immobile molecules in the crude oil phase with components in the solvent phase that results in a classic diffusive mixing zone otherwise observed in bulk dimensions. The return to a diffusively-dominant regime restores the fractal dimensionality towards DLA (Fig. 7.8a, $D_f \rightarrow 1.67$, and Figs. 7.8b,c, shaded red).

7.4 Conclusion

The two-stage spontaneous dispersive mechanism observed reveals a surprising mechanism that underlies the Saffman-Taylor instability for miscible, multicomponent fluids. In this work, mixing between heptane and a multicomponent crude oil were studied under no imposed flow conditions (*i.e.*, imposed Peclet number $Pe = 0$). Fractal-like fingers of solvent formed spontaneously. The fingers originated at the edge of the crude oil/heptane boundary and extended into the crude oil droplet without external pressure gradients. The direction of finger propagation was orthogonal to the original interface between the crude oil-solvent fluid-pair. Stage I of the two-stage interaction corresponded to rapid mass exchange between light components in the crude oil and the heptane. Interestingly, the rate of light components liberation, *i.e.*, interface retraction velocity, was much larger than the diffusivity of heavy components into the heptane, and as a result a distinct interface was observed. Dynamic interfacial tension calculations based on the measured length and velocity quantities indicate a strong spatial gradient in dynamic interfacial tension. Fluid systems with gradients in interfacial tension experience diffusocapillary flow, or, the Marangoni

effect, where convection cells are induced. The Marangoni convection cells enhance light components extraction from the crude oil and thus propagate the spontaneous fingers. After light components erosion, heptane and the heavy components of the crude oil enter a purely diffusive regime, corresponding to stage II.

Chapter 8

Conclusions and Future Work

Microfluidics is emerging to be a powerful, critical tool in understanding subsurface transport geared towards energy resources management and environmental remediation [107]. As it stands, energy and the environment present some of the most daunting challenges that society has faced and will face moving forward – issues in health, education, and the economy can be improved largely with the availability of reliable energy.

Petroleum resources, specifically, pervade our economy from transportation to electricity and manufacturing [226]. Hydrocarbon combustion has resulted in significant changes to the climate - geological storage of CO_2 presents an opportunity to mediate this issue [50]. These important subsurface resource challenges are ultimately dictated by micro- and nano-scale fluid-solid interactions due to the porous nature of geological materials. Fundamental understanding of small-scale fluid behavior in the subsurface is limited due to complexities in fluid composition and phase behavior, mineralogical heterogeneities in subsurface reservoirs, micro- and nano-scale fluid-mineral interactions, and, importantly, the extrapolation of small-scale behavior to reservoir-scale ($\sim$ km) phenomena. Microfluidic methods provide direct, real-time insight on these fundamental pore-level interactions by providing a means to visualize

these important fluid-mineral interactions directly [227]. Fundamental understanding of small-scale behavior provides the basis for upscaled modeling of flow behavior and prediction of reservoir-scale environmental impacts. The foundation that mechanistic understanding provides enables decision-making in engineering practice that ultimately leads to improved methods of fueling our society's future sustainably with the least environmental impact.

8.1 Summary of Present Work

This dissertation contributes to the fundamental understanding of fluid-fluid and fluid-solid interactions in subsurface reservoir systems through enabling-technology development and fundamental scientific discovery. The contributions are organized into five themes: (i) development of realistic microvisualization platforms for the study of transport through clay-rich sandstone; (ii) investigation of formation damage in clay-rich sandstone as a result of fines migration at low salinity conditions; (iii) investigation of pore-scale dynamics during low salinity waterflooding, the discovery of a spontaneous Pickering emulsification and flow diversion mechanism, and the design of a cyclic salinity injection process to enhance oil recovery; (iv) development of calcite-functionalized microvisual devices, its usage in investigating reactive transport through carbonate CO_2 storage reservoirs, and the discovery of a new protective mechanism termed here the "grain-engulfment effect"; (v) the investigation of miscible fluid interactions at the microscale and the discovery of spontaneous fractal-like fingering in the absence of an external pressure gradient due to compositional complexity of the fluids. The contributions to device development, fundamental mechanistic understanding, and applied engineering practice are described in the following.

First, clay-rich petroleum reservoirs hold promise for significant energy resources recovery. Of particular industrial interest is low salinity waterflooding due to its low

impact to the environment and low cost. The fundamental mechanisms that dictate this process, however, are poorly understood due to conflicting core flooding and field evidence. To provide a mechanistic understanding of the low salinity effect, this work enables direct visualization of the pore-scale dynamics through the development of a two-dimensional silicon microfluidic networks with representative pore geometry (*i.e.*, micromodels) and representative surface characteristics of clay-rich rock. Specifically, a method is developed to deposit clay particles into the micromodel pore space. Surface morphology, wettability, and salinity sensitivity properties of the clay-functionalized model are validated with those of clay-rich rock. The surface-functionalized models also corroborate the hypothesis of clay insensitivity to brine salinity after thermal treatment. Upon validation of the surface functionalization process, the clay-functionalized micromodels are then used to determine the conditions at which stably adhered clay particles detach and to study the pore-level interactions between the crude oil, brine, and solid surfaces during aging and during low salinity brine injection. Specifically, kaolinite clay particles were adsorbed stably for salt concentrations greater than the critical salt concentration (CSC) of 4000 ppm NaCl and were mobilized for salt concentrations below the CSC limit. These results correspond well to reported CSC values of real clay-rich reservoir rock from the literature. The experimental results provide a basis for improving the basic understanding of the mechanisms at play, including fine clay particles mobilization, ion exchange, and emulsification. Pore-scale flow simulation is used to corroborate experimental observations of the dominant mechanism(s) at play during low salinity waterflooding in sandstones. Mechanistic understanding of pore-level behavior sets the basis for upscaling and informing the design of optimal injection fluids at the field scale.

Second, formation damage observed during field-scale low salinity waterflooding due to fine clay particles mobilization is studied using the clay-functionalized micromodels. Using the clay-functionalized micromodel developed in this work, the

mobilization of clay particles, its impact on flow paths, and its effect on oil recovery is investigated. Under low salinity conditions, a 6-fold reduction in permeability was identified through pressure measurements due to kaolinite migration and flow path blockage. Montmorillonite clay swelling was also observed at low salinities. Pore-scale imaging and mapping show that the pores most susceptible to particle mobilization and flow path blockage are correlated inversely with improved oil recovery. Flow diversion due to preferential flow path blockage is proposed as a mechanism dictating improved oil recovery at low salinities.

Third, clay-functionalized micromodels were used to investigate the evolution of pore-surface wettability, or, aging, and the interplay between clay minerals and the crude oil and brine. Creation of initial subsurface reservoir conditions in the laboratory is central to understanding the underlying mechanisms of the low salinity effect and remains an open question. Direct observation of water-wet surfaces shifting towards mixed-wettability due to attraction between charged clay particles and crude oil is achieved using the kaolinite-functionalized micromodel. Initial high salinity brine injection into the aged micromodel corresponding to conventional waterflooding processes showed $\sim$ 38 % oil recovery. Low salinity waterflooding using 4000 ppm brine increased the recovery factor by an additional $\sim$ 6.5 % of the original oil in place (OOIP). Interestingly, further low salinity waterflooding of this aged system using deionized water reveals a new spontaneous Pickering emulsification mechanism by which preferential flow paths are obstructed, leading to flow diversion through oil-filled pores to improve overall oil recovery. The pore-level Pickering emulsions generated in the preferential flow paths are $\sim$ 5 to 30 μm in diameter and have remained stable since January 2016. Bulk-scale Pickering emulsions show similar stability. Importantly, the pressure differential required for subsequent fluids to flow through the emulsion-filled paths is increased significantly, thus enabling flow diversion through oil-filled pores. Leveraging the flow diversion mechanism, a new salinity

cycling method is developed that increases overall oil recovery by an additional ~ 8 % OOIP.

Fourth, fundamental understanding of the dynamics dictating reactive transport through carbonates is required to engineer effective formation stimulation and safe CO_2 storage projects. Calcite-functionalized microfluidic systems are developed and used in this work to delineate the interplay between dissolution, flow, and surface wettability. Novel two-dimensional calcite-functionalized micromodels with representative pore geometry and surface reactive properties are developed in this work to study the dissolution of carbonates under acidic flows. Importantly, a new mechanism is discovered whereby the reaction product CO_2 is wetted on the reactive grain surface and protects the grain from further dissolution. Experimental results show similar effects at a range of temperatures, pressures, and acidities corresponding to both surface and subsurface conditions. One-dimensional non-reactive polymer-based microchannel containing an embedded reactive calcite post is developed to further delineate the conditions required for the grain-engulfment effect to dominate. The calcite post is an octagonal prism of 500 μm width and 300 μm height, and the channel is 1.5 mm in width. Flow regimes corresponding to the observed grain-engulfment mechanism in porous media were delineated using the one-dimensional reactive transport devices and provide a first order understanding for large-scale CO_2 storage security assessments.

Fifth, miscible fluid interactions between crude oil and solvent are investigated to understand mechanisms underlying improved heavy-oil recovery of highly viscous and immobile crude oil. Specifically, interactions between crude oil and solvent are investigated under microconstrained geometries similar to geological porous media. Significantly, spontaneous fingering between the crude oil with complex composition and the solvent is observed. That is, fractal-like fingers are generated in the absence

of an applied external pressure gradient, i.e., zero Peclet number. The surprising dynamics observed are a result of the complex composition of the crude oil; light mobile crude-oil components are exchanged with the solvent phase while heavy immobile crude-oil components remain in the crude-oil phase. Recursive diffusion-driven mass exchange leads to local instabilities at the interface that result in differences in dynamic interfacial tension along the interface and leads to fractal-like fingering. The resulting Marangoni flow enhances the mass exchange until components in the crude oil phase reach local equilibrium with those in the solvent phase.

The geochemically-representative devices developed in this work enable a wide range of investigations to the fundamental mechanisms dictating transport through subsurface systems. Importantly, the new fundamental mechanisms delineated in this work are of fundamental importance to the understanding and design subsurface energy and environmental resources management and to the broader field of engineering science.

8.2 Future Opportunities for Geochemical Microfluidics

Indeed, there is plenty of room at the bottom [228]. Resolution of fluid-mineral interactions at the micro- and nanoscale are of increasing importance to improving subsurface, and, surface, energy and environmental resources engineering processes. The scientific community has only begun to leverage microfluidics in studying energy and environmental resources in the subsurface; there remain immense opportunities to take full advantage of the fundamental micro- and nano-scale understanding that microfluidics offers.

8.2.1 Visualization of Flow in Three Dimensions

Moving forward, one key challenge to address is in the dimensionality of the visualization devices. Specifically, microfluidics are inherently two-dimensional flow visualization platforms. Real geological materials, on the other hand, are in three dimensions. Some work has been started in capturing the contrast in length scales between pore bodies and pore throats of glass-based micromodels [127] and in magnified porous media through additive manufacturing [229, 230]. 3D printed rock enables repetition through control of three-dimensional pore geometry but are challenged by limitations in printing resolution and geometric integrity after resin polymerization. Similar to polymer-, glass-, and silicon-based microfluidics, 3D printed rock lack the representative surface properties of real rock. Importantly, direct real-time visualization of the microscale fluid-fluid and fluid-mineral dynamics are difficult to capture due to the opaque resin material.

Confocal imaging of refractive index-matched fluids and glass beads provides an alternate route to flow visualization in a three-dimensional porous medium [231, 232, 233, 234, 235, 236]. Use of real mineral surfaces such as clays and carbonates and of real fluids such as crude oils and brine, however, are difficult to achieve. At best, images are taken at the surface of the three-dimensional porous medium. Pore-level visualization of petroleum fluid dynamics in three-dimensional media at real-time, real-scale, surface-representative conditions provides a host of opportunities for novel device and visualization development.

8.2.2 Nanoscale

At the nanometer scale, while significant headway has been made using nano- and nanoconfined-geometries [83, 110], direct visualization of fundamental fluid dynamics and fluid-solid interactions such as adsorption at length scales below the wavelengths

of visible light remain an opportunity. Of particular interest to the subsurface energy resources community are the nanoscale pores in shale. While fabrication of etched-silicon nanochannels ($\sim$ nm in two dimensions) and nanoconfined channels ($\sim$ nm in one dimension) is possible with electron-beam lithography and plasma etching [85, 237, 238, 83, 84, 239, 86] and sacrificial layer etching and microchannel bonding [110], direct optical visualization is difficult. Specifically, nanochannels of the size of shale pores are shorter than the wavelength of light. That is, nanoscale systems are diffraction-limited with respect to visible light. Direct optical observation of nanoscale dynamics are hence limited. In this respect, use of luminescence provides a possible route in providing super-resolution microscopy. Specifically, fluorescent tagging of fluid molecules, ions, and solid particles provide an avenue toward super-resolved fluorescence to enable optical visualization of nanometer dynamics.

The complexity of subsurface systems, especially those pertinent to petroleum and CO_2 storage resources, provides exciting, and, important opportunities that microfluidics are well positioned to pursue.

Appendix A

Reactive Transport Model

A reservoir-scale reactive transport model is developed to upscale the pore-scale grain-engulfment mechanism to the reservoir. The code follows from the equations developed in Chapter 6 and is shown here.

A.1 Main input file

Input parameters are adjusted in this file.

```
1
2  clear
3  close all
4  clc
5
6
7  %% BOUNDARY CONDITIONS
8  % left constant pressure boundary
9  % right constant pressure boundary
10 % top no flow boundary
11 % bottom no flow boundary
12
13 P_downstream = 1200*6894.76;     % 1200 psi, [Pa]
14 kc = 8.4e-5; %REACTION RATE CONSTANT FOR [H+] WITH CaCO3 [m/s
       ]
15 c_inject = 10; %pH = 2 %550; %injection [H+] concentration [
       mol/m3_water]
16 timesteps=1e2%5e3;
17 u_inj = 50/24/3600;                          % [m/s]
18
19 %% RESERVOIR FLUID PROPERTIES
20 mu = 0.7255e-3;      % dynamic viscosity water at 35C [Pa-s]
21 %% RESERVOIR GRID PROPERTIES
22 L = 100;       % RESERVOIR LENGTH IN i-DIRECTION
```

```
23 W = 25;       % RESERVOIR WIDTH IN j-DIRECTION
24 H = 10;       % RESERVOIR HEIGHT IN k-DIRECTION
25 dx = 1;      % block size in x
26 dy = 1;      % block size in y
27 Nx = L/dx;   % number of blocks in i-direction
28 Ny = W/dy;   % number of blocks in j-direction
29
30 %% populate initial reservoir properties
31 phi_0_file = load('phi_0');
32 phi_0 = phi_0_file.phi_0(1:25,:);
33
34 phi = phi_0;
35 k_init = zeros(Ny,Nx);
36 Dp = 100e-6*ones(Ny,Nx);      % grain diameter, [m]
37 [k_0, P_0] = pressure(u_inj, P_downstream, mu, phi_0, Dp, dx,
       dy, Nx, Ny);
38
39 figure
40 surf(P_0/6894.76)
41 k_old = k_0;
42 NUMBER_GRAINS = (1-phi)*dx*dy*H./(4/3*pi*(Dp/2).^3);
43 MOLAR_MASS_CaCO3 = 100.0869; %[g_CaCO3/mol_CaCO3]
44 DENSITY_CaCO3 = 2.71e6; %[g_CaCO3/m3]
45 DENSITY_WATER = 1000; %[kg WATER/m3 WATER]
46 %% CO2 PROPERTIES
47
48
```

```
49 c_H_0 = zeros(Ny,Nx);
50 c_H_old = c_H_0;
51 moles_H_cum_old = zeros(Ny,Nx);
52 flux_rate_old = zeros(Ny,Nx);
53 moles_CaCO3_total= (1-phi)*dx*dy*H * DENSITY_CaCO3 /
       MOLAR_MASS_CaCO3; % density =2.7g/cm3 and 100g/gmol CaCo3
54 c_CO2_old = zeros(Ny,Nx);
55
56 dt = 0.001*24*60*60;
57
58
59 c_CO2_sep_phase = zeros(Ny,Nx,timesteps);
60
61
62 for ii = 1:timesteps
63     a = ii
64
65     %% MASS BALANCE ON WATER : PERMEABILITY AND PRESSURE
66     [k, P] = pressure(u_inj, P_downstream, mu, phi, Dp, dx,
           dy, Nx, Ny);
67     k_old = k;
68     %% ACID VELOCITIES ACROSS INTERFACES
69     [u_acid_x_interface, u_acid_y_interface] =
           velocity_acid_interface(mu, Nx, Ny, dx, dy, P, u_inj,
           P_downstream, k);
70
71     %% SURFACE AREA AND VOLUME FOR REACTION
```

```
72      [SA,Volume_CaCO3] = reaction_area_per_block(Dp, dx, dy, H
            , phi);
73
74      %% MASS BALANCE ON ACID - solve for concentration at next
            time step explicitly
75      [c_H_new, moles_H_cum_new, flux_rate_new, Q_rxn,Da] =
            acid_concentration_flux_then_react(phi, flux_rate_old,
            moles_CaCO3_total, moles_H_cum_old, c_H_old, kc,
            c_inject, SA, Nx, Ny, dt, dx, dy, H,
            u_acid_x_interface, u_acid_y_interface);
76      c_H_old = c_H_new; %[mol/m3]
77      flux_rate_old = flux_rate_new;%[mol/s]
78
79      %% CO2 CONCENTRATION
80      [solubility_CO2] = CO2solubility(P,Nx,Ny);
81      [c_CO2_new, c_CO2_separate_phase] = concentration_CO2(
            u_acid_x_interface, u_acid_y_interface, Nx, Ny,
            c_CO2_old, dx,dy,H,dt,Q_rxn,solubility_CO2,phi);
82      c_CO2_old = c_CO2_new;
83
84      c_CO2_sep_phase(:,:,ii) = c_CO2_separate_phase;
85
86      %% VOLUME OF CaCO3 dissolved in time step and new
            porosity...     %     volume of CaCO3 dissolved in time
            step
87      moles_CaCO3_dissolved = 0.5 * Q_rxn * dt; %[moles]
```

```
88      volume_CaCO3_dissolved = moles_CaCO3_dissolved *
            MOLAR_MASS_CaCO3 / DENSITY_CaCO3; %[moles_CaCO3]*[
            g_CaCO3/moles_CaCO3]*[m3/g_CaCO3]
89      phi = phi + volume_CaCO3_dissolved/dx/dy/H;
90      phi(phi>1)=1;
91      Dp = 2*((1-phi)*dx*dy*H ./ NUMBER_GRAINS * 3/4/pi).^(1/3)
            ;
92
93
94  end
95
96  save('c_CO2_sep_phase.mat','c_CO2_sep_phase','-v7.3')
```

A.2 Reaction and Flow Routine

Reaction and flow are coupled in this routine for each time step.

```
% function [c_new, flux_rate_new] =
    acid_concentration_flux_then_react(c_old, c_inject, Nx,
    Ny, dt, dx, dy, H, u_acid_x_interface, u_acid_y_interface)
function [c_new, moles_H_cum_new, flux_rate_new, Q_rxn,Da] =
    acid_concentration_flux_then_react(phi, flux_rate_old,
    moles_CaCO3_total, moles_H_cum_old, c_old, kc, c_inject,
    SA, Nx, Ny, dt, dx, dy, H, u_acid_x_interface,
    u_acid_y_interface)

u_L_mat = u_acid_x_interface(:,1:Nx);
c_L = [c_inject*dt*u_L_mat(:,1)/dx c_old(:,1:Nx-1)].*(u_L_mat
    >0) + c_old.*(u_L_mat<=0);
u_R_mat = u_acid_x_interface(:,2:Nx+1);
c_R =c_old.* (u_R_mat>=0) + [c_old(:,2:Nx) zeros(Ny,1)].*(
    u_R_mat<0);

u_T_mat = u_acid_y_interface(1:Ny,:);
c_T = (u_T_mat>0).*[zeros(1,Nx); c_old(1:Ny-1,:)] + (u_T_mat
    <=0).*c_old;

u_B_mat = u_acid_y_interface(2:Ny+1,:);
c_B = (u_B_mat>=0).*c_old + (u_B_mat<0).*[c_old(2:Ny,:);
    zeros(1,Nx)];

```

```
15 %% ACID FLUX
16 flux_rate_new = (u_L_mat/dx.*c_L - u_R_mat/dx.*c_R + u_T_mat/
       dy.*c_T - u_B_mat/dy.*c_B); % [mol/s]
17 c_intermediate = c_old + flux_rate_new*dt; %[mol/m3]
18
19 %% ACID REACTION
20 %max amount of reaction possible for geometry
21 Q_rxn_max = kc.*c_intermediate.*SA;
22
23 %max amount of reaction possible s.t. [H+] is conserved (i.e
       ., only react
24 %as much as the amount of acid that is there
25 Q_rxn_H_conservation = Q_rxn_max.*(Q_rxn_max*dt <=
       c_intermediate*dx*dy*H) + (c_intermediate*dx*dy*H/dt).*(
       Q_rxn_max*dt>c_intermediate*dx*dy*H);
26
27 moles_H_cum_projected = moles_H_cum_old +
       Q_rxn_H_conservation*dt;
28 Q_rxn = (moles_H_cum_projected<moles_CaCO3_total*2).*
       Q_rxn_H_conservation + (moles_H_cum_projected==
       moles_CaCO3_total*2).*zeros(Ny,Nx) + (
       moles_H_cum_projected>moles_CaCO3_total*2).* (
       moles_H_cum_projected-moles_CaCO3_total*2)/dt;
29 Q_rxn = Q_rxn.*(phi<1) + zeros(Ny,Nx).*(phi>=1);
30 moles_H_cum_new = moles_H_cum_old + Q_rxn*dt;
31
32 %% NEW ACID CONCENTRATION
```

```
33 c_new = c_intermediate - Q_rxn*dt/dx/dy/H;
34 c_new(c_new<1e-16)=0;
35 % c_new = (c_new1>0).*c_new1 + (c_new1<0)*c_inject;
36
37 %% DAMKOHLER NUMBER
38 u_avg = (abs(u_L_mat)+abs(u_R_mat)+abs(u_T_mat)+abs(u_B_mat))
       /4;
39 % Da = Q_rxn_H_conservation./(u_L_mat*dy*H.*c_L - u_R_mat*dy*
       H.*c_R + u_T_mat*dx*H.*c_T - u_B_mat*dy*H.*c_B);
40 Da = kc*SA./u_avg/dx/H;
41 %Da = kc*c_intermediate.*SA./(u_L_mat*dy*H.*c_L - u_R_mat*dy*
       H.*c_R + u_T_mat*dx*H.*c_T - u_B_mat*dy*H.*c_B);
42 Da(isnan(Da))=0;
43
44
45
46 end
```

A.3 Solubility of CO_2 in the Aqueous Phase

The solubility of CO_2 in the aqueous phase as a function of pressure and temperature is generated.

```
function [solubility_CO2] = CO2solubility(P,Nx,Ny)


P_ref = [1; 5; 10; 50; 100; 200; 300; 400; 500; 600; 700;
    800; 900; 1000; 1100; 1200; 1300; 1400; 1500; 1600; 1700;
    1800; 1900; 2000];
solubility_CO2_30C = [.0286; .1442; .2809; 1.0811; 1.3611;
    1.4889; 1.5989; 1.7005; 1.7965; 1.8883; 1.9767; 2.0622;
    2.1450; 2.2254; 2.3034; 2.3792; 2.4527; 2.5240; 2.5933;
    2.6605; 2.7251; 2.7882; 2.8486; 2.9071];
solubility_CO2_60C = [.0137; .0803; .1602; .6695; 1.0275;
    1.2344; 1.3495; 1.4478; 1.5368; 1.6194; 1.6970; 1.7703;
    1.8399; 1.9062; 1.9692; 2.0292; 2.0864; 2.1407; 2.1924;
    2.2413; 2.2875; 2.3312; 2.3725; 2.4110];

solubility_CO2_35C = solubility_CO2_30C + (solubility_CO2_60C
    -solubility_CO2_30C)/30*5;

for i = 1:Ny
    for j = 1:Nx
        solubility_CO2(i,j) = interp1(P_ref,
            solubility_CO2_35C,P(i,j)/1e5);
    end
```

```
14 end
```

A.4 Concentration of CO_2

The concentration of CO_2 in the aqueous and separate phases are calculated for each block. If the total CO_2 in each block exceeds the solubility of CO_2 in the aqueous phase, then a separate phase is generated.

```
function [c_CO2_new, c_CO2_separate_phase] =
    concentration_CO2(u_acid_x_interface, u_acid_y_interface,
    Nx, Ny, c_CO2_old, dx,dy,H,dt,Q_rxn,solubility_CO2,phi)
%% CO2 FLUX FROM PREVIOUS CONCENTRATIONS
    u_L_mat = u_acid_x_interface(:,1:Nx);
    c_CO2_L = [zeros(Ny,1) c_CO2_old(:,1:Nx-1)].*(u_L_mat>0)
        + c_CO2_old.*(u_L_mat<=0);
    u_R_mat = u_acid_x_interface(:,2:Nx+1);
    c_CO2_R =c_CO2_old.* (u_R_mat>=0) + [c_CO2_old(:,2:Nx)
        zeros(Ny,1)].*(u_R_mat<0);
    u_T_mat = u_acid_y_interface(1:Ny,:);
    c_CO2_T = (u_T_mat>0).*[zeros(1,Nx); c_CO2_old(1:Ny-1,:)]
        + (u_T_mat<=0).*c_CO2_old;
    u_B_mat = u_acid_y_interface(2:Ny+1,:);
    c_CO2_B = (u_B_mat>=0).*c_CO2_old + (u_B_mat<0).*[
        c_CO2_old(2:Ny,:); zeros(1,Nx)];

    %% FLUX
    flux_CO2 = (u_L_mat/dx.*c_CO2_L - u_R_mat/dx.*c_CO2_R +
        u_T_mat/dy.*c_CO2_T - u_B_mat/dy.*c_CO2_B); % [mol/m3s
        ]
    %c_intermediate = c_CO2_old + flux_rate_CO2*dt; %[mol/m3]
```

```
15
16      %% GENERATION OF CO2 THROUGH REACTION
17      conc_CO2_rxn = .5 * Q_rxn * dt / dx/dy/H;
18
19      %% CO2 CONCENTRATION
20      c_CO2_new = c_CO2_old + flux_CO2*dt + conc_CO2_rxn;
21      %% SOLUBILITY OF CO2 IN WATER
22      %assuming single phase flow, maximum amount of CO2 that
            can dissolve into
23      %water
24      conc_CO2_max_aq = solubility_CO2.*phi;
25
26      c_CO2_separate_phase = (c_CO2_new - conc_CO2_max_aq).*(
            c_CO2_new>conc_CO2_max_aq) + zeros(Ny,Nx).*((c_CO2_new
            <=conc_CO2_max_aq));
27  end
```

A.5 Pressure

The pressure equation is solved to determine the pressure of each grid block in the reservoir.

```
function [k, P] = pressure(u_inj, P_downstream, mu, phi, Dp,
    dx, dy, Nx, Ny)
tau = 3*ones(Ny,Nx);            % tortuosity, usually 2<tau<5
k = 1/72./tau.*phi.^3.*Dp.^2./(1-phi).^2; % permeability from
     Carman-Kozeny, [m2]
k(isnan(k))=1;
% k = 1.*(phi>=1) + k.*(phi<1);
%% TRANSMISSIBILITY MATRIX
permx = reshape(k',Ny*Nx,1);
permy = reshape(k, Ny*Nx,1);
K_Harx_minus = permx;
K_Harx_plus = permx;

K_Harx_minus(2:end) = 2*permx(2:end).*permx(1:end-1)./(permx
    (2:end)+permx(1:end-1));%harmonic average
K_Harx_plus(1:end-1) = 2*permx(2:end).*permx(1:end-1)./(permx
    (2:end)+permx(1:end-1));%harmonic average
K_Harx_minus(1:Nx:end)=permx(1:Nx:end);
K_Harx_plus(Nx:Nx:end)=permx(5:Nx:end);

K_Hary_minus = permy;
K_Hary_plus = permy;
```

```
19 K_Hary_minus(2:end) = 2*permy(2:end).*permy(1:end-1)./(permy
       (2:end)+permy(1:end-1)); %harmonic average
20 K_Hary_plus(1:end-1) = 2*permy(2:end).*permy(1:end-1)./(permy
       (2:end)+permy(1:end-1));%harmonic average
21 K_Hary_minus(1:Ny:end)=permy(1:Ny:end);
22 K_Hary_plus(Ny:Ny:end)=permy(Ny:Ny:end);
23
24 K_Hary_minus_mat=reshape(K_Hary_minus,Ny,Nx);
25 K_Hary_minus = reshape(K_Hary_minus_mat',Ny*Nx,1);
26 K_Hary_plus_mat=reshape(K_Hary_plus,Ny,Nx);
27 K_Hary_plus = reshape(K_Hary_plus_mat',Ny*Nx,1);
28
29 length_P = Nx*Ny;
30 Txplus = K_Harx_plus/dx^2/mu;              %transmissibility
       across x+
31 Txminus = K_Harx_minus/dx^2/mu;            %transmissibility
       across x-
32 Typlus = K_Hary_plus/dy^2/mu;              %transmissibility
       across y+
33 Tyminus = K_Hary_minus/dy^2/mu;            %transmissibility
       across y-
34
35 Tyminus(1:Nx) = 0;
36 Typlus(end-Nx+1:end) = 0;
37 Txminus(1:Nx:end) = 0;
38 Txplus(Nx:Nx:end) = 0;
39
```

```
40 Tdiag = -(Txminus + Txplus + Tyminus + Typlus);
41 Tdiag(Nx:Nx:end) = Tdiag(Nx:Nx:end)-2*permx(Nx:Nx:end)/dx^2/
       mu;
42
43 TRANS_MATRIX = spdiags([ Typlus Txplus Tdiag Txminus Tyminus
       ],[-Nx -1 0 1 +Nx],Nx*Ny,Nx*Ny)';
44
45 %% SOLVE FOR PRESSURE
46 b = zeros(length_P,1);
47 b(1:Nx:end) = -u_inj;
48 b(Nx:Nx:end) = -permx(Nx:Nx:end)/dx^2*2*P_downstream/mu;
49 P = TRANS_MATRIX\b;
50 P = reshape(P,Nx,Ny)';
51 end
```

A.6 Reaction Rates

The amount of reacted calcite rock material is calculated for each block based on the available surface area for reaction.

```
1 function [SA,Volume_CaCO3] = reaction_area_per_block(Dp, dx,
    dy, H, phi)
2 av = 6./Dp;                    % reaction surface area per
    volume of CaCO3, assuming spherical grains [1/m]
3 Volume_CaCO3 = (1-phi)*dx*dy*H; %VOLUME OF CaCO3 PER GRID
    BLOCK
4 SA = Volume_CaCO3.*av;         %SURFACE AREA OF CaCO3
    AVAILABLE FOR REACTION PER GRID BLOCK
5 SA(isnan(SA))=0;
6 end
```

```
function [u_acid_x_interface, u_acid_y_interface] =
    velocity_acid_interface(mu, Nx, Ny, dx, dy, P, u_inj,
    P_downstream, k)
%% ACID FLOW RATE IN x-DIRECTION
u_acid_x_interface = zeros(Ny,Nx+1);
u_acid_x_interface(:,1) = u_inj; %-k(:,1).*(P(:,1)-P_upstream
    )*2/dx/mu;
u_acid_x_interface(:,Nx+1) = -k(:,Nx).*(P_downstream-P(:,Nx))
    *2/dx/mu;
u_acid_x_interface(:,2:Nx) = -2*(k(:,2:Nx).*k(:,1:Nx-1)./(k
    (:,2:Nx)+k(:,1:Nx-1))).*(P(:,2:Nx)-P(:,1:Nx-1))/dx/mu;

%% ACID FLOW RATE IN y-DIRECTION
u_acid_y_interface = zeros(Ny+1,Nx);
u_acid_y_interface(1,:) = 0;
u_acid_y_interface(Ny+1,:) = 0;
u_acid_y_interface(2:Ny,:) = -2*(k(2:Ny,:).*k(1:Ny-1,:)./(k
    (2:Ny,:)+k(1:Ny-1,:))).*(P(2:Ny,:)-P(1:Ny-1,:))/dy/mu;

end
```

Appendix B

CMG Input Code

```
1  ** ------------------------------------**
2  ** GMGHG012.DAT:  CO2 Sequestration With No Trace Component
                    **
3  ** ------------------------------------**
4  ** ------------------------------------**
5  ** **
6  ** FILE:  GMGHG012.DAT
                                                          **
7  ** **
8  ** MODEL: CART 9x9x4 GRID                  CO2 INJECTION INTO AN
                  **
9  ** 1 COMPONENT                          AQUIFER WITH GEOCHEMISTRY
            **
10 ** WATER-GAS MODEL
                                                       **
```

```
** SI UNITS                                                    **
** **
** ------------------------------------**
** **
** This template data set is constructed to model gas sequestration   **
** into an  aquifer.  CO2 injection is done for first 25 years.        **
** The injector is shutin thereafter and the fate of CO2 is modelled   **
** for next 225 years. Chemical equilibrium constants are functions    **
** of temperature. Trace gas is not used (AQFILL ON). CO2 inventory    **
** information is output for plotting.                                 **
** **
** ------------------------------------**
** CONTACT CMG at (403)531-1300 or support@cmgl.ca                     **
** ------------------------------------**
** 2018-01-05, 4:26:01 PM, wensong
RESULTS SIMULATOR GEM 201210

** ------- Input/Output ----------------
FILENAMES OUTPUT SRFOUT RESTARTOUT INDEXOUT MAINRESULTSOUT
```

```
30 RANGECHECK ON
31 *INUNIT *SI
32 INTERRUPT INTERACTIVE
33 *XDR *ON
34 REWIND 3
35 *MAXERROR 20
36 WRST TIME
37 WPRN WELL TIME
38 WPRN GRID TIME
39 WPRN ITER BRIEF
40 WSRF WELL 1
41 WSRF GRID TIME
42 OUTSRF WELL PSPLIT
43 *DIARY *CHANGES
44 OUTPRN WELL BRIEF
45 OUTPRN GRID DPORMNR IMPL MINERAL 'Calcite' MOLALITY 'CO2' PH
       TEMP
46 OUTPRN RES NONE
47 OUTSRF GRID DENG DENW DPORMNR DROP MINERAL 'Calcite' MOLALITY
       'CO2' MOLALITY 'CO3--' MOLALITY 'Ca++' MOLALITY 'H+'
       MOLALITY 'HCO3-' MOLALITY 'OH-'
48                 PH POROS PRES SG SW TEMP W 'CO2' X 'CO2' XALL Y '
                       CH4' Y 'CO2'
49                 Z 'CO2'
50 OUTPRN RES ALL
51 OUTSRF RES ALL
52
```

```
53
54 ** ———————— Grid ————————————————————
55 RESULTS AXES-DIRECTIONS 1. 1. 1.
56 *GRID *VARI 90 90 1
57 *KDIR DOWN
58 *DI *CON 17.5
59 *DJ *CON 17.5
60 *DK *CON 10.
61 *DTOP 8100*900.
62 **$  0 = null block, 1 = active block
63 NULL CON              1
64 *POR CON 0.38
65 *PERMI CON 2000.
66 PERMJ EQUALSI
67 PERMK EQUALSI
68 **$  0 = pinched block, 1 = active block
69 PINCHOUTARRAY CON              1
70 *CPOR  MATRIX    1.E-08
71 *PRPOR MATRIX    1000.
72
73 ** ———————————— Fluid Model ————————————
74 *MODEL  *PR
75 *NC       2     2
76 *TRES     50
77 *COMPNAME
78 'CO2'            'CH4'
79 ** The Hydrocarbon component flag values, 1 - HC, 0 - non-HC
```

```
80 ** the read-in HC-HC BIN values (provided below in this file)
81 ** will be overwritten by the internal GEM calculated values.
82 ** If you want to use FULL BIN values provided in this file
83 ** in your GEM simulation these values have to be manually
84 ** changed to 0.
85 *HCFLAG      0                1
86 *SG          8.1800000E-01   3.0000000E-01
87 *TB         -7.8450000E+01  -1.6145000E+02
88
89 *RESULTS EOSSET_ID     1
90
91 *PCRIT       7.2800000E+01   4.5400000E+01
92 *VCRIT       9.4000000E-02   9.9000000E-02
93 *TCRIT       3.0420000E+02   1.9060000E+02
94 *AC          2.2500000E-01   8.0000000E-03
95 *MW          4.4010000E+01   1.6043000E+01
96 *PVC3   1.20000000E+00
97 *BIN
98 1.0500000E-01
99 *VSHIFT      0.0000000E+00   0.0000000E+00
100 *VISCOR   *HZYT
101 *MIXVC      1.0000000E+00
102 *VISVC      9.4000000E-02   9.9000000E-02
103 *VISCOEFF    1.0230000E-01   2.3364000E-02   5.8533000E-02
        -4.0758000E-02
104 9.3324000E-03
105 *OMEGA      4.5723553E-01   4.5723553E-01
```

```
106 *OMEGB          7.7796074E-02   7.7796074E-02
107 *PCHOR          7.8000000E+01   7.7000000E+01
108
109 *SOLUBILITY
110 *HENRY-CORR-CO2
111 *TRACE-COMP  2
112
113 *ENTHCOEF
114 9.6880000E-02   1.5884300E-01  -3.3712000E-05   1.4810500E-07
115 -9.6620300E-11   2.0738320E-14
116 -2.8385700E+00   5.3828500E-01  -2.1140900E-04   3.3927600E-07
117 -1.1643220E-10   1.3896120E-14
118
119 *AQUEOUS-DENSITY   *ROWE-CHOU
120 *AQUEOUS-VISCOSITY   *KESTIN
121
122 **GEOCHEM_V2
123 **WINPROP  *GEOCHEM_DATABASE   *WOLERY
124
125
126
127
128 *YAQU-RATE-CUTOFF
129 1.000000E-10     0.000000E+00
130
131 *DER-CHEM-EQUIL   *ANALYTICAL
132 *DER-REACT-RATE   *ANALYTICAL
```

```
133
134 PERM_VS_POR K_C
135
136 *ACTIVITY_MODEL    *B_DOT
137 *AQFILL    *OFF
138
139 *NC_AQUEOUS        5
140 *COMPNAME_AQUEOUS
141 'H+'  'Ca++'  'HCO3_'  'CO3__'  'OH_'
142 *MW_AQUEOUS
143 0.1007900E+01     0.4008000E+02     0.6101710E+02     0.6000920E+02
          0.1700730E+02
144 *ION_SIZE_AQUEOUS
145 9.000          6.000          4.500          4.500          3.500
146 *CHARGE_AQUEOUS
147 1.000          2.000         -1.000         -2.000         -1.000
148
149 *NC_MINERAL        1
150 *COMPNAME_MINERAL
151 'Calcite'
152 *MW_MINERAL
153 0.1000892E+03
154 *MASSDENSITY_MINERAL
155 2709.947
156
157 *N_RATE_REACT  1
158 *N_CHEM_EQUIL  3
```

```
159
160
161 ** *LOG-CHEM-EQUIL-CONST is calculated at     5.50 deg. C (
       41.90    deg. F)
162 **REACTION-CHEM   'CO2' + 'H2O' = 'H+' + 'HCO3-'
163 ** *LOG-CHEM-EQUIL-CONST     -6.50277678E+00
164
165 *STOICHIOMETRY
166 -1  0 -1  1  0  1  0  0  0
167
168 *LOG-CHEM-EQUIL-COEFS
169 -6.549243E+00     9.001740E-03    -1.021150E-04     2.761879E-07
       -3.561421E-10
170 **REACTION-CHEM   'CO3--' + 'H+' =   'HCO3-'
171 ** *LOG-CHEM-EQUIL-CONST      1.05413299E+01
172
173 *STOICHIOMETRY
174 0  0  0 -1  0  1 -1  0  0
175 *LOG-CHEM-EQUIL-COEFS
176 1.060796E+01    -1.276757E-02     1.202581E-04    -3.017312E-07
       2.693722E-10
177
178 **REACTION-CHEM   'OH-' + 'H+' =   'H2O'
179 ** *LOG-CHEM-EQUIL-CONST      1.47037154E+01
180
181 *STOICHIOMETRY
182 0  0  1 -1  0  0  0 -1  0
```

```
183 *LOG-CHEM-EQUIL-COEFS
184 1.492816E+01   -4.187619E-02    1.973673E-04   -5.549510E-07
        7.581093E-10
185
186 **REACTION-RATE-TST   'Calcite' + 'H+' = 'Ca++' + 'HCO3-'
187 **  *LOG-CHEM-EQUIL-CONST      1.99026226E+00
188
189 *STOICHIOMETRY
190 0  0  0  -1  1  1  0  0  -1
191 *LOG-CHEM-EQUIL-COEFS
192 2.068889E+00   -1.426678E-02   -6.060961E-06    1.459215E-07
        -4.189284E-10
193 *REACTIVE-SURFACE-AREA      8.800000E+01
194 *ACTIVATION-ENERGY      3.000000E+04
195 *LOG-TST-RATE-CONSTANT      -8.79588
196
197 ANNIH-MATRIX
198 1.00   0.00   0.00   0.00   0.00   1.00   1.00   0.00
199
200 0.00   1.00   0.00   0.00   0.00   0.00   0.00   0.00
201
202 0.00   0.00   1.00   0.00   0.00   1.00   1.00   1.00
203
204 0.00   0.00   0.00   1.00   0.00  -1.00  -2.00  -1.00
205
206 0.00   0.00   0.00   0.00   1.00   0.00   0.00   0.00
207
```

```
208
209
210
211 *DERIVATIVEMETHOD *NUMERALL
212 ** Factors for INVENTORY-CO2
213 *CO2-AQU-FACT
214 0.  0.  1. 1. 0.
215 *CO2-MNR-FACT
216 1.
217
218
219 ** ------------------------ Rock Fluid ------------------
220 *ROCKFLUID
221 *RPT 1  *DRAINAGE
222 *SWT
223 0.000000  0.000000  0.000000  0.000000
224 0.050000  0.000000  0.000000  0.000000
225 0.100000  0.000000  0.000000  0.000000
226 0.150000  0.000010  0.000000  0.000000
227 0.200000  0.000150  0.000000  0.000000
228 0.250000  0.000770  0.000000  0.000000
229 0.300000  0.002440  0.000000  0.000000
230 0.350000  0.005950  0.000000  0.000000
231 0.400000  0.012350  0.000000  0.000000
232 0.450000  0.022870  0.000000  0.000000
233 0.500000  0.039020  0.000000  0.000000
234 0.550000  0.062500  0.000000  0.000000
```

```
235 0.600000   0.095260   0.000000   0.000000
236 0.650000   0.139470   0.000000   0.000000
237 0.700000   0.197530   0.000000   0.000000
238 0.750000   0.272070   0.000000   0.000000
239 0.800000   0.365950   0.000000   0.000000
240 0.850000   0.482250   0.000000   0.000000
241 0.900000   0.624300   0.000000   0.000000
242 0.950000   0.795620   0.000000   0.000000
243 1.000000   1.000000   0.000000   0.000000
244
245 *SGT
246 0.000000   0.000000   0.000000   0.000000
247 0.050000   0.000080   0.000000   0.000000
248 0.100000   0.000680   0.000000   0.000000
249 0.150000   0.002330   0.000000   0.000000
250 0.200000   0.005610   0.000000   0.000000
251 0.250000   0.011140   0.000000   0.000000
252 0.300000   0.019610   0.000000   0.000000
253 0.350000   0.031740   0.000000   0.000000
254 0.400000   0.048370   0.000000   0.000000
255 0.450000   0.070420   0.000000   0.000000
256 0.500000   0.098940   0.000000   0.000000
257 0.550000   0.136180   0.000000   0.000000
258 0.600000   0.180650   0.000000   0.000000
259 0.650000   0.232750   0.000000   0.000000
260 0.700000   0.307520   0.000000   0.000000
261 0.750000   0.395200   0.000000   0.000000
```

```
0.800000   0.506570   0.000000   0.000000
0.850000   0.655620   0.000000   0.000000
0.900000   0.954430   0.000000   0.000000
0.950000   0.977220   0.000000   0.000000
1.000000   1.000000   0.000000   0.000000

*KROIL  *STONE2  *SWSG

** ------------------ Initial ------------------------------
*INITIAL
*VERTICAL  *BLOCK_CENTER  *WATER_GAS
*ZOIL                0.999  0.001
*ZGAS                0.999  0.001

REFPRES
   800.

REFDEPTH
   800.

DWGC
   100.

SWOC
   1.0

**MOLALITY-GASAQU
```

```
289 **0
290
291 *MOLALITY-AQUEOUS-PRIMARY
292 1E-7     0.0001
293
294 **CALC-MOLALITYAQ-SECONDARY *OFF ** (Retain initial molality
       of secondary aq species as is)
295 *VOLUMEFRACTION-MINERAL
296 0.62      **1
297
298 ** ---------- Numerical ----------
299 *NUMERICAL
300 *NORM *PRESS              100.
301 *NORM *SATUR              0.1
302 *NORM *GMOLAR             0.1
303 *NORM *AQUEOUS            0.2
304 *CONVERGE *MAXRES         1.e-4
305 *NORTH 80
306 *DTMIN 1.E-015
307 *DTMAX 20
308
309 ** ---------- Recurrent ----------
310 *RUN
311
312 *DATE 2000 01 01
313 *DTWELL 0.01
314 *AIMWELL *WELLNN
```

```
315 **
316 ** *WELL  1 'CO2-Injector'
317 **$
318 WELL  'CO2-Injector'
319 *INJECTOR 'CO2-Injector'
320 *INCOMP AQUEOUS  0 0 1 0 0 0 1E-14
321 *OPERATE MAX STW  1.4E+01 CONT
322 *OPERATE *MAX *BHP 1.E+05
323 **$            rad  geofac  wfrac  skin
324 GEOMETRY  I  0.2  0.37  1.0  0.0
325 PERF  GEO  'CO2-Injector'
326 **$ UBA       ff    Status  Connection
327       50 50 1  1.0  OPEN    FLOW-FROM  'SURFACE'
328 **
329 ** *WELL  2 'CO2-Producer1'
330 **$
331 WELL  'CO2-Producer1'
332 *PRODUCER 'CO2-Producer1'
333 *OPERATE MAX STW  1.4E+01 CONT
334 *OPERATE *MIN *BHP 14.7
335 **$            rad  geofac  wfrac  skin
336 GEOMETRY  I  0.2  0.37  1.0  0.0
337 PERF  GEO  'CO2-Producer1'
338 **$ UBA       ff    Status  Connection
339       75 75 1  1.0  OPEN    FLOW-TO  'SURFACE'
340 **
341 ** *WELL  3 'CO2-Producer2'
```

```
342 **$
343 WELL   'CO2-Producer2'
344 *PRODUCER 'CO2-Producer2'
345 *OPERATE MAX STW   1.4E+01 CONT
346 *OPERATE *MIN *BHP 14.7
347 **$             rad   geofac   wfrac   skin
348 GEOMETRY   I   0.2   0.37   1.0   0.0
349 PERF   GEO   'CO2-Producer2'
350 **$ UBA         ff     Status   Connection
351       25 25 1   1.0    OPEN     FLOW-TO   'SURFACE'
352
353
354 DATE 2000 02 29
355 DATE 2000 03 31
356 DATE 2000 04 30
357 DATE 2000 05 31
358 DATE 2000 06 30
359 DATE 2000 07 31
360 DATE 2000 08 31
361 DATE 2000 09 30
362 DATE 2000 10 31
363 DATE 2000 11 30
364
365 DATE 2001 01 01
366 DATE 2002 01 01
367 DATE 2003 01 01
368 DATE 2004 01 01
```

```
369 DATE 2005 01 01
370
371 DATE 2006 01 01
372 DATE 2007 01 01
373 DATE 2008 01 01
374 DATE 2009 01 01
375 DATE 2010 01 01
376
377 DATE 2011 01 01
378 DATE 2012 01 01
379 DATE 2013 01 01
380 DATE 2014 01 01
381 DATE 2015 01 01
382
383 DATE 2016 01 01
384 DATE 2017 01 01
385 DATE 2018 01 01
386 DATE 2019 01 01
387 DATE 2020 01 01
388
389 DATE 2021 01 01
390 DATE 2022 01 01
391 DATE 2023 01 01
392 DATE 2024 01 01
393 DATE 2025 01 01
394
395 DATE 2026 01 01
```

```
396 DATE 2027 01 01
397 DATE 2028 01 01
398 DATE 2029 01 01
399 DATE 2030 01 01
400
401 DATE 2031 01 01
402 DATE 2032 01 01
403 DATE 2033 01 01
404 DATE 2034 01 01
405 DATE 2035 01 01
406
407 DATE 2036 01 01
408 DATE 2037 01 01
409 DATE 2038 01 01
410 DATE 2039 01 01
411 DATE 2040 01 01
412
413 DATE 2050 01 01
414 DATE 2060 01 01
415 DATE 2070 01 01
416 DATE 2080 01 01
417 DATE 2090 01 01
418 DATE 2100 01 01
419
420 DATE 2110 01 01
421 DATE 2120 01 01
422 DATE 2130 01 01
```

```
423 DATE 2140 01 01
424 DATE 2150 01 01
425 DATE 2160 01 01
426 DATE 2170 01 01
427 DATE 2180 01 01
428 DATE 2190 01 01
429 DATE 2200 01 01
430
431 DATE 2210 01 01
432 DATE 2220 01 01
433 DATE 2230 01 01
434 DATE 2240 01 01
435 DATE 2250 01 01
436
437 DATE    2260    1    1
438 DATE    2270    1    1
439 DATE    2280    1    1
440 DATE    2290    1    1
441 DATE    2300    1    1
442 DATE    2310    1    1
443 DATE    2320    1    1
444 DATE    2330    1    1
445 DATE    2340    1    1
446 DATE    2350    1    1
447 DATE    2360    1    1
448 DATE    2370    1    1
449 DATE    2380    1    1
```

```
450 DATE     2390     1     1
451 DATE     2400     1     1
452 DATE     2410     1     1
453 DATE     2420     1     1
454 DATE     2430     1     1
455 DATE     2440     1     1
456 DATE     2450     1     1
457 DATE     2460     1     1
458 DATE     2470     1     1
459 DATE     2480     1     1
460 DATE     2490     1     1
461 DATE     2500     1     1
462 *STOP
463
464
465 RESULTS SPEC 'Permeability J'
466 RESULTS SPEC SPECNOTCALCVAL -99999
467 RESULTS SPEC REGION 'All Layers (Whole Grid)'
468 RESULTS SPEC REGIONTYPE 'REGION_WHOLEGRID'
469 RESULTS SPEC LAYERNUMB 0
470 RESULTS SPEC PORTYPE 1
471 RESULTS SPEC EQUALSI 0 1
472 RESULTS SPEC SPECKEEPMOD 'YES'
473 RESULTS SPEC STOP
474
475
476 RESULTS SPEC 'Permeability K'
```

```
477 RESULTS SPEC SPECNOTCALCVAL -99999
478 RESULTS SPEC REGION 'All Layers (Whole Grid)'
479 RESULTS SPEC REGIONTYPE 'REGION_WHOLEGRID'
480 RESULTS SPEC LAYERNUMB 0
481 RESULTS SPEC PORTYPE 1
482 RESULTS SPEC EQUALSI 0 1
483 RESULTS SPEC SPECKEEPMOD 'YES'
484 RESULTS SPEC STOP
```

Appendix C

Molecular Dynamics Code

A simplified Molecular Dynamics (MD) simulation is developed to capture the diffusive behavior of complex miscible fluid interactions observed experimentally. Diffusive fluid particle motion at short time intervals is modeled using the Monte Carlo approach. As explained in the mechanistic depiction of the spontaneous fingering between the miscible fluid-pair crude oil and solvent, small mobile crude-oil molecules mix with the small mobile solvent molecules at early times while large immobile molecules remain in the crude-oil phase (Fig. C.1 t = 0 to 18). Mixing between the large immobile crude-oil molecules with the solvent are captured at later times (Fig. C.1 t $>$ 18).

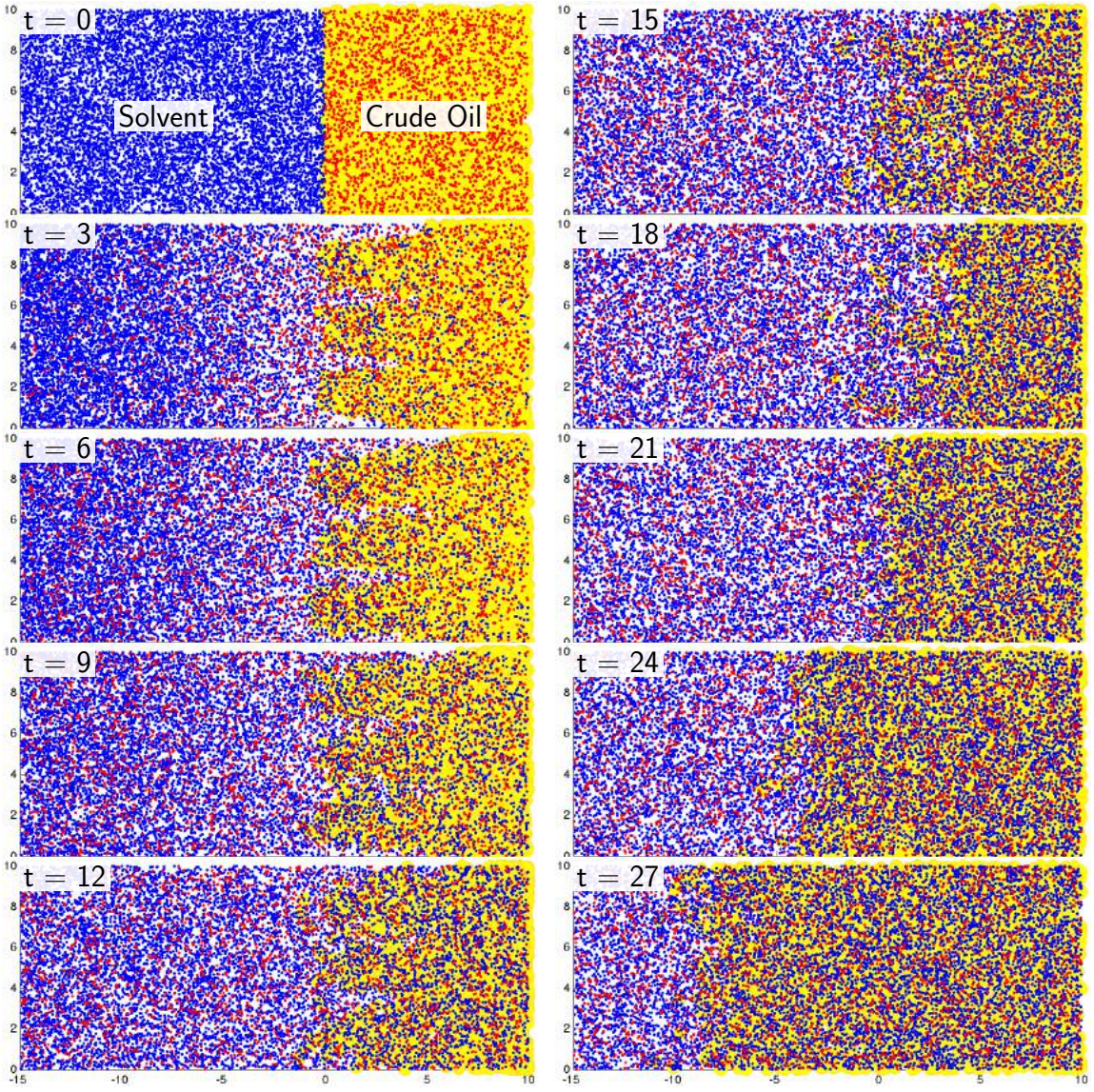

Figure C.1: Monte Carlo molecular dynamics simulation of crude oil interactions with solvent. Solvent (blue) is introduced to the crude oil (red for small molecules and yellow for large molecules). The molecules are allowed to move according to Monte Carlo diffusion and are bounded by the critical wavelength for the instability. Early fingering (t = 0 to 18) and late bulk diffusion (t > 18) are observed.

```
clear all
close all
clc

xlim_min = -15;
xlim_max = 10;
ylim_min = 0;
ylim_max = 10;

boundaries.xmin = -15;
boundaries.xmax = 10;
boundaries.ymin = 0;
boundaries.ymax = 10;
heptane_0.sqrt_num_molecules = 100;
crudeLight_0.sqrt_num_molecules = heptane_0.
    sqrt_num_molecules/2;
crudeHeavy_0.sqrt_num_molecules = heptane_0.
    sqrt_num_molecules/2;
%MD simulation
%potential function for spherical molecules, Lennard-Jones,
    params (IFT)
%start with flat interface, reflection boundaries
%move to radial, wedge
heptane_0.diffusivity = 1;
crudeHeavy_0.diffusivity = heptane_0.diffusivity/30;
crudeLight_0.diffusivity = crudeHeavy_0.diffusivity +
    heptane_0.diffusivity;
```

```
24
25
26 heptane_0.adv.x = 0;
27 heptane_0.adv.y = 0;
28 crudeLight_0.adv.x = 0;
29 crudeLight_0.adv.y = 0;
30 crudeHeavy_0.adv.x = 0;
31 crudeHeavy_0.adv.y = 0;
32 heptane_0.amplitude = 0;
33
34 heptaneMarkerSize = 2;
35 crudeLightMarkerSize = 2;
36 crudeHeavyMarkerSize = 12;
37
38 %% t0: initial fluid distributions
39 heptane_0.x = boundaries.xmin*rand(heptane_0.
       sqrt_num_molecules);
40 heptane_0.y = boundaries.ymax* rand(heptane_0.
       sqrt_num_molecules);
41
42 crudeLight_0.x = boundaries.xmax*rand(crudeLight_0.
       sqrt_num_molecules);
43 crudeLight_0.y = boundaries.ymax* rand(crudeLight_0.
       sqrt_num_molecules);
44
45 crudeHeavy_0.x = boundaries.xmax*rand(crudeHeavy_0.
       sqrt_num_molecules);
```

```
46 crudeHeavy_0.y = boundaries.ymax* rand(crudeHeavy_0.
       sqrt_num_molecules);%crude_heavy.t0.y ;%50* rand(
       crude_heavy.sqrt_num_molecules);
47
48
49
50
51 %% t1: small interfacial perturbations due to thermal
       fluctuations
52 dt =5;
53 heptane_0 = heptane_0;
54 crudeLight_0 = crudeLight_0;
55 crudeHeavy_0 = crudeHeavy_0;
56
57
58
59 for i = 1:1:30
60
61     i
62     t = i*dt;
63
64     if i == 1
65         figure(i)
66         figure('units','normalized','outerposition',[0 0 1
               1]);
67         hold on
68
```

```
69          plot(crudeHeavy_0.x, crudeHeavy_0.y, 'o', 'MarkerSize
                ',crudeHeavyMarkerSize, 'MarkerEdgeColor',[1 .8
                .2], 'MarkerFaceColor','y');
70          plot(heptane_0.x, heptane_0.y, 'bo', 'MarkerSize',
                heptaneMarkerSize, 'MarkerFaceColor','b');
71          plot(crudeLight_0.x, crudeLight_0.y, 'ro', '
                MarkerSize',crudeLightMarkerSize, 'MarkerFaceColor
                ','r');
72          %% plot(crudeLight.x(crudeLight.x<0), crudeLight.y(
                crudeLight.x<0), 'ro', 'MarkerSize',4, '
                MarkerFaceColor','r');
73          axis equal
74          xlim([xlim_min xlim_max])
75          ylim([ylim_min ylim_max])
76          F(i) = getframe;
77          figname = sprintf('_%5.5d.png', i);
78          saveas(gcf,figname,'png')
79
80          heptane_old = heptane_0;
81          crudeLight_old = crudeLight_0;
82          crudeHeavy_old = crudeHeavy_0;
83      else
84          [heptane, crudeLight, crudeHeavy ] = monteCarlo(
                heptane_old, crudeLight_old, crudeHeavy_old, dt, t
                , boundaries);
85
86          figure(i)
```

```
87          figure('units','normalized','outerposition',[0 0 1
                1]);
88          hold on
89          axis equal
90          xlim([xlim_min xlim_max])
91          ylim([ylim_min ylim_max])
92
93          plot(crudeHeavy.x, crudeHeavy.y, 'o', 'MarkerSize',
                crudeHeavyMarkerSize, 'MarkerEdgeColor',[1 .8 .2],
                 'MarkerFaceColor','y');
94          plot(heptane.x, heptane.y, 'bo', 'MarkerSize',
                heptaneMarkerSize, 'MarkerFaceColor','b');
95          plot(crudeLight.x, crudeLight.y, 'ro', 'MarkerSize',
                crudeLightMarkerSize, 'MarkerFaceColor','r');
96          figname = sprintf('_%5.5d.png', i);
97
98          F(i) = getframe;
99          saveas(gcf,figname,'png')
100
101
102         heptane_old = heptane;
103         crudeLight_old = crudeLight;
104         crudeHeavy_old = crudeHeavy;
105     end
106
107 end
108
```

```
109 movie(F,1)
110 v = VideoWriter('newfile.avi');
111 v.FrameRate = 10;
112 v.Quality = 100;
113 open(v)
114 writeVideo(v,F)
115 close(v)
```

```
function [heptane, crudeLight, crudeHeavy ] = monteCarlo(
    heptane_old, crudeLight_old, crudeHeavy_old, dt, t,
    boundaries)
heptane.lambda_C =.5;
shift =  heptane.lambda_C*.5;
a = -4;
b = -3;
% new position = old position + diffusion + advection

crudeLight.sqrt_num_molecules = crudeLight_old.
    sqrt_num_molecules;
crudeHeavy.sqrt_num_molecules = crudeHeavy_old.
    sqrt_num_molecules;
heptane.sqrt_num_molecules = heptane_old.sqrt_num_molecules;

%% crudeLight
crudeLight_x_adv = crudeLight_old.x + crudeLight_old.adv.x*dt
    ;
crudeLight_y_adv = crudeLight_old.y + crudeLight_old.adv.y*dt
    ;
crudeLight.x = crudeLight_x_adv + crudeLight_old.diffusivity*
    dt*normrnd(0,1,size(crudeLight_old.x));
crudeLight.y = crudeLight_y_adv + crudeLight_old.diffusivity*
    dt*normrnd(0,1,size(crudeLight_old.y));
while min(min(crudeLight.x)) < boundaries.xmin || max(max(
    crudeLight.x)) > boundaries.xmax
```

```
18      crudeLight.x = (crudeLight.x>boundaries.xmin).*crudeLight
            .x...
19          + (crudeLight.x<boundaries.xmin).*(crudeLight.x+2*(
                boundaries.xmin-crudeLight.x));
20      crudeLight.x = (crudeLight.x<boundaries.xmax).*crudeLight
            .x...
21          +(crudeLight.x>boundaries.xmax).*(crudeLight.x-2*(
                crudeLight.x-boundaries.xmax));
22  end
23  while min(min(crudeLight.y)) < boundaries.ymin || max(max(
        crudeLight.y)) > boundaries.ymax
24      crudeLight.y = (crudeLight.y>boundaries.ymin).*crudeLight
            .y...
25          + (crudeLight.y<boundaries.ymin).*(crudeLight.y+2*(
                boundaries.ymin-crudeLight.y));
26      crudeLight.y = (crudeLight.y<boundaries.ymax).*crudeLight
            .y...
27          +(crudeLight.y>boundaries.ymax).*(crudeLight.y-2*(
                crudeLight.y-boundaries.ymax));
28  end
29  % crudeLight.diffusivity = crudeLight_old.diffusivity;
30  crudeLight.adv.x = crudeLight_old.adv.x;
31  crudeLight.adv.y = crudeLight_old.adv.y;
32
33
34
35  %% heptane
```

```
36 heptane_x_adv = heptane_old.x + heptane_old.adv.x*dt;
37 heptane_y_adv = heptane_old.y + heptane_old.adv.y*dt;
38 heptane.diffusivity = heptane_old.diffusivity;
39 heptane.adv.x = heptane_old.adv.x;
40 heptane.adv.y = heptane_old.adv.y;
41
42 y_heptane = heptane_y_adv;
43 heptane.amplitude = abs(max(max(heptane_x_adv)) + heptane.
       diffusivity*dt - heptane.adv.x*t)/2;
44 x_heptane = min(min(crudeHeavy_old.x)) + heptane.adv.x*t +
       heptane.amplitude*(cos(y_heptane/heptane.lambda_C - shift)
       );%  heptane.amplitude*cos(y_heptane/3);%+crudeHeavy_old.
       adv.x*dt;
45 heptane_x_adv = (heptane_x_adv).*(heptane_x_adv<x_heptane) +
       ...
46       (x_heptane + min(min(heptane_old.x))*rand(size(x_heptane)
             )).*(heptane_x_adv>x_heptane);
47 heptane.x = heptane_x_adv + heptane_old.diffusivity*dt*
       normrnd(0,1,size(heptane_old.x));
48 heptane.y = heptane_y_adv + heptane_old.diffusivity*dt*
       normrnd(0,1,size(heptane_old.y));
49
50 while min(min(heptane.x)) < boundaries.xmin || max(max(
       heptane.x)) > boundaries.xmax
51       heptane.x = (heptane.x>boundaries.xmin).*heptane.x...
52           + (heptane.x<boundaries.xmin).*(heptane.x+2*(
                boundaries.xmin-heptane.x));
```

```
53      heptane.x = (heptane.x<boundaries.xmax).*heptane.x...
54          +(heptane.x>boundaries.xmax).*(heptane.x-2*(heptane.x
                -boundaries.xmax));
55  end
56  while min(min(heptane.y)) < boundaries.ymin || max(max(
        heptane.y)) > boundaries.ymax
57      heptane.y = (heptane.y>boundaries.ymin).*heptane.y...
58          + (heptane.y<boundaries.ymin).*(heptane.y+2*(
                boundaries.ymin-heptane.y));
59      heptane.y = (heptane.y<boundaries.ymax).*heptane.y...
60          +(heptane.y>boundaries.ymax).*(heptane.y-2*(heptane.y
                -boundaries.ymax));
61  end
62
63  heptane.diffusivity = heptane_old.diffusivity+heptane_old.
        diffusivity*((heptane.amplitude)^(1/a)-(heptane.amplitude)
        ^(1/b))%(heptane.amplitude)^(1/strength) * exp(-1*heptane.
        amplitude)
64
65  %% crudeHeavy
66  crudeHeavy_x_adv = crudeHeavy_old.x + crudeHeavy_old.adv.x*dt
        ;
67  crudeHeavy_y_adv = crudeHeavy_old.y + crudeHeavy_old.adv.y*dt
        ;
68  crudeHeavy.diffusivity = crudeHeavy_old.diffusivity;
69  crudeHeavy.adv.x = crudeHeavy_old.adv.x;
70  crudeHeavy.adv.y = crudeHeavy_old.adv.y;
```

```
71
72 y_crudeHeavy = crudeHeavy_y_adv;
73 x_crudeHeavy = min(min(crudeHeavy_old.x))+(heptane_old.adv.x*
       t) + heptane.amplitude*cos(crudeHeavy_y_adv/heptane.
       lambda_C - shift);%+crudeHeavy_old.adv.x*dt;
74 crudeHeavy_x_adv = crudeHeavy_x_adv.*(crudeHeavy_x_adv>
       x_crudeHeavy) + x_crudeHeavy .* (crudeHeavy_x_adv<
       x_crudeHeavy);
75 crudeHeavy.x = crudeHeavy_x_adv + crudeHeavy_old.diffusivity*
       dt*normrnd(0,1,size(crudeHeavy_old.x));
76 crudeHeavy.y = crudeHeavy_y_adv + crudeHeavy_old.diffusivity*
       dt*normrnd(0,1,size(crudeHeavy_old.y));
77
78 crudeHeavy.x = (crudeHeavy.x>boundaries.xmin).*crudeHeavy.x
       ...
79      + (crudeHeavy.x<boundaries.xmin).*(crudeHeavy.x+2*(
           boundaries.xmin-crudeHeavy.x));...
80 crudeHeavy.x = (crudeHeavy.x<boundaries.xmax).*crudeHeavy.x
       ...
81      +(crudeHeavy.x>boundaries.xmax).*(crudeHeavy.x-2*(
           crudeHeavy.x-boundaries.xmax));
82 crudeHeavy.y = (crudeHeavy.y>boundaries.ymin).*crudeHeavy.y
       ...
83      + (crudeHeavy.y<boundaries.ymin).*(crudeHeavy.y+2*(
           boundaries.ymin-crudeHeavy.y));...
84 crudeHeavy.y = (crudeHeavy.y<boundaries.ymax).*crudeHeavy.y
       ...
```

```
85      +(crudeHeavy.y>boundaries.ymax).*(crudeHeavy.y-2*(
            crudeHeavy.y-boundaries.ymax));
86  crudeHeavy.diffusivity = crudeHeavy.diffusivity+crudeHeavy.
        diffusivity*((heptane.amplitude)^(1/a)-(heptane.amplitude)
        ^(1/b));%* exp(-1*heptane.amplitude);
87
88  crudeLight.diffusivity = crudeHeavy.diffusivity + heptane.
        diffusivity;
89  end
```

Bibliography

[1] IEA. Short-Term Energy Outlook September 2018. Technical report, U.S. Energy Information Adminstration, 2018.

[2] Michael Leahy, Justine L Barden, Brian T Murphy, Nancy Slater-thompson, and David Peterson. International Energy Outlook 2013. Technical report, U.S. Energy Information Adminstration, 2013.

[3] Mark Andersen. Oilfield Glossary: Enhanced Oil Recovery Module. Technical report, Schlumberger, 2018.

[4] Guo-Qing Tang and Norman R. Morrow. Influence of brine composition and fines migration on crude oil/brine/rock interactions and oil recovery. *Journal of Petroleum Science and Engineering*, 24:99–111, 1999.

[5] A. Lager, K.J. Webb, and C.J.J. Black. Impact of Brine Chemistry on Oil Recovery. In *IOR-2007 - 14th European Symposium on Improved Oil Recovery*, 2007.

[6] Xiam-min Zhou, Ole Torsaeter, Xina Xie, and N.R. Morrow. The Effect of Crude-Oil Aging Time and Temperature on the Rate of Water Imbibition and Long-Term Recovery by Imbibition. *SPE Formation Evaluation*, 10(04), 1995.

[7] S. Berg, A. W. Cense, E. Jansen, and K. Bakker. Direct Experimental Evidence of Wettability Modification By Low Salinity. In *International Symposium of the Society of Core Analysts*, number 1996, pages 1–12, Noordwijk, The Netherlands, 2009.

[8] Edin Alagic, Kristine Spildo, Arne Skauge, and Jonas Solbakken. Effect of crude oil ageing on low salinity and low salinity surfactant flooding. *Journal of Petroleum Science and Engineering*, 78(2):220–227, 2011.

[9] Nanji J Hadia, Tone Hansen, and Medad T Tweheyo. Influence of Crude Oil Components on Recovery by High and Low Salinity Water flooding. *Energy Fuels*, 26:4328–4335, 2012.

[10] Arnaud Lager, K J Webb, C J J Black, M Singleton, and K S Sorbie. Low Salinity Oil Recovery - An Experimental Investigation. *Petrophysics*, 49(1):28–35, 2008.

[11] A. R. Kovscek, H. Wong, and C. J. Radke. A pore-level scenario for the development of mixed wettability in oil reservoirs. *AIChE Journal*, 39(6):1072–1085, 6 1993.

[12] F C Benner and F E Bartell. The Effect Of Polar Impurities Upon Capillary And Surface Phenomena In Petroleum Production. *Drilling and Production Practice*, pages 341–48, 1941.

[13] Bijon Sharma. Techniques for mapping the types, volumes, and distribution of clays in petroleum reservoirs for determining their effects on oil production. Technical report, 1994.

[14] P V Brady, R T Cygan, and K L Nagy. *Surface charge and metal sorption to kaolinite*. Woodhead Publishing Limited, 1998.

[15] R C Mackenzie. The classification and nomenclature of clay minerals. *Clay Minerals*, pages 52–66, 1959.

[16] R.H. Worden and S. Morad. *Clay minerals in sandstones: controls on formation, distribution and evolution*, volume 34. 2003.

[17] Cynthia M. Ross. Personal communication., 2018.

[18] Zhihono Zhou and William D. Gunter. The nature of the surface charge of kaolinite. *Clays and Clay Minerals*, 40(3):365–368, 1992.

[19] Patrick V. Brady, Randall T. Cygan, and Kathryn L. Nagy. Molecular Controls on Kaolinite Surface Charge. *Journal of Colloid and Interface Science*, 183:356–364, 1996.

[20] Donahue, Miller, and Shickluna. *Soils: an introduction to soils and plant growth.* Inglewood Cliffs, New Jersey 07632, 4 ed edition, 1977.

[21] Minjune Yang, Michael D Annable, and James W Jawitz. Back Diffusion from Thin Low Permeability Zones. *Environmental Science & Technology*, 49(1):415–422, 2015.

[22] Evgenia V Lebedeva and Andrew Fogden. Adhesion of oil to kaolinite in water. *Environmental science & technology*, 44(24):9470–5, 12 2010.

[23] Tiziana Tosco, Alberto Tiraferri, and Rajandrea Sethi. Ionic Strength Dependent Transport of Microparticles in Saturated Porous Media: Modeling Mobilization and Immobilization Phenomena under Transient Chemical Conditions. *Environmental Science & Technology*, 43(1):4425–4431, 2009.

[24] David M. Clementz. Interaction of Petroleum Heavy Ends with Montmorillonite. *Clays and Clay Minerals*, 24(6):312–319, 1976.

[25] David M Clementz. Alteration of rock properties by adsorption of petroleum heavy ends: implications for enhanced oil recovery. *SPE Enhanced Oil Recovery Symposium*, (4), 1982.

[26] Eliza Czarnecka and J. E. Gillott. Formation and Characterization of Clay Complexes with Bitumen from Athabasca Oil Sand. *The Clay Minerals Society*, 28(3):197–203, 1980.

[27] L.E. Cueic. Evaluation of Reservoir Wettability and Its Effect on Oil Recovery. In N.R. Morrow, editor, *Interfacial Phenomena in Oil Recovery*, chapter 9, pages 319–375. Marcel Dekker New York, 1991.

[28] Jill S Buckley. Evaluation of Reservoir Wettability and its Effect on Oil Recovery. Technical report, 1997.

[29] Andrew Fogden, Munish Kumar, Norman R. Morrow, and Jill S. Buckley. Mobilization of fine particles during flooding of sandstones and possible relations to enhanced oil recovery. *Energy and Fuels*, 25:1605–1616, 2011.

[30] Robert J.S. Brown and Irving Fatt. Measurements Of Fractional Wettability Of Oil Fields' Rocks By The Nuclear Magnetic Relaxation Method. In *Fall Meeting of the Petroleum Branch of AIME*, Los Angeles, CA, 1956.

[31] R.a. Salathiel. Oil Recovery by Surface Film Drainage In Mixed-Wettability Rocks. *Journal of Petroleum Technology*, 25(10), 1973.

[32] J. M. Schembre and A. R. Kovscek. Mechanism of Formation Damage at Elevated Temperature. *Journal of Energy Resources Technology*, 127(3):171, 2005.

[33] J.M. Schembre and Anthony R. Kovscek. Thermally Induced Fines Mobilization : Its Relationship to Wettability and Formation Damage. In *SPE International*

Thermal Operations and Heavy Oil Symposium, pages 1–16, Bakersfield, CA, 2004. Society of Petroleum Engineers.

[34] A Lever and R A Dawe. Water sensitivity and migration of fines in the Hopeman sandstone. *Journal of Petroleum Geology*, 7(1):97–108, 1984.

[35] P.L. L Mcguire, J.R. R Chatham, F.K. K Paskvan, D.M. M Sommer, F.H. H Carini, and B P Exploration. Low Salinity Oil Recovery: An Exciting New EOR Opportunity for Alaska's North Slope. *SPE Western Regional Meeting*, pages 1–15, 2005.

[36] S. Boussour, M. Cissokho, P. Cordier, H. Bertin, and G. Hamon. Oil recovery by low salinity brine injection: Laboratory results outcrop and reservoir cores. *Proceedings - SPE Annual Technical Conference and Exhibition*, 3(2005):1595–1606, 2009.

[37] Nanji Hadia, Håvard Heldal Lehne, Kanwar G Kumar, Kristoffer Selboe, Jan Åge Stensen, Ole Torsæter, Norwegian U Science, and Technology Ntnu. Laboratory Investigation of Low Salinity Waterflooding on Reservoir Rock Samples from the Frøy Field. In Society of Petroleum Engineers, editor, *SPE Middle East Oil and Gas Show and Conference*, 2011.

[38] K Skrettingland, T Holt, M T Tweheyo, and I Skjevrak. Snorre Low-Salinity-Water Injection — Coreflooding Experiments and Single-Well Field Pilot. *SPE Reservoir Evaluation and Engineering*, pages 182 – 192, 2011.

[39] K. S. Sorbie and I. R. Collins. A Proposed Pore-Scale Mechanism for How Low Salinity Waterflooding Works. In *SPE Improved Oil Recovery Symposium*, pages 1–18, Tulsa, Oklahoma, 2010. Society of Petroleum Engineers.

[40] J.M. Schembre, G.-Q. Tang, and a.R. Kovscek. Wettability alteration and oil recovery by water imbibition at elevated temperatures. *Journal of Petroleum Science and Engineering*, 52(1-4):131–148, 6 2006.

[41] K.C. Khilar and H.S. Fogler. The Existence of a Critical Salt Concentration for Particle Release. *Journal of Colloid and Interface Science*, 101(I):214–224, 1984.

[42] A. Lager, K. J. Webb, R. I. Collins, and D. M. Richmond. LoSal Enhanced Oil Recovery : Evidence of Enhanced Oil Recovery at the Reservoir Scale. *Paper SPE 113976 Presented at the 2008 SPE/DOE Improved Oil Recovery Symposium held in Tulsa, Oklahoma, U.S.A., 19-23 April*, 2008.

[43] J.A. Jensen and C.J. Radke. Chromatographic Transport of Alkaline Buffers Through Reservoir Rock. *SPE Reservoir Engineering*, 3(3), 1988.

[44] C A J Appelo. Cation and proton exchange , pH variations , and carbonate reactions in a freshening aquifer. *Water Resources Research*, 30(10):2793–2805, 1994.

[45] Alireza Emadi and Mehran Sohrabi. Visual Investigation of Oil Recovery by Low Salinity Water Injection : Formation of Water Micro-Dispersions and Wettability Alteration. In *SPE Annual Technical Conference and Exhibition*, number 1999, pages 1–15, New Orleans, LA, 2013.

[46] A. Rezaeidoust, T. Puntervold, S. Strand, and T. Austad. Smart water as wettability modifier in carbonate and sandstone: A discussion of similarities/differences in the chemical mechanisms. *Energy and Fuels*, 23(9):4479–4485, 2009.

[47] Jean E. Elkhoury, Pasha Ameli, and Russell L. Detwiler. Dissolution and deformation in fractured carbonates caused by flow of CO2-rich brine under reservoir conditions. *International Journal of Greenhouse Gas Control*, 16:S203–S215, 6 2013.

[48] International Energy Agency. World Energy Outlook. Technical report, 2006.

[49] Naveed Arsalan, Sujeewa S. Palayangoda, Daniel J. Burnett, Johannes J. Buiting, and Quoc P. Nguyen. Surface energy characterization of carbonate rocks. *Colloids and Surfaces A: Physicochemical and Engineering Aspects*, 436:139–147, 9 2013.

[50] Franklin M Orr. Onshore geologic storage of CO2. *Science (New York, N.Y.)*, 325(5948):1656–1658, 9 2009.

[51] C.F. Jordan and J. Lee Wilson. Carbonate reservoir rocks, 1994.

[52] Christopher N. Fredd and H. Scott Fogler. Influence of transport and reaction on wormhole formation in porous media. *AIChE Journal*, 44(9):1933–1949, 9 1998.

[53] Kasper Lund, H. S. Fogler, C.C. McCune, and J.W. Ault. Acidization II: The Dissolution of Calcite in Hydrochloric Acid. *Chemical Engineering Science*, 30:825–835, 1975.

[54] Bert B. Williams, John L. Gidley, Robert S. Schechter, and Society of Petroleum Engineers of AIME. *Acidizing fundamentals*. Richardson, TX, monograph edition, 1979.

[55] Giovanni Paccaloni and Mauro Tambini. Advances in Matrix Stimulation Technology. *Journal of Petroleum Technology*, 45(3):256–263, 1993.

[56] G. Daccord, E. Touboul, and R. Lenormand. Carbonate Acidizing : Toward a Quantitative Model of the Wormholing Phenomenon. *SPE Production Engineering*, 4(1):63–68, 1989.

[57] Jasem M. Al-Besharah, Omar A. Salman, and Saed A. Akashah. Viscosity of Crude Oil Blends. *Industrial and Engineering Chemistry Research*, 26:2445–2449, 1987.

[58] Emil D. Attanasi and Richard F. Meyer. Survey of energy resources. Technical report, World Energy Council, 2010.

[59] P. G. Saffman and Sir Geoffrey Taylor. The penetration of a fluid into a porous medium or Hele-Shaw cell containing a more viscous liquid. *Proceedings of the Royal Society A*, 1958.

[60] Richard F. Meyer, Emil D. Attanasi, and Philip A. Freeman. Heavy oil and natural bitumen resources in geological basins of the world. *U.S. Geological Survey*, 36, 2007.

[61] Huazhou Li, Sixu Zheng, and Daoyong Yang. Enhanced Swelling Effect and Viscosity Reduction of Solvent(s)/CO2/Heavy-Oil Systems. *Society of Petroleum Engineers*, pages 12–14, 2013.

[62] A.A. Prakoso, A.D. Punase, and B. Hascakir. A Mechanistic Understanding of Asphaltene Precipitation from Varying Saturate Concentration Perspective. *Society of Petroleum Engineers*, 2015.

[63] R L Chuoke, P van Meurs, and C. van der Poel. The instability of slow, immiscible, viscous liquid-liquid displacements in permeable media. *Petroleum Transactions, AIME*, 216:188–194, 1959.

[64] Gerard Daccord, Johann Nittmann, and H Eugene Stanley. Radial Viscous Fingers and Diffusion-Limited Aggregation: Fractal Dimension and Growth Sites. *Physical Review Letters*, 56(4), 1986.

[65] G.M. Homsy. Viscous Fingering in Porous Media. *Annual Review of Fluid Mechanics*, 19:271–311, 1987.

[66] D. A. Weitz, J. P. Stokes, R. C. Ball, and A. P. Kushnick. Dynamic Capillary Pressure in Porous Media: Origin of the Viscous-Fingering Length Scale. *Physical Review Letters*, 59(26):2967–2970, 1987.

[67] Zhengming Yang and Yanis C. Yortsos. Asymptotic solutions of miscible displacements in geometries of large aspect ratio. *Physics of Fluids*, 9(2):286–298, 1997.

[68] E Lajeunesse, J Martin, N Rakotomalala, D Salin, and Y C Yortsos. Miscible displacement in a Hele-Shaw cell At High Rates. *J. Fluid Mech.*, 398:299–319, 1999.

[69] N. Goyal and E. Meiburg. Miscible displacements in Hele-Shaw cells: Two-dimensional base states and their linear stability. *Journal of Fluid Mechanics*, 558:329–355, 2006.

[70] Irmgard Bischofberger, Radha Ramachandran, and Sidney R. Nagel. Fingering versus stability in the limit of zero interfacial tension. *Nature Communications*, 5:1–6, 2014.

[71] M. A. Hesse and A. W. Woods. Buoyant dispersal of CO2 during geological storage. *Geophysical Research Letters*, 37(1), 1 2010.

[72] P Zitha, R Felder, D Zornes, K Brown, and K Mohanty. Increasing Hydrocarbon Recovery Factors. *Society of Petroleum Engineers*, pages 1–9, 2011.

[73] Bert Metz, Ogunlade Davidson, Heleen de Coninck, Manuela Loos, and Leo Meyer. IPCC 2005 Special Report on Carbon Capture and Storage. *IPCC*, 2005.

[74] George M Whitesides. The origins and the future of microfluidics. *Nature*, 442(7101):368–373, 2006.

[75] M. Buchgraber, A. R. Kovscek, and L. M. Castanier. A Study of Microscale Gas Trapping Using Etched Silicon Micromodels. *Transport in Porous Media*, 95(3):647–668, 8 2012.

[76] Wen Song and A. R. Kovscek. Direct visualization of pore-scale fines migration and formation damage during low-salinity waterflooding. *Journal of Natural Gas Science and Engineering*, 34:1276–1283, 2016.

[77] Bo Bao, Jason Riordon, Yi Xu, Huawei Li, and David Sinton. Direct Measurement of the Fluid Phase Diagram. *Analytical Chemistry*, 88(14):6986–6989, 2016.

[78] Alfred Chatenever and John C. Calhoun. Visual Examinations of Fluid Behavior in Porous Media - Part I. *Journal of Petroleum Technology*, 4(06):149–156, 1952.

[79] M. Buchgraber, M. Al-Dossary, C.M. Ross, and Anthony R. Kovscek. Creation of a dual-porosity micromodel for pore-level visualization of multiphase flow. *Journal of Petroleum Science and Engineering*, 86-87:27–38, 5 2012.

[80] Wen Song and Anthony R. Kovscek. Functionalization of micromodels with kaolinite for investigation of low salinity oil-recovery processes. *Lab Chip*, 15:3314–3325, 2015.

[81] Naga Siva Kumar Gunda, Bijoyendra Bera, Nikolaos K. Karadimitriou, Sushanta K. Mitra, and S. Majid Hassanizadeh. Reservoir-on-a-Chip (ROC): A new paradigm in reservoir engineering. *Lab on a Chip*, 11(22):3785, 2011.

[82] Junjie Zhong, Jason Riordon, Seyed Hadi Zandavi, Yi Xu, Aaron H. Persad, Farshid Mostowfi, and David Sinton. Capillary Condensation in 8 nm Deep Channels. *Journal of Physical Chemistry Letters*, 9(3):497–503, 2018.

[83] Arnav Jatukaran, Junjie Zhong, Aaron H. Persad, Yi Xu, Farshid Mostowfi, and David Sinton. Direct Visualization of Evaporation in a Two-Dimensional Nanoporous Model for Unconventional Natural Gas. *ACS Applied Nano Materials*, 1(3):1332–1338, 2018.

[84] Bo Bao, Seyed Hadi Zandavi, Huawei Li, Junjie Zhong, Arnav Jatukaran, Farshid Mostowfi, and David Sinton. Bubble nucleation and growth in nanochannels. *Physical Chemistry Chemical Physics*, 19(12):8223–8229, 2017.

[85] Junjie Zhong, Seyed Hadi Zandavi, Huawei Li, Bo Bao, Aaron H. Persad, Farshid Mostowfi, and David Sinton. Condensation in One-Dimensional Dead-End Nanochannels. *ACS Nano*, 11(1):304–313, 2017.

[86] Huawei Li, Junjie Zhong, Yuanjie Pang, Seyed Hadi Zandavi, Aaron Harrinarine Persad, Yi Xu, Farshid Mostowfi, and David Sinton. Direct visualization of fluid dynamics in sub-10 nm nanochannels. *Nanoscale*, 9(27):9556–9561, 2017.

[87] ZhenBang Qi, Ali Abedini, Atena Sharbatian, Yuanjie Pang, Adriana Guerrero, and David Sinton. Asphaltene Deposition during Bitumen Extraction with Natural Gas Condensate and Naphtha. *Energy & Fuels*, page acs.energyfuels.7b03495, 2017.

[88] L. P. Hauge, J. Gauteplass, M. D. Høyland, G. Ersland, A. Kovscek, and M. A. Fernø. Pore-level hydrate formation mechanisms using realistic rock structures in high-pressure silicon micromodels. *International Journal of Greenhouse Gas Control*, 53:178–186, 2016.

[89] Stian Almenningen, Josef Flatlandsmo, Anthony R. Kovscek, Geir Ersland, and Martin A. Fernø. Determination of pore-scale hydrate phase equilibria in sediments using lab-on-a-chip technology. *Lab on a Chip*, 17(23):4070–4076, 2017.

[90] Sandy Morais, Na Liu, Abdou Diouf, Dominique Bernard, Carole Lecoutre, Yves Garrabos, and Samuel Marre. Monitoring CO ¡sub¿2¡/sub¿ invasion processes at the pore scale using geological labs on chip. *Lab Chip*, 16(18):3493–3502, 2016.

[91] Sunniva B. Fredriksen, Arthur U. Rognmo, and Martin A. Fernø. Pore-scale mechanisms during low salinity waterflooding: Oil mobilization by diffusion and osmosis. *Journal of Petroleum Science and Engineering*, 163:650–660, 2017.

[92] Soheil Talebi, Ali Abedini, Pushan Lele, Adriana Guerrero, and David Sinton. Microfluidics-based measurement of solubility and diffusion coefficient of propane in bitumen. *Fuel*, 210(August):23–31, 2017.

[93] Lining Xu, Ali Abedini, Zhen Bang Qi, Mira Kim, Adriana Guerrero, and David Sinton. Pore-scale analysis of steam-solvent coinjection: azeotropic temperature, dilution and asphaltene deposition. *Fuel*, 220(November 2017):151–158, 2018.

[94] Wen Song, Thomas W de Haas, Hossein Fadaei, and David Sinton. Chip-off-the-old-rock: the study of reservoir-relevant geological processes with real-rock micromodels. *Lab Chip*, 14(22):4382–4390, 2014.

[95] Wen Song, Folake Ogunbanwo, Marianne Steinsbø, Martin A. Fernø, and Anthony R. Kovscek. Mechanisms of multiphase reactive flow using biogenically calcite-functionalized micromodels. *Lab Chip*, 2018.

[96] Mark L Porter, Joaquín Jiménez-Martínez, Ricardo Martinez, Quinn McCulloch, J William Carey, and Hari S Viswanathan. Geo-material microfluidics at reservoir conditions for subsurface energy resource applications. *Lab on a chip*, 15(20):4044–53, 2015.

[97] Shilo A. Mahoney, Thomas E. Rufford, Victor Rudolph, Kai Yu Liu, Sandra Rodrigues, and Karen M. Steel. Creation of microchannels in Bowen Basin coals using UV laser and reactive ion etching. *International Journal of Coal Geology*, 144-145:48–57, 2015.

[98] Amélie Neuville, Louis Renaud, Thi Thuy Luu, Mona Wetrhus Minde, Espen Jettestuen, Jan Ludvig Vinningland, Aksel Hiorth, and Dag Kristian Dysthe. Xurography for microfluidics on a reactive solid. *Lab on a Chip*, 17(2):293–303, 2017.

[99] A L Harrison, G M Dipple, W Song, I M Power, K U Mayer, A Beinlich, and D Sinton. Changes in mineral reactivity driven by pore fluid mobility in partially wetted porous media. *Chemical Geology*, 463(January):1–11, 2017.

[100] Willem-Bart Bartels, Hassan Mahani, Steffen Berg, Robin Menezes, Jesse A. van der Hoeven, and Ali Fadili. Oil Configuration Under High-Salinity and Low-Salinity Conditions at Pore Scale: A Parametric Investigation by Use of a Single-Channel Micromodel. *SPE Journal*, 2017.

[101] Tammy Amirian, Manouchehr Haghighi, and Peyman Mostaghimi. Pore Scale Visualization of Low Salinity Water Flooding as an Enhanced Oil Recovery Method. *Energy and Fuels*, 31(12):13133–13143, 2017.

[102] Stephen A. Bowden, Yukie Tanino, Blessing Akamairo, and Magali Christensen. Recreating mineralogical petrographic heterogeneity within microfluidic chips: assembly, examples, and applications. *Lab on a Chip*, 16(24):4677–4681, 2016.

[103] R. W. Liefferink, A. Naillon, D. Bonn, M. Prat, and N. Shahidzadeh. Single layer porous media with entrapped minerals for microscale studies of multiphase flow. *Lab on a Chip*, 18:1094–1104, 2018.

[104] Yukie Tanino, Xanat Zacarias-Hernandez, and Magali Christensen. Oil/water displacement in microfluidic packed beds under weakly water-wetting conditions: competition between precursor film flow and piston-like displacement. *Experiments in Fluids*, 59(2):1–11, 2018.

[105] Hyundo Lee, Seung Goo Lee, and Patrick Doyle. Photopatterned oil-reservoir micromodels with tailored wetting properties. *Lab Chip*, 15:3047–3055, 2015.

[106] Seung Goo Lee, Hyundo Lee, Ankur Gupta, Sehoon Chang, and Patrick S. Doyle. Site-Selective In Situ Grown Calcium Carbonate Micromodels with Tunable Geometry, Porosity, and Wettability. *Advanced Functional Materials*, 2016.

[107] David Sinton. Energy: the microfluidic frontier. *Lab on a chip*, 14(17):3127–3134, 2014.

[108] Wen Song, Hossein Fadaei, and David Sinton. Determination of Dew Point Conditions for CO2 with Impurities Using Microfluidics. *Environmental Science & Technology*, 48:3567–3574, 2014.

[109] Yi Xu, Jason Riordon, Xiang Cheng, Bo Bao, and David Sinton. The Full Pressure–Temperature Phase Envelope of a Mixture in 1000 Microfluidic Chambers. *Angewandte Chemie - International Edition*, 56(45):13962–13967, 2017.

[110] C. Duan, R. Karnik, M.-C. Lu, and A. Majumdar. Evaporation-induced cavitation in nanofluidic channels. *Proceedings of the National Academy of Sciences*, 109(10):3688–3693, 2012.

[111] Paolo Arosio, Kevin Hu, Francesco A. Aprile, Thomas Müller, and Tuomas P.J. Knowles. Microfluidic Diffusion Viscometer for Rapid Analysis of Complex Solutions. *Analytical Chemistry*, 88(7):3488–3493, 2016.

[112] Siddhartha Gupta, William S. Wang, and Siva A. Vanapalli. Microfluidic viscometers for shear rheology of complex fluids and biofluids. *Biomicrofluidics*, 10(4):1–26, 2016.

[113] Christopher J. Pipe and Gareth H. McKinley. Microfluidic rheometry. *Mechanics Research Communications*, 36(1):110–120, 2009.

[114] L. E. Rodd, J. J. Cooper-White, D. V. Boger, and G. H. McKinley. Role of the elasticity number in the entry flow of dilute polymer solutions in micro-fabricated contraction geometries. *Journal of Non-Newtonian Fluid Mechanics*, 143(2-3):170–191, 2007.

[115] Lucy E. Rodd, Timothy P. Scott, David V. Boger, Justin J. Cooper-White, and Gareth H. McKinley. The inertio-elastic planar entry flow of low-viscosity elastic fluids in micro-fabricated geometries. *Journal of Non-Newtonian Fluid Mechanics*, 129(1):1–22, 2005.

[116] Mohammad Heshmati and Mohammad Piri. Interfacial boundary conditions and residual trapping: A pore-scale investigation of the effects of wetting phase flow rate and viscosity using micro-particle image velocimetry. *Fuel*, 224(March):560–578, 2018.

[117] Andrew Sell, Hossein Fadaei, Myeongsub Kim, and David Sinton. Measurement of CO2 Diffusivity for Carbon Sequestration: A Microfluidic Approach for Reservoir-Specific Analysis. *Environmental Science & Technology*, 47(1):71–78, 2013.

[118] Atena Sharbatian, Ali Abedini, Zhenbang Qi, and David Sinton. Full Characterization of CO2-Oil Properties On-Chip: Solubility, Diffusivity, Extraction Pressure, Miscibility, and Contact Angle. *Analytical Chemistry*, 90(4):2461–2467, 2018.

[119] Hossein Fadaei, John M. Shaw, and David Sinton. Bitumen–Toluene Mutual Diffusion Coefficients Using Microfluidics. *Energy & Fuels*, 27(4):2042–2048, 4 2013.

[120] Phong Nguyen, Danyal Mohaddes, Jason Riordon, Hossein Fadaei, Pushan Lele, and David Sinton. Fast Fluorescence-Based Microfluidic Method for Measuring Minimum Miscibility Pressure of CO2 in Crude Oils. *Analytical Chemistry*, 87(6):3160–3164, 2015.

[121] Jinbo Wu, Tsz Yan Kwok, Xiaolin Li, Wenbin Cao, Yu Wang, Junying Huang, Yaying Hong, Dongen Zhang, and Weijia Wen. Mapping three-dimensional temperature in microfluidic chip. *Scientific Reports*, 3:1–7, 2013.

[122] Quentin Brosseau, Jérémy Vrignon, and Jean-Christophe Baret. Microfluidic Dynamic Interfacial Tensiometry (μDIT). *Soft Matter*, 10(17):3066, 2014.

[123] Scott S. H. Tsai, Jason S. Wexler, Jiandi Wan, and Howard A. Stone. Microfluidic ultralow interfacial tensiometry with magnetic particles. *Lab Chip*, 13(1):119–125, 2013.

[124] J H Xu, S W Li, W J Lan, and G S Luo. Microfluidic Approach for Rapid Interfacial Tension Measurement Microfluidic Approach for Rapid Interfacial Tension Measurement. *Langmuir*, 24(22):11287–11292, 2008.

[125] Hao Gu, Michel H.G. Duits, and Frieder Mugele. Interfacial tension measurements with microfluidic tapered channels. *Colloids and Surfaces A: Physicochemical and Engineering Aspects*, 389(1-3):38–42, 2011.

[126] Brendon Morin, Yafei Liu, Vladimir Alvarado, and John Oakey. A microfluidic flow focusing platform to screen the evolution of crude oil-brine interfacial elasticity. *Lab on a Chip*, 16(16):3074–3081, 2016.

[127] Ke Xu, Peixi Zhu, Tatiana Colon, Chun Huh, and Matthew Balhoff. A Microfluidic Investigation of the Synergistic Effect of Nanoparticles and Surfactants in Macro-Emulsion-Based Enhanced Oil Recovery. *SPE Journal*, 22(02):459–469, 2017.

[128] Phong Nguyen, Hossein Fadaei, and David Sinton. Pore-Scale Assessment of Nanoparticle-Stabilized CO ¡sub¿2¡/sub¿ Foam for Enhanced Oil Recovery. *Energy & Fuels*, 28(10):6221–6227, 2014.

[129] Ali Telmadarreie and Japan J. Trivedi. Post-Surfactant CO2 Foam/Polymer-Enhanced Foam Flooding for Heavy Oil Recovery: Pore-Scale Visualization in Fractured Micromodel. *Transport in Porous Media*, 113(3):717–733, 2016.

[130] Marc H. Schneider, Vincent J. Sieben, Abdel M. Kharrat, and Farshid Mostowfi. Measurement of asphaltenes using optical spectroscopy on a microfluidic platform. *Analytical Chemistry*, 85(10):5153–5160, 2013.

[131] Myeongsub Kim, Andrew Sell, and David Sinton. Aquifer-on-a-Chip: understanding pore-scale salt precipitation dynamics during CO2 sequestration. *Lab on a chip*, 13(13):2421–2662, 3 2013.

[132] Benzhong Zhao, Christopher W. MacMinn, and Ruben Juanes. Wettability control on multiphase flow in patterned microfluidics. *Proceedings of the National Academy of Sciences*, 113(37):10251–10256, 2016.

[133] Ran Hu, Jiamin Wan, Yongman Kim, and Tetsu K. Tokunaga. Wettability impact on supercritical CO2 capillary trapping: Pore-scale visualization and quantification. *Water Resources Research*, 53(8):6377–6394, 2017.

[134] Chung Hyuk Lee, James Hinebaugh, Rupak Banerjee, Stephane Chevalier, Rami Abouatallah, Rainey Wang, and Aimy Bazylak. Influence of limiting throat and flow regime on oxygen bubble saturation of polymer electrolyte membrane electrolyzer porous transport layers. *International Journal of Hydrogen Energy*, 42(5):2724–2735, 2017.

[135] Rajveer Singh, Mayandi Sivaguru, Glenn A. Fried, Bruce W. Fouke, Robert A. Sanford, Martin Carrera, and Charles J. Werth. Real rock-microfluidic flow cell: A test bed for real-time in situ analysis of flow, transport, and reaction in a subsurface reactive transport environment. *Journal of Contaminant Hydrology*, 204(April):28–39, 2017.

[136] A.R. Kovscek, G.-Q. Tang, and C.J. Radke. Verification of Roof snap off as a foam-generation mechanism in porous media at steady state. *Colloids and Surfaces A: Physicochemical and Engineering Aspects*, 302(1-3):251–260, 7 2007.

[137] F.A.L. Dullien. *Porous Media: Fluid Transport and Pore Structure*. Academic Press, San Diego, 2nd ed. edition, 1992.

[138] Vincent Linder, Hongkai Wu, Xingyu Jiang, and George M. Whitesides. Rapid Prototyping of 2D Structures with Feature Sizes Larger than 8 um. *Analytical Chemistry*, 75(10):2522–2527, 2003.

[139] Frieder Mugele, Bijoyendra Bera, Andrea Cavalli, Igor Siretanu, Armando Maestro, Michel Duits, Martien Cohen-Stuart, Dirk van den Ende, Isabella Stocker, and Ian Collins. Ion adsorption-induced wetting transition in oil-water-mineral systems. *Scientific Reports*, 5:10519, 2015.

[140] H Mahani, S Berg, D Ilic, W Bartels, and V Joekar-Niasar. Kinetics of Low-Salinity-Flooding Effect. *SPE Journal*, (February), 2015.

[141] Bolivia Vega, Abhishek Dutta, and Anthony R. Kovscek. CT Imaging of Low-Permeability, Dual-Porosity Systems Using High X-ray Contrast Gas. *Transport in Porous Media*, 101:81–97, 2014.

[142] Phong Nguyen, Hossein Fadaei, and David Sinton. Microfluidics Underground: A Micro-Core Method for Pore Scale Analysis of Supercritical CO2 Reactive Transport in Saline Aquifers. *Journal of Fluids Engineering*, 135(2):021203, 3 2013.

[143] Thomas W de Haas, Hossein Fadaei, Uriel Guerrero, and David Sinton. Steam-on-a-chip for oil recovery: the role of alkaline additives in steam assisted gravity drainage. *Lab on a chip*, 13(19):3832–9, 7 2013.

[144] S. A. Bowden, P. B. Monaghan, R. Wilson, J. Parnell, and J. M. Cooper. The liquid-liquid diffusive extraction of hydrocarbons from a North Sea oil using a microfluidic format. *Lab on a chip*, 6(6):740–743, 2006.

[145] Stephen A. Bowden, Rab Wilson, John Parnell, and Jonathan M. Cooper. Determination of the asphaltene and carboxylic acid content of a heavy oil using a microfluidic device. *Lab on a chip*, 9(6):828–832, 2009.

[146] Stephen A. Bowden, Jonathan M. Cooper, Fritz Greub, Dali Tambo, and Andrew Hurst. Benchmarking methods of enhanced heavy oil recovery using a microscaled bead-pack. *Lab on a chip*, 10(7):819–823, 2010.

[147] Igor Bondino, Shashvat Doorwar, Raed Ellouz, and Gerald Hamon. Visual microscopic investigations about the role of pH, salinity, and clay on oil adhesion. In *International Symposium of the Society of Core Analysts*, pages 1–12, Nappa Valley, CA, 2013.

[148] Jing Peng. Heavy-Oil Solution Gas Drive and Fracture Reconsolidation of Diatomite During Thermal Operations. Master's thesis, Stanford University, 2009.

[149] John W Neasham. The Morphology Of Dispersed Clay In Sandstone Reservoirs And Its Effect On Sandstone Shaliness Pore Space And Fluid Flow Properties. In *SPE Annual Fall Technical Conference and Exhibition*, Denver, CO, 1977.

[150] S.F. Kia, H.S. Fogler, and M.G. Reed. Effect of salt composition on clay release in Berea sandstones. *SPE*, pages 277–283, 1987.

[151] K.Krishna Mohan, Ravimadhav N. Vaidya, Marion G. Reed, and H.Scott Fogler. Water sensitivity of sandstones containing swelling and non-swelling clays. *Colloids and Surfaces A: Physicochemical and Engineering Aspects*, 73:237–254, 1993.

[152] Phillip Lemon, Abbas Zeinijahromi, Pavel Bedrikovetsky, Ibrahim Shahin, and B G Group Business. Effects of Injected Water Chemistry on Waterflood Sweep

Efficiency via Induced Fines Migration. *J. Canadian Petroleum Technology*, page SPE 140141, 2011.

[153] Abbas Zeinijahromi, Hammam Al-Jassasi, Steve Begg, and Pavel Bedrikovetski. Improving sweep efficiency of edge-water drive reservoirs using induced formation damage. *Journal of Petroleum Science and Engineering*, 130:123–129, 2015.

[154] F Hussain, New South, A Zeinijahromi, P Bedrikovetsky, A Badalyan, and T Carageorgos. Enhanced Oil Recovery Through Low Salinity Fines-Assisted Waterflooding : Laboratory and Mathematical Modelling Physics Mechanisms of Fines Mobilization , Permeability Decline and. *SPE*, pages SPE–171525–MS, 2014.

[155] Cyprien Soulaine. Personal communication., 2016.

[156] E. Hilner, M. P. Andersson, T. Hassenkam, J. Matthiesen, P. A. Salino, and S. L. S. Stipp. The effect of ionic strength on oil adhesion in sandstone – the search for the low salinity mechanism. *Scientific Reports*, 5(9933), 2015.

[157] Xiongyu Chen, Shuang Gao, Amir Kianinejad, and David A. DiCarlo. Steady-state supercritical CO2 and brine relative permeability in Berea sandstone at different temperature and pressure conditions. *Water Resources Research*, pages 6312–6321, 2003.

[158] D.A. DiCarlo, S. Akshay, and M.J. Blunt. Three-Phase Relative Permeability of Water-Wet, Oil-Wet, and Mixed-Wet Sandpacks. *Society of Petroleum Engineers*, 2000.

[159] Xianmin Zhou, N. Morrow, and Shouxiang Ma. Interrelationship of Wettability, Initial Water Saturation, Aging Time, and Oil Recovery by Spontaneous Imbibition and Waterflooding. *SPE Journal*, 5(2):21–24, 2000.

[160] A.R. Kovscek and Y. Wang. Geologic storage of carbon dioxide and enhanced oil recovery. I. Uncertainty quantification employing a streamline based proxy for reservoir flow simulation. *Energy Conversion and Management*, 46(11-12):1920–1940, 7 2005.

[161] S Pacala and R Socolow. Stabilization Wedges : Solving the Climate Problem for the Next 50 Years with Current Technologies. *Science*, 305(August):968–973, 2004.

[162] S. Solomon, D. Qin, M. Manning, Z. Chen, M. Marquis, K.B. Averyt, M. Tignor, and H.L. Miller. *Contribution of Working Group I to the Fourth Assessment Report of the Intergovernmental Panel on Climate Change, 2007*. Cambridge University Press, 2007.

[163] Ed Dlugokencky and Pieter Tans. Trends in Atmospheric Carbon Dioxide, 2016.

[164] A.R. Kovscek and M.D. Cakici. Geologic storage of carbon dioxide and enhanced oil recovery. II. Cooptimization of storage and recovery. *Energy Conversion and Management*, 46(11-12):1941–1956, 7 2005.

[165] Mark D Zoback and Steven M Gorelick. Earthquake triggering and large-scale geologic storage of carbon dioxide. *Proceedings of the National Academy of Sciences of the United States of America*, 109(26):10164–8, 6 2012.

[166] Kurt Zenz House, Daniel P Schrag, Charles F Harvey, and Klaus S Lackner. Permanent carbon dioxide storage in deep-sea sediments. *Proceedings of the*

National Academy of Sciences of the United States of America, 103(33):12291–5, 8 2006.

[167] Jürg M. Matter and Peter B. Kelemen. Permanent storage of carbon dioxide in geological reservoirs by mineral carbonation. *Nature Geoscience*, 2(12):837–841, 11 2009.

[168] Steve Whittaker. IEA GHG Weyburn CO2 Monitoring & Storage Project. Technical report, IEAGHG, 2004.

[169] JJ Dooley, RT Dahowski, CL Davidson, MA Wise, N Cupta, SH Kim, and EL Malone. Carbon Dioxide Capture and Geologic Storage - A Core Element of Global Energy Technology Strategy to Address Climate Change. Technical report, EPA, 2006.

[170] M. A. Celia, S. Bachu, J. M. Nordbotten, and K. W. Bandilla. Status of CO2 storage in deep saline aquifers with emphasis on modeling approaches and practical simulations. *Water Resources Research*, 51(9):6846–6892, 2015.

[171] X Fu, L Cueto-Felgueroso, D Bolster, and R Juanes. Rock dissolution patterns and geochemical shutdown of CO2-brine-carbonate reactions during convective mixing in porous media. *Journal of Fluid Mechanics*, 764:296–315, 2015.

[172] Mike J Bickle. Geological carbon storage. *Nature Geoscience*, 2(December):815–819, 2009.

[173] Thomas A Buscheck, Joshua A White, Susan A Carroll, Jeffrey M Bielicki, and Roger D Aines. Managing geologic CO2 storage with pre-injection brine production: a strategy evaluated with a model of CO2 injection at Snøhvit. *Energy & Environmental Science*, 9(1):1504–1512, 2016.

[174] E Bemer and J.M. Lombard. From Injectivity to Integrity Studies of CO2 Geological Storage. *Oil & Gas Science and Technology – Revue de l'Institut Français du Pétrole*, 65(3):445–459, 2010.

[175] Daniel J Garcia, Hongbo Shao, Yandi Hu, Jessica R Ray, and Young-shin Jun. Supercritical CO2–brine induced dissolution, swelling, and secondary mineral formation on phlogopite surfaces at 75–95 C and 75 atm. *Energy & Environmental Science*, pages 5758–5767, 2012.

[176] M. Fleury, J. Pironon, Y. M. Le Nindre, O. Bildstein, P. Berne, V. Lagneau, D. Broseta, T. Pichery, S. Fillacier, M. Lescanne, and O. Vidal. Evaluating sealing efficiency of caprocks for CO2 storage: An overview of the geocarbone integrity program and results. *Energy Procedia*, 4:5227–5234, 2011.

[177] Brett K. Brunk, Gerhard H. Jirka, and Leonard W. Lion. Effects of salinity changes and the formation of dissolved organic matter coatings on the sorption of phenanthrene: Implications for pollutant trapping in estuaries. *Environmental Science and Technology*, 31(1):119–125, 1997.

[178] Holger Ott and Sjaam Oedai. Wormhole formation and compact dissolution in single- and two-phase CO2-brine injection. *Geophysical Research Letters*, pages 2270 – 2276, 2015.

[179] C N Fredd and H Scott Fogler. Alternative Stimulation Fluids and Their Impact on Carbonate Acidizing. *SPE Journal*, pages 34–41, 1998.

[180] M. L. Hoefner and H. S. Fogler. Pore evolution and channel formation during flow and reaction in porous media. *AIChE Journal*, 34(1):45–54, 1 1988.

[181] Yi Yang, Christian Ronziob, and Young-Shin Jun. Environmental Science effects of initial acetate concentration on CO2– brine-anorthite interactions under

geologic CO2 sequestration conditions. *Energy & Environmental Science*, pages 4596–4606, 2011.

[182] Svenja K. Reinke, Stephan V. Roth, Gonzalo Santoro, JosÃ©lio Vieira, Stefan Heinrich, and Stefan Palzer. Tracking Structural Changes in Lipid-based Multicomponent Food Materials due to Oil Migration by Microfocus Small-Angle X-ray Scattering. *Applied Materials and Interfaces*, 18:9929–9936, 2015.

[183] Richard S. Middleton, Gordon N. Keating, Philip H. Stauffer, Amy B. Jordan, Hari S. Viswanathan, Qinjun J. Kang, J. William Carey, Marc L. Mulkey, Enid J. Sullivan, Shapin P. Chu, Richard Esposito, and Timothy A. Meckel. The cross-scale science of CO2 capture and storage: from pore scale to regional scale. *Energy & Environmental Science*, 5:7328–7345, 2012.

[184] Yongman Kim, Jiamin Wan, Timothy J. Kneafsey, and Tetsu K. Tokunaga. Dewetting of silica surfaces upon reactions with supercritical CO2 and brine: Pore-scale studies in micromodels. *Environmental Science and Technology*, 46(7):4228–4235, 2012.

[185] Tetsu K. Tokunaga, Jiamin Wan, Jong Won Jung, Tae Wook Kim, Yongman Kim, and Wenming Dong. Capillary pressure and saturation relations for supercritical CO2 and brine in sand: High-pressure Pc(Sw) controller/meter measurements and capillary scaling predictions. *Water Resources Research*, 49(8):4566–4579, 2013.

[186] Markus Buchgraber, Torsten Clemens, Louis Castanier, and Anthony Kovscek. A Microvisual Study of the Displacement of Viscous Oil by Polymer Solutions. *SPE Journal*, 14(3):269–280, 2011.

[187] Jiamin Wan, Tetsu K. Tokunaga, Chin-Fu Tsang, and Gudmundur S. Bodvarsso. Improved glass micromodel methods for studies of flow and transport in fractured porous media. *Water Resources Research*, 32(7):1955–1964, 1996.

[188] Markus Buchgraber. *Microvisual Investigations to Assess and Understand Enhanced Oil Recovery Processes Using Etched Silicon Micromodels*. PhD thesis, Stanford University, 2013.

[189] Gráinne El Mountassir, Rebecca J. Lunn, Heather Moir, and Erica Maclachlan. Hydrodynamic coupling in microbially mediated fracture mineralization: Formation of self-organized groundwater flow channels. *Water Resources Research*, 50(1):1–16, 2014.

[190] Ellen G. Lauchnor, Logan N. Schultz, Steven Bugni, Andrew C. Mitchell, Alfred B. Cunningham, and Robin Gerlach. Bacterially induced calcium carbonate precipitation and strontium coprecipitation in a porous media flow system. *Environmental Science and Technology*, 47(3):1557–1564, 2013.

[191] E. G. Lauchnor, D. M. Topp, A. E. Parker, and R. Gerlach. Whole cell kinetics of ureolysis by Sporosarcina pasteurii. *Journal of Applied Microbiology*, 118(6):1321–1332, 2015.

[192] Ali Vahabi, Ali Akbar Ramezanianpour, Hakimeh Sharafi, Hossein Shahbani Zahiri, Hojatollah Vali, and Kambiz Akbari Noghabi. Calcium carbonate precipitation by strain Bacillus licheniformis AK01, newly isolated from loamy soil: A promising alternative for sealing cement-based materials. *Journal of Basic Microbiology*, 55(1):105–111, 2015.

[193] S. Yoosathaporn, P. Tiangburanatham, S. Bovonsombut, A. Chaipanich, and W. Pathom-aree. A cost effective cultivation medium for biocalcification of

Bacillus pasteurii KCTC 3558 and its effect on cement cubes properties. *Microbiological Research*, 186-187:132–138, 2016.

[194] Kevin G. Knauss, James W. Johnson, and Carl I. Steefel. Evaluation of the impact of CO2, co-contaminant gas, aqueous fluid and reservoir rock interactions on the geologic sequestration of CO2. *Chemical Geology*, 217(3-4 SPEC. ISS.):339–350, 2005.

[195] Sally M. Benson and David R. Cole. CO2sequestration in deep sedimentary formations. *Elements*, 4(5):325–331, 2008.

[196] Pierre Chiquet, Jean-Luc Daridon, Daniel Broseta, and Sylvain Thibeau. CO2/water interfacial tensions under pressure and temperature conditions of CO2 geological storage. *Energy Conversion and Management*, 48:736–744, 2007.

[197] S. Bekri, J.F. Thovert, and P.M. Adler. Dissolution of porous media. *Chemical Engineering Science*, 50(17):2765–2791, 1995.

[198] John W Buza. An Overview of Heavy Oil Carbonate Reservoirs in the Middle East. In *International Petroleum Technology Conference*, volume 10277, pages 1–8, 2010.

[199] R. G. Santos, W. Loh, A. C. Bannwart, and O. V. Trevisan. An overview of heavy oil properties and its recovery and transportation methods. *Brazilian Journal of Chemical Engineering*, 31(3):571–590, 2014.

[200] George Hirasaki and Danhua Leslie Zhang. Surface Chemistry of Oil Recovery From Fractured, Oil-Wet, Carbonate Formations. *SPE Journal*, 9(02):151–162, 2004.

[201] A. R. Kovscek. Emerging challenges and potential futures for thermally enhanced oil recovery. *Journal of Petroleum Science and Engineering*, 98-99:130–143, 2012.

[202] T.J. Boone, K. Sampath, and D.E. Courtnage. Assessment of GHG Emissions Associated with In-Situ Heavy Oil Recovery Processes. In *World Heavy Oil Congress*, Aberdeen, Scotland, 2012.

[203] ZhenBang Qi, Ali Abedini, Pushan Lele, Nader Mosavat, Adriana Guerrero, and David Sinton. Pore-scale analysis of condensing solvent bitumen extraction. *Fuel*, 193:284–293, 2017.

[204] Tao Jiang, Fanhua Zeng, Xinfeng Jia, and Yongan Gu. A new solvent-based enhanced heavy oil recovery method: Cyclic production with continuous solvent injection. *Fuel*, 115:426–433, 2014.

[205] I Bogdanov, S Cambon, M Mujica, and A Brisset. Heavy Oil Recovery via Combination of Radio-Frequency Heating With Solvent Injection. *SPE Canada Heavy Oil Technical Conference*, pages 1–14, 2016.

[206] Birendra Jha, Luis Cueto-Felgueroso, and Ruben Juanes. Fluid Mixing from Viscous Fingering. *Physical Review Letters*, 106(19):194502, 5 2011.

[207] Xiaojing Fu, Luis Cueto-Felgueroso, and Ruben Juanes. Viscous fingering with partially miscible fluids. *Physical Review Fluids*, 2(10):20–24, 2017.

[208] Thomas E. Videbæk and Sidney R. Nagel. Transition to diffusion-driven viscous fingering. 2018.

[209] E. Lajeunesse, J. Martin, N. Rakotomalala, and D. Salin. 3D instability of miscible displacements in a hele-shaw cell. *Physical Review Letters*, 79(26):5254–5257, 1997.

[210] P.M.J. Trevelyan, C. Almarcha, and A. De Wit. Buoyancy-driven instabilities of miscible two-layer stratifications in porous media and Hele-Shaw cells. *Journal of Fluid Mechanics*, 670:38–65, 2011.

[211] Satyajit Pramanik, A. De Wit, and Manoranjan Mishra. Viscous fingering and deformation of a miscible circular blob in a rectilinear displacement in porous media. *Journal of Fluid Mechanics*, 782, 2015.

[212] Domenico Truzzolillo, Serge Mora, Christelle Dupas, and Luca Cipelletti. Off-Equilibrium Surface Tension in Colloidal Suspensions. *Physical Review Letters*, 112(12), 2014.

[213] Domenico Truzzolillo, Serge Mora, Christelle Dupas, and Luca Cipelletti. Nonequilibrium Interfacial Tension in Simple and Complex Fluids. *Physical Review X*, 6(4), 2016.

[214] Domenico Truzzolillo and Luca Cipelletti. Off-equilibrium surface tension in miscible fluids. *Soft Matter*, 13:13 – 21, 2017.

[215] Domenico Truzzolillo and Luca Cipelletti. Hydrodynamic instabilities in miscible fluids. *Journal of Physics: Condensed Matter*, 30, 2018.

[216] Tae Wook Kim, E. Vittoratos, and Anthony R. Kovscek. An Experimental Investigation of Viscous-Oil Recovery Efficiency as a Function of Voidage-Replacement Ratio. *SPE Journal*, 21(04):1236–1253, 2016.

[217] James W. Moore and Robert M. Wellek. Diffusion Coefficients of n-Heptane and n-Decane in n-Alkanes and n-Alcohols at Several Temperatures. *Journal of Chemical and Engineering Data*, 19(2):136–140, 1974.

[218] Olivier Praud and Harry L. Swinney. Fractal dimension and unscreened angles measured for radial viscous fingering. *Physical Review E - Statistical, Nonlinear, and Soft Matter Physics*, 72(1):1–10, 2005.

[219] Paul Meakin. Diffusion-controlled cluster formation in 2-6 dimensional space. *Physical Review A*, 27(3):1495–1507, 1983.

[220] Johann Nittmann, Gerard Daccord, and H. Eugene Stanley. Fractal growth viscous fingers: quantitative characterization of a fluid instability phenomenon. *Nature*, (314):141–144, 1985.

[221] T. A. Witten Jr. and L. M. Sander. Diffusion-Limited Aggregation, a Kinetic Critical Phenomenon. *Physical Review Letters*, 47, 1981.

[222] T. A. Witten Jr. and L. M. Sander. Diffusion-Limited Aggregation. *Physical Review B*, 27, 1983.

[223] Lincoln Paterson. Radial Fingering in a Hele Shaw Cell. *Journal Fluid Mechanics*, 113:513 – 529, 1981.

[224] Muhammad Sahimi and Yanis C. Yortsos. Pattern formation in viscous fingering: A diffusion-limited aggregation approach. *Physical Review A*, 32(6):3762 – 3764, 1985.

[225] W. Hayduk and B. S. Minhas. Correlations for prediction of molecular diffusivities in liquids. *The Canadian Journal of Chemical Engineering*, 60:295–299, 1982.

[226] Steven Chu and Arun Majumdar. Opportunities and challenges for a sustainable energy future. *Nature*, 488(7411):294–303, 2012.

[227] H.A. Stone, A.D. Stroock, and A. Ajdari. Engineering Flows in Small Devices. *Annual Review of Fluid Mechanics*, 36(1):381–411, 2004.

[228] Richard P. Feynman. There's plenty of room at the bottom. In *American Physical Society*, Pasadena, CA, 1959.

[229] Timothy Anderson. Applications of Additive Manufacturing to Rock Analogue Fabrication. *SPE Annual Technical Conference and Exhibition*, 2016.

[230] Sergey Ishutov, T. Dawn Jobe, Shuo Zhang, Miguel Gonzalez, Susan M. Agar, Franciszek J. Hasiuk, Francesca Watson, Sebastian Geiger, Eric Mackay, and Richard Chalaturnyk. Three-dimensional printing for geoscience: Fundamental research, education, and applications for the petroleum industry. *AAPG Bulletin*, 102(1):1–26, 2018.

[231] Sujit S. Datta, T. S. Ramakrishnan, and David A. Weitz. Mobilization of a trapped non-wetting fluid from a three-dimensional porous medium. *Physics of Fluids*, 26(2):022002, 2 2014.

[232] Sujit S. Datta and David A. Weitz. Drainage in a model stratified porous medium. *Europhysics Letters*, 101, 2013.

[233] Sujit S. Krummel, Amber T. Datta, Stefan Münster, and David A. Weitz. Visualizing multiphase flow and trapped fluid configurations in a model three-dimensional porous medium. *AIChE Journal*, 59, 2013.

[234] Sujit S. Datta, Jean-Baptiste Dupin, and David A. Weitz. Fluid breakup during simultaneous two-phase flow through a three-dimensional porous medium. *Physics of Fluids*, (26), 2014.

[235] Alimohammad Anbari, Hung-Ta Chien, Sujit S. Datta, Wen Deng, David A. Weitz, and Jing Fan. Microfluidic Model Porous Media: Fabrication and Applications. *Small*, 14, 2018.

[236] Sujit S. Datta, H. Chiang, T. S. Ramakrishnan, and David A. Weitz. Spatial Fluctuations of Fluid Velocities in Flow through a Three-Dimensional Porous Medium. *Physical Review Letters*, (111), 2013.

[237] Aleem A. Hasham, Ali Abedini, Arnav Jatukaran, Aaron Persad, and David Sinton. Visualization of fracturing fluid dynamics in a nanofluidic chip. *Journal of Petroleum Science and Engineering*, 165(November 2017):181–186, 2018.

[238] Junjie Zhong, Yinuo Zhao, Chang Lu, Yi Xu, Zhehui Jin, Farshid Mostowfi, and David Sinton. Nanoscale Phase Measurement for the Shale Challenge: Multicomponent Fluids in Multiscale Volumes. *Langmuir*, 34, 2018.

[239] Bo Bao, Jason Riordon, Farshid Mostowfi, and David Sinton. Microfluidic and nanofluidic phase behavior characterization for industrial CO2, oil and gas. *Lab Chip*, 17:2740–2759, 2017.